Advances in colloidal and solute groundwater tracing for hygienic risk assessment

Zur Erlangung des akademischen Grades eines
Doktors der Naturwissenschaften an der
Fakultät für Bauingenieur-, Geo- und Umweltwissenschaften
der Universität Karlsruhe
genehmigte

Dissertation

von

Nadine Göppert

aus

Lahr/Schwarzwald

2008

Tag der mündlichen Prüfung: 21. Mai 2008
Referent: Prof. Dr. H. Hötzl
Korreferent: Prof. Dr. C. Groves

Abstract

Tracing techniques are often applied in order to characterize groundwater flow and to delineate drinking water protection zones. Within the scope of the BWPLUS-Project BWR 23008 „Development of an optimized tracing technique to evaluate the hygienic risk for groundwater resources using fluorescent microspheres“ the application of invisible and non-toxic microspheres for this purpose was proposed and the available experimental and analytical methods were further developed and optimized. The transport characteristics of particle tracers were compared with those of well-established solute tracers, such as fluorescent dyes and salts.

Laboratory experiments were performed in order to compare four different detection methods: 1) counting under the fluorescence microscope, 2) fluorescence particle counter, 3) spectrofluorometer and 4) photometer. The different methods were validated and showed reproducible and reliable results. The different methods showed strengths in different fields of application.

A novel method for the continuous online detection of fluorescent microspheres using a spectrofluorometer was developed, including a software tool that allows the transfer of fluorometer data into a format that can be read by conventional evaluation software. The detection limit of the microspheres measured through the use of a photometer is several orders of magnitude higher. For low particle numbers as they are usually related to field experiments, a particle counter with fluorescence detection was used to validate the microscope counting.

Comparative laboratory tests with particles, microorganisms and solute tracers showed distinct tailing for all particles whereas detection of the solute tracer breakthrough started later and stopped earlier than for most of the colloids.

Field tracer tests were carried out in alluvial, fractured and karst aquifers. These have shown that 1 µm spheres and larger particles (up to 5 µm) can be transported in significant concentrations.

The flow behavior of an alpine karst aquifer was highly influenced by the hydrologic conditions. During low-flow conditions, particles travel at higher mean velocities than solutes; during high-flow conditions, the differences between solute and particle transport become smaller. The same behavior was confirmed from a second alpine karst test site.

Particles, solute tracers and bacteria were introduced in an alluvial aquifer.

Particles show an earlier first detection and also reached the most distant sampling point at 200 m. Bacteria were still detected after 50 days.

Solute tracers and particles were also applied in a fractured aquifer. The breakthrough curve of the solutes shows a pronounced tailing while particles show a narrower curve and a small recovery rate which can be explained by non-reversible sorption onto fracture walls.

In consequence, the delineation of groundwater protection zones has to be reviewed and the variable hydrologic conditions must be considered, particularly for karst aquifers. Tracer tests should be repeated during low- and high-flow conditions. The increasing number of floods due to climate change leads to increasing hygienic risk. The application of colloid tracing techniques seems to be essential when the emphasis is placed on hygienic aspects.

Zusammenfassung

Markierungstechniken finden bei der hydraulischen Charakterisierung der Grundwasserleiter im Rahmen von Schutzgebietsabgrenzungen ein weites Anwendungsgebiet. Im Rahmen des BWPLUS-Projektes BWR 23008 „Entwicklung einer optimierten Tracertechnik unter Verwendung von fluoreszierenden Mikrokügelchen zur Bewertung der hygienischen Gefährdung von Grundwässern“ wurde der Einsatz von im Wasser unsichtbaren, human- und ökotoxikologisch unbedenklichen Mikrosphären bei Labor- und Feldversuchen weiterentwickelt und optimiert. Das Transportverhalten der Partikel wurde mit dem von herkömmlichen, löslichen Fluoreszenztracern oder Salzen verglichen.

Mit den Laborexperimenten bot sich eine gute Vergleichsmöglichkeit zwischen den vier verschiedenen Analysenmethoden: 1) Auszählen am Fluoreszenzmikroskop und 2) anhand eines Partikelzählers, 3) Bestimmen der Partikelzahl mit einem Spektralfluorometer und 4) mit einem Photometer. Die verschiedenen Methoden konnten miteinander validiert werden und liefern stabile Messergebnisse. Allerdings bieten sich für die unterschiedlichen Methoden jeweils unterschiedliche Anwendungsbereiche.

Im Rahmen von Laborversuchen wurde eine neue Methode der Online-Messung mit einem Spektrofluorometer und eine Auswertesoftware entwickelt, die es ermöglicht die Datenmenge weiterzuverarbeiten und in ein für gängige Auswertesoftware lesbares Format umzuwandeln. Die Nachweisgrenze ist höher als beim direkten Auszählen, der Aufwand aber erheblich geringer. Das Fluorimeter ist dem Photometer um mehrere Größenordnungen bezüglich der Nachweisgrenze überlegen. Bei niedrigen Partikelkonzentrationen, die üblicherweise bei Feldversuchen auftreten, wurde die Auszählmethode mit einem Partikelzähler validiert.

Vergleichende Laborversuche von Partikeln, Mikroorganismen und gelösten Tracern ergaben ein ausgeprägteres Tailing für alle Partikel, während der Durchgang der Fluoreszenzfarbstoffe später einsetzte und früher beendet war als derjenige der meisten Partikeltracer.

Es wurden Feldversuche in Poren-, Kluft- und Karst-Grundwasserleitern durchgeführt. Diese haben gezeigt, dass die 1-µm-Sphären und auch größere Partikelgrößen (bis 5 µm) in signifikanter Konzentration transportiert werden können.

Für einen Karstgrundwasserleiter konnte ein bedeutender Einfluss der hydrologischen Bedingungen auf das Fließgeschehen gezeigt werden. Bei

Niedrigwasser besitzen die Partikel eine höhere mittlere Fließgeschwindigkeit als die gelösten Stoffe, während bei Hochwasserbedingungen die Unterschiede geringer werden. Dieses Verhalten konnte in einem zweiten alpinen Karst-Testgebiet bestätigt werden.

In einem Porengrundwasserleiter konnten gleichzeitig zu den Partikeln und Fluoreszenzfarbstoffen Bakterien eingegeben werden. Die Partikel treten früher auf und konnten bis zu der am weitesten entfernt gelegenen Probenahmestelle bei 200 m beobachtet werden. Ein weiterer Transport ist nicht auszuschließen. Die Bakterien konnten länger als 50 Tage nachgewiesen werden.

In einem Kluftgrundwasserleiter konnten ebenfalls Partikel und weitere gelöste Tracer gemeinsam eingesetzt werden. Dort findet sich ein Tailing des Fluoreszenzfarbstoffs, die Partikel besitzen eine schmalere Durchgangskurve und zeigen einen deutlich erniedrigten Wiedererhalt, der mit nicht reversibler Sorption an Kluftflächen zu erklären ist.

Für die Ausweisung von Schutzgebieten bedeutet dies, dass Abgrenzungen neu überdacht werden sollen und – beispielsweise in Karstgebieten – die hydrologischen Bedingungen stärker berücksichtigt werden müssen. Die Zunahme der Hochwasserereignisse infolge des Klimawandels verstärkt das hygienische Risiko zusätzlich. Eine Grundwassermarkierung mit Partikeln ist erforderlich, wenn hygienische Fragen im Vordergrund stehen.

Acknowledgement

Meinem Doktorvater Herrn Hötzl bin ich für große Freiheit bei der Auswahl und Bearbeitung des Themas und das dabei entgegengebrachte Vertrauen sehr dankbar. Besonders hervorheben möchte ich die Unterstützung bei den intensiven Feldarbeiten im In- und Ausland, den verschiedenen Konferenzbesuchen und der Umsetzung des halbjährigen Forschungsaufenthalts in den USA.

I am very grateful to Prof. Chris Groves for spontaneously being my Co-Referee and proofreading my thesis.

Im Rahmen der Dissertation konnte ich mit verschiedenen Einrichtungen und Instituten zusammenarbeiten. Diesen möchte ich an dieser Stelle ausdrücklich danken.

Dr. Jakob Zopfi vom Labor für Mikrobiologie der Universität Neuchâtel (LAMUN) für die Durchführung und das Anleiten beim Auszählen der Bakterien und der Bakteriophagen sowie für die Benutzung des Fluoreszenzmikroskops.

Dr. Nico Goldscheider und Michiel Pronk für die Zusammenarbeit im Karstsystem Yverdon-les-Bains und im Hölloch (Kleinwalsertal), Dr. Pierre-André Schnegg und Mathieu Beck für das Feldfluorimeter, die Geoelektrik und die damit verbundene vielfältige Hilfe beim Auswerten der Daten.

Herrn Prof. Werner Käß und seiner Frau Hanna danke ich für die Unterstützung in ihrem Testgebiet in Merdingen, die Hilfe bei der Planung und Durchführung der Versuche, die zahlreichen Analysen und die abschließenden Beprobungen während meines Auslandsaufenthalts.

Dem Umweltamt Vorarlberg für die Durchführung der mikrobiologischen und der begleitenden hydrochemischen Analysen.

Markus Klotz GmbH danke ich für die 5-µm-Partikel und das Auszählen am Partikelzähler.

Die Geodaten wurden vom Landesamt für Geovermessung Bayern in München, vom Landesamt für Vermessung Vorarlberg und von Swisstopo zur Verfügung gestellt. Hydrologische und hydrographische Daten habe ich vom Landeswasserbauamt in Bregenz erhalten. Für die schnelle und unbürokratische Lieferung dieser wertvollen Datensätze danke ich den beteiligten Instituten sehr.

Ein großer Schwerpunkt der Arbeit lag in der Durchführung der Feldarbeiten, die teils unter eher schwierigen Witterungsbedingungen

stattfinden mussten – deshalb bin ich meinen Helfern vor Ort zu besonderem Dank verpflichtet. Dazu gehört neben meinen Eltern und Geschwistern, Laura Muñoz, Fritz Rüf, Familie Paul und Anton Bechter, Tiburt Fritz und Karl Keßler, den Höhlenforschern Sonthofen mit Andreas Wolf und Günther Stautz und Studenten der Universität Karlsruhe. Michel Lambert danke ich für die Unterstützung im Versuchsstollen Lindau, dem Laborpersonal Christine Roske-Stegemann und Chris Buschhaus sowie den Studenten für die Mithilfe im Labor. Verena Herrmann danke ich sehr für ihr stets offenes Ohr und die manchmal durchaus nötige Ablenkung von der umfangreichen Laborarbeit.

Ein großes Dankeschön geht an Nicolette Frech für das unermüdliche Korrekturlesen meiner englischsprachigen Fachartikel und der Dissertation.

Meine Eltern Andreas und Elisabeth Göppert und vor allem meine beiden älteren Geschwister Diane und Ingo haben mich durch ihre stete Diskussionsbereitschaft auf Studium und Promotion sehr gut vorbereitet. Sie sind sicher meine besten Freunde und haben für den Ausgleich zur Arbeit gesorgt.

Dem Mann an meiner Seite vielen Dank für alles.

Contents

List of figures

List of tables

Notation

Latin character

A	Hamaker constant
A_s	Happel parameter
C	concentration
D_e	effective diffusion coefficient
D_L	longitudinal dispersion coefficient
D_m	molecular diffusion
D_o	diffusion coefficient
D_p	pore diffusion coefficient
L	transport length
M	injected tracer mass
N_A	attraction number
N_G	gravity number
N_{gr}	gravitational number
N_{vdw}	van der Waals number
No	total number of injected colloids
Pe	Peclet number
Pe*	modified Peclet number
Q	discharge
R	recovery
T	temperature
V_{DL}	diffuse double layer repulsion
V_{tot}	total electrostatic interaction
V_{vdW}	van der Waals forces

a	diffusion parameter
b	main hydraulic fracture width
c	concentration
c_i	ionic strength
d	grain size
d_p; d_c	diameter ($_p$ – particle; $_c$ – collector)
e	elementary charge
g	gravitational constant
h	distance between particle and collector
i	hydraulic gradient
k_B	Boltzmann constant
k_f	hydraulic conductivity
m	saturated thickness
n	porosity
n_e	effective porosity
n_n	normalization constant
q	volumetric flow rate
r_p; r_c	radius ($_p$ – particle; $_c$ – collector)
r_w	borehole radius
t_o	mean tracer transit time
t_1	first detection time (FDT)
t_4	last detection time
t_a	average colloid travel time
t_f	last colloid detection time
t_m	half-life time
t_p	time of highest concentration
v_p	particle velocity
v_x	average flow velocity
v_y	Darcy velocity
x	distance
z	ionic valence

Greek character

$\Delta\lambda$	Stokes shift
ΔH	piezometric level difference
Ψ_P, Ψ_C	surface potential of particle and collector
α	attachment (=collision) efficiency
α_L	longitudinal dispersivity
β	partition coefficient for mobile and immobile fluid regions
γ	single-collector efficiency
γ_D	single-collector efficiency for transport by diffusion
γ_I	single-collector efficiency for transport by interception
γ_G	single-collector efficiency for transport by sedimentation
ε	dielectric constant
ε_m	matrix porosity
ε_f	fracture porosity
η	single-collector removal efficiency
η_0	single-collector contact efficiency
η_D	single-collector contact efficiency for transport by diffusion
η_I	single-collector contact efficiency for transport by interception
η_G	single-collector contact efficiency for transport by gravitation
ι	fracture tortuosity factor
κ	Debye-Hückel length
κ_d	particle deposition rate coefficient
λ	filter coefficient
μ	dynamic viscosity (water)
ν	kinematic viscosity
$\rho_p; \rho_w$	density ($_p$ – particle; $_w$ – fluid)
ς	integration variable
ω	mass transfer coefficient

Abbrevations

ADE	Advection-dispersion equation
FDT	First detection time
RSD	Relative standard deviation
SFDM	Single fissure dispersion model
TBC	Tracer breakthrough curve
2RNE	Two-region non-equilibrium model

Further abbreviations are discussed as they occur.

That was the fun - seeing it work out.
Maria Göppert-Mayer,
Nobel Prize for Physics (1963)

1 Introduction

1.1 Motivation

Waterborne diseases caused by pathogenic microorganisms are of major concern in developing countries where inadequate drinking water quality (and quantity) and poor sanitation lead to preventable illnesses and deaths. However, the 3.4 million water-related deaths per year [WHO 2006] are not only limited to developing countries. Even in industrialized countries waterborne diseases have not been eradicated, new diseases emerge or previously known ones re-emerge (Tab. 1.1) [Auckenthaler & Huggenberger 2003, Montgomery 2007, Schindler 2003, WHO 1999]. Source water protection and drinking water treatment are supposed to provide protection against disease outbreaks. However, drinking water treatment may not provide sufficient protection against the large variety of possibly occurring pathogens, especially during hydrologically difficult conditions (e.g. storm rainfall). When appropriate treatment concepts or groundwater protection fail, disease outbreaks can occur even in industrialized countries.

The link between disease outbreaks and water has been known since Hippocrates (460-377 B.C.), who was among the first to identify the importance of water without “impurities” for healthiness and recommended in his essay “On air, water and places” to boil water before use. More than two millenia later, Robert Koch (1843-1910) and Friedrich Löffler (1852-1915) postulated four criteria that can be used for identification of a causal relationship between microorganisms and disease outbreaks. With isolation techniques, they were able to find the medical proof of what Hippocrates assumed. With increasing levels of research and new detection methods, it was possible to isolate microorganisms that were causing diseases. It was then the hydrogeologists' contribution to identify the pathway of the microorganisms and the source of contamination. This was the starting point for groundwater tracing experiments.

The first quantitative tracer test was carried out in the Danube-Aach System in Southern Germany by Prof. A. Knop from Karlsruhe in 1877 [Käss 2004]. He used 600 kg of oil shale, 10000 kg of salt and 10 kg of natriumfluorescein and all three appeared 2.5 days later in the Aach spring. In order to better understand the pathway of bacteria, *Serratia marcescens* were first introduced into groundwater in 1896 by Pfuhl. Since 1968 bacteriophages have been used as groundwater tracers.

The use of groundwater tracers and especially that of biological tracer

substances is currently under discussion, because of potential human and ecological toxicity. Tracers are considered to be an artificial preventable impact on an ecosystem. In many countries, the use of groundwater tracing techniques therefore requires special permission and local authorities tend to deny tests in particular due to environmental health aspects. Solute tracers can not be used to adequately simulate the transport behavior of pathogens. In order to find surrogates for biological tracers, harmless latex particles of similar size are increasingly being used [Auckenthaler et al. 2002, Käss 2004].

Tab. 1.1: Selected waterborne diseases after Schindler 2003, Schoenen et al. 2001 (only outbreaks with a number of cases exceeding 1000 are listed).

Year	Location	Country	Disease	Number of cases
1854	Munich	Germany	Cholera	2223
1873	Munich	Germany	Cholera	3075
1885/88	Hamburg	Germany	Typhus	15804
1892	Hamburg	Germany	Cholera	16956
1901	Gelsenkirchen	Germany	Typhus	3231
1908	Petersberg	Germany	Cholera	9000
1919	Pforzheim	Germany	Typhus	4000
1926	Hannover	Germany	Typhus	2500
1946/48	Neuötting	Germany	Typhus	1000
1954/55	Portland	USA	Giardiasis	50000
1955	New Delhi	India	Hepatitis	28745
1974/75	Rome	USA	Giardiasis	4800-5300
1977	Berlin	USA	Giardiasis	approx. 7000
1978	Vail	USA	Giardiasis	5000
1978	Ismaning	Germany	Dysentery	2450
1979	Bradford	USA	Giardiasis	3500
1980	Arizona	USA	Giardiasis	2000
1984	Braun Station	USA	Cryptosporidiosis	2006
1986	Sälen	Sweden	Giardiasis	>1400
1987	Carrolton	USA	Cryptosporidiosis	>13000
1992	Jackson	USA	Cryptosporidiosis	15000
1993	Kitchener-Waterloo	Canada	Cryptosporidiosis	approx. 23900
1993	Milwaukee	USA	Cryptosporidiosis	403000
1994	Nummy Lake	USA	Cryptosporidiosis	2070
1996	Ogose	Japan	Cryptosporidiosis	approx. 9000
1996	Cranbrook	Canada	Cryptosporidiosis	>2000
1996	Kelowna	Canada	Cryptosporidiosis	approx. 4000
1998	La Neuveville	Switzerland	Diarrhea (Norovirus *Campylobacter jejuni*, *Shigella sonnei)*	~2213
2000	Walkerton	USA	Diarrhea (*E.coli* O157)	2300

Today tracer tests are used as valuable tools in order to obtain the hydraulic parameters for the delineation of groundwater protection zones, as specified for Germany in the “Richtlinie W101, Ausweisung von Grundwasserschutz-zonen” - Guideline W101, Delineation of Groundwater Protection Zones”. This is mostly done with fluorescent and salt tracers, although the major concern is often the microbial spring water quality, rather than the chemical contamination, especially in rural areas with intensive agricultural land use (Fig. 1.1). Source water protection necessarily requires good knowledge of general hydrogeological conditions and hydraulic behavior along the pathway through the underground rock or soil. Frequently, this is not the case.

Different types of aquifers, e.g. karst, fractured and porous aquifers, generally show significantly different hydraulic characteristics and therefore a different behavior of solutes or tracer-colloids. Within the same type of aquifers the characteristics can vary due to heterogeneity of different levels.

Over the last 25 years, colloid transport was mainly investigated under laboratory conditions, large scale field experiments in all types of aquifers are lacking [McCarthy et al. 2002]. The general hydrogeology is often not fully characterized and local heterogeneities are not considered.

Fig. 1.1: Cattle and cow dung in the alpine test site that are sources for strong microbial contamination of spring waters.

1.2 Objectives and scope of dissertation

The overall goal of this thesis was to deepen the knowledge of the fundamental hydraulic transport characteristics of colloids (particularly surrogates for microorganisms) compared to those of solutes in different aquifer types and laboratory tests. The work was focused on analysis

methodologies and their feasibility in field studies.

Therefore, the main scientific questions are:

- What are the fundamental differences of the transport parameters for the tested colloids and solutes in different aquifer types and laboratory tests?
- Do the surrogates show the same hydraulic properties and transport behavior as commonly used tracer microorganisms?
- Is it possible to find an appropriate analysis method for microspheres in order to optimize the analysis effort or provide an easy-to-apply validation technique for previously applied methods?

Geology and general hydrogeological aspects are discussed for each test site. This includes also microbial and hydrochemical spring water quality, morphological features and the general infiltration conditions at the surface.

Laboratory tests offer a high level of control and require therefore an accordingly large number of precise experiments to characterize the overall laboratory system (pretests, parallel tests).

Software limitations and data management restrictions that arose during the laboratory work required the development of new software tools, which are based on OpenOffice.org Basic.

1.3 Funding and international cooperation

This thesis shows the results of one major project and selected international co-projects.

The major project was funded by BWPLUS (**B**aden-**W**ürttemberg **P**rogramm **L**ebensgrundlage **U**mwelt und ihre **S**icherung – Baden-Wuerttemberg Program: Environment and its Protection; BWR 23008), which is supported by the Ministry of Environment Baden-Württemberg. It was focused on field experiments, especially tracer tests, in different aquifer types located in Baden-Württemberg and laboratory tests with colloids and solutes in order to find a better way to delineate groundwater protection zones and to investigate the basic transport characteristics of colloids. Within the scope of this project it was possible to cooperate with Prof. Dr. Werner Käss, Umkirch; Markus Klotz GmbH, Bad Liebenzell and Dr. J. Zopfi from the Microbiology Laboratory (LAMUN) at the University of Neuchâtel in Switzerland.

Furthermore, it was possible to participate in the Karstdyn Project (Swiss National Foundation – Project No. 200020-105427) at the Yverdon-les-Bains

test site in cooperation with the Center of Hydrogeology (CHYN) at the University of Neuchâtel (Dr. N. Goldscheider, M. Pronk). The national land survey administration (Swisstopo) provided three-dimensional data (DEM).

The Raiffeissen Holding Kleinwalsertal supported the examination of the hydrogeology of the Hölloch cave system. Speleologists and local people provided data and assistance during the field work. The national land survey of Bavaria (Germany) and Vorarlberg (Austria) provided air photographs and three-dimensional data.

For the Hölloch Project, and for the Hochgrat-Gunzesried Project as well, the Vorarlberg State Administration, Water Management Department, provided local spring water data, the Department of Geographic Information Systems (VoGiS) provided air photographs and laser-scanning data; and the Environmental Institute made microbiological data available.

At the University of Tennessee at Knoxville a project was carried out under supervision of Prof. Dr. L.D. McKay, Prof. Dr. J.F. McCarthy and Prof. Dr. J. Zhuang with financial support by the Department of Earth and Planetary Sciences Jones Hydrogeology Endowment and the U.S. Department of Energy, Environmental Management Science Program. Its intention was to study the capillary force induced transient transport of colloids in horizontal soil columns.

1.4 Thesis organization

Chapter 2 provides the general hydrogeological background of solute and colloid transport characteristics and modeling in different types of aquifers and laboratory tests. It explains the hydrochemical tools that are used in order to characterize the tracer colloids and solutes.

Chapter 3 describes the experimental set-up, column test processing and data management. It shows results and an interpretation of the laboratory tests. It further deals with the necessarily developed software tools that were used to manage the considerably high amount of data obtained during the laboratory tests.

Chapter 4 gives an overview over the field test sites which contains general geology, hydrogeology and hydrochemistry. It focuses on tracer tests and analytical modeling results. One test site is located in a fractured granite, three karst test sites follow. The chapter ends with the description of the alluvial aquifer.

In chapter 5 the results of all previously described tests are summarized, and an outlook provides concepts for future work.

1.5 Major achievements

The main achievement of this thesis is to clarify:

- Application of a novel method of microsphere analysis using a 3D Synchron-Scan method of a spectrofluorometer and software development.
- Testing of a novel particle counter with fluorescence detection in field and laboratory tests.
- Comparison of solute and colloidal tracers in different aquifers and laboratory columns.
- Hydrogeology of the test site Hochgrat-Gunzesried and classification as karst system.

This list gives an overview of the published papers that followed directly from this research:

Göppert, N. & Goldscheider, N.: Solute and colloidal transport in a karst conduit system during low-flow and high-flow conditions, Ground Water (accepted).

Goldscheider, N. & **Göppert**, N. (2006): Das Wasser im Hölloch - Hydrogeologie. In: Das Hölloch im Mahdtal, 100 Jahre Höhlenforschung im Kleinwalsertal, 245-253.

Andreo, B., Vadillo, I., Carrasco, F., Neukum, C., Jimenez, P., Linan, C., Goldscheider, N., Hötzl, H., Ferrer, R., Del Campo, L., **Göppert**, N., Vias, J.M., Perez, I., Sanchez, D. & Cobo, A. (2005): Consideraciones sobre el funcionamiento hidrogeológico y la vulnerabilidad a la contaminación de la Sierra de las Nieves (Málaga) a partir de un ensayo de trazador en condiciones de estiaje.- Geogaceta, 37, 143-146, Madrid.

Göppert, N. (2005): Hydrogeologische und karstkundliche Exkursionen in der Faltenmolasse in Vorarlberg und im Oberallgäu.- Laichinger Höhlenfreund, 40(1), 19-30.

Goldscheider N., **Göppert**, N., Rodenbücher, A., Staib, R. (2004): Partikelzähler und Fluoreszenzdetektion.- Wasser 1, 28.

Goldscheider, N. & **Göppert**, N. (2004): Hydrogeologie der alpinen Karstlandschaften Vorarlbergs.- Vorarlberger Naturschau, 15, 41-62, Dornbirn.

Andreo, B., Vadillo, I., Carrasco, F., Neukum, C., Jimenez, P., Goldscheider, N., Hötzl, H., Vias, J.M., Perez, I., **Göppert**, N. (2004):

Precisiones sobre el funcionamiento hidrodinámico y la vulnerabilidad a la contaminación del acuífero kárstico de la Sierra de Líbar (Provincias de Málaga y Cádiz, sur de España) a partir de un ensayo de trazadores.- Revista de la Sociedad Geológica de España, 17(3-4), 187-197.

Göppert, N., Goldscheider, N. & Scholz, H. (2003): Karsterscheinungen in Konglomeraten im Gebiet Hochgrat-Lecknertal bei Hittisau (Bregenzerwald).- Vorarlberger Naturschau, 12, 9-29, Dornbirn.

Göppert, N., Goldscheider, N. & Scholz, H. (2002): Karsterscheinungen und Hydrogeologie karbonatischer Konglomerate der Faltenmolasse im Gebiet Hochgrat und Lecknertal (Bayern/Vorarlberg).- Beitr. z. Hydr., 53, 21-44, Graz.

The results were presented at conferences and in three annual reports:

Goldscheider, N., **Göppert**, N. & Pronk, M. (2006): Comparison of solute and particle transport in shallow and deep karst aquifer systems.- 8th Conf. on Limestone Hydrogeology, September 21-23, 2006, Neuchâtel, Switzerland.

Göppert, N. & Hötzl, H. (2006): Microbial monitoring and particle tracing as tools for assessing the hygienic risk of alpine karst springs.- AQUAinMED International Congress, April 24-28, 2006, Malaga, Spain.

Göppert, N., Goldscheider, N. & Hötzl, H. (2005): Transport of colloidal and solute tracers in three different types of alpine karst aquifers – Examples from southern Germany and Slovenia.– 10th Multidisciplinary Conference on Sinkholes and the Engineering and Environmental Impacts of Karst, September 24-28, 2005, San Antonio, USA.

Göppert, N., Goldscheider, N. & Hötzl, H. (2003): Overview of karst development in carbonate conglomerates in Europe: A contribution to the IGCP 448 "World Correlation on Karst Ecosystem".- Internat. Conf. on Karst Hydrogeology and Ecosystems, June 3-6, 2003, Bowling Green, USA.

Goldscheider, N., **Göppert**, N., Pochon, A. & Scholz, H. (2002): Karst development in conglomerates of the northern Alps and consequences for groundwater protection.- Karst and Environment, 61-67; Nerja, Spain.

2 Background

2.1 Pathogens and other pollutants in groundwater

2.1.1 Introduction

According to the DVGW (*Deutsche Vereinigung des Gas- und Wasserfaches e.V. - Technisch-wissenschaftlicher Verein = DVGW German Technical and Scientific Association for Gas and Water*) directive, "*Groundwater Protection Zones*" [DVGW 1995] should cover the entire surface and subsurface catchment area and provide sustainable protection against any contamination. Pathogens and other biocolloids adversely affect our groundwater and drinking water quality and can cause waterborne diseases in developing countries and industrialized countries as well (Tab. 2.1). In cases where adequate source protection or the treatment concept fails, considerably high levels of contaminations can occur in drinking water. To evaluate the potential risk of pathogenic contaminations, pathogen-associated fecal bacteria are used as indicators according to the "*Drinking Water Ordinance*" [DVGW 2001].

The regulation for the delineation of groundwater protection zone II, which is defined to protect against pathogens and other pollutants, takes into account the importance of microbial contaminants by using a 50-day-limit because it was assumed that pathogens, particularly protozoan cysts, can survive up to 50 days in groundwater [DVGW 1995]. Today, it is well known that microorganisms can exceed this limit (Fig. 2.1), but it emerged that filtration and decay are effective processes to reduce a large proportion of microorganisms and therefore the limit is an adequate instrument for delineation. Filtration processes are highly dependent on the particle size and characteristics of the geological medium (Fig. 2.2). Different geology and thus aquifer types with different pore space geometries or fissure apertures require special protection schemes.

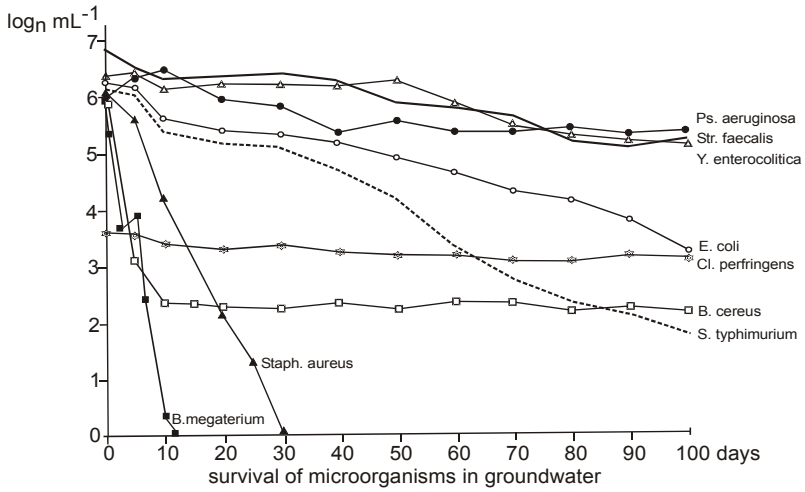

Fig. 2.1: Survival time of microorganisms in groundwater at 10 ± 1°C [Kaddu-Mulindwa et al. 1983].

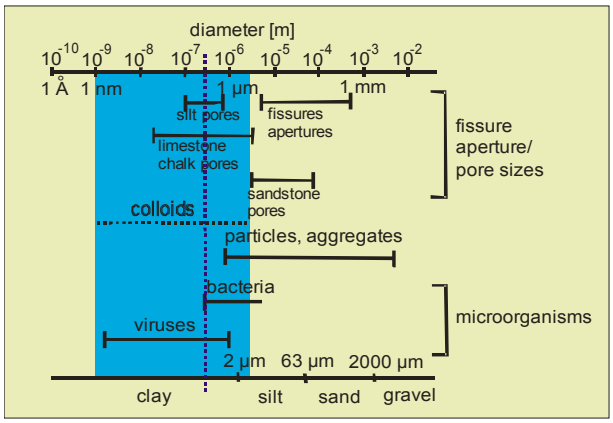

Fig. 2.2: Diameter of microorganisms and pores or fissures; modified after Hofmann 2004, West et al. 1998.

Tab. 2.1: General definitions [Everett 1972, Johnson 2007, Montgomery 2007].

Pathogen: Derived from the Greek παθογένεια which means “that which produces suffering”. The term pathogen is used to refer to infectious organisms, like viruses, bacteria or protozoa.

Fecal bacteria: Bacteria typically found in the wastes of warm-blooded animals. Their presence in water is used to assess the sanitary quality of water for consumption. Their presence indicates contamination by the wastes of warm-blooded animals and the possible presence of pathogenic organisms

Disease category	Description
waterborne	caused by water contaminated by excreta or urine containing pathogens
water-based	caused by parasites found in intermediate organisms living in water
water-related	caused by microorganisms with life cycles associated with insects that live or breed in water
water collection and storage	caused by secondary contamination within the water treatment system
toxin-related	caused by toxic bacteria

Colloid: defined by size limits between 1 nm and 1 µm
Biological colloids: abbr.: biocolloid
biological material in the size of colloids (e.g. viruses, bacteria, protozoa)
Non-biological colloids: colloids of non-biological material, generally means the term colloids (e.g. microspheres, club moss spores, clay minerals)

Pesticides, toxic metals and radionuclides can also be transported as colloids or associated to colloids [McCarthy & Zachara 1989]. Colloids are transported with higher flow velocities and at a higher concentration than expected from conservative solute transport equations.

This thesis is focused on the transport behavior of tracer- and bio-colloids

(Tab. 2.1), although results can be extended to the other colloidal pollutants. The following gives an overview of the general characteristics of the microorganisms and aquifers considered.

2.1.2 Microorganisms

Microorganisms, like viruses, bacteria or protozoa, are on the one hand part of the natural groundwater biocenoses [Hunkeler et al. 2006], on the other hand, some microorganisms cause a large number of waterborne diseases and therefore attract special consideration. It is essential to know about the sources of microbial contamination, the behavior and properties of the microorganisms and underground flow characteristics to delineate an appropriate catchment area and protect against the contamination. Tab. 2.2 gives an overview of the general characteristics of the most important microorganisms in water.

2.1.3 Other colloid-bound contaminants

Besides bio-colloids there are several other pollutants and substances transported as colloids, like radionuclides, that adversely effect groundwater quality as well. Especially in karst systems where microbial quality problems occur very often, turbidity is used as a parameter to give an idea about the potential microbial risk in order to effectively adjust the timing of water treatment. However, an adequate delineation concept avoiding any contamination at a spring is preferred. This could only be undertaken via groundwater tracing.

Tab. 2.2: General characteristics of microorganisms (after Hunkeler et al. 2006, Lytle et al. 2002).

Virus	A virus is a microscopic particle that can infect the cells of a biological organism.
Size	10 – 300 nm
Surface properties (pH=7)	negative
Examples for waterborne diseases caused by viruses	Hepatitis A, gastroenteritis, polio, SARS
Bacteriophage (abbr.: phage)	A bacteriophage is a virus that infects and destroys bacteria.

Bacteria	Bacteria are single-celled, procaryotic microorganisms; they are spherical, rod-shaped or spiral.
Size	0.5 -5 µm
Surface properties (pH=7)	negative
Examples for waterborne diseases caused by bacteria	botulism, cholera, typhoid, diarrheal disease, dysentery, legionellosis

Protozoa	Protozoa are single-celled eucaryotes, some are able to survive hostile environmental conditions as reversible cysts.
Size	1 µm – 50 µm (- 2 mm)
Surface properties (pH=7)	negative
Examples for waterborne diseases caused by protozoa	cryptosporidiosis, giardiasis

2.2 Groundwater landscapes and aquifer types

2.2.1 Introduction

Groundwater landscapes are characterized by common geological-geomorphological characteristics which reflect the properties of the underlying aquifer types (Fig. 2.3). Typically, three different types of aquifers are known: karst, fractured/fissured and porous/alluvial aquifers (Tab. 2.3, Fig. 2.4). Fig. 2.3 shows the distribution of groundwater landscapes and aquifer types in Baden-Württemberg. Aquifers are formations that contain sufficiently saturated permeable material to yield significant quantities of water to springs and wells (Tab. 2.3). The German equivalent to aquifer is *Grundwasserleiter.* While the English term assumes that the underground actually contains water, the German equivalent means merely the possibility of containing water.

In Baden-Württemberg, the proportion of groundwater for drinking water supply is about 70% [Büringer 2006], in Switzerland it is about 80% [Kozel & Schürch 2005]. Due to the high importance for drinking water supplies, groundwater protection and vulnerability concepts are among the key issues for hydrogeologists. In different aquifer types the hydraulic behavior of solutes and particles can vary considerably (Tab. 2.4). The vulnerability of karst and fractured aquifers is very high, but in Baden-Württemberg they are only used for local water supply. The overall vulnerability of porous aquifers is comparably low, but the importance for drinking water is very high and as a

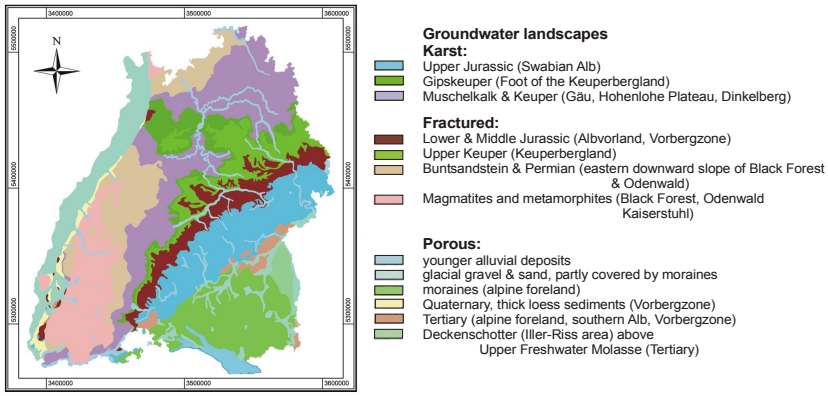

Fig. 2.3: Groundwater landscapes in Baden-Württemberg (modified after Liesch 2006).

result of high-level contaminations with PAHs or other pollutants like nitrate, those aquifers can be at risk as well.

Tab. 2.3: Definition of aquifer types [*Fetter 2001, Lawrence et al. 2001, Zwahlen 2004*].

Aquifer	A geologic formation, group of formations, or part of a formation that contains sufficient saturated permeable material to yield significant quantities of water to springs and wells.
Aquifer type	
Karst	A body of limestone or other soluble rocks in which the landforms are mainly the result of dissolution by water and where most drainage takes place underground in enlarged conduits and fractures.
Fractured	Geological material like granite or sandstone that has undergone deformation to produce fractures in the rock which store and transmit water.
Porous	Sediments, like gravel and sand, that are able to yield groundwater due to their porosity.

Tab. 2.4: General characteristics of different aquifer types.

Aquifer type	Karst	Fractured	Porous
heterogeneity	high	low-high	low-high
anisotropy	high	moderate to high	low-moderate
hydraulic conductivity	~ 10^{-6} - 10^{-2} m/s	~ 10^{-6} - 10^{-4} m/s	~ 10^{-4} - 10^{-2} m/s
flow velocity	~ 1 m/d – 500 m/h	~ 0,1 m/d – 1 m/h	~ 1 m/d
vulnerability	often very high	moderate-high	Low-moderate

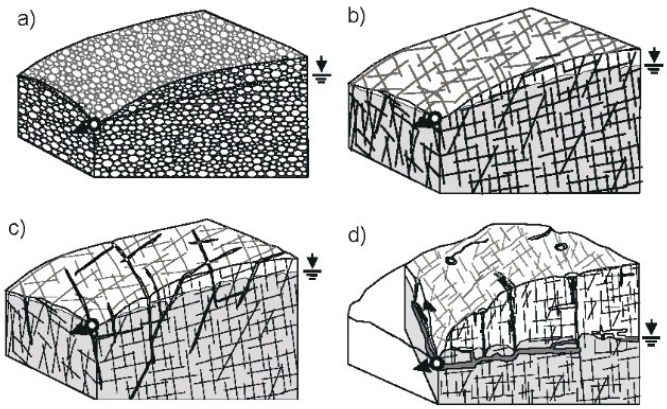

Fig. 2.4: Different types of aquifers: a - homogeneous porous aquifer, b - heterogeneous fractured aquifer, c - highly heterogeneous fractured aquifer and d - karst aquifer [Pochon & Zwahlen 2003].

2.2.2 Karst aquifers

Karst aquifers consist of soluble rocks like limestone, dolostone and evaporites. Preexisting cracks, weakness zones, fractures or joints can be enlarged by chemical dissolution of the surrounding rock through carbonic-acid-containing water [Ford & Williams 2007]. These conduits allow pollutants to be transported in high concentration at high flow velocities. Storage is relatively small, discharge variations of karst springs are very common, they can run dry in dry seasons. The vulnerability of karst aquifers is often very high.

Karst aquifers go along with special landforms, such as karren, dolines (or sinkholes), swallow holes, poljes, sinking streams or blind valleys. In the underground, conduits can be widened to caves, and speleothems like stalagmites and stalactites can be used to date back the climate during its formation and therefore give insight into the cave formation processes and circumstances.

2.2.3 Fractured aquifers

Fractured aquifers are formed in crystalline rocks (e.g. granite) or sedimentary rocks (e.g. sandstone) and show a network of joint faces that is able to transport water. Karst aquifers behave similarly to fractured aquifers in cases where large conduits or caves are missing and the flow behavior is strongly controlled by fractures. The vulnerability varies accordingly. In cases where the fracture density is very high and allows a relatively heterogeneous transport, it can behave like a porous aquifer and vulnerability is comparable low.

2.2.4 Porous aquifers

Alluvial aquifers are often considered as relatively homogeneous. However, in detail the hydraulic properties can vary significantly in space and time. Flow velocities are often about several decimeters to meters per day. Due to filtration and retardation in the overlaying layers, pollutants can be retarded and the amount of pollutants can be reduced. Wells provide a constant amount of water with relatively similar hydrochemical properties. Thick alluvial aquifers are important drinking water resources and therefore need to be protected by adequate source protection concepts.

The behavior of porous aquifers is simulated by using laboratory columns. Scale dependencies of processes are very likely and results need to be considered with care. Laboratory columns are always a simplification of any natural process that occurs, but provide a good means to study basic principles of the transport behavior and are therefore an essential instrument for studying contaminant transport.

2.3 Groundwater Protection

2.3.1 European law

The European Community passed *Directive 2000/60/EC*, a *framework for Community action in the field of water policy* [European Union 2000], whose intention is to create a baseline on which the European member states are forced to protect their groundwater resources and prevent pollution at any rate. In the first paragraph it states that “water is not a commercial product like any other but, rather, a heritage which must be protected, defended and treated as such”.

Directive 98/83/EC on the quality of water intended for human consumption

[European Union 1998] further describes the quality standards, quality control, parameters and parametric values, indicator parameters, monitoring and specifications for the analysis of parameters.

On a national level, European directives are implemented into German law through national regulations.

2.3.2 German law

2.3.2.1 Technical regulation – W 101

Guideline W101 [DVGW 1995] gives a brief explanation of the groundwater protection zones and lists which utilization restrictions need to be regarded. Zone III – the wider protection zone – should protect against extensive negative effects, in particular persistent or radioactive substances. It can be subdivided in Zone IIIA and IIIB. Zone II is supposed to protect against microbial contamination and other negative impacts. Zone I is the capture zone and has to be protected against all kinds of contamination or negative impacts.

2.3.2.2 Technical regulation - W 109

Guideline W 109 “Design, implementation and interpretation of groundwater tracing tests for water supply” [DVGW 2001] explains how to conduct a tracer test for the delineation of groundwater protection zones. It describes the relevant hydraulic parameters (flow velocity, sorption, advection, dispersion, retardation), methodology, design, sampling and interpretation principles of tracer tests with solute tracers.

2.4 Methodology: Tracer tests

2.4.1 Overview

During a tracer test, artificial substances (tracers) are introduced into the subsurface, e.g. into swallow holes or boreholes, and other locations, usually springs or wells, are sampled for them. With tracer tests the following questions can be addressed:

- Is there a connection between an injection point and the point of measurement?
- What are the hydraulic characteristics of the aquifer (e.g. flow

velocities and flow time, dispersion, diffusion, retardation, decay)?

- What is the catchment area of a spring?
- What are the processes that control the concentration of a pollutant at a spring?

By mapping zones with identical hydraulic conditions, point information resulting from tracer tests can be extended to areal information. Tracer tests are commonly used when a certain point, i.e. a spring, is contaminated and the source of the contamination is unknown. However, contamination is often a hygienic problem, and simulation of microorganisms cannot be adequately described by tracings with solutes.

Therefore, the goal of this project is to evaluate the application of particle tracers for groundwater tracing as tool for assessing the hygienic risk. The central issues this project addresses are the following:

- Are there significant differences between particle and solute tracers? Is it possible to describe the transport of microorganisms adequately by particle tracers?
- What are the controlling factors influencing the behavior of these tracers? How significant are the type of aquifer or the hydrologic conditions?
- How can classical analysis methods be adjusted with regard to particle tracers?

In order to answer the abovementioned questions, tracer tests were performed in the three different types of aquifers and in saturated laboratory columns.

2.4.2 Tracer types

2.4.2.1 Fluorescent dyes

To be an ideal conservative tracer, fluorescent tracers or salts should meet the following criteria [Käss 2004]:

- not sorptive
- chemically stable
- water soluble
- inexpensive

- human- and ecotoxicologically harmless
- simple to analyze
- low detection limit
- absent in groundwater

Fluorescent tracers are organic substances that emit light of a higher wavelength (which gives the emission spectrum) after an excitation with a special wavelength (excitation spectrum) (Tab. 2.5). The difference between the maximum excitation and emission wavelength is called delta lambda. By using the synchronous-scan method with the optimum delta lambda, maximum intensity values can be reached and different tracers can be discriminated from each other [Käss 2004]. Intensity values can additionally be maximized by adjusting the pH-value or using mirrored cuvettes.

Fluorescent tracers are generally suitable for tracer tests, however they do not meet all of the criteria. Some fluorescent tracers are biodegradable via microorganisms under certain circumstances, some show sorption effects and others are not chemically stable.

Within this project, the tracers summarized in Tab. 2.5 were used.

Tab. 2.5: Properties of the applied tracers [Käss 2004, Benischke et al. 2007].

Tracer	CAS	Natural background	Toxicology	Absorption [nm]	Fluorescence [nm]	$\Delta\lambda$ [nm]	Detection limit [µg/L]
Amidorhodamine G	5873-16-5	absent	safe	530	551	21	10^{-2}
Eosin	17372-87-1	absent	safe	516	538	22	10^{-2}
Sodium-Naphthionate	130-13-2	absent	safe	320	430	110	10^{-1}
Pyranine	6358-69-6	absent	safe	405	445	40	10^{-2}
Sulforhodamin B	3520-42-1	absent	exotox. unsafe	564	583	19	10^{-2}
Uranine	518-47-8	absent	safe	491	512	21	10^{-3}

2.4.2.2 Biocolloids

Biocolloids should meet the same criteria as explained previously for solute tracers. They should also meet the following :

- large number of microorganisms available at low cost
- absent in groundwater or in laboratory material
- quantitatively countable without high effort
- no active motion
- long survival time
- no reproduction in groundwater
- good differentiation from other tracers (microorganisms)
- no interference with other microorganisms

Several microorganisms were used as tracers in cooperation with Dr. Jakob Zopfi (LAMUN, University of Neuchâtel) and Prof. Dr. Werner Käss (Umkirch): one type of bacteriophage (H40/1) and two types of bacteria: *Serratia marcescens* and *Ralstonia eutropha (Tab. 2.6)*. For the tracers tests in Merdingen, the analysis was done at Prof. Käß' laboratory in Umkirch, and the analysis for the column tests were performed at the Laboratory of Microbiology in Neuchâtel. Surface properties and sizes are listed in Tab. 2.6.

Tab. 2.6: Applied microorganisms: size and zetapotential (after Rossi 1994)*

microorganism	size [nm]	zetapotential [mV]
H40/1	91	-42*
Serratia marcescens	1100	-21.8
Ralstonia eutropha	1040	-20.9

The bacteriophage H40/1 belongs to the family Siphoviridae which is a marine phage that is harmless to human beings and therefore has been applied several times previously in field tracer tests [Rossi 1994]. H40/1 has an icosahedral head and a flexible tail. Dynamic light scattering gave a size of 91 nm, which is probably the longitudinal diameter (head and tail), the head

itself is supposed to have a diameter of about 30 nm [Rossi 1994]. The detection limit is about 1 phage per 2 mL. The abovementioned criteria are fulfilled.

Serratia marcescens is a bacteria that belongs to the family enterobacteria. It is a gram-negative facultative anaerobic, non spore forming, rod-formed bacteria (Fig. 2.5) that actively moves by peritrichous ordered flagella. These bacteria form peculiar red colonies and are therefore easy to separate from other bacteria. With a size of about 1 µm they are in the range of the applied particles. *Serratia marcescens* is able to move by its own and thus does not necessarily rely on the transport through groundwater. Käss 2004 Was the first to describe the application of S*erratia marcescens* during field tracer tests. In groundwater this bacterium is mostly absent, however it has been described as an opportunistic human pathogen occurring in hospitals. The detection limit is about 1 bacterium per mL.

Ralstonia eutropha was used for the first time in laboratory tests. It is a gram-negative, facultative chemoautotrophic bacterium that belongs to the family Ralstoniaceae. A synonym for *Ralstonia eutropha* is *Cupriavidus necator*. It has a size of about 1 µm (Fig. 2.6). It grows under a hydrogen atmosphere, thus it can be completely excluded that it reproduces in groundwater and therefore is only affected by the general transport processes, die-off or filtration processes. Due to its ability of degrading chloraromatic pollutants arose a strong interest in the behavior and the transport characteristics of *Ralstonia eutropha*. The detection limit is about 10 bacteria per mL.

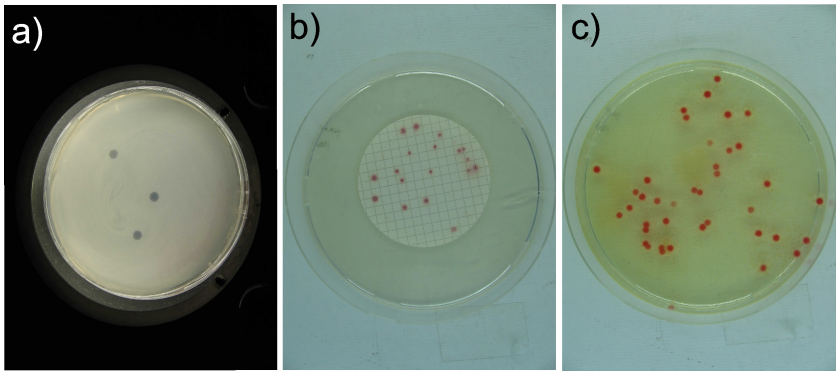

Fig. 2.5: a) H40/1 plaque and the plates of the bacteria b) Ralstonia eutropha growing on a filter paper under a hydrogen atmosphere and c) Serratia marcescens growing on agar under a normal atmosphere.

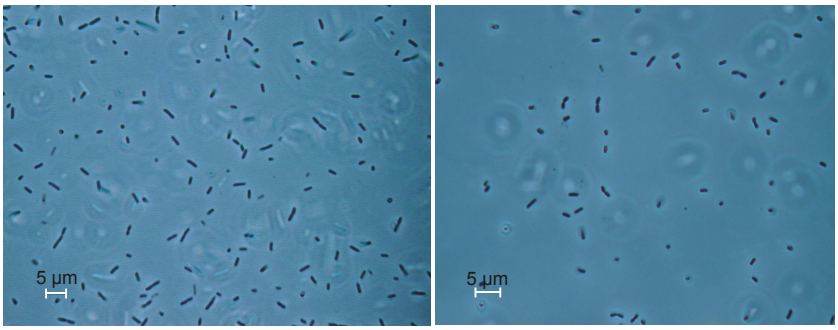

Fig. 2.6: Serratia marcescens (left) and Ralstonia eutropha (right) under a transmitted light microscope (provided by Dr. J. Zopfi, LAMUN, University of Neuchâtel).

2.4.2.3 Particle tracers

Besides bio-colloids, artificial particle tracers were applied. These microspheres are industrially produced particles, generally made of polystyrene with different surface groups attached and therefore of different surface charge. They are usually used for medical purposes. They are available in different sizes and fluorescent colors that make it possible to distinguish between them (Tab. 2.7, Tab. 2.8). Zetapotential and the actual particle diameter were measured with a Malvern Zetasizer NanoZS (Engler-Bunte-Institute, University Karlsruhe, in cooperation with Dipl.-Ing. George Metreveli) by dynamic light scattering (Tab. 2.7, Fig. 2.7). In general, the manufacturer's size data fit well to the measured sizes – but the data actually measured (that varies with different composition of the background solution) were preferred.

Together with other particles and solutes, microspheres were tested in a study of their toxicity for human beings and the ecosystem commissioned by the German Environmental Ministry [Umweltbundesamt 1997]. It came out that they are not toxic and can be applied in the environment as tracers.

Tab. 2.7: Selected microspheres, measured size and zetapotential.

size class (given by manufacturer) [µm]	size (measured) [nm]	zetapotential [mV]
0.2	221	-40.6
0.5	608	-31.6
1	1161	-53.2
5	5303	-77.5

Tab. 2.8: Applied particle tracers and their properties in distilled water.

Size [µm]	Manufacturer	Natural background	Toxicology	Absorption [nm]	Fluorescence [nm]	Stokes shift [nm]	Particle number/mL	Name
0.2	M	absent	safe	580	605	25	3.90×10^{12}	FluoSphere red carboxylate-modified
0.5	P	absent	safe	529	546	17	3.64×10^{11}	Fluoresbrite YO carboxylate
1	P	absent	safe	441	486	45	4.55×10^{10}	Fluoresbrite YG carboxylate
2	P	absent	safe	442	487	45	5.68×10^{9}	Fluoresbrite YG carboxylate
3	P	absent	safe	529	546	17	1.68×10^{9}	Fluoresbrite YO carboxylate
5	M	absent	safe	660	680	20	3.2×10^{8}	FluoSpheres dark red carboxylate-modified
6	P	absent	safe	441	486	45	2.10×10^{8}	Fluoresbrite YG carboxylate

M = Molecular Probes
P = Polysciences

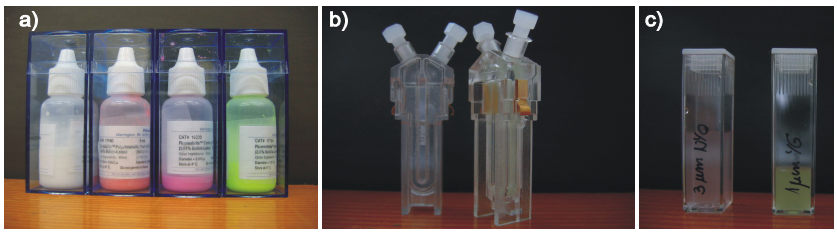

Fig. 2.7: Differently sized microspheres dyed with fluorescent colors (a); suspended microspheres in a cell for measuring zetapotential (b) and for size distribution (c) by dynamic light scattering.

2.4.3 Measurement techniques and software

The fluorescent dyes were analyzed by using a spectrofluorometer (LS 55, Perkin Elmer). Salts were analyzed using AAS and IC. This analysis followed standardized measurement techniques.

The counting of *Serratia marcescens* during the tracer test in Merdingen at Prof. Dr. W. Käss' laboratory followed the procedure described in Käss 2004. Counting of *Serratia marcescens* and *Ralstonia eutropha* during laboratory tests was done at the LAMUN in Neuchâtel under the supervision of Dr. J. Zopfi and followed the bacteriophage guidelines presented in the thesis of Rossi 1994.

The analysis of the fluorescent microspheres was done by using the following methods:

I. Direct counting under a fluorescence microscope

II. Counting using a particle counter with fluorescence detection

III. Measurement of the intensity using a photometer

IV. Measurement of the intensity using a spectrofluorometer

Measurement method I is described in Käss 2004. Prior to filtration, samples are homogenized with a sonicator (Sonopuls HD 2200, Bandelin), filtered through a 0.8 µm-cellulose nitrate membrane filter (Type 113, Sartorius) with imprinted reticule and enumerated using an epifluorescence microscope (Standard FL, Zeiss). Yellow-green microspheres (Fig. 2.8) are

enumerated at an excitation wavelength of 450 to 490 nm and a beam splitter at 510 nm, red microspheres at an excitation wavelength of 390 to 420 nm and a beam splitter at 425 nm.

With the following criteria the applied fluorescent microspheres can be distinguished from other particles occurring in groundwater:

- fluorescence intensity
- fluorescence colors at two different excitations
- shape (spherical)
- diameter

For enumeration an adequate concentration of microspheres has to be adjusted. When the microsphere concentration is too high, the suspension can be diluted simply by adding distilled water prior to sonication and filtration. This procedure can be applied also in cases where a large amount of sediments in the original water sample begins to interfere with the microspheres – in water samples from laboratory tests or field tracer tests in this project, the background concentration of other particles was generally low and did not interfere.

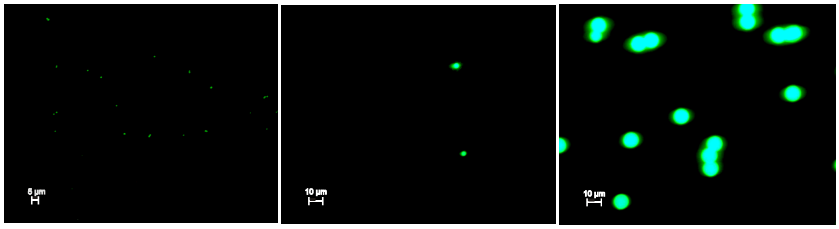

Fig. 2.8: 1 µm (left), 3 µm (center) and 10 µm (right) yellow-green fluorescent microsphere reference samples under a fluorescence microscope, LAMUN Neuchâtel (Filter: BP Ex 480/40).

The detection limit is very low. In field tracer tests, typically 200 mL are analyzed, thus 1 microsphere/ 200 mL is the detection limit. Depending on the quality of the water sample, up to 500 mL can be filtered without restrictions. The detection limit then decreases to 1 microsphere/500 mL.

Thus, a large interval of microsphere concentrations can be analyzed by using this method. In this project, the interval ranged from 1 particle/500 mL to

2000 particles/10 µL.

The water samples for microsphere analysis have to be filled in brown glass bottles. Plastic bottles need to be avoided in any case due to sorption properties of plastic material. This needs to be followed for the membrane filtration assembly as well.

The method is time-consuming, analyzing one water sample can take up to 30 minutes. Due to this disadvantage, other measurement techniques were tested and the results validated.

A novel particle counter with fluorescent detection (Syringe, Markus Klotz GmbH, Bad Liebenzell) was used to enumerate microspheres with a specific excitation wavelength (655 nm) and size (5 µm) (Fig. 2.9) [Goldscheider et al. 2004]. This device uses a 10 mL syringe to pass the sample through a 0.2 mm glass tube. A particle passes a laser beam with an excitation wavelength of 655 nm, which results in a decrease in laser light in detector 1 (Fig. 2.9) for both fluorescent (particle 2 in Fig. 2.9) and non-fluorescent particles (particles 1 and 3 in Fig. 2.9). The extent of decrease is given by assuming a spherical shape for the diameter of the particle. Particle 2 has the same diameter as particle 3 (Fig. 2.9), but only particle 2 is labeled with a fluorescent dye. When the fluorescent particle passes the 655 nm laser light, this results in emission of the fluorescence light of 680 nm measured at the perpendicular detector 2.

Natural particles do not show a fluorescence at this wavelength. In laboratory tests, the instrument never gave erroneous results - even in turbid water samples from surface waters, the instrument gave reliable results.

The detection limit depends on the volume that passes through the syringe and is typically 1 microsphere/10 mL for laboratory tests. It was extended to 1 microsphere/100 mL (1/10x10mL) for field tests.

Furthermore, the microsphere's intensity was measured in laboratory tests by using a spectrofluorometer and for the purpose of comparison by a photometer. In order to do this, additional methods and software tools had to be developed, that allow extension of the interpretation opportunities and data transfer. A detailed description is part of chapter 3: Laboratory tests. At this point, the principle of a spectrofluorometer has to be pointed out.

Fig. 2.10 sets out the composition of a spectrofluorometer. Light source for a Perkin Elmer LS55 is a xenon lamp. Slit width is typically 10 nm, which allows the noise to be reduced, while resolution and intensity increase. Scan speed is 500 nm. Excitation and emission paths are arranged perpendicularly. In order to increase fluorescence, intensity mirrors are fixed on the two outer sides of the inner part of the cuvette holder. Intensity can be further increased by mirrors sprayed directly onto two close-by cuvette walls.

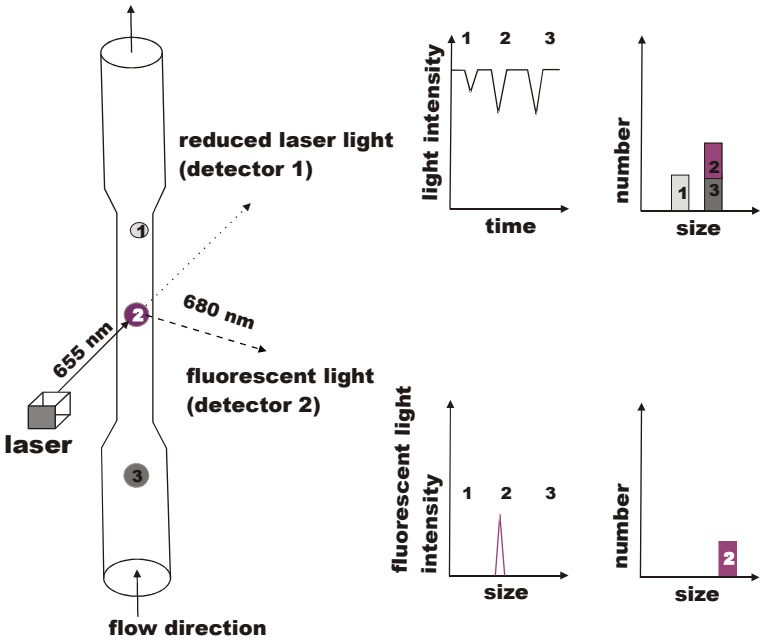

Fig. 2.9: Measurement method of the particle counter with fluorescence detection.

In order to distinguish between different tracers and to obtain the highest possible fluorescence intensity, the synchronous-scan method has been applied. Excitation and emission wavelengths are controlled by the two corresponding monochromators that scan a spectrum simultaneously separated by a certain wavelength difference, the Stokes shift or Δλ. The Stokes shift is a characteristic feature of all tracers. Together with the peak position, the Stokes shift allows identification of a tracer (Tab. 2.5, Tab. 2.8) for both solute fluorescent and colloidal fluorescent tracers.

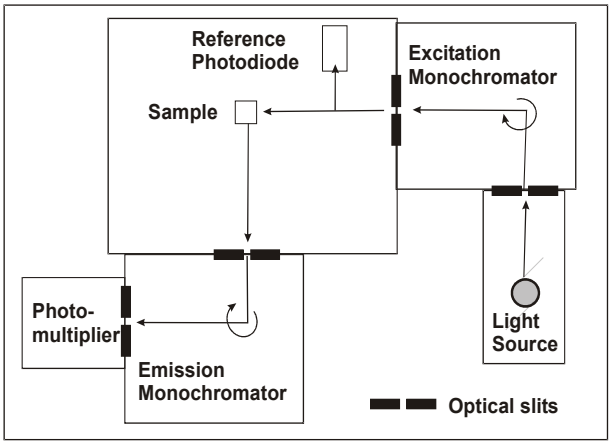

Fig. 2.10: Composition of a spectrofluorometer [Goldscheider & Drew 2007].

2.5 Solute and colloid transport

2.5.1 Introduction

Hydraulic properties vary with the different aquifer types and with the sort of tracer, e.g. karst aquifers show different flow velocities than porous aquifers and solutes and colloids show different flow velocities within the same system. The main hydraulic properties for both solutes and colloids are explained in the following chapters. Hydraulic processes like advection, dispersion and diffusion affect the transport of both solutes and colloids, while other parameters, like filtration and straining, affect only particles.

To evaluate the transport parameters, curve fitting programs are used. This will be explained in detail in chapter 2.6 Modeling Tracer Breakthrough Curves.

2.5.2 Advection, dispersion & diffusion

A general definition of advection, dispersion and diffusion processes is shown in Tab. 2.9, and Fig. 2.11 gives an overview on how these affect an injected tracer mass along the flow path.

Tab. 2.9: General definition of the main hydraulic transport processes [Fetter 2001, Lawrence 2001]

Advection	The process by which solutes are transported by the motion of water.
Dispersion	The phenomenon by which a solute in flowing ground water is mixed with uncontaminated water and becomes reduced in concentration. Dispersion is caused both by differences in the velocity with which the water travels at the pore level (**longitudinal dispersion –** in flow direction) and differences in the rate at which water travels through different strata in the flow path (**transversal dispersion –** perpendicular to the flow direction). **Hydrodynamic dispersion**: the process by which groundwater containing a contaminant mixes with and is diluted by uncontaminated groundwater as it moves through the aquifer.
Diffusion	The process by which both ionic and molecular species dissolved in water move from areas of higher concentration to areas of lower concentration.

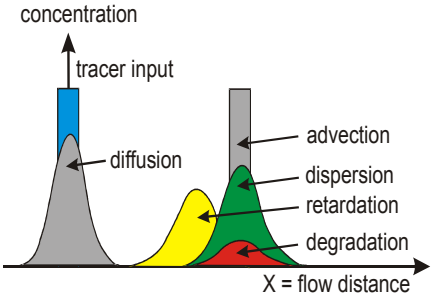

Fig. 2.11: Transport processes that can occur along the flow path.

Advection means that the transport along a flow path is only affected by the average groundwater velocity (Fig. 2.11). Pollutants are transported by advection at the average groundwater velocity. If only advection occurs, the

tracer concentration profile is supposed to be identical at each step between the injection point and the sampling point, tailing should not occur (Fig. 2.11).

According to Darcy, the average flow velocity is given by the following equation:

$$
\begin{aligned}
v_x &= \frac{k_f \cdot i}{n_e} \\
v_x &= \textit{average flow velocity} \\
k_f &= \textit{hydraulic conductivity} \\
i &= \textit{hydraulic gradient} \\
n_e &= \textit{effective porosity}
\end{aligned}
\qquad (1)
$$

The hydrodynamic dispersion is composed of the two processes: molecular diffusion and hydromechanical dispersion, which cannot be separated in flowing groundwater and need to be considered in conjunction [Fetter 2001] (Eq. 2).

The molecular diffusion means the process to reach concentration equilibrium due to the Brownian motion and can be described by Fick's laws. The hydromechanical dispersion means the differences in flow velocity due to pore space, fracture or conduit geometry. When different aquifers have to be considered, the hydromechanical dispersion can vary considerably as an effect of the completely different void geometry. Hydrodynamical dispersion results in a widening of the breakthrough curve without extension of area. The peak concentration decreases without loss of substance, which means that tracers can reach a sampling point before or after a time assumed by advection. Some molecules or particles can travel faster than the average flow velocity because they can take preferential flow paths (with higher flow velocities, e.g. in the pore centers) and reach a sampling point at earlier times. Another part of the tracer mass takes other flow paths where smaller flow velocities occur (at the pore margins) and thus travels more slowly and reach the the sampling point later. The curve presented in Fig. 2.11 is laterally reversed, because it is assumed that dispersion does not vary with flow distance.

For the calculation of the 1-D hydrodynamical dispersion the following equation can be used:

$$\begin{aligned} D_L &= \alpha_L \cdot v_x + D_m \\ D_L &= \textit{longitudinal dispersion coefficient} \\ \alpha_L &= \textit{longitudinal dispersivity} = \textit{dispersion length} \\ v_x &= \textit{average flow velocity} \\ D_m &= \textit{molecular diffusion} \end{aligned} \tag{2}$$

The longitudinal dispersion coefficient can be estimated from TBCs by the following equation:

$$\begin{aligned} D_L &= v_x^2 \frac{(t_{0.84} - t_{0.16})^2}{8 \cdot t_{0.5}} \\ t_{0.84} &= \textit{transit time at } 84\,\% \textit{ percentile} \\ t_{0.16} &= \textit{transit time at } 16\,\% \textit{ percentile} \\ t_{0.5} &= \textit{transit time at } 0.5\,\% \textit{ percentile} \end{aligned} \tag{3}$$

The Peclet number (Pe) describes the ratio between advection and hydrodynamical dispersion processes:

$$\begin{aligned} Pe &= \frac{v_x \cdot L}{D_L} \\ Pe &= \textit{Peclet number} \\ L &= \textit{transport length} \end{aligned} \tag{4}$$

$$\begin{aligned} Pe^* &= \frac{v_x \cdot d}{D_O} \\ Pe^* &= \textit{modified Peclet number} \\ d &= \textit{grain size} \\ D_O &= \textit{diffusion coefficient} \end{aligned} \tag{5}$$

A high Peclet number is associated with predominant advection, a low Peclet number with predominant dispersion processes. The reciprocal Peclet

number is named P_D.

When exclusively diffusive processes are of importance, the diffusion coefficient of colloids can be used as a means for quantifying particle mobility according to the Stokes-Einstein-Equation:

$$
\begin{aligned}
D_O &= \frac{k_B \cdot T}{6 \cdot \Pi \cdot \mu \cdot r_p} \\
D_O &= \textit{diffusion coefficient} \\
k_B &= \textit{Boltzmann constant} \\
T &= \textit{temperature} \\
\mu &= \textit{dynamic viscosity}(\textit{water}) \\
r_p &= \textit{radius}(\textit{particle})
\end{aligned}
$$

Stokes-Einstein Equation (6)

Retardation of a tracer without sorption can be achieved by matrix diffusion which depends on the size and the roughness of contact surfaces in the adjacent rock matrix. When matrix diffusion occurs, the tracer first moves into the rock matrix and removes into the flowing water volume after the concentration gradient has become reversed. This results in a certain tailing of a tracer breakthrough curve that can be determined by a slope of -1.5 in a log-log scale tracer breakthrough curve [Tsang 1995] - the so called t = -1.5 criterion.

Other retardation processes, like sorption, or degradation and decay can occur as well. The non-reversible processes reduce the amount of tracer recovered, or distinctly slow down tracer movement (Fig. 2.11). These processes are not covered by the general transport equation and therefore need special consideration. Due to the short time span, these processes can be excluded for laboratory tests. Field tracer tests show a distinct behavior for tracers like pyranine that might be explained by microbial degradation.

The 1D-Advection-Dispersion-Equation (ADE) is as follows:

$$
\frac{\delta C}{\delta t} = D_L \frac{\delta^2 C}{\delta x^2} - v_x \frac{\delta C}{\delta x}
$$

1D-ADE (7)

An analytical solution of Equation 7 is given in Equation 11 by assuming a Dirac-injection, a constant distance and variable time t with the following marginal and initial conditions [Kreft & Zuber 1978]:

$$C(0,t) = \frac{M}{Q}\delta t \tag{8}$$

$$C(x,t) = 0 \quad x>o\,,\ t=0 \tag{9}$$

$$\lim_{x\to\infty} C(x,t) = 0 \tag{10}$$

$$C_{(x,t)} = \frac{M}{Q\cdot t_0\cdot\sqrt{4\cdot\Pi\cdot P_D\cdot(\frac{t}{t_o})^3}}\cdot\exp\left[-\frac{(1-\frac{t}{t_o})^2}{4\cdot P_D\cdot\frac{t}{t_0}}\right] \tag{11}$$

C = *tracer concentration*
M = *injected tracer mass*
Q = *discharge*
x = *distance*
t_o = *mean tracer transit time*

This solution was initially developed for porous media, but has been applied in karst as well. A model that takes the hydraulic behavior of fractured rock into account was developed by Maloszewski & Zuber 1985. They give an analytical solution that assumes mass flux from parallel fractures into the rock matrix within convergent flow experiments and Dirac injection:

$$C(x,t) = \frac{a\,M}{2\,\pi\,Q}\cdot\sqrt{Pe\cdot t_o}\cdot\int_o^t \exp\left[-\frac{Pe(t_o-\varsigma)^2}{4\,t_o\varsigma}-\frac{(\varsigma\,a)^2}{t-\varsigma}\right]\cdot\frac{d\,\varsigma}{\sqrt{\varsigma(t-\varsigma)^3}} \tag{12}$$

ς = *integration variable*
a = *diffusion parameter*

The fit parameters are the Peclet number Pe, the diffusion parameter a and the mean transit time t_0. The diffusion parameter a describes the diffusive mass transfer between fracture and adjacent matrix.

$$\begin{aligned} a &= \frac{\epsilon_m \sqrt{D_P}}{b} \\ \epsilon_m &= \textit{matrix porosity} \\ D_P &= \textit{pore diffusion coefficient} \\ b &= \textit{main hydraulic fracture width} \end{aligned} \tag{13}$$

Under a radial-convergent flow field, the fracture porosity ε_f can be calculated as follows [Zuber 1974] by assuming that the drawdown cone volume is negligible in relation to the entire water volume:

$$\begin{aligned} \epsilon_f &= \frac{Q t_0}{\pi m x^2} \\ \epsilon_f &= \textit{fracture porosity} \\ m &= \textit{saturated thickness} \\ x &= (\textit{lateral})\ \textit{distance} \end{aligned} \tag{14}$$

Maloszewski & Zuber 1985 calculate the main fracture hydraulic width as follows:

$$\begin{aligned} b &= \sqrt{\ln(\frac{x}{r_w}) \frac{6 \nu \iota}{g t_0} \frac{x^2}{\Delta H}} \\ r_w &= \textit{borehole radius} \\ \nu &= \textit{kinematic viscosity} \\ \iota &= \textit{fracture tortuosity factor}\ (ca. 1.5) \\ g &= \textit{gravitational constant} \\ \Delta H &= \textit{piezometric level difference} \end{aligned} \tag{15}$$

The effective diffusion coefficient D_e can be calculated by assuming that the entire matrix porosity is available for flow as follows:

$$\begin{aligned} D_e &= \frac{(ab)^2}{\epsilon_m} \\ D_e &= \textit{effective diffusion coefficient} \\ \epsilon_m &= \textit{matrix porosity} \end{aligned} \tag{16}$$

Further analytical solutions are given in chapter 2.6 Modeling Tracer Breakthrough Curves, which discusses different software tools and the evaluation procedure in more detail.

2.5.3 Colloid stability

Colloid stability in a hydrogeological context means the property of colloids being transported suspended in groundwater [Hofmann et al. 2003] and thus their ability to be transported during tracer tests from injection to sampling point. When the physico-chemical conditions are not favorable, colloids became unstable, aggregate and sediment, they are removed from the solution. The colloid stability depends on the total energy interaction between the repulsive forces (Born & double layer repulsion) and the attractive forces (van der Waals) (Fig. 2.12).

A colloid approaching aquifer material first experiences van der Waals attraction and double layer repulsion. It reaches the secondary minimum where bonding forces are low and particles can be easily removed by shear forces. In order to reach the first minimum and experience irreversible attachment, the colloid has to negotiate the energy barrier. The height of this energy barrier depends on the ionic strength of the pore water and the surface charge. In cases when an energy barrier exists, conditions are non-favorable for attachment; in the absence of the energy barrier, conditions are favorable [Ryan & Elimelech 1996].

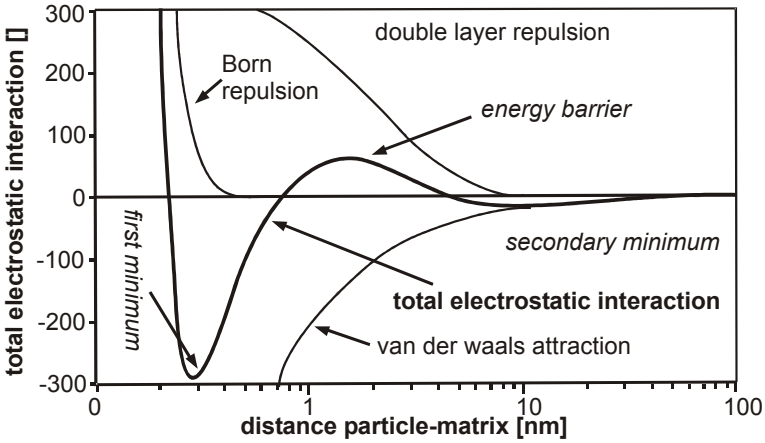

Fig. 2.12: Physico-chemical model of the colloid stability [Hofmann 2004].

2.5.4 DLVO-theory

The DLVO theory is named after the two research groups that developed it (Derjarguin & Landau, Verwey & Overbeek). It describes the total electrostatic interaction (V_{tot}) between the double layer repulsion (V_{DL}), the van der Waals attraction (V_{vdW}) and the Born repulsion.

The calculation of the individual forces can be obtained by assuming a system with spherical-shaped particles and collectors. The diffuse double layer repulsion is as follows:

$$
\begin{aligned}
V_{DL} &= \frac{\varepsilon \cdot r_p \cdot r_c (\Psi_P^2 + \Psi_C^2)}{4(r_p + r_c)} \left[\frac{2 \cdot \Psi_P \cdot \Psi_C}{(\Psi_P^2 + \Psi_C^2)} \cdot \ln \frac{(1 + e^{-kh})}{(1 - e^{-kh})} + \ln(1 - e^{-2kh}) \right] \\
V_{DL} &= \textit{diffuse double layer repulsion} \\
\varepsilon &= \textit{dielectric constant} \\
r_p, r_c &= \textit{particle and collector radius} \\
\Psi_P, \Psi_C &= \textit{surface potential of particle and collector} \\
\kappa &= \textit{Debye} - \textit{Hückel} - \textit{length} \\
h &= \textit{distance between particle and collector}
\end{aligned}
\tag{17}
$$

The reciprocal Debye-Hückel length gives the distance to the collector in which the potential decreases to 1/e:

$$
\begin{aligned}
\kappa &= \sqrt{\frac{(8 \cdot \Pi \cdot c_i \cdot e^2 \cdot z^2)}{(\varepsilon \cdot k_B \cdot T)}} \\
\kappa &= \textit{Debye} - \textit{Hückel length} \\
c_i &= \textit{ionic strength} \\
e &= \textit{elementary charge} \\
\varepsilon &= \textit{dielectric constant} \\
z &= \textit{ionic valence}
\end{aligned}
\tag{18}
$$

Van der Waals forces can be calculated as follows:

$$
\begin{aligned}
V_{vdw} &= -\frac{A \cdot r_p \cdot r_c}{6 \cdot h (r_p + r_c)} \\
V_{vdW} &= \textit{van der Waals forces} \\
A &= \textit{Hamaker constant}
\end{aligned}
\tag{19}
$$

Fig. 2.13 and Fig. 2.14 show that ionic strength and surface charge strongly influence the energy interaction. Due to this, both parameters are diversified during the laboratory tests. At higher ionic strengths the energy barrier decreases and an attachment is more likely to occur (Fig. 2.13). At a low surface charge, the energy barrier decreases as well and the chances for attachment are higher (Fig. 2.14). The calculation of the total energy interaction was done without the Born repulsion.

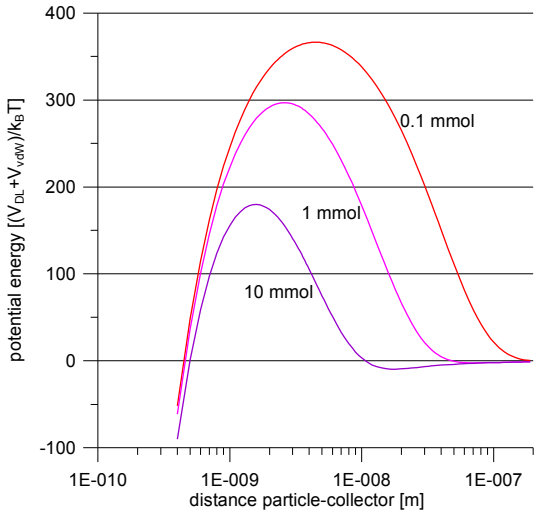

Fig. 2.13: Total interaction energy depending on the ionic strength (without Born repulsion).

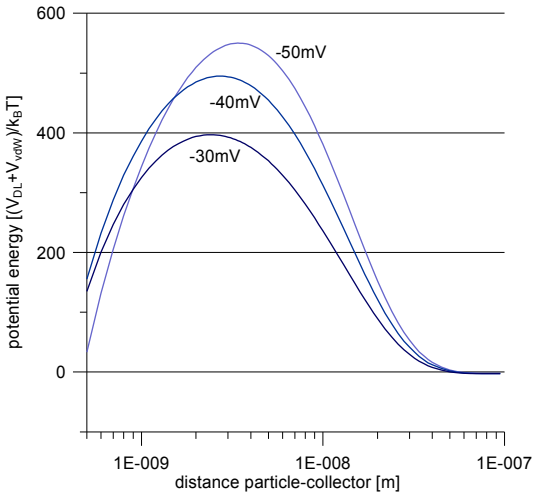

Fig. 2.14: Total interaction energy depending on the surface charge (without Born repulsion).

By applying the DLVO theory the general mechanisms of colloid stability can be explained, although there are certain weaknesses, e.g. in material with heterogeneously charged surfaces.

2.5.5 Filtration theory

The tracer particles applied have a significantly smaller diameter than the laboratory column material. Thus, physico-chemical filtration is the most important process. The collision and the probability that this collision results in an attachment needs to be considered. For balancing the forces that affect a particle near a spherical-shaped collector, semi empirical equations were developed [Rajagopalan & Tien 1976].

$$\gamma = \gamma_D + \gamma_I + \gamma_G \qquad (20)$$

γ = *single−collector efficiency*
γ_D = *single−collector efficiency for transport by diffusion*
γ_I = *single−collector efficiency for transport by interception*
γ_G = *single−collector efficiency for transport by sedimentation*

$$\gamma_D = 0{,}9\, A_S \left(\frac{k_B \cdot T}{\mu \cdot d_p \cdot d_c \cdot v_x}\right)^{\left(\frac{2}{3}\right)}$$

d_p = *particle diameter*
d_c = *collector diameter*

Diffusion (21)

$$\gamma_I = A_S \left(\frac{4 \cdot A}{9 \cdot \Pi \cdot \mu \cdot d_p^2 \cdot v_f}\right)^{\left(\frac{1}{8}\right)} \cdot \left(\frac{d_p}{d_c}\right)^{\left(\frac{15}{8}\right)}$$

Interception (22)

$$\gamma_G = 0{,}00338\, A_S \left[\frac{(\rho_p - \rho_w) \cdot g \cdot d_p^2}{18 \cdot \mu \cdot v_f}\right]^{1{,}2} \cdot \left(\frac{d_c}{d_p}\right)^{0{,}4}$$

ρ_p = *particle density*
ρ_w = *fluid density*

Sedimentation (23)

The porosity-dependent Happel-Parameter [Happel 1958] is defined as follows:

$$A_S = \frac{1 - \gamma^5}{\left(1 - \frac{3}{2} \cdot \gamma + \frac{3}{2} \cdot \gamma^5 - \gamma^6\right)}$$

A_S = *Happel parameter*
$\gamma = (1 - n)^{\frac{1}{3}}$
n = *porosity*

Happel series (24)

Based on numerical solutions of the ADE, semi empirical equations were developed that stand for a broader application spectrum in natural and artificial flow regimes [Tufenkji & Elimelech 2004].

The single-collector contact efficiency is defined as follows:

$\eta_O = \eta_D + \eta_I + \eta_G$
η_O = *single−collector contact efficiency* [*elementarer Abscheidegrad*]
η_D = *single−collector contact efficiency for transport by diffusion*
η_I = *single−collector contact efficiency for transport by interception*
η_G = *single−collector contact efficiency for transport by gravitation*

(25)

The solution of the filtration equation relies on different dimensionless parameters which are defined after Tufenkji & Elimelech 2004:

$$\begin{aligned} N_R &= \frac{d_p}{d_c} \\ N_{Pe} &= \frac{v \cdot r_c}{D_O} \\ N_{vdW} &= \frac{A}{k_B \cdot T} \\ N_{gr} &= \frac{4}{3} \cdot \frac{\Pi \cdot r_p^4 (\rho_p - \rho_f) \cdot g}{k_B \cdot T} \\ N_A &= \frac{A}{12 \cdot \pi \cdot \mu \cdot r_p^2 \cdot v} = N_{vdW} \cdot N_R^{-1} \cdot N_{Pe}^{-1} \\ N_G &= \frac{2}{9} \cdot \frac{r_p^2 (\rho_p - \rho_f) \cdot g}{\mu \cdot v} = 2 \cdot N_{gr} \cdot N_R^{-1} \cdot N_{Pe}^{-1} \end{aligned} \tag{26}$$

The contribution of diffusion, interception and gravitation is defined by the following equations:

$$\eta_D = 2.4 \cdot A_S^{\frac{1}{3}} \cdot N_R^{-0.081} \cdot N_{vdW}^{0.052} \qquad \text{Diffusion (27)}$$

$$\eta_I = 0.55 \cdot A_S \cdot N_R^{1.675} \cdot N_A^{0.125} \qquad \text{Interception (28)}$$

$$\eta_G = 0.222 \cdot N_R^{-0.24} \cdot N_G^{1.11} \cdot N_{vdW}^{0.053} \qquad \text{Gravitation (29)}$$

The overall equation is as follows:

$$\eta_O = 2.44 \cdot A_S^{\frac{1}{3}} \cdot N_R^{-0.081} \cdot N_{Pe}^{-0.715} \cdot N_{vdW}^{0.052} + 0.55 \cdot A_S \cdot N_R^{1.675} \cdot N_A^{0.125} + 0.22 \cdot N_R^{-0.24} \cdot N_B^{1.11} \cdot N_{vdW}^{0.053} \tag{30}$$

A calculation of the different forces in laboratory tests of porous media is shown in Fig. 2.15. For the colloid size of approximately 1 µm the single-collector contact efficiency is lowest, which means that for this size class, an attachment is rather unlikely to occur. Smaller particles show a lower tendency for sedimentation and interception, but a higher one for diffusion. A collision results in attachment because of the Born diffusion. Larger particles show a higher tendency to settle out or intercept with a collector and thus show a higher attachment efficiency.

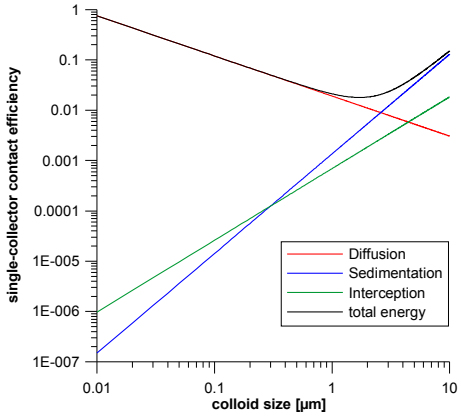

Fig. 2.15: Results of the calculation of the single-collector contact efficiency after Tufenkji & Elimelech 2004, a readily identifiable limit at approximately 1 µm.

In aquatic systems, the actual single-collector removal efficiency (η) is due to repulsive forces lower than the single-collector contact efficiency (η_0). Both are linked by the empirical attachment (=collision) efficiency α [Tufenkji & Elimelech 2004].

$$\begin{aligned} \eta &= \alpha \cdot \eta_0 \\ \eta &= single-collector\ removal\ efficiency \\ \alpha &= attachment(=collision)\ efficiency \\ \eta_0 &= single-collector\ contact\ efficiency \end{aligned} \tag{31}$$

The particle deposition rate coefficient κ_d stands for physico-chemical filtration.

$$\begin{aligned} \kappa_d &= \frac{3}{2}\frac{(1-n)}{d_c n} v \cdot \alpha \cdot \eta_0 \\ \kappa_d &= particle\ deposition\ rate\ coefficient \end{aligned} \tag{32}$$

For pulse tests, Kretzschmar et al. 1997 define the particle deposition rate as follows:

$$\begin{aligned} \kappa &= \frac{-1}{t_a}\cdot\ln\frac{q}{N_o}\int_o^{t_f} C(t)\,dt \\ t_a &= \textit{average colloid travel time} \\ q &= \textit{volumetric flow rate} \\ N_o &= \textit{total amount of colloids injected into the column} \\ t_f &= \textit{last colloid detection time} \end{aligned} \tag{33}$$

The filter coefficient λ is related to the single-collector contact efficiency as follows [Tufenkji & Elimelech 2004]:

$$\begin{aligned} \lambda &= \frac{3}{2}\frac{(1-n)}{d_c}\alpha\cdot\eta_o \\ \lambda &= \textit{filter coefficient} \end{aligned} \tag{34}$$

For pulse tests, Grolimund et al. 1998 define the filter coefficient as follows:

$$\begin{aligned} \kappa &= \lambda\cdot v_p \\ v_p &= \textit{particle velocity} \end{aligned} \tag{35}$$

For the transport of colloids in a semi-infinite column and a Dirac pulse, a Laplace transformation of the one-dimensional advection-dispersion equation considering particle deposition results after Grolimund et al. 1998 in:

$$\begin{aligned} c(x,t) &= n_n e^{-\kappa t}\cdot\frac{x}{2\sqrt{\pi t^3 D}}\; e^{\frac{-(x-vt)^2}{4Dt}} \\ n_n &= \textit{normalization constant} \\ &\quad (\textit{total amount of particles injected divided by total volumetric flux}) \end{aligned} \tag{36}$$

2.6 Modeling Tracer Breakthrough Curves

2.6.1 Overview

Basic parameters can directly be obtained from the tracer breakthrough curves (TBC), a first evaluation can be done using simple spreadsheet programs (Tab. 2.10). For further interpretation certain software tools are used (Tab. 2.11). Such parameters are the peak concentration (c_p), first detection time (t_1), peak time (t_p) (Fig. 2.16, Tab. 2.10), and the corresponding maximum (v_{max}) and peak velocities (v_p). Recovery is calculated from discharge (Q), concentration (c) and injected tracer mass (M) after Equation 37. Half-load (c_m) and the corresponding median flow velocity (v_m) can be obtained by spreadsheet calculation as well.

$$R = \frac{1}{M}\int_{t=0}^{\infty}(Qc)\,dt \qquad (37)$$

R = *recovery*
Q = *discharge*
c = *concentration*

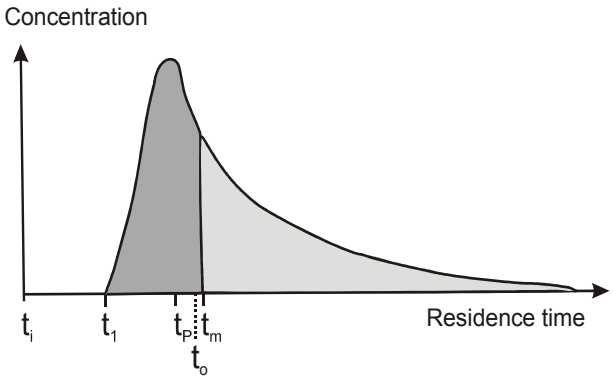

Fig. 2.16: Basic parameters of tracer breakthrough curves, modified after Käss 2004 (explanation see Tab. 2.10).

Tab. 2.10: Basic parameters of a TBC and the corresponding concentrations and flow velocities.

point of time		concentration	flow velocity
t_i=0	injection time	-	-
t_1	first detection time	detection limit	fastest flow velocity (maximum flow velocity)
t_p	highest concentration (peak) time	maximal concentration (peak concentration)	dominating flow velocity (peak velocity)
t_o	mean residence time mean transit time	mean concentration	mean flow velocity
t_m	half-life time	half load	median flow velocity
t_4	last detection time	detection limit	-

Tab. 2.11: Overview over the tracer tests and applied curve-fitting software

		Traci95		CXTFIT	
		ADM	SFDM	ADM	2RNE
Laboratory tests		✓		✓	
Porous aquifer	Merdingen	✓		✓	
Fractured aquifer	Lindau	✓	✓	✓	✓
Karst aquifer	Hölloch	✓		✓	✓
	Gunzesried	✓		✓	✓
	Yverdon	✓		✓	✓

Transport characteristics vary considerably in different aquifer types, and different model types show their strengths in different aquifer types. It is therefore recommended to obtain the hydraulic parameters by using different

curve-fitting programs, to compare and evaluate the results and to choose the best-fit for further interpretation (Tab. 2.11). The following chapters describe the freely available software tools and give a short overview over the evaluation procedure.

The next chapter describes the evaluation procedure for each software tool. Equations are only given if not mentioned previously.

2.6.2 Traci95: ADE, SFDM

Generally, the ADE requires two fit parameters, advection and dispersion. An analytical solution for the general ADE is given in Equation 11. Accordingly, P_D and t_o (or sometimes M) are used as fit parameters. If flowpath length L is available, the mean flow velocity, dispersion coefficient and dispersivity can be calculated.

For a fractured aquifer an SFDM (single fissure dispersion model) is used. The analytical solution is given in Equation 12. Fit parameters are Pe, t_o and a.

With the relatively simple software tool Traci95 [Käss 2004, Werner 1998], the TBCs were fitted first in order to get an idea on what the characteristics of the hydraulic parameters are. Especially for the karst aquifers, the fit for the ADE with Traci95 does not give satisfying values. However, they can be used as a starting point for other software tools like CXTFIT.

Traci95 was developed for solute transport. Transport parameters for colloids can be calculated in the same way as for the solutes, whereas units need to be transferred from particle to solute and – after computing the best-fit - reversed.

2.6.3 CXTFIT: ADE, 2RNE

The software tool CXTFIT [Toride et al. 1999] provides a large set of analytical solutions including a conventional ADE and the 2RNE (two-region non-equilibrium) model for analytical fit of TBCs. The 2RNE was developed for porous media first, where an exchange between mobile water in large pores and an immobile fluid phase in fine pores or adsorbed water causes a tailing of the TBC. A conventional ADE is not able to fit this tailing of the curves. This model was also applied in karst aquifers [Geyer et al. 2007, Birk et al. 2005, Field & Pinsky 2000], because larger conduits represent the mobile fluid phase, while the immobile region are still water zones or the adjacent fractured rock area. Fit parameters for the 2RNE are therefore v, D, β and ω.

In the first instance the 2RNE was developed for solutes; colloids are

affected by additional processes (filtration, sedimentation, exclusion). But due to the lack of appropriate models, the 2RNE was used for the curve fitting of the colloids as well. Unit transformation (colloids-solute-colloids) is simple – similar to Traci95, but not necessary for the 2RNE because a non-unit run can be chosen.

Additional fit-parameters for the 2RNE are the following:

β	partition coefficient for mobile and immobile fluid regions	$0< \beta <1$ high values indicate high proportion of mobile water
ω	mass transfer coefficient	$\omega > 0$ high values indicate high mass transfer

3 Laboratory tests

3.1 Introduction

Laboratory tests provide a good means to quantify the general transport behavior of microorganisms, microspheres and solute tracers. Laboratory tests are run under well controlled conditions that allow investigation of one process separately from others – which is not possible in field experiments. However, due to up-scaling problems, results of laboratory tests have to be considered with care.

Furthermore, laboratory column tests are an excellent tool to validate all measurement methods (Tab. 3.1), especially the microsphere counting method under the fluorescence microscope. Calibration curves for all tracers were generated and compared to the counting methods. Afterwards a time- (and cost-) saving method was developed particularly with regard to the laboratory tests. It emerged that all methods provide reliable results and are usable over a wide range of application areas (Tab. 3.2).

In field tracer tests the application of microorganisms and tracers (colloids and solutes) is restricted – the use of pathogenic microorganisms is prohibited. For pathogenic microorganisms laboratory tests are the only way to study the behavior in detail. Only accidental injections of pathogens (e.g. injection of pathogens associated with land use activities [Worthington et al. 2003]) provide a way to study the behavior (e.g. the survival time in groundwater) in detail and validate the laboratory results. Naturally occurring pathogens are typically difficult to trace back to a distinct source, especially in porous aquifers where infiltration is diffuse. Complex physico-chemical conditions in an aquifer make it difficult to study the microorganisms' behavior in situ.

Moreover, microorganisms are expected to show a different behavior caused by different surface properties and surface charges, sizes or forms. Two representative bacteria and one bacteriophage were used as tracer microorganisms. With that the range of transport parameters should be pointed out. It is clear that other microorganisms might behave slightly differently and parameters then need to be adjusted.

3.2 Analytics

3.2.1 Overview

Four different instruments were used for analysis (Tab. 3.1): fluorescence microscope (Standard FL, Zeiss), particle counter (Syringe, Markus Klotz GmbH), spectrophotometer (Cary 500, Varian) and spectrofluorometer (LS 55, Perkin Elmer). They were tested for different application fields (Tab. 3.2). An overview over the range of detection limits that are calculated by using the German Industry Norm (DIN) 32645 for each measurement method is given in Tab. 3.3.

Particles with a diameter less than 1 µm (0.2 µm; 0.5 µm) can be evaluated using a photometer or fluorometer. The microscope has a relatively low resolution, therefore it can be used for the counting of particle sizes about 1 µm or larger; the detection limit depends solely on the sample volume. The photometer and spectrofluorometer can be used to analyze microspheres of all sizes and all types of spectral characteristics (Fig. 3.1, Fig. 3.2). A detailed description of the measurement technique follows in the next chapter. The detection limit of the photometer is generally several orders of magnitude higher than that for the fluorometer (Tab. 3.3, Fig. 3.4, Fig. 3.3) and thus has a lower sensitivity. So it is highly recommended not to use the photometer, but the fluorometer instead. Although the detection limit for the fluorometer is low, for the size classes 1 µm and larger, the fluorescence microscope method has a detection limit that is in any case several magnitudes lower. Therefore the fluorescence microscope is highly recommended in field tracer tests (Tab. 3.2) where water samples usually contain a relatively small number of microspheres and TBC tend to be more irregular. For laboratory tracer tests that are generally characterized by a very high number of samples, a higher number of microspheres per sample and regular TBCs, the fluorometer method was thoroughly tested, validated and provides reliable results.

The particle counter with fluorescence detection provides an additional device that can be used in both field and laboratory tests. As for the microscope method, the detection limit depends on the sample volume. If a larger volume needs to be injected into the syringe (100 mL), it starts to become time consuming. This device is tested for 5 µm microspheres only, the instruments' restrictions do not allow measurements of colloids that are smaller than 1 µm.

In laboratory tests the fluorometer method is less time consuming, provides reliable results and is therefore recommended (Tab. 3.2).

Tab. 3.1: Overview over the microsphere sizes and the analysis methods applied.

size	measurement technique			
[µm]	fluorescence microscope	particle counter	photometer	fluorometer
0.2			X	X
0.5			X	X
1	X		X	X
2	X		X	X
3	X		X	X
5	X	X	X	X

Tab. 3.2: *Measurement methods and suggested application fields. ✓ recommended without restrictions; - not recommended; (✓) recommended with restrictions (restriction: method is more time consuming than equal method).*

measurement method	laboratory tests	field tracer test
fluorescence microscope (≥1 µm)	(✓)	✓
particle counter (5 µm)	(✓)	✓
spectrofluorometer (all sizes)	✓	-

Tab. 3.3: Measurement techniques, colloid diameter and corresponding detection limits (for further description of the detection limits see chapter 3.2.2 Spectrofluorometer measurement technique).

measurement techniques	colloid size	detection limit [n/mL]
fluorescence microscope	1 µm	1/sampled volume
	3 µm	1/sampled volume
	5 µm	1/sampled volume
particle counter	5 µm	1/sampled volume
photometer	0.2 µm	10^8
	0.5 µm	10^7
	1 µm	10^6
	3 µm	10^4
	5 µm	10^4
fluorometer	0.2 µm	10^5
	0.5 µm	10^3
	1 µm	10^2
	3 µm	10^2
	5 µm	10^2

3.2.2 Spectrofluorometer measurement technique

Prior to the calibration procedure, different cuvettes were tested for their optical accuracy: a flow-through quartz glass cuvette with a volume of 100 µL (Hellma, Müllheim) and two quartz glass cuvettes with and without mirrored walls and a volume of 3,5 mL (QS 101, Hellma, Müllheim). The flow-through cells were used for the online measurements, the cuvettes with mirrored walls for the corresponding collected samples.

With the instrument LS 55 (Perkin Elmer) and the software FLWinlab 4.0, a synchron scan method with several 3D-options can be used to identify the

optical properties of the fluorescent microspheres in order to develop an appropriate measurement method (points of maximal intensity, Stokes shift) in different background solutions and corresponding detection limits respectively calibration lines for this (Fig. 3.4, Fig. 3.3). First, an optimal wavelength interval had to be found (Fig. 3.1, Fig. 3.2) (the optimum wavelength interval will lead to an optimal scan time, it should be large enough to cover the peak and a buffer zone of 20 nm and small enough to allow a large number of online measurements in short time and a constant repeat time of the measurements). The peak intensities and Stokes shift found through this method differ slightly from the supplier's information, which can be explained by the influence of the background solution ($NaNO_3$) on the optical properties. Fluorescence quenching effects were not found.

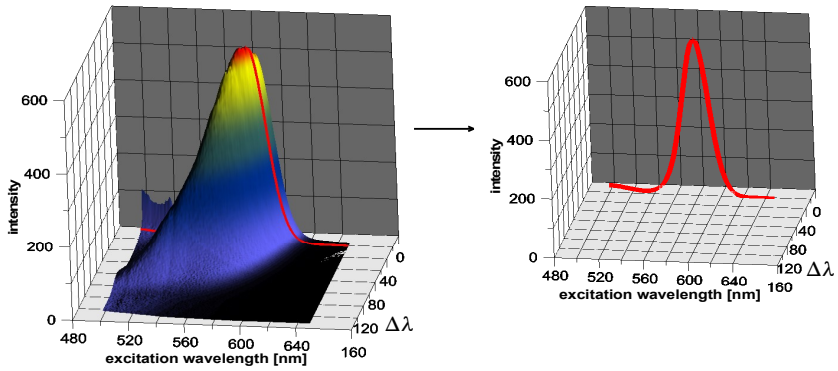

Fig. 3.1: Complete optimized 3D synchron scan of 0.2 µm-spheres with fixed excitation-emission pairs and variable Stokes shift (picture left), optimum scan method (picture right) at a Stokes shift of 25 nm and a clearly visible peak position of 580 nm.

The detection limits were calculated by applying the DIN 32645 prior to each measurement cycle for different background solutions by scanning all concentration areas adequately as required by the norm.

The 3D-synchron scan was applied in two modes:

- Certain excitation and emission wavelengths and a variable Stokes shift (Δλ) for identifying the optimum Stokes shift and corresponding peak wavelengths in order to find an appropriate measurement methodology.

- Certain excitation and emission wavelengths, a fixed Stokes shift (Δλ) and variable time in order to measure the TBC online.

The first mode resulted in the optimum optical properties for all tracers that are displayed in Fig. 3.1 and Fig. 3.2.

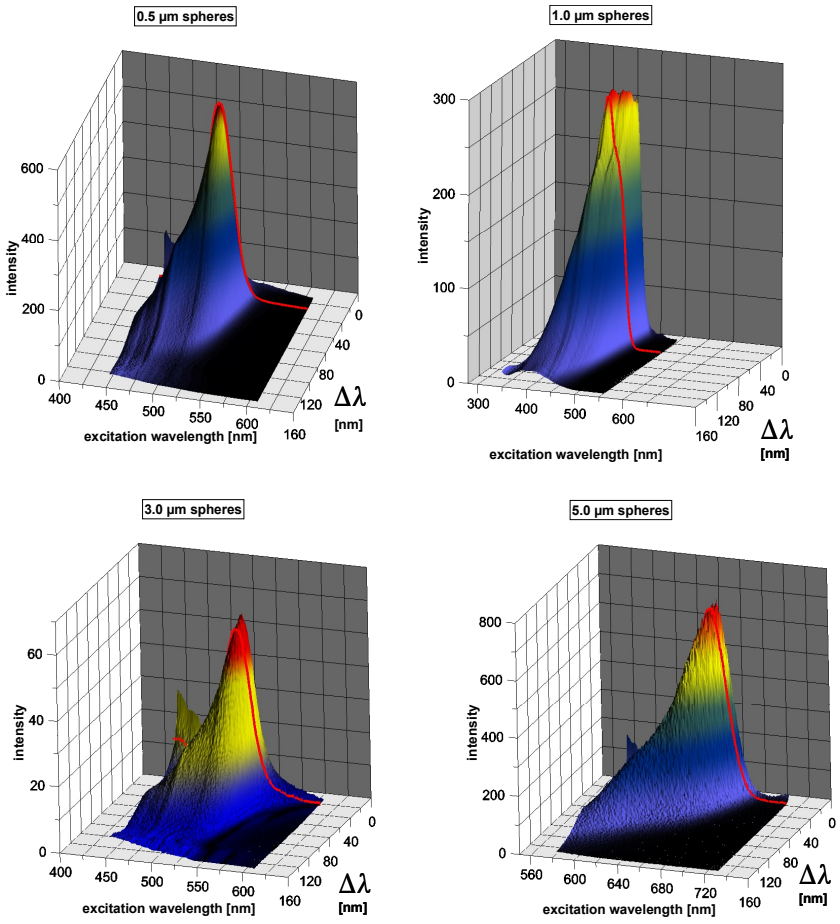

Fig. 3.2: 3D synchron scans of 0,5 µm, 1 µm, 3 µm and 5 µm microspheres with variable Stokes shift. The optimum Δλ is shown in red.

This shows that the applied fluorescent particles can be measured with a spectrofluorometer without restrictions. The background solution shows no significant influence on the optical properties, it results merely in a negligible shift of the peak properties. There are no interfering peaks or colloid instabilities during particle measurement. To avoid the effect of sedimentation, manually taken samples are homogenized by ultrasound prior to measurement. During online measurement, sedimentation effects can be ruled out. The calibration lines based on the abovementioned methodologies are shown in Fig. 3.3 and Fig. 3.4.

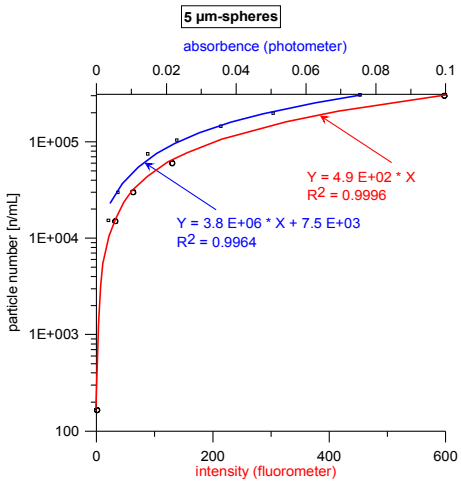

Fig. 3.3: Calibration lines for the fluorometer and photometer measurement of the 5 µm microspheres (please note: y-axis is in logarithmic scale).

The second online method for measuring the TBC uses constant Δλ, then the the interval usually is about 30 seconds. During one TBC, over 300 scans (and thus over 300 scan data files) are created with over 200 single measurements (=excitation wavelength – intensity pairs). For background measurement or during flushing, over 1000 scans are collected.

In order to adjust the manual sampling, the actual breakthrough curve needs to be known immediately in order to make column handling and a intelligent reduction of the sample number possible. Without online measuring, the actual TBC is completely unknown and manual samples need to be

collected and (partially) analyzed. An example of an evaluated TBC is given in Fig. 3.5.

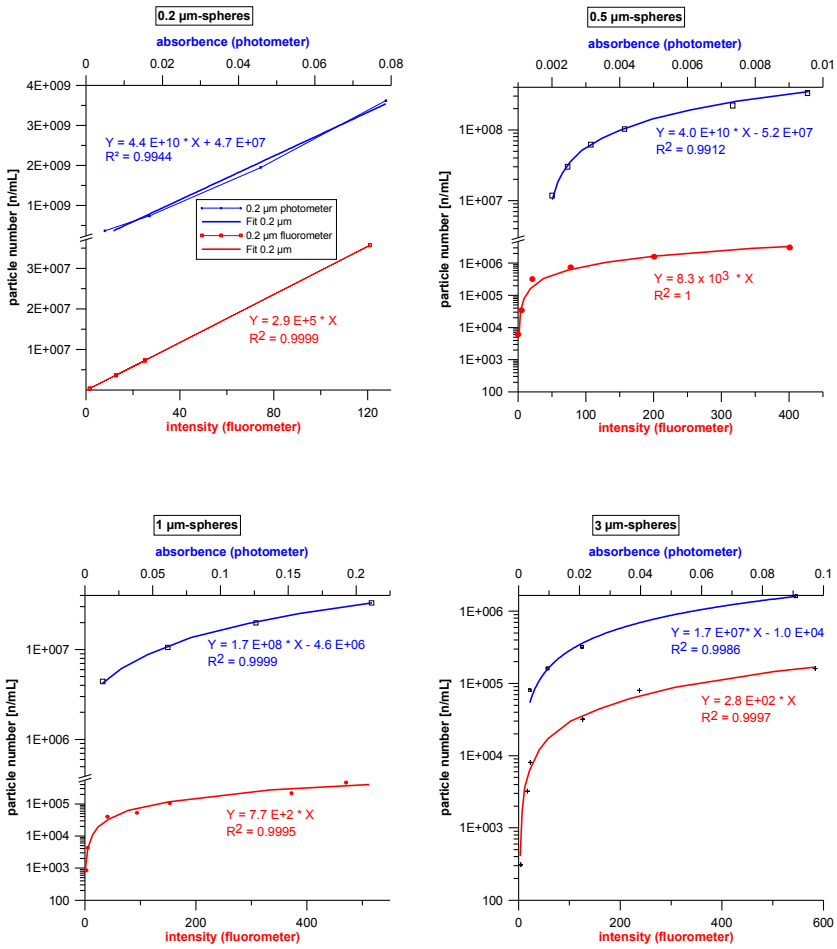

Fig. 3.4: Comparison of the accuracy of the fluorometer and photometer measurement of the microsphere sizes 0.2 µm, 0.5 µm, 1 µm and 3 µm (please note: y-axis units linear or logarithmic).

By choosing the optimum fluorescence wavelength, the 3D scan can be transformed into a conventional TBC (Fig. 3.5). By further multiplying with the calibration factor, intensities can be transferred into concentrations (for both solutes and particles). The individual steps are further described in chapter 3.2.3 Software development.

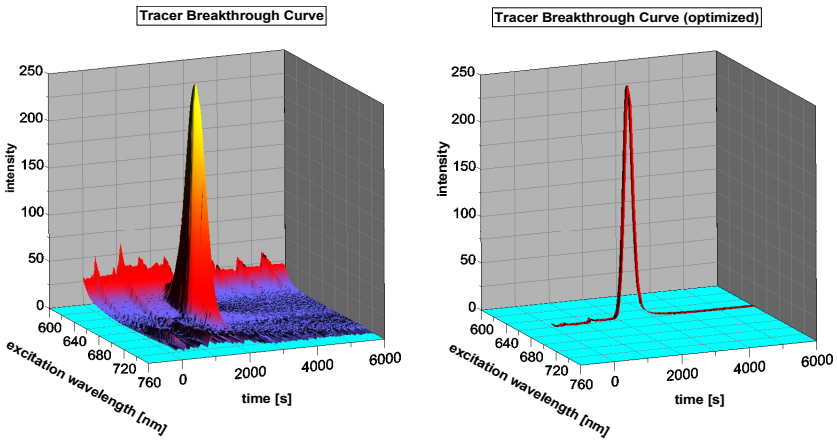

Fig. 3.5: Complete 3D scan of a TBC (left) and computed TBC after choosing the optimum wavelength (right).

3.2.3 Software development

The FLWinlab software generally does not allow to implement the scan file (*.sp) directly into any calculation software; it has to be imported individually. In fact, the software creates a 3D-scan-file (*.sp3), but shows no exportation mode and no advanced graphic or calculation interface.

Therefore an OpenOffice.org Basic software tool was developed to improve the data handling by an open source software.

The software includes the following features:

- ➔ opens *.sp files, arranges them in an x,y,z- file (wavelength, intensity, time or Δλ), corrects the original spectrum time into the real measurement time or time after injection

- ➔ calculates the spectrum of selectable data-files (background or flushing data) by arithmetics
- ➔ reduces the spectrum by the background
- ➔ optimum wavelength can be selected and TBC is computed
- ➔ multiplies intensity with a given calibration factor

Screenshots show the simple structure of the so-called Cocos Software (ColloidCounting) (Fig. 3.6, Fig. 3.7).

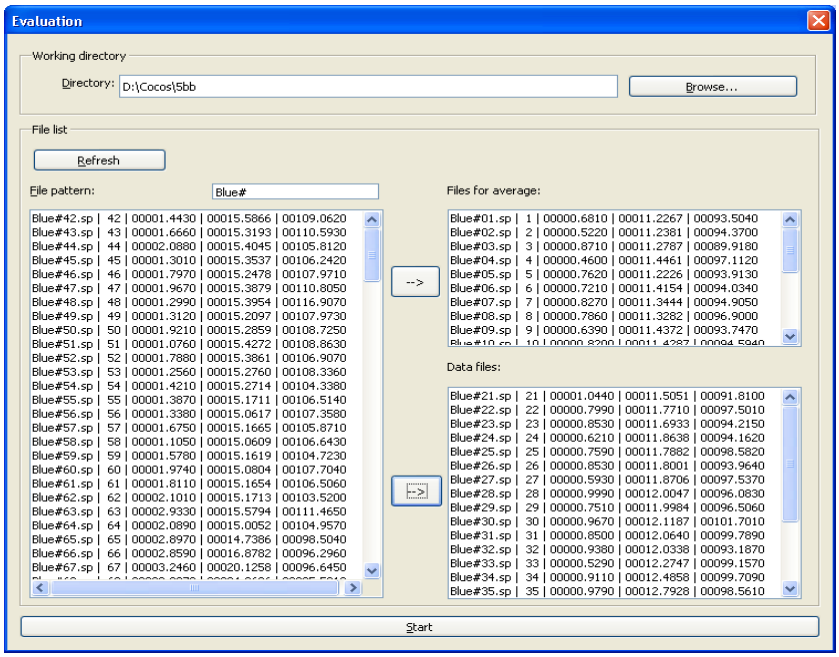

Fig. 3.6: Selection of the data files for background and measurement.

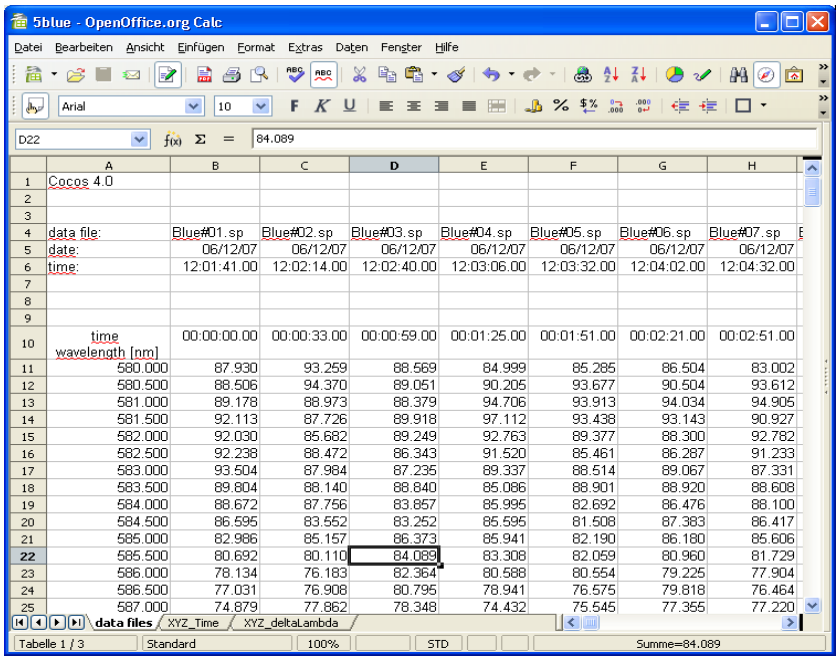

Fig. 3.7: Result file after arranging the files depending on the analysis time.

3.2.4 Microorganism evaluation

The microorganism counting followed standard methods described in Rossi 1994 or Käss 2004. For each dilution step, triplicates are prepared. The actual number of microorganisms is the arithmetic mean of the calculated number gained from the optimum dilution (Fig. 3.8). The influent concentration was determined by the same way.

A compilation of *Ralstonia eutropha* at different pore volumes or with different dilutions from the column test can be seen in Fig. 3.8. It is noteworthy that there is no obvious background concentration of other types of microorganisms, thus there is no influence of any other microorganisms that might disturb the microorganism counting procedure (Fig. 3.8).

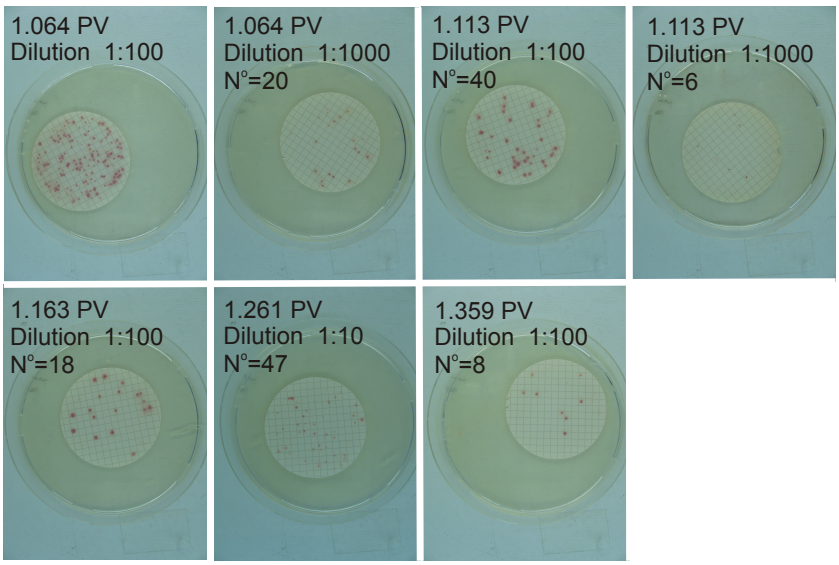

Fig. 3.8: Membrane filters (on growth media) with Ralstonia eutropha (obtained from column test with Dr. J. Zopfi, LAMUN, Neuchâtel), PV means pore volume. At PV 1.064 the dilution of 1:100 is obviously too low, a dilution of 1:1000 provides better data. At PV 1.113 the dilution of 1:1000 is too high, a dilution of 1:100 and a corresponding bacteria number of 40 is more accurate. The following filters (PV 1.261 and 1.359 PV) show that a significant bacteria concentration lasts over a relatively long time period (more than 1.359 PV).

As visible from Fig. 3.8, *Ralstonia eutropha* is first filtered through a membrane filter assembly and then grows on a Petri dish under a hydrogen atmosphere. By using the filtering method, a small number of the microorganisms can be counted even in larger water volumes. In this project, the number and recovery of this bacteria was completely unknown, therefore a large set of dilutions (and also the filter assembly in case of a small number of bacteria) was used, for instance a number of about 40 as shown for PV 1.113 in Fig. 3.8 is countable, whereas larger or smaller number show a certain level of uncertainty.

Serratia marcescens grows under a normal atmosphere and does not need

to be filtered [Käss 2004]. An example is given in Fig. 2.5c. A volume of 2 mL was used for enumeration.

H40/1 was evaluated by using the double agar layer technique [Rossi 1994]. For this method, 2 mL samples are needed, mixed with 0.2 mL of the adequate marine bacterial culture and left for 15 mins at room temperature. Then the mixture is distributed onto a Petri dish that contains 20 mL solid medium (1% agar). Shortly afterwards, 4 mL of 0.6% soft medium are added, mixed and the Petri dish is incubated. This gives the lysis plaques of the phage H40/1 as shown in Fig. 2.5a.

3.3 Vertical column tests

3.3.1 Overview

Vertical saturated column tests with different media and different background solutions (different ionic strength) were conducted as pulse-injections. An overview of the applied medium, tracers and background solution is given in Tab. 3.4.

The tracer tests with solutes and microspheres were repeated three times (triplicate) (Fig. 3.9). The differences in TBC were shown to be negligible for all

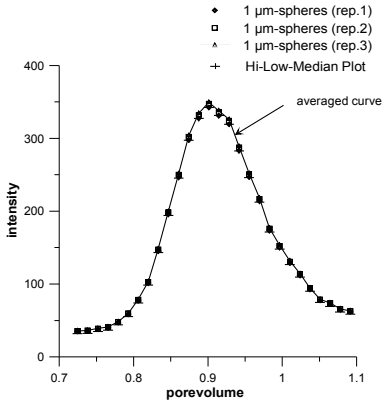

Fig. 3.9: Reproducibility of a representative TBC.

solutes and the microspheres, therefore triplet tests were waived for the microorganisms, and besides this the entire tracer set-up and analysis was proven to be independent and reliable.

The procedure for obtaining the reproducibility of the tracer experiments in saturated soil columns was similar for all tracers (except for the microorganisms). The relative standard deviation (RSD) was calculated for all triplets to show the reproducibility of the TBC. The RSD is defined as: RSD= 100 (standard deviation / mean value). For the TBC a very good accuracy was obtained (RSD = 0 – 3 %).

An example for the RSD of 1 µm spheres along a TBC is given in Fig. 3.9. Thus, for clarity reasons, solute and microsphere TBC are displayed as the arithmetic mean of the three curves, whereas microorganisms are the actual (single) TBC.

3.3.2 Medium preparation

The two media (quartz glass beads and quartz sand) with a diameter of 0.3 - 0.4 mm diameter and a density of 2.64 respectively 2.50 g/cm³ were chemically washed in order to remove chemical impurities and accompanying charge heterogeneities. In an additional step, the so washed medium was partly silanised after a standard-method [Han et al. 2006] to get defined surface heterogeneities (positively charged particle surfaces).

The chemical washing procedure includes the following steps:

- 300 g substrate is shaken in 500 mL of a 0.2 M citrate-buffer-solution (44.1 g/L $Na_2C_6H_5O_7 \cdot 2H_2O$; 10.5 g/L $H_2C_6H_5O_7$) and heated at 80°C for the next 12 h.
- Addition of 15 g sodium-dithionite ($Na_2S_2O_4$) and shaking it hard.
- Decanting of the solute; three repeats of the abovementioned procedure.
- Washing of the medium with distilled water and drying in the oven at 105°C for at least 24 hours.

The so treated medium is called hydrophilic substrate hereafter. Partly hydrophobic (silanised) particles are obtained through the following instruction [Han et al. 2006]:

- 300 g substrate are shaken in 300 mL of a solution of 0.375 mL OTS (octadecyl-trichlorosilane) for 2 hours and dried at 110°C for 24 hours.

- 50 g portions are rinsed twice with 150 mL pentane and methanol, 1 M HCl and distilled water until a neutral pH-value is reached (Fig. 3.10).
- Oven drying at 105°C for 24 hours.

*Fig. 3.10: Quartz glass beads in a suction filter (*Büchner funnel*) prior to the rinsing with pentane.*

As background solution 0.1, 1 and 10 mM $NaNO_3$-solutions were used and tested prior to application of their fluorescence properties. The applied microspheres and solutes were found not to interfere with the background solutions. Fluorescence quenching effects of the background solution were tested through adding higher concentrated solutions to colloid suspensions of different concentrations (in the range of the expected particle concentration values). Significant intensity variations were not observed and therefore quenching effects can be excluded.

Tab. 3.4: Overview over the substrates, tracers and background solutions of the vertical saturated column tests.

substrate	tracer	background solution
quartz beads (chemically washed)	microspheres (0.2, 0.5, 1, 3, 5 µm) uranine lithium chloride	0.1 mM $NaNO_3$ 10 mM $NaNO_3$
	microspheres (0.2, 0.5, 1, 3, 5 µm) uranine lithium chloride *serratia marcescens* *ralstonia eutropha* H 40/1	1 mM $NaNO_3$
quartz beads (chemically washed & treated with silane)	microspheres (1 µm) uranine	0.1 mM $NaNO_3$ 10 mM $NaNO_3$
	microspheres (0.2, 0.5, 1, 3, 5 µm) uranine lithium chloride *serratia marcescens*	1 mM $NaNO_3$
quartz sand (chemically washed)	microspheres (1 µm) uranine	0.1 mM $NaNO_3$ 10 mM $NaNO_3$
	microspheres (0.2, 0.5, 1, 3, 5 µm) uranine lithium chloride *serratia marcescens*	1 mM $NaNO_3$
quartz sand (chemically washed & treated with silane)	microspheres (1 µm) uranine	0.1 mM $NaNO_3$ 10 mM $NaNO_3$
	microspheres (0.2, 0.5, 1, 3, 5 µm) uranine lithium chloride *serratia marcescens*	1 mM $NaNO_3$

3.3.3 Column set-up

Fig. 3.12 illustrates the operation of the vertical soil columns. The vertical column has a 26 mm inner diameter and a length of 30 cm (Fig. 3.11). The columns were filled with the substrate by the fill and tap method which together with the relatively small diameter prevents against preferential flow paths and grain bridges inside the substrate. On both sides (inlet and outlet) are threads of screws on the column outside that must be closed with compatible caps (Fig. 3.11). The caps have a 9 mm opening in which a connector can be introduced that narrows the width to under 1.5 mm, which is the diameter of the Teflon-tube. Inside the connector, glass wool can be introduced to avoid flushing or gravitational settling of soil particles into the connected Teflon-tubes. An examination of the glass wool after the end of each investigation cycle indicated that removal of the colloids by the glass wool is negligible.

On the inlet side, the reservoir is connected to a peristaltic pump by Teflon-tubing and over an injection loop the tracer can be directly introduced into the soil column. The injection loop permits a very low injection volume (up to 100 µL) which is approximately 1/5000 pore volumes. Kretzschmar et al. 1997 used pulse injections to minimize the effect of clogging and ripening of colloids and make colloid column tests more accurate and reliable. The further decrease of the injection volume within this study is in excellent agreement with Kretzschmar et al. 1997.

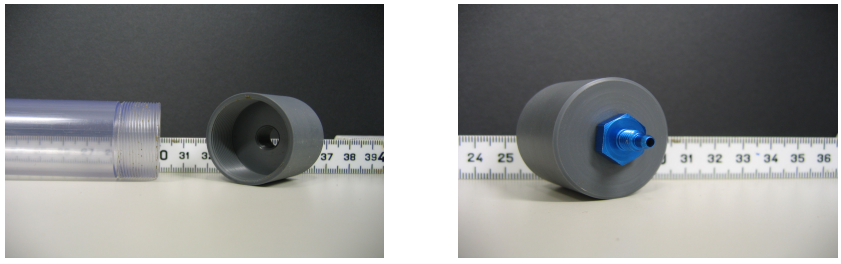

Fig. 3.11: Laboratory column with outside thread of screws and cap with inside threads (left) and cap with connector (right).

A non-return valve (mini non-return valve, 1/8”, Viton membrane, PP, novodirect GmbH) arranged in front of the injection loop prevents against back flushing of the tracer towards the reservoir during injection.

After the column outlet the flow-through cell inside the laboratory spectrofluorometer measured the fluorescence intensity online in a

30 seconds-interval. Additional samples were collected by a micro-fraction sampler (FC 203, Gilson). The sampling interval was adjusted so that a sample of 2 mL was obtained. The electrical conductivity, temperature and pH-values were also measured for each sample.

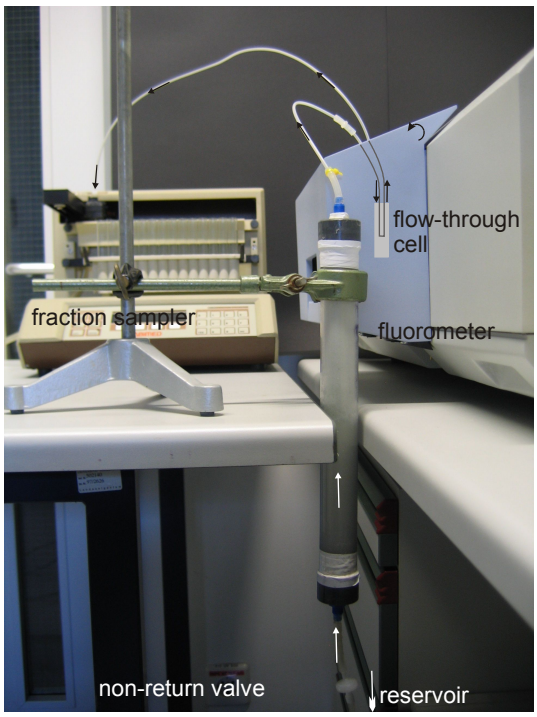

Fig. 3.12: Column set-up (column and tubes are covered with aluminum foil during test).

3.3.4 Column test procedure

During the test the following parameters were modified:

- matrix
- surface properties (hydrophilic and hydrophobic)
- background solutions (ionic strength: 0.1 mM, 1 mM and 10 mM

$NaNO_3$)

- tracers

The flow velocity was constant. All column tests were conducted in an air-conditioned environment (around 20°C air temperature) in three different repetitive phases (Fig. 3.13):

1. Flushing with background solution until hydrochemical conditions are stable and air bubbles are absent, online measurement of the intensity (and besides this: at the outlet measurement of electrical conductivity, temperature, pH-value) for monitoring purposes, at least 15 pore volumes.
2. Injection of the tracer through the injection loop (volume: 100 µL).
3. Online measurement of the TBC (parallel collection of samples by the fraction collector).
4. (rep. 1) Flushing with background solution, parallel online-measuring for monitoring purposes, at least 15 pore volumes.
5. (rep. 2.) Injection of the tracer through the injection loop.

End: inspection of the soil columns, repacking.

After the end of an experiment phase (i.e. after the end of the TBCs of all tracers that are the subject of one investigation cycle), the soil columns were depacked and repacked with new substrate for the next experiment. The soil columns were not stored.

After each investigation cycle, the samples collected by the fraction sampler were analyzed. The online measurements were computed and the results compared to the manual samples. As previously mentioned, the solute and microsphere investigation cycles were repeated three times, whereas the microorganism tests were single tests. They followed a different procedure:

1. Flushing with background solution until hydrochemical conditions are stable and air bubbles are absent, measurement for monitoring purposes of electrical conductivity, temperature and pH-value, at least 15 pore volumes.
2. Injection of the tracer through the injection loop (volume: 100 µL).
3. Collection of samples by the fraction collector.
4. (rep. 1) Flushing with background solution, parallel measurements for monitoring purposes, at least 15 pore volumes.

5. (rep. 2.) Injection of the tracer through the injection loop.

End: inspection of the soil columns, repacking.

To avoid growth or decay, the microorganisms were analyzed immediately after collection by methods described in Rossi 1994.

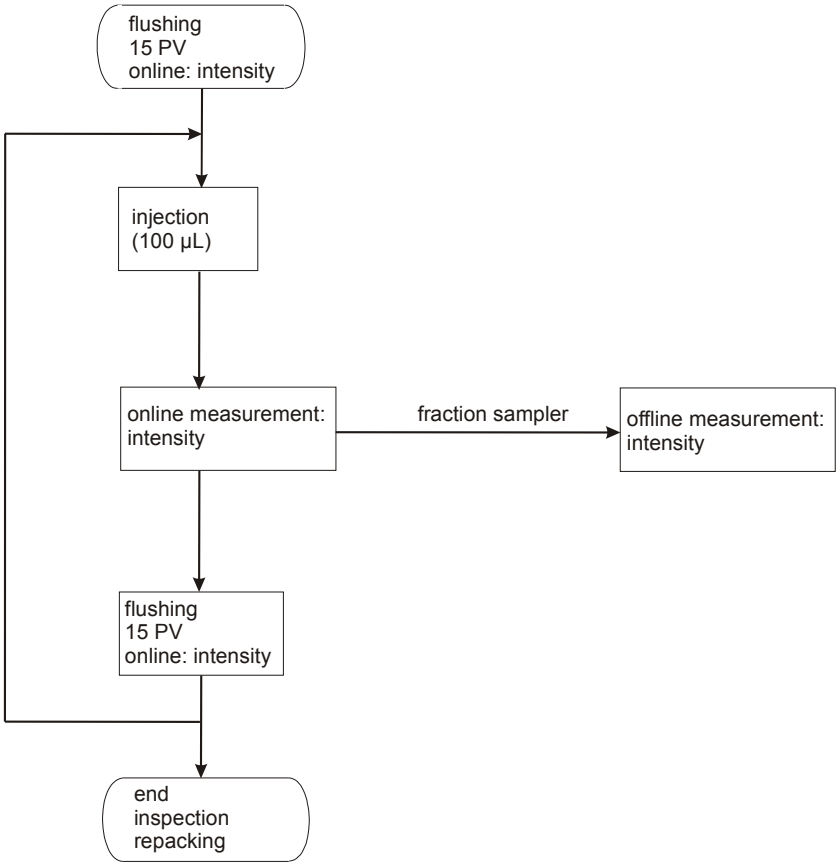

Fig. 3.13: Flow chart of column test procedure.

3.4 Results and discussion

3.4.1 Introduction

3.4.1.1 Manual vs. online measurements

Pulse injections have the advantage that particle transport is not affected by blocking or filter ripening and therefore transport interpretation can more clearly be attributed to the transport parameters [Kretzschmar et al. 1997]. Thus to keep low both the particle injection number and the sampling interval is of prime importance.

First of all, the injection volume of a pulse injection has to be short, i.e. much smaller than 1 pore volume [Kretzschmar et al. 1997]. In this study the injection volume was about 0,001 pore volume.

The online measurement method uses a short sampling interval of 30 s, which is the optimum time for the instrument to scan the entire spectrum required for data analysis, save the data file and start the next measurement. With custom-built fluorescence field data loggers, potential background concentrations are be subtracted by standard mathematical functions – though a subtraction of a real measured background afterwards as applied by the online measurement using a laboratory instrument is preferable.

Fig. 3.14 and Fig. 3.15 illustrate the advantages of the online measurements by combination of online and offline measurements. It is clearly visible that the short intervals during online measuring allow a more precise evaluation of TBCs whereas the larger intervals of manual measurements show significant data gaps in pulse tests.

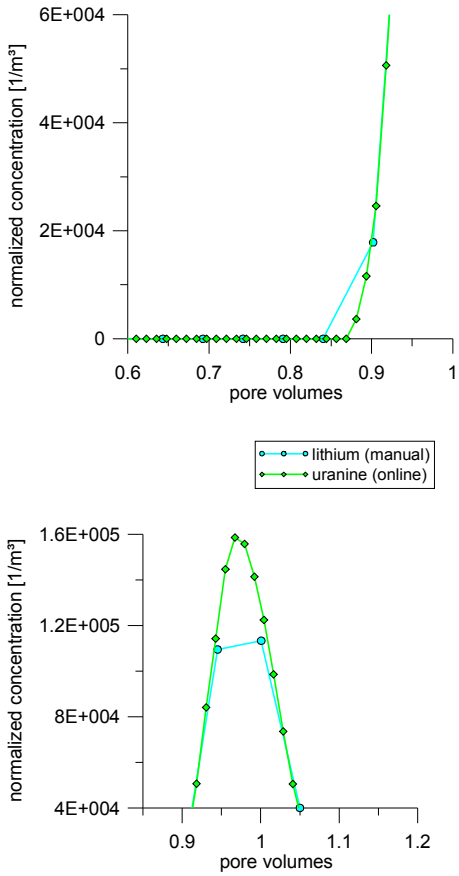

Fig. 3.14: Comparison of manual (lithium) and online (uranine) measurements with clearly visible better resolution of the first detection time (above) and peak concentrations (below) of online measurements (both diagrams without smoothing).

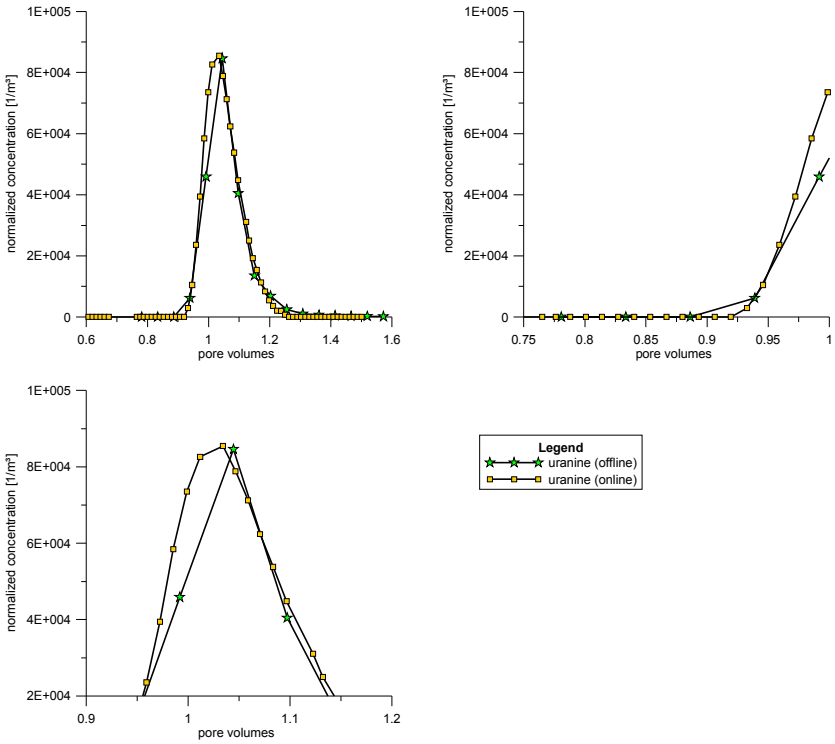

Fig. 3.15: Comparison of online and offline measurements of uranine (without smoothing data). The complete TBC is shown on the upper left. First detection time is more precisely defined by the online measurements (upper right) and peak concentrations as well (lower left).

3.4.1.2 Introduction to experimental data and modeling

All results of the column tests are shown as breakthrough curves on a pore volume x-axis and normalized concentration y-axis. A common scale (i.e. normalized concentration [1/m³]) is used in order to avoid scaling effects due to different axis units for solutes and particles [Zhang et al. 2001].

Afterwards, travel times and flow velocities, peak concentration, dispersion

coefficient, dispersivity and Peclet number are shown for each tracer. The first detection time (FDT) and corresponding fastest flow velocity, the peak time and corresponding peak velocity are given from basic data, whereas the mean transit time and the corresponding median flow velocity are based on modeling the TBC with a conventional ADE. The mean transit time usually corresponds to the half-life time after a 50% recovery rate.

The dispersion coefficient, the corresponding dispersivity and Peclet numbers are calculated based on equations 3 and 4.

The quartz beads and quartz sand chapters close with a modeling chapter where the results of the modeling based on filtration theory are shown. The results of the diffusion and dispersion parameters and Peclet numbers are composed in order to understand the diffusion behavior of the different tracer types.

The relative importance of dispersion and diffusion is visible from Fig. 3.16, where three different regions with different transport characteristics can be distinguished [Rehfeldt et al. 2004]. Region I is dominated by diffusion over the

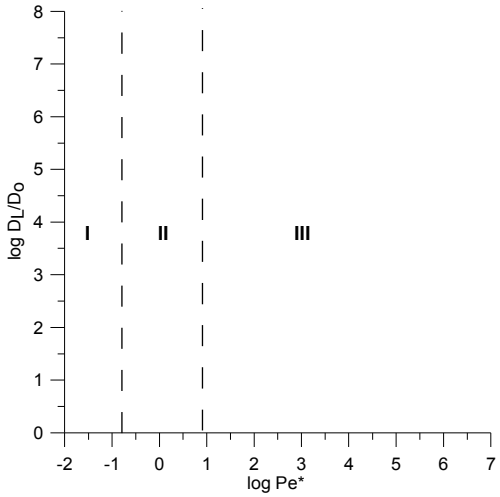

Fig. 3.16: Rate of dispersion to diffusion as a function of Pe.*

mechanical dispersion – logarithmic modified Peclet numbers Pe* are smaller than -0.8. Region II (between log Pe* -0.8 and 0.8) is a transition zone with both processes operating in the same order of magnitude. In region III with logarithmic Pe* larger than 0.8 mechanical dispersion dominates. The results of the column tests are plotted in this diagram and the predominant process for each tracer for all experiments is determined.

In a final discussion chapter, the results of all tracer types and all matrix types are discussed. There is no general concept on how to interpret the different TBCs of particles and solutes. Some authors use the first detection time (FDT), some use the peak concentration time as criteria and others a combination of both together with fit results. In order to evaluate this concept, results for all of them are shown in tables and are finally discussed in the closing chapter. Finally, the results of the diffusion coefficients for particles based on modeling in contrast to theoretical considerations are discussed.

3.4.2 Quartz beads – experimental data

3.4.2.1 Hydrophilic quartz beads

Fig. 3.17, Fig. 3.18, Fig. 3.19 and Fig. 3.20 summarize the TBCs for all tracers in vertical saturated column tests with hydrophilic quartz beads at different background solutions (0.1 mM, 1 mM and 10 mM $NaNO_3$).

Fig. 3.17 illustrates the TBCs of the 0.2 µm, 0.5 µm, 1 µm, 3 µm and 5 µm-spheres, the bacteriophage H40/1, the bacteria *Ralstonia eutropha* and *Serratia marcescens* and two solute tracers (uranine, lithiumchloride) at 1 mM $NaNO_3$. All tracers are plotted on a common scale (i.e. normalized concentration [1/m³]).

Fig. 3.18 shows in detail the microorganism and 1 µm spheres compared to the solute tracer at a background solution of 1 mM $NaNO_3$ on a logarithmic scale.

Fig. 3.19 shows the results for microspheres and solute tracers for a background solution of 10 mM $NaNO_3$ and Fig. 3.20 the 1 µm spheres at different ionic strengths (0.1 mM, 1 mM and 10 mM $NaNO_3$).

Tab. 3.5 and Tab. 3.6 give an overview over the transport parameters of the applied tracers, i.e. the travel times and corresponding flow velocities, the dispersion parameters and Peclet numbers. Tab. 3.10 gives an overview of the calculated recovery, effective porosity and the parameters evaluated based on filtration theory.

The solute tracers lithium and uranine show a sharper TBC and a higher peak concentration than all particle tracers. The travel times for the solutes are around one pore volume whereas the travel times for the particle tracers differ significantly – some precede, some show retardation compared to the solutes.

A discussion of the processes that cause preceding particles is given in chapter 3.4.6.3 Peak shift analysis.

Serratia marcescens and the 1 µm spheres show very similar TBCs (Tab. 3.15), a behavior that can be explained by similar particle size (*Serratia marcescens* is about 1.1 µm) and surface properties. The recoveries for 1 µm spheres and *Serratia marcescens* are identical (79.79% resp. 80.32%). The shape of the curve (First detection time = FDT) and the peak concentrations are similar, although there are some irregularities at the tailing of the *S. marcescens* curves (Tab. 3.18). Compared to the solute tracers, the recovery is smaller for the 1 µm spheres and *S. marcescens*, the first detection time (FDT) is earlier, as well as peak time and mean transit time.

The second bacterium, *Ralstonia eutropha,* shows a slightly higher recovery (85.99%), but very similar FDT, peak time and median transit time compared to *Serratia marcescens* and 1 µm spheres.

The recovery for the bacteriophage H40/1 is one order of magnitude lower (8.14%), the TBC is more irregular and peak time and median transit time are higher.

The microspheres (except the 1 µm spheres) show significantly higher mean transit times and lower recovery than *Serratia marcescens*. The mean transit time increases with the following order: 0.2 µm, 0.5 µm, 3 µm and 5 µm spheres. The peak times for the 0.5 µm, 3 µm and 5 µm spheres are higher than for the solutes and lower for the 0.2 µm spheres. However, the FDTs of most microspheres are lower than for the solutes and in the range of the microorganisms.

The dispersion coefficient is lowest for TBCs with a narrow peak and without a distinctive tail. In this case the dispersion coefficient is lowest for the solutes that do not show large tailing – an effect which for column tests is better visible in log-diagrams (Fig. 3.18) (D_L for uranine: 0.003 m²/day, lithium 0.004 m²/day).

Dispersion coefficients for the microspheres and microorganisms are higher. The highest dispersion coefficients were obtained by the bacteria *Serratia marcescens* (0.041 m²/day) and 1 µm spheres (0.035 m²/day).

The results for the microspheres with a background solution of 10 mM $NaNO_3$ show significantly lower recovery rates which can be explained by

filtration theory. Microorganisms were not tested for these experimental conditions.

The relationship between the microspheres and the solutes is constant. Again, the 1 µm spheres precede the solute tracers and reach the highest recovery rate (17.21%). The FDT is lower for most microspheres or equal (5 µm spheres). Peak time and mean transit time do not differ much for the two background solutions.

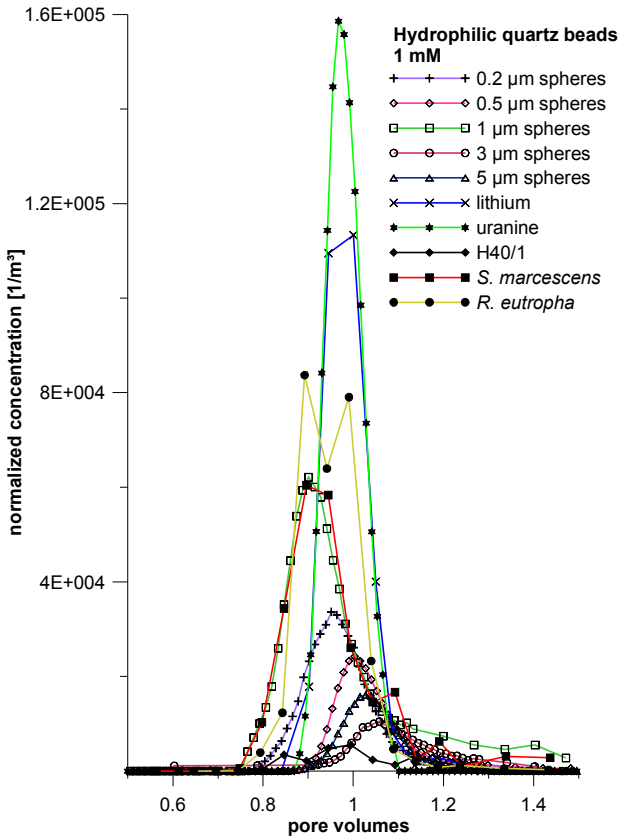

Fig. 3.17: Summarized TBCs of microspheres, microorganisms and solute tracers for hydrophilic quartz beads (background solution 1 mM $NaNO_3$).

The dispersion coefficient is higher for uranine in this experiment, which indicates that uranine may show some retardation effects and reactions with the matrix. Therefore lithium is used as a conservative tracer in the following experiments.

The dispersion coefficient is highest for the 0.5 µm spheres (0.622 m²/day), followed by the 1 µm spheres (0.580 m²/day).

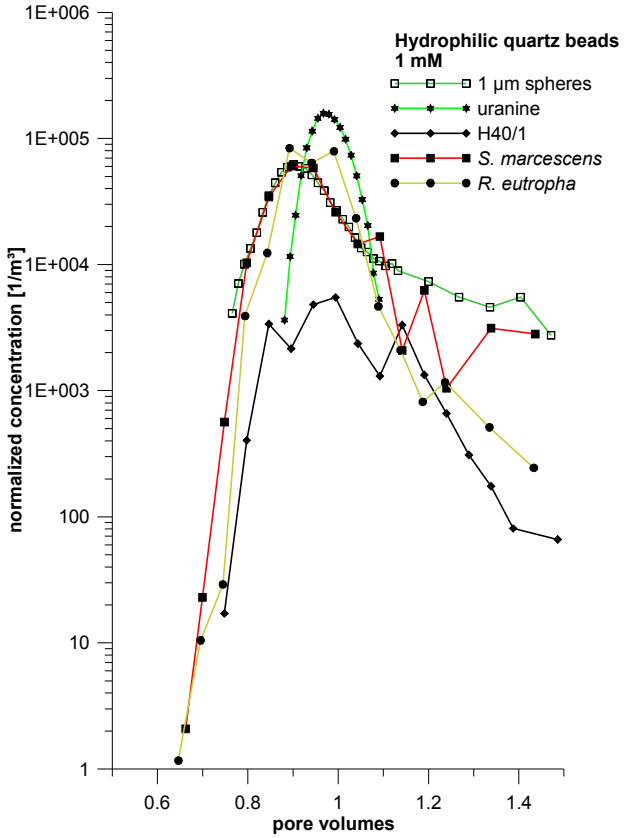

Fig. 3.18: TBCs of the solute tracer, the 1 µm spheres and the microorganism for hydrophilic quartz beads and a 1 mM $NaNO_3$ background solution in a log diagram.

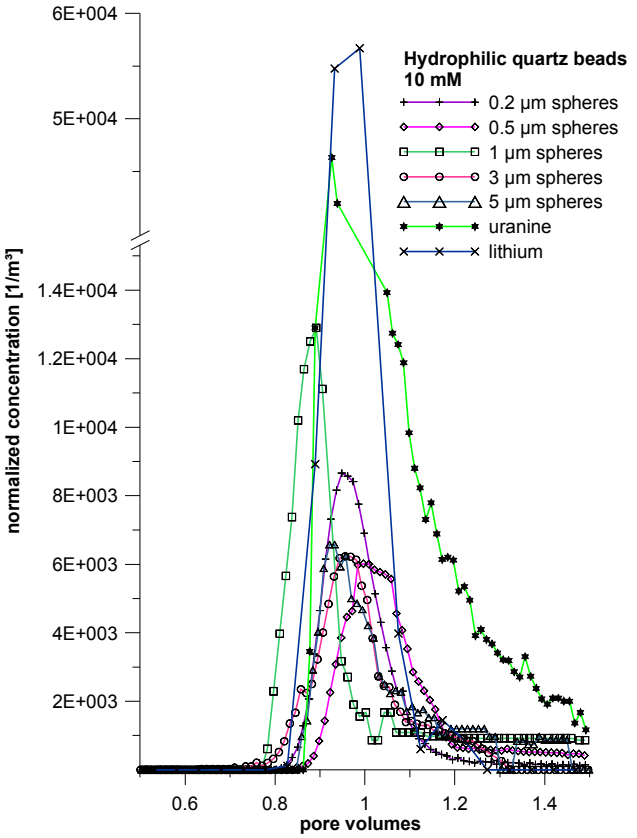

Fig. 3.19: TBCs of all tracers applied in hydrophilic quartz beads and a background solution of 10 mM $NaNO_3$ (please note the y axis break).

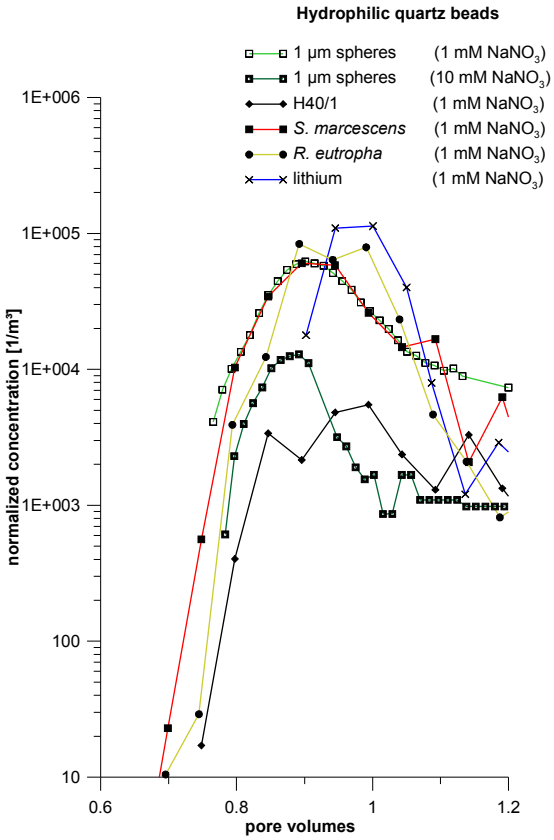

Fig. 3.20: Summarized TBCs of the microbiological and microsphere tracers (1 µm spheres) at two different background solutions (1 and 10 mM $NaNO_3$).

Tab. 3.5: Travel times and flow velocities of solute and colloidal tracers in an experimental column filled with hydrophilic quartz beads.

	first detection time (FDT) t_1 PV	fastest flow velocity v_{max} [m/day]	peak time t_p PV	peak concentration c_{max}/M [1/m³]	peak velocity v_p [m/day]	median transit time t_m PV	median flow velocity v_m [m/day]
matrix: hydrophilic quartz beads							
background solution: 1 mM $NaNO_3$							
microspheres							
[µm]							
0.2	0.78	13.7	0.95	3.37E+04	11.2	0.96	11.1
0.5	0.62	17.2	1.00	2.42E+04	10.6	1.03	10.4
1	0.77	13.9	0.90	6.21E+04	11.8	0.94	11.1
3	0.60	17.7	1.06	1.05E+04	10.1	1.07	10.0
5	0.87	12.3	1.03	1.61E+04	10.4	1.04	10.3
solute tracers							
uranine	0.88	12.1	0.97	1.59E+05	11.0	0.98	10.8
lithium	0.90	11.8	1.00	1.13E+05	10.6	1.00	10.6
microorganisms							
H40/1	0.75	14.2	0.99	5.50E+03	10.7	0.99	10.7
S. marcescens	0.66	16.0	0.90	6.04E+04	11.9	0.94	11.2
R. eutropha	0.65	16.4	0.89	8.37E+04	11.9	0.94	11.3
background solution: 10 mM $NaNO_3$							
microspheres							
[µm]							
0.2	0.81	13.1	0.95	8.66E+03	11.2	0.97	11.0
0.5	0.85	12.6	1.00	6.02E+03	10.7	1.09	9.7
1	0.78	13.6	0.89	1.29E+04	11.9	0.99	10.8
3	0.64	16.8	0.96	6.23E+03	11.2	0.97	11.0
5	0.86	12.4	0.92	6.58E+03	11.6	0.99	10.7
solute tracers							
uranine	0.88	12.1	0.93	4.63E+04	11.5	0.99	10.8
lithium	0.83	12.0	0.99	5.67E+04	10.8	0.99	10.8

Tab. 3.6: Dispersion coefficients, dispersivities and Peclet numbers for hydrophilic quartz beads.

	dispersion coefficient D_L [m²/day]	dispersivity α_L [m]	Peclet number Pe [ ]
matrix: hydrophilic quartz beads			
background solution: 1 mM $NaNO_3$			
microspheres			
[µm]			
0.2	0.012	1.04E-03	289
0.5	0.011	1.06E-03	283
1	0.034	3.08E-03	98
3	0.026	2.64E-03	114
5	0.005	5.28E-04	568
solute tracers			
uranine	0.003	2.90E-04	1036
lithium	0.004	4.11E-04	729
microorganisms			
H40/1	0.025	2.29E-03	131
S. marcescens	0.041	3.66E-03	82
R. eutropha	0.010	9.21E-04	326
background solution: 10 mM $NaNO_3$			
microspheres			
[µm]			
0.2	0.015	1.36E-03	220
0.5	0.623	6.40E-02	5
1	0.581	5.39E-02	6
3	0.019	1.76E-03	170
5	0.033	3.06E-03	98
solute tracers			
uranine	0.033	3.03E-03	99
lithium	0.005	4.24E-04	707

3.4.2.2 Hydrophobic quartz beads

The TBCs for the hydrophobic quartz beads at different background solutions (1 mM and 10 mM $NaNO_3$) are described in this chapter. The TBCs for a background solution of 1 mM are shown in Fig. 3.21, Fig. 3.22 and Fig. 3.23. An overview over travel times and flow velocities is given in Tab. 3.7, dispersion coefficients, dispersivity and Peclet numbers in Tab. 3.8.

Fig. 3.21 illustrates the results of the 1 mM background solution for all tracers and the microorganism *Serratia marcescens*. The tracers are plotted on a common y-axis for the normalized concentration (1/m³) that was broken due to visibility reasons.

Fig. 3.22 shows in detail the microorganism, the 1 µm spheres and solute tracers in a background solution of 1 mM $NaNO_3$ on a logarithmic scale.

Fig. 3.23 shows the results for the microspheres and tracers for a background solution of 10 mM $NaNO_3$.

Tab. 3.11 gives an overview over the calculated recovery, effective porosity and the parameters evaluated based on filtration theory.

As for the hydrophilic quartz beads, the solute tracers show a sharper TBC and a higher peak concentration than all particle tracers, the recovery rate is equal to the tests for hydrophilic quartz beads: about 95% resp. 100%. Travel times are about one pore volume, the microspheres' travel times vary.

The recovery rate for the microspheres and the bacteria varies strongly compared to the results of the hydrophilic quartz beads. The recovery for the hydrophobic matrix of the 1 µm spheres is about 1/4th of the hydrophilic matrix. For the microorganisms (*Serratia marcescens*) the recovery is about 1/60th. The solutes show equal recovery for both tests.

1 µm spheres and *Serratia marcescens* show similarly shaped TBCs (Fig. 3.22). FDT, peak times and median transit times are similar, they show a similar tailing as well. Thus the dispersion coefficient (1 µm spheres: 0.235 m²/day; *Serratia marcescens*: 0.236 m²/day), dispersivity and Peclet numbers are similar.

The other microsphere sizes show higher transit times and lower recovery rates than the 1 µm spheres. At lower particle concentrations, the TBCs tend to be more irregular.

The larger microspheres (3 µm and 5 µm spheres) are usually slower than the solutes, the 1 µm spheres are the fastest microspheres, followed by 0.5 µm and 0.2 µm spheres.

The highest dispersion coefficient is reached by the bacteria, followed by the 1 µm spheres.

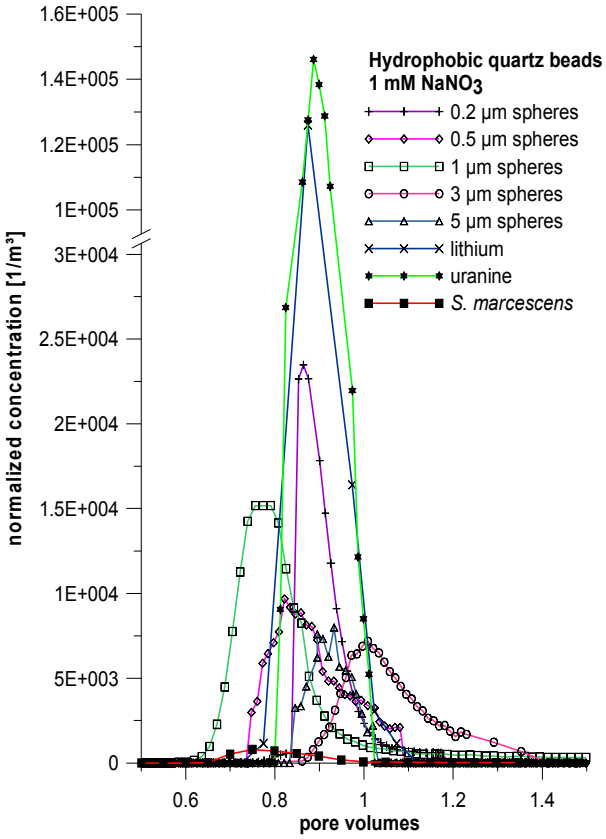

Fig. 3.21: TBCs of all tracers for hydrophobic quartz beads and a 1 mM $NaNO_3$ background solution (please note the y axis break).

The results of the microspheres with a background solution of 10 mM $NaNO_3$ show the same behavior as for the hydrophilic beads. They show significantly lower recovery rates, which can be explained by filtration as well. Microorganisms were not tested for the background solution with a higher ionic strength.

The solutes again show a narrow peak with a higher recovery rate without tailing of the breakthrough curve.

The relationship between the microspheres and the solutes is constant. The 1 µm spheres precede the solute tracers and reach the highest recovery rate (8.06%). The solute tracer lithium shows a higher flow velocity than the larger microspheres (3 µm and 5 µm spheres). The dispersion coefficient is highest

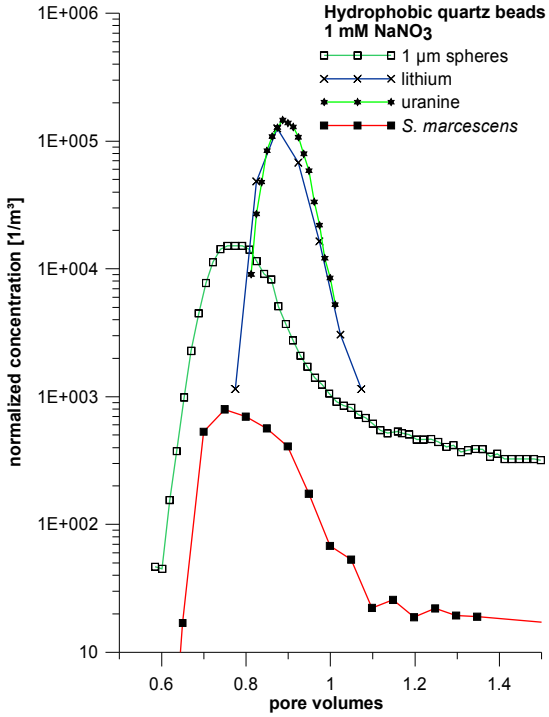

Fig. 3.22: TBCs for 1 µm spheres, Serratia marcescens, uranine and lithium on a logarithmic scale.

for the 1 µm spheres; 0.5 µm and 3 µm spheres show a dispersion coefficient one magnitude lower.

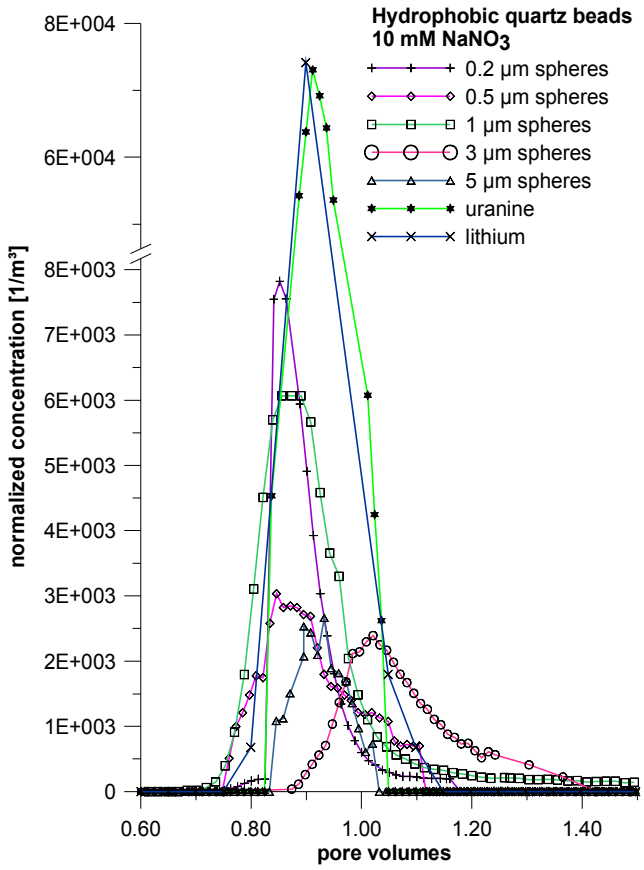

Fig. 3.23: TBCs for all tracers for the hydrophobic quartz beads and the 10 mM $NaNO_3$ background solution (please note the y axis break).

Tab. 3.7: Travel times and flow velocities for hydrophobic quartz beads.

	first detection time (FDT) t_1 PV	fastest flow velocity v_{max} [m/day]	peak time t_p PV	peak concentration c_{max}/M [1/m³]	peak velocity v_p [m/day]	median transit time t_m PV	median flow velocity v_m [m/day]
matrix: hydrophobic quartz beads							
background solution: 1 mM $NaNO_3$							
microspheres							
[µm]							
0.2	0.69	15.7	0.86	2.35E+04	12.5	0.90	12.0
0.5	0.75	14.3	0.82	9.67E+03	13.0	0.87	12.2
1	0.58	18.5	0.77	1.52E+04	14.0	0.81	13.4
3	0.86	12.4	1.01	7.18E+03	10.6	1.05	10.2
5	0.85	12.8	0.93	7.98E+03	11.6	0.92	11.7
solute tracers							
uranine	0.81	13.3	0.89	1.46E+05	12.2	0.90	12.0
lithium	0.77	13.9	0.87	1.26E+05	12.3	0.87	12.3
microorganisms							
S. marcescens	0.60	17.9	0.75	7.97E+02	14.4	0.85	12.7
background solution: 10 mM $NaNO_3$							
microspheres							
[µm]							
0.2	0.68	16.0	0.85	7.82E+03	12.7	0.89	12.1
0.5	0.76	14.0	0.85	3.04E+03	12.6	0.90	11.9
1	0.68	15.8	0.86	6.07E+03	12.6	0.91	11.9
3	0.87	12.2	1.02	2.39E+03	10.4	1.06	10.1
5	0.85	12.8	0.90	2.53E+03	12.1	0.91	11.9
solute tracers							
uranine	0.84	12.9	0.91	7.30E+04	11.8	0.92	11.7
lithium	0.80	13.5	0.90	7.41E+04	12.0	0.90	12.0

Tab. 3.8: Dispersion coefficients, dispersivities and Peclet numbers for hydrophobic quartz beads.

	dispersion coefficient D_L [m²/day]	dispersivity α_L [m]	Peclet number Pe [ ]
matrix: hydrophobic quartz beads			
background solution: 1 mM $NaNO_3$			
microspheres			
[µm]			
0.2	0.004	3.46E-04	866
0.5	0.021	1.69E-03	177
1	0.235	1.76E-02	17
3	0.019	1.88E-03	159
5	0.005	4.60E-04	652
solute tracers			
uranine	0.003	2.63E-04	1141
lithium	0.006	4.88E-04	615
microorganisms			
S. marcescens	0.236	1.86E-02	16
background solution: 10 mM $NaNO_3$			
microspheres			
[µm]			
0.2	0.006	4.67E-04	643
0.5	0.019	1.60E-03	188
1	0.145	1.22E-02	25
3	0.015	1.47E-03	204
5	0.006	4.67E-04	643
solute tracers			
uranine	0.003	2.49E-04	1205
lithium	0.006	4.61E-04	651

3.4.3 Quartz beads – modeling

3.4.3.1 Role of dispersion and diffusion

The relative importance of dispersion and diffusion is described in chapter 3.4.1.2 Introduction to experimental data and modeling. Diffusion parameters are calculated using the Stokes-Einstein equation 6. Dispersion is calculated for each tracer experimentally by evaluation of the TBCs.

The results of the hydrophilic and hydrophobic quartz beads (Tab. 3.9) fall into region III of the dispersion and diffusion diagram (Fig. 3.24). Thus dispersion is the predominantly operating process for hydrophilic and hydrophobic quartz beads.

The ratio D_L/D_o for hydrophilic and hydrophobic quartz beads increases with increasing Pe*. Diffusion generally increases for smaller particles. Thus the diffusion coefficient is smallest for the larger microspheres (Tab. 3.9).

For the hydrophilic quartz beads, the ratio D_L/D_o for a 1 mM background solution (b.s.) increases with increasing particle size (for all but the 5 µm spheres) and Pe* as well. For a 10 mM b.s., diffusion coefficient and Pe* remain constant, but the D_L/D_o ratio is highest for 1 µm and 0.5 µm spheres and lower for the other microsphere sizes. 1 µm, 0.5 µm and 5 µm spheres give a significantly larger dispersion coefficient at larger ionic strength. This is in turn an effect of the wider TBCs compared to those of lower ionic strength. *Serratia marcescens* and *Ralstonia eutropha* are close to the 1 µm spheres results, whereas the virus H40/1 is nearby the 0.2 µm spheres located. Thus the general transport behavior seems to be characterized by similar processes.

For the hydrophobic quartz beads, the D_L/D_o ratio behaves comparably to the 10 mM hydrophilic quartz beads for both ionic strengths: the ratio is largest for 1 µm spheres and decreases with smaller and larger microsphere sizes whereas the Pe* number increases for increasing microsphere sizes. The differences at different ionic strengths are negligible. *Serratia marcescens* behaves like the 1 µm spheres.

Tab. 3.9: Diffusion parameters for both types (hydrophilic and hydrophobic) of quartz beads.

	diffusion coefficient D_o [m²/day]	log D_L/D_o [ ]	log Pe* [ ]		diffusion coefficient D_o [m²/day]	log D_L/D_o [ ]	log Pe* [ ]
matrix: hydrophilic quartz beads				**matrix: hydrophobic quartz beads**			
background solution: 1 mM $NaNO_3$				**background solution: 1 mM $NaNO_3$**			
microspheres				**microspheres**			
[µm]				[µm]			
0.2	9.25E-08	5.10	4.62	0.2	9.25E-08	4.65	4.66
0.5	3.70E-08	5.47	4.99	0.5	3.70E-08	5.75	5.06
1	1.85E-08	6.27	5.32	1	1.85E-08	7.10	5.40
3	6.17E-09	6.63	5.75	3	6.17E-09	6.49	5.76
5	3.70E-09	6.17	5.99	5	3.70E-09	6.16	6.04
microorganisms				**microorganisms**			
H40/1	2.06E-07	5.08	4.26				
S. marcescens	1.68E-08	6.39	5.37	*S. marcescens*	1.68E-08	7.15	5.42
R. eutropha	1.78E-08	5.77	5.35				
background solution: 10 mM $NaNO_3$				**background solution: 10 mM $NaNO_3$**			
microspheres				**microspheres**			
[µm]				[µm]			
0.2	9.25E-08	5.21	4.62	0.2	9.25E-08	4.79	4.66
0.5	3.70E-08	7.23	4.96	0.5	3.70E-08	5.71	5.05
1	1.85E-08	7.50	5.31	1	1.85E-08	6.89	5.35
3	6.17E-09	6.50	5.80	3	6.17E-09	6.38	5.76
5	3.70E-09	6.95	6.01	5	3.70E-09	6.18	6.05

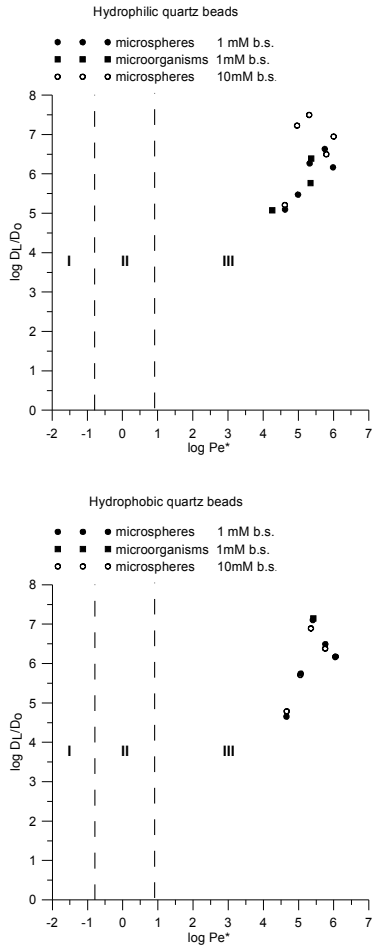

Fig. 3.24: Empirical relationship between dispersion and diffusion for the quartz beads and the simplified results of a column experiment (b.s. = background solution).

3.4.3.2 Filtration parameters

For modeling quartz beads (and quartz sand), equations and parameters described in chapter 2.5 Solute and colloid transport were used.

Tab. 3.10 and Tab. 3.11 give an overview over the computed parameters based on filtration theory.

Tab. 3.10: Results for hydrophilic quartz beads.

tracer	recovery	effective porosity	deposition rate coefficient	filter coefficient	single-collector removal efficiency	single-collector contact efficiency	attachment efficiency
		n_{eff}	κ	λ	η	η_o	α
	[%]	[ ]	[1/s]	[1/m]	[ ]	[ ]	[ ]
matrix: hydrophilic quartz beads							
background solution: 1 mM $NaNO_3$							
microspheres							
[µm]							
0.2	37.8	0.37	4.16E-04	3.25	1.21E-03	2.63E-02	4.59E-02
0.5	24.0	0.4	5.72E-04	4.76	1.84E-03	1.30E-02	1.42E-01
1	80.0	0.36	9.75E-05	0.75	2.73E-04	8.30E-03	3.29E-02
3	16.3	0.41	6.97E-04	6.05	2.41E-03	9.02E-03	2.67E-01
5	14.5	0.4	7.65E-04	6.45	2.51E-03	1.60E-02	1.57E-01
microorganisms							
H40/1	8.1	0.39	1.03E-03	8.36	3.17E-03	4.95E-02	6.41E-02
S. marcescens	80.3	0.37	9.50E-05	0.73	2.69E-04	7.94E-03	3.39E-02
R. eutropha	86.0	0.36	6.57E-05	0.5	1.85E-04	8.15E-03	2.27E-02
background solution: 10 mM $NaNO_3$							
microspheres							
[µm]							
0.2	9.4	0.38	1.00E-03	7.90	2.95E-03	2.63E-02	1.12E-01
0.5	11.5	0.42	8.12E-04	7.21	2.91E-03	1.30E-02	2.24E-01
1	17.2	0.38	7.31E-04	5.86	2.21E-03	8.30E-03	2.67E-01
3	7.5	0.37	1.10E-03	8.62	3.21E-03	9.02E-03	3.56E-01
5	8.2	0.38	1.04E-03	8.35	3.16E-03	1.60E-02	1.98E-01

Tab. 3.11: Results of the hydrophobic quartz beads.

tracer	recovery	effective porosity	deposition rate coefficient	filter coefficient	single-collector removal efficiency	single-collector contact efficiency	attachment efficiency
		n_{eff}	κ	λ	η	η_o	α
	[%]	[ ]	[1/s]	[1/m]	[ ]	[ ]	[ ]
matrix: hydrophobic quartz beads							
background solution: 1 mM $NaNO_3$							
microspheres							
[µm]							
0.2	13.8	0.34	9.14E-04	6.59	2.34E-03	2.66E-02	8.82E-02
0.5	10.5	0.34	1.07E-03	7.53	2.65E-03	1.41E-02	1.87E-01
1	20.1	0.31	8.26E-04	5.34	1.80E-03	8.41E-03	2.14E-01
3	9.5	0.4	9.25E-04	7.84	3.07E-03	9.02E-03	3.40E-01
5	5.6	0.35	1.31E-03	9.62	3.46E-03	1.63E-02	2.13E-01
microorganisms							
S. marcescens	1.3	0.32	2.13E-03	14.52	5.02E-03	8.04E-03	6.24E-01
background solution: 10 mM $NaNO_3$							
microspheres							
[µm]							
0.2	4.6	0.34	1.44E-03	10.26	3.62E-03	2.66E-02	1.36E-01
0.5	3.5	0.35	1.54E-03	11.19	3.99E-03	1.41E-02	2.83E-01
1	8.1	0.35	1.15E-03	8.4	3.00E-03	8.41E-03	3.56E-01
3	3.2	0.41	1.34E-03	11.5	4.54E-03	9.02E-03	5.03E-01
5	1.9	0.35	1.83E-03	13.29	4.74E-03	1.63E-02	2.92E-01

The calculated effective porosity (Fig. 3.26) shows that the pore space that is actually used by the colloid tracers differs according to the recovery rate. Tracers with a larger recovery rate are traveling faster. They use a smaller pore volume for flow than tracers with a smaller recovery rate. Obviously there are differences between the differently treated quartz beads that can be explained electrostatically. The hydrophobic quartz beads show a lower effective porosity for all colloid tracers. The hydrophobic quartz beads are positively charged and therefore colloids may be either attached (and thus show lower recovery rates) or are transported along with repelled fluid (which results in smaller effective pore space).

The calculated deposition rate coefficients and filter coefficients reflect the observed recovery that is largest for the 1 µm spheres, followed by 0.2 µm, 0.5 µm, 3 µm and 5 µm spheres. This is also valid for the microorganisms and

the different ionic strengths. Increasing ionic strength results in a reduction of the tracer recovery (Fig. 3.25) and therefore an increase of the deposition rate (Fig. 3.27) and filter coefficient. A change in the matrix surface properties from hydrophilic to hydrophobic quartz beads results in an increase of the filter coefficients and the deposition rate coefficients (Fig. 3.27). The filter coefficient for the hydrophobic quartz beads and a background solution of 1 mM $NaNO_3$ corresponds to the filter coefficient of the hydrophilic quartz beads and a background solution of 10 mM $NaNO_3$.

Due to repulsive interactions between colloids and collectors, the actual single-collector removal efficiency is lower than the semi-empirical single-collector contact efficiency which can be seen from Tab. 3.10 and Tab. 3.11. This repulsion effect is expressed by the attachment efficiency which reduces

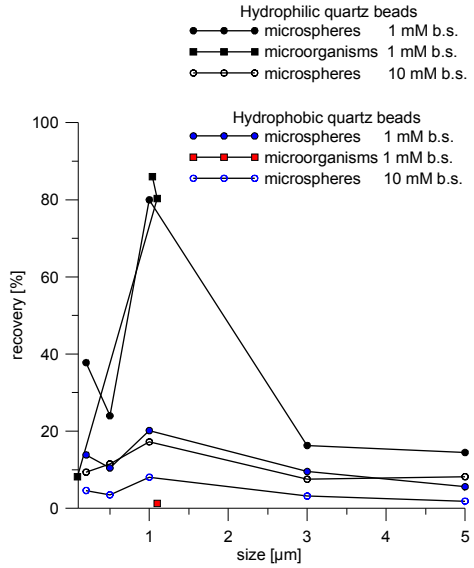

Fig. 3.25: Recovery for all particle tracers in hydrophilic and hydrophobic quartz beads.

the single-collector contact efficiency. The attachment efficiency represents the number of collisions that lead to attachment. A smaller number of the attachment efficiency means that a smaller number of collisions leads to

attachment. A smaller number of the single-collector efficiencies means that a smaller number of particles is deposited onto a collector in relation to the overall flux of particles towards the collector.

For the hydrophilic quartz beads and a background solution of 1 mM, the attachment efficiency is lowest for the 0.2 µm and 1 µm spheres. The microorganisms have attachment efficiencies in the same order of magnitude as the 1 µm spheres.

The semi-empirically calculated single-collector contact efficiency, and thus single-collector removal efficiency and attachment efficiency, show a slightly different picture compared to the filtration coefficient results for the different size classes of microspheres. This may be because the equations of single-collector contact efficiency do not consider the actual surface charge of the applied material and tracers and therefore may not give proper results for the different tracer types.

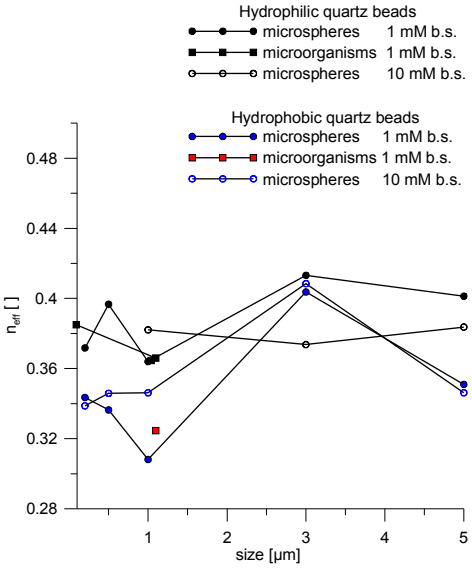

Fig. 3.26: Effective porosities for all particle tracers and microorganisms in hydrophilic and hydrophobic quartz beads.

According to the equations in Tufenkji 2007, the single-collector contact efficiency is lowest for the 3 µm, 1 µm and 0.2 µm microspheres. The actually calculated single-collector removal efficiency is lowest for 1 µm spheres, 5 µm and 3 µm spheres. The single-collector contact efficiency of the bacteria is in the range of the 1 µm spheres, the actual single-collector removal efficiency as well.

A higher ionic strength (10 mM) reduces the recovery of all tracers, increases the general filtration and decreases the differences between the parameters of different particle size classes. This is true of both bead types (hydrophilic and hydrophobic) equally. Furthermore, differences in the parameters for the different size classes in the hydrophobic matrix are lower due to the generally lower recovery rates.

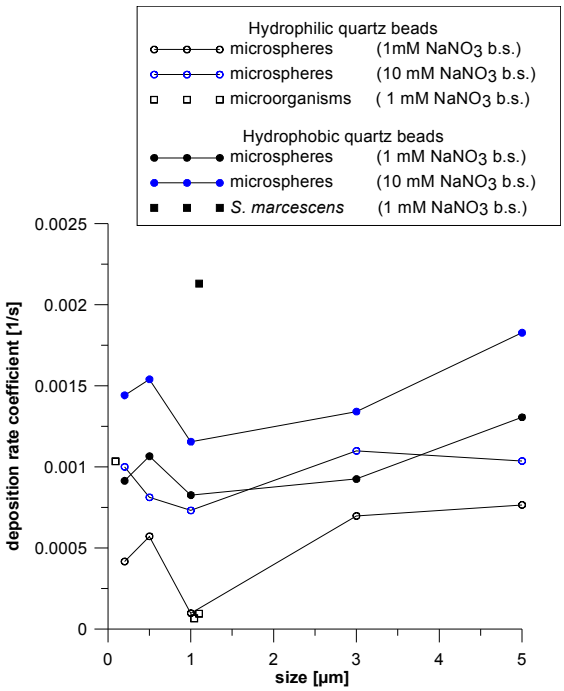

Fig. 3.27: Deposition rate coefficients for all tracers in a quartz beads matrix (b.s. = background solution).

For the bacteria this effect is obviously more distinct. The filter coefficient for *Serratia marcescens* in hydrophobic quartz beads is much higher (14.52 /m compared to 0.73 /m in hydrophilic quartz beads) as for the 1 µm spheres (5.34 /m compared to 0.75 /m).

3.4.4 Quartz sand – experimental data

3.4.4.1 Hydrophilic quartz sand

Fig. 3.28, Fig. 3.29 and Fig. 3.30 present the results of the column tests with hydrophilic quartz sand at different ionic strengths (0.1 mM, 1 mM and 10 mM $NaNO_3$).

Fig. 3.28 illustrates the TBCs of the microspheres, the bacteria *Serratia marcescens* and the solute tracers at a 1 mM background solution. The TBCs are plotted on a common scale that is broken to achieve better visibility of the results.

Fig. 3.29 shows in more detail the results of the 1 µm spheres, the solute tracer and the bacteria on a logarithmic scale.

Fig. 3.30 gives an overview over the 1 µm spheres at different ionic strengths, the bacteria *Serratia marcescens* and the solute tracer.

Tab. 3.12 and Tab. 3.13 give an overview over the transport parameters – travel times, corresponding flow velocities and Peclet numbers. Tab. 3.16 gives an overview over the calculated recovery, effective porosity and the parameters based on filtration theory.

The solute tracer lithium again shows a sharper TBC and a higher peak concentration than all other tracers. The travel time is about one pore volume whereas travel times for colloids show the same variability as for the previously described tests.

For the hydrophilic quartz sand, the *Serratia marcescens* precede the 1 µm spheres clearly. The recovery of *Serratia marcescens* is one order of magnitude lower than for the 1 µm spheres. However, the shape of the TBCs (rising limb, peak and tailing) of the 1 µm spheres and the bacteria are very similar. The solute tracer does not show a tailing of the curve. The FDT of the microorganism and the 0.2 µm spheres precedes all other sized microspheres.

The recovery rates are generally lower for the quartz sand than for the quartz beads at same ionic strength of the background solution. This may be an effect of the irregular shape and roughness of natural quartz sand

compared to the artificial quartz beads. Dead-end pores may be another explanation, since they are more likely to occur in natural porous media than in perfectly round shaped material.

The bacteria show a tailing of the TBC that cannot be reproduced by lithium. The dispersion coefficient of the 1 µm spheres (0.754 m²/day) is higher than for the previous tests, but one order of magnitude higher than for the bacteria (0.071 m²/day). The dispersion coefficients for the other microsphere size classes are one order of magnitude lower.

The results of the microspheres with different background solutions show that the recovery rate decreases with increasing ionic strength, an effect that is not visible from the solute tracer. Mean tracer travel times for the microspheres are higher at higher ionic strengths, the peak time increases as well. Microorganisms were not tested at different ionic strengths.

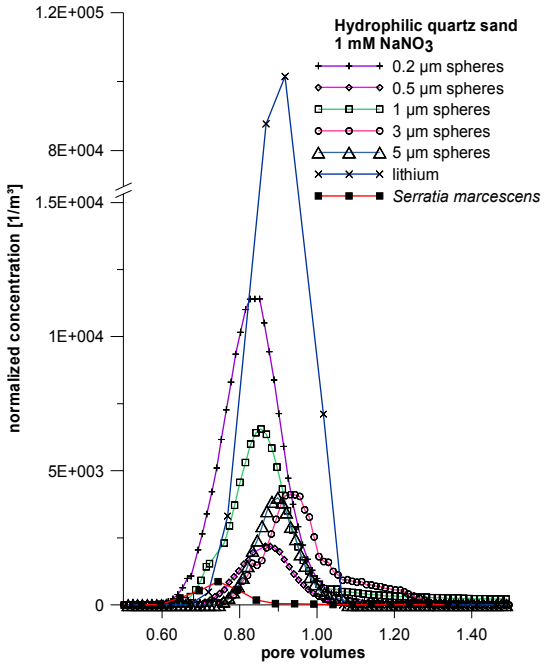

Fig. 3.28: TBCs of all tracers applied in hydrophilic quartz sand with a background solution of 1 mM $NaNO_3$ (please note the y axis break).

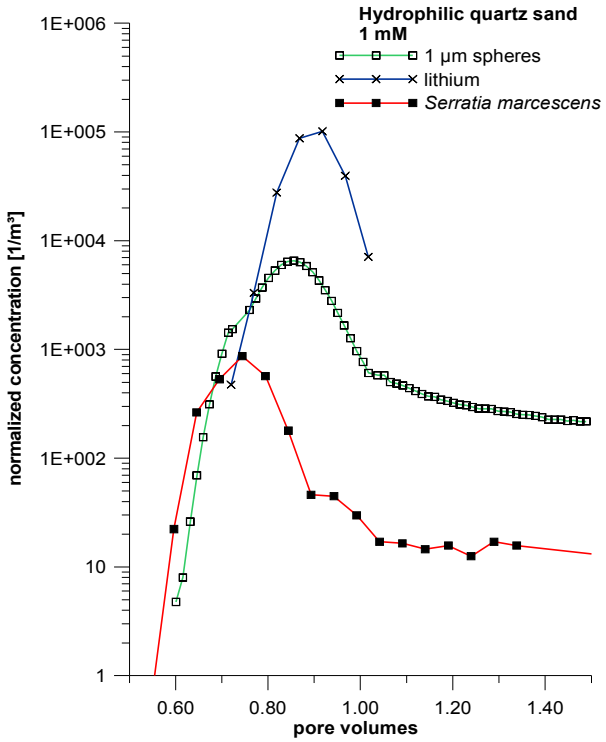

Fig. 3.29: TBCs of Serratia marcescens, 1 µm spheres and the solute tracers lithium and uranine for hydrophilic quartz beads and a background solution of 1 mM $NaNO_3$ in logarithmic scale.

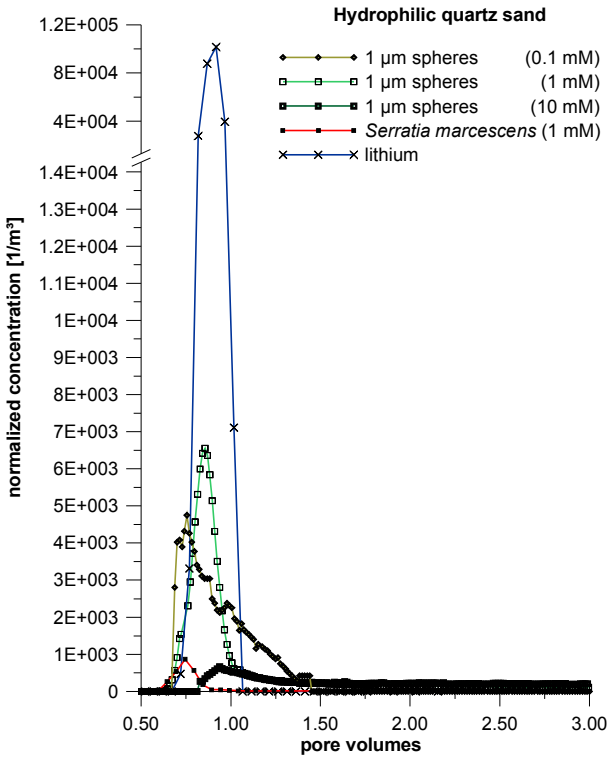

Fig. 3.30: TBCs of 1 µm spheres at different ionic strengths, Serratia marcescens and the two solute tracers uranine and lithium (please note the y axis break).

Tab. 3.12: Travel times and flow velocities for all tracers in hydrophilic quartz sand.

	first detection time (FDT) t_f PV	fastest flow velocity v_{max} [m/day]	peak time t_p PV	peak concentration c_{max}/M [1/m³]	peak velocity v_p [m/day]	median transit time t_m PV	median flow velocity v_m [m/day]
matrix: hydrophilic quartz sand							
background solution: 0.1 mM $NaNO_3$							
microspheres							
[µm]							
1	0.69	15.7	0.76	4.75E+03	14.3	0.87	12.4
solute tracers							
uranine	0.97	11.1	1.52	7.48E+03	7.1	1.79	6.0
background solution: 1 mM $NaNO_3$							
microspheres							
[µm]							
0.2	0.54	19.9	0.83	1.14E+04	13.0	0.84	12.8
0.5	0.71	15.1	0.87	2.19E+03	12.4	0.87	12.4
1	0.60	17.9	0.86	6.55E+03	12.5	0.88	12.1
3	0.61	17.5	0.93	4.11E+03	11.5	0.96	11.2
5	0.76	14.2	0.90	4.00E+03	12.0	0.90	12.0
solute tracers							
uranine	0.88	12.1	1.09	1.30E+04	9.8	1.18	9.1
lithium	0.72	14.9	0.92	1.01E+05	11.7	0.92	11.7
microorganisms							
S. marcescens	0.55	19.6	0.74	8.68E+02	14.4	0.79	13.5
background solution: 10 mM $NaNO_3$							
microspheres							
[µm]							
1	0.83	13.0	0.94	6.65E+02	11.4	2.60	4.1
solute tracers							
uranine	1.01	10.6	1.36	2.46E+03	7.9	1.57	6.8

Tab. 3.13: Dispersion coefficients, dispersivities and Pe for hydrophilic quartz sand.

	dispersion coefficient D_L [m^2/day]	dispersivity α_L [m]	Peclet number Pe [ ]
matrix: hydrophilic quartz sand			
background solution: 0.1 mM $NaNO_3$			
microspheres			
[µm]			
1	0.098	7.93E-03	38
solute tracers			
uranine	0.089	1.48E-02	20
background solution: 1 mM $NaNO_3$			
microspheres			
[µm]			
0.2	0.020	1.60E-03	188
0.5	0.013	1.03E-03	291
1	0.754	6.21E-02	5
3	0.020	1.81E-03	166
5	0.007	5.81E-04	516
solute tracers			
uranine	0.053	5.83E-03	51
lithium	0.011	9.82E-04	306
microorganisms			
S. marcescens	0.071	5.26E-03	57
background solution: 10 mM $NaNO_3$			
microspheres			
[µm]			
1	0.217	5.28E-02	6
solute tracers			
uranine	0.065	9.57E-03	31

3.4.4.2 Hydrophobic quartz sand

Fig. 3.31, Fig. 3.32, Fig. 3.33, Fig. 3.34 represent the results of the column tests with hydrophobic quartz sand at different ionic strengths (0.1 mM, 1 mM and 10 mM $NaNO_3$).

Fig. 3.31 illustrates the TBCs of the microspheres, the bacteria *Serratia marcescens* and the solute tracers at the 1 mM background solution. The TBCs are normalized and plotted on a common scale.

Fig. 3.32 shows the same results plotted on a logarithmic scale for better visibility of the bacteria tracers.

Fig. 3.33 gives an overview of the 1 µm spheres at different ionic strengths, the bacteria *Serratia marcescens* and the solute tracer, Fig. 3.34 shows the same results, but different axes for microspheres, bacteria and solute tracer. Generally, TBCs should be plotted on a common axis to avoid scaling effects. However, due to visibility reasons, differently sectioned axes provide a better overview over the general travel times and are hence preferred.

Tab. 3.14 and Tab. 3.15 list the transport parameters (travel time, corresponding flow velocities, Peclet numbers). Tab. 3.17 provides the calculated recovery, effective porosity and the parameters based on filtration theory.

The recoveries are much smaller for the colloid tracers compared to all previous tests. Therefore TBCs show a greater tendency for irregularities, which are visible from the logarithmic plot (Fig. 3.32). The recovery rate for the bacteria is one or two orders of magnitude lower than for the microspheres.

The solute tracer lithium again shows no tailing, mean travel time is about one pore volume. The travel times for the microspheres show the same arrangement as for the previous tests.

The FDT is lower for the bacteria than for the solutes and varies for the microspheres. The differences in peak time and median travel time between the differently sized microspheres become less significant. The median travel time for the bacteria increases, which leads to a greater dispersion coefficient.

Thus the dispersion coefficient is largest for the bacteria (1.6 m²/day) and magnitudes lower for the microspheres (0.16 m²/day for 1 µm spheres).

The extremely low recovery rate may lead to erroneous interpretation

results. The further interpretation of the bacteria results for hydrophobic quartz sand needs to be considered with care.

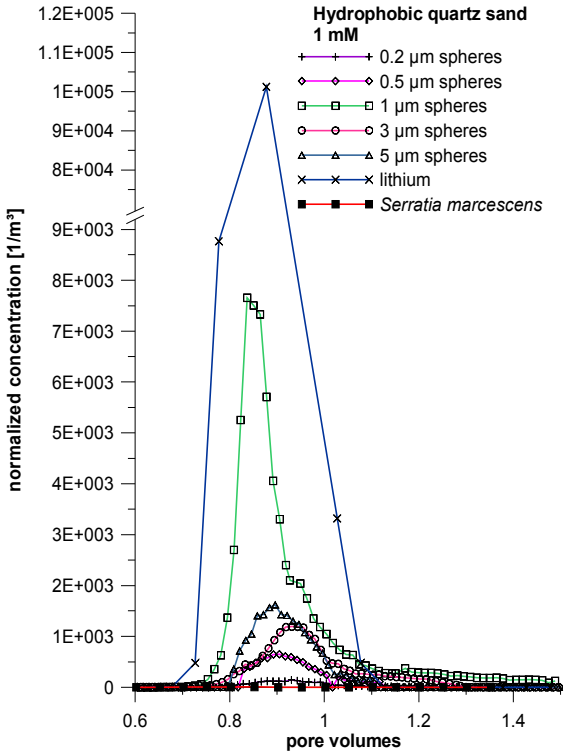

Fig. 3.31: TBCs of all tracers in hydrophobic quartz sand and a background solution of 1 mM $NaNO_3$ (please note y axis break).

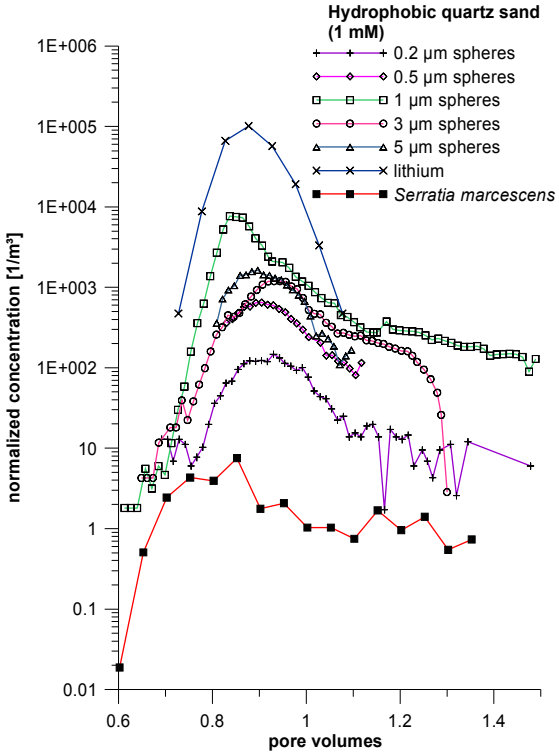

Fig. 3.32: TBCs from all tracers for hydrophobic quartz sand and a background solution of 1 mM $NaNO_3$ (logarithmic scale).

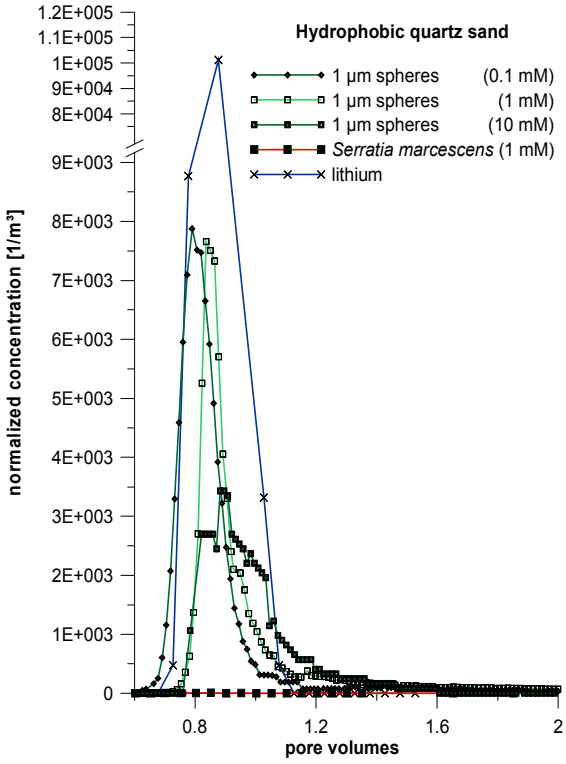

Fig. 3.33: 1 µm spheres (at different ionic strengths), Serratia m. and lithium tracer for hydrophobic quartz sand.

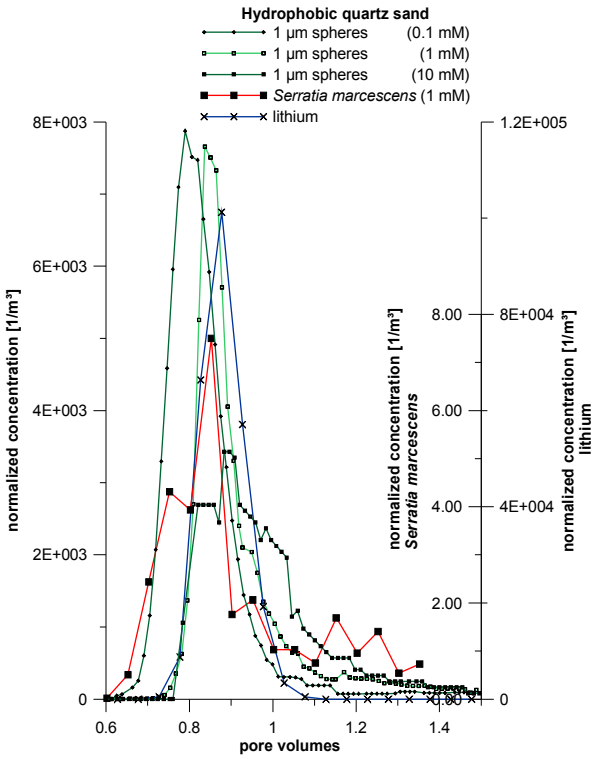

Fig. 3.34: TBCs of 1 µm spheres (at different ionic strengths), Serratia marcescens and lithium for hydrophobic quartz sand.

Tab. 3.14: Travel times and flow velocities for all tracer in hydrophobic quartz sand.

	first detection time (FDT) t_f PV	fastest flow velocity v_{max} [m/day]	peak time t_p PV	peak concentration c_{max}/M [1/m³]	peak velocity v_p [m/day]	median transit time t_m PV	median flow velocity v_m [m/day]
matrix: hydrophobic quartz sand							
background solution: 0.1 mM $NaNO_3$							
microspheres							
[µm]							
1	0.63	17.3	0.79	7.88E+03	13.7	0.82	13.2
solute tracers							
uranine	1.02	10.6	1.46	6.59E+03	7.4	1.81	6.0
background solution: 1 mM $NaNO_3$							
microspheres							
[µm]							
0.2	0.59	18.4	0.93	1.47E+02	11.7	0.95	11.4
0.5	0.83	13.1	0.90	6.49E+02	12.0	0.92	11.8
1	0.52	20.9	0.84	7.66E+03	12.9	0.89	12.1
3	0.61	17.5	0.93	1.19E+03	11.5	0.94	11.3
5	0.81	13.4	0.90	1.62E+03	12.1	0.91	11.9
solute tracers							
uranine	1.39	7.8	1.83	4.45E+03	5.9	2.04	5.3
lithium	0.73	14.9	0.88	1.01E+05	12.3	0.88	12.3
microorganisms							
S. marcescens	0.60	17.9	0.85	7.50E+00	12.7	1.15	9.4
background solution: 10 mM $NaNO_3$							
microspheres							
[µm]							
1	0.78	13.8	0.88	3.43E+03	12.3	0.93	11.6
solute tracers							
uranine	1.26	8.6	1.64	1.54E+03	6.6	1.80	6.0

Tab. 3.15: Dispersion coefficients, dispersivities and Peclet numbers for hydrophobic quartz sand.

	dispersion coefficient D_L [m²/day]	dispersivity α_L [m]	Peclet number Pe [ ]
matrix: hydrophobic quartz sand			
background solution: 0.1 mM $NaNO_3$			
microspheres			
[µm]			
1	0.018	1.37E-03	219
solute tracers			
uranine	0.135	2.26E-02	13
background solution: 1 mM $NaNO_3$			
microspheres			
[µm]			
0.2	0.184	1.61E-02	19
0.5	0.008	7.02E-04	427
1	0.160	1.32E-02	23
3	0.019	1.64E-03	183
5	0.010	8.67E-04	346
solute tracers			
uranine	0.053	9.91E-03	30
lithium	0.006	4.88E-04	615
microorganisms			
S. marcescens	1.558	1.66E-01	2
background solution: 10 mM $NaNO_3$			
microspheres			
[µm]			
1	0.036	3.09E-03	97
solute tracers			
uranine	0.033	5.44E-03	55

3.4.5 Quartz sand – modeling

3.4.5.1 Role of dispersion and diffusion

The importance of dispersion and diffusion was pointed out previously. The results of the hydrophilic and hydrophobic quartz sand (Tab. 3.16) fall into region III of the dispersion-diffusion-diagram (Fig. 3.35). For this region, dispersion is the predominant process.

Tab. 3.16: Diffusion parameters for both quartz sands.

	diffusion coefficient D_o [m²/day]	log D_L/D_o [ ]	log Pe* [ ]		diffusion coefficient D_o [m²/day]	log D_L/D_o [ ]	log Pe* [ ]
matrix: hydrophilic quartz sand				**matrix: hydrophobic quartz sand**			
background solution: 0.1 mM $NaNO_3$				**background solution: 0.1 mM $NaNO_3$**			
microspheres				**microspheres**			
[µm]				[µm]			
1	1.85E-08	6.73	5.37	1	1.85E-08	5.99	5.40
background solution: 1 mM $NaNO_3$				**background solution: 1 mM $NaNO_3$**			
microspheres				**microspheres**			
[µm]				[µm]			
0.2	9.25E-08	5.34	4.68	0.2	9.25E-08	6.30	4.63
0.5	3.70E-08	5.54	5.07	0.5	3.70E-08	5.35	5.05
1	1.85E-08	7.61	5.36	1	1.85E-08	6.94	5.36
3	6.17E-09	6.51	5.80	3	6.17E-09	6.48	5.81
5	3.70E-09	6.27	6.05	5	3.70E-09	6.45	6.05
microorganisms				**microorganisms**			
S. marcescens	1.68E-08	6.62	5.45	*S. marcescens*	1.68E-08	7.97	5.29
background solution: 10 mM $NaNO_3$				**background solution: 10 mM $NaNO_3$**			
microspheres				**microspheres**			
[µm]				[µm]			
1	1.85E-08	7.07	4.89	1	1.85E-08	6.29	5.34

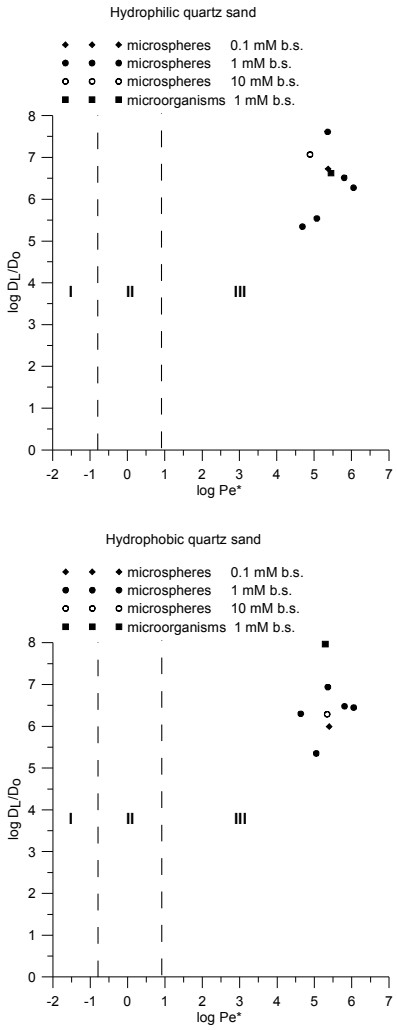

Fig. 3.35: Relationship between dispersion and diffusion for quartz sand.

Pe* increases for increasing particle size (Fig. 3.35), which reflects the decreasing influence of diffusion for larger particles. The D_L/D_o ratio is largest for the 1 µm spheres and decreases for smaller and larger microsphere size classes. This can be observed for hydrophilic and hydrophobic quartz sand. Dispersion seems to be more pronounced for 1 µm spheres than for other size classes. Thus, dispersion of the 1 µm spheres clearly overrides the effect of a larger reciprocal diffusion of larger microsphere sizes.

3.4.5.2 Filtration parameters

For modeling quartz beads (and quartz sand), equations and parameters described in chapter 2.5 Solute and colloid transport were used.

Tab. 3.17 and Tab. 3.18 give an overview of the computed parameters based on filtration theory.

The differences in the effective porosity reported for quartz beads cannot be fully confirmed for the quartz sands. The effective porosity (Fig. 3.37) does not vary this much for the microspheres from one sand type to another. The natural sand seems to be more suited for attachment than the artificial glass beads. This fact can be explained by a rougher surface of natural sand, compared to the smooth surface of the glass beads. Another explanation might be the shape of the matrix particles. Natural sand might be more irregularly shaped, the diameter might be only an averaged size between perfectly round and oblong particles. This allows a more effective arrangement of the soil matrix in a laboratory column. Thus, a lower porosity for the quartz sand can be expected – independent of the surface charge.

Thus, the lower effective porosity values of the sands compared to the beads are not surprising.

The loss of the microspheres in natural sand is higher. The interaction with the sand is generally higher (due to roughness and pore space geometry), the pore space is generally lower, so the water repellent effect of the hydrophobic matrix does not lead to an adequately smaller effective porosity for the microspheres that consequently can be attached onto the hydrophobic (positively charged) matrix walls.

For the bacteria a strengthened trend towards attachment exists. The effective porosity of the hydrophobic quartz sand is much higher (0.44) compared to the hydrophilic quartz sand (0.31). More pore space is available, the mean flow velocity is lower and thus effective porosity is larger than for the hydrophilic quartz sand. This might be explained by an increased interaction of the bacteria in a matrix of overall lower porosity. The electrostatic attraction of

the matrix may affect the bacteria more intensively than the homogeneously charged microspheres because of surface charge heterogeneities on the bacteria wall surface (note: the measured zeta potential is an averaged value for a certain number of bacteria, individual measurements of bacteria are not possible with dynamic light scattering).

Tab. 3.17: Results of hydrophilic quartz sand.

tracer	recovery	effective porosity	deposition rate coefficient	filter coefficient	single-collector removal efficiency	single-collector contact efficiency	attachment efficiency
		η_{eff}	κ	λ	η	η_o	α
	[%]	[ ]	[1/s]	[1/m]	[ ]	[ ]	[ ]
matrix: hydrophilic quartz sand							
background solution: 0.1 mM $NaNO_3$							
microspheres							
[µm]							
1	9.2	0.33	1.14E-03	7.96	2.78E-03	8.40E-03	3.31E-01
background solution: 1 mM $NaNO_3$							
microspheres							
[µm]							
0.2	14.4	0.32	9.57E-04	6.46	2.22E-03	2.64E-02	8.41E-02
0.5	2.3	0.33	1.81E-03	12.61	4.40E-03	1.31E-02	3.37E-01
1	10.0	0.34	1.08E-03	7.69	2.72E-03	8.35E-03	3.25E-01
3	5.0	0.37	1.29E-03	10	3.70E-03	9.02E-03	4.10E-01
5	3.3	0.34	1.58E-03	11.4	4.06E-03	1.61E-02	2.52E-01
microorganisms							
S. marcescens	0.9	0.31	2.42E-03	15.55	5.22E-03	7.99E-03	6.54E-01
background solution: 10 mM $NaNO_3$							
microspheres							
[µm]							
1	6.1	0.36	1.23E-03	9.32	3.40E-03	8.35E-03	4.07E-01

Tab. 3.18: Results of hydrophobic quartz sand.

tracer	recovery	effective porosity	deposition rate coefficient	filter coefficient	single-collector removal efficiency	single-collector contact efficiency	attachment efficiency
		n_{eff}	κ	λ	η	η_o	α
	[%]	[ ]	[1/s]	[1/m]	[ ]	[ ]	[ ]
matrix: hydrophobic quartz sand							
background solution: 0.1 mM $NaNO_3$							
microspheres							
[µm]							
1	8.0	0.31	1.29E-03	8.44	2.86E-03	8.44E-03	3.39E-01
background solution: 1 mM $NaNO_3$							
microspheres							
[µm]							
0.2	0.2	0.36	2.67E-03	20.28	7.42E-03	2.66E-02	2.78E-01
0.5	0.6	0.35	2.31E-03	16.87	6.04E-03	1.32E-02	4.59E-01
1	6.8	0.34	1.26E-03	8.96	3.16E-03	8.44E-03	3.75E-01
3	1.4	0.36	1.85E-03	14.13	5.18E-03	9.02E-03	5.75E-01
5	1.5	0.34	1.93E-03	13.96	4.97E-03	1.63E-02	3.04E-01
microorganisms							
S. marcescens	0.02	0.44	3.15E-03	29.05	1.21E-02	8.07E-03	1.50E+00
background solution: 10 mM $NaNO_3$							
microspheres							
[µm]							
1	6.7	0.37	1.15E-03	9.02	3.36E-03	8.44E-03	3.99E-01

As previously mentioned, recovery for bacteria in this sand is low and therefore interpretation results need to be considered with care.

To confirm these hypotheses, further tests with bacteria need to be performed.

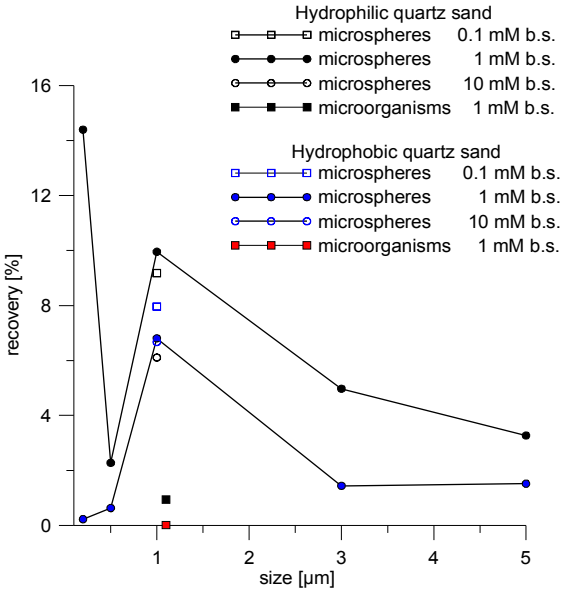

Fig. 3.36: Recovery for all particle tracers in hydrophilic and hydrophobic quartz sand.

Deposition rate coefficients and filter coefficients reflect the observed recovery, which is largest for 0.2 µm and 1 µm spheres (Fig. 3.36), respectively. The increasing ionic strength (from 1 mM to 10 mM) results in a lower recovery and therefore higher filter coefficient and lower deposition rate coefficient (Fig. 3.38). An effect that is more evident for the bacteria (filter coefficient increase: 15.55 /m – 29.05 /m) compared to 1 µm spheres (filter coefficient increase: 7.69 /m – 8.96 /m).

The change in the matrix surface properties from hydrophilic to hydrophobic results in an increase of the filter coefficients.

The differences of the calculated filtration parameters of the quartz sands are smaller than for the quartz beads.

As for the beads, the single-collector contact efficiency is lowest for the 3 µm, 1 µm and 0.2 µm microspheres. The actually calculated single-collector removal efficiency is lowest for 0.5 µm spheres, 5 µm and 3 µm spheres. The

single-collector contact efficiency of the bacteria is in the range of the microspheres for the hydrophilic sand, the actual single-collector removal efficiency as well.

The attachment efficiency for the bacteria is equal to one which means that all collisions of bacteria with matrix walls lead to an attachment.

A higher ionic strength (10 mM) reduces the recovery rate of the microspheres and increases the filtration. This can be observed for both bead types (hydrophilic and hydrophobic) equally. Furthermore, differences in the parameters for the different size classes in hydrophobic matrix are lower due to the generally lower recovery rates.

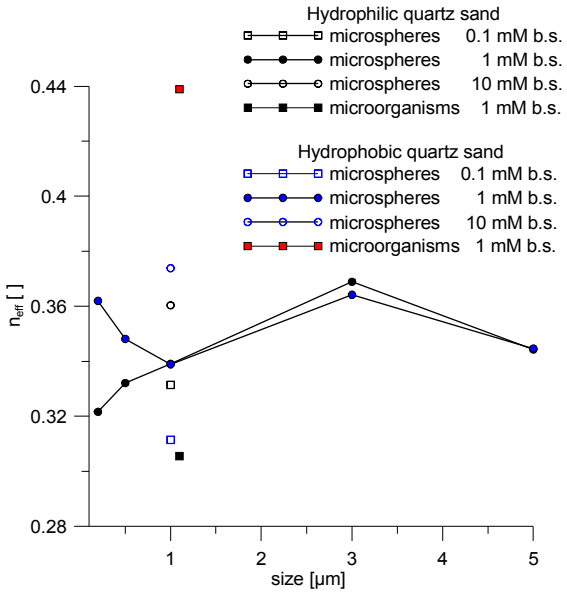

Fig. 3.37: Effective porosities for all tracers in hydrophilic and hydrophobic quartz sand.

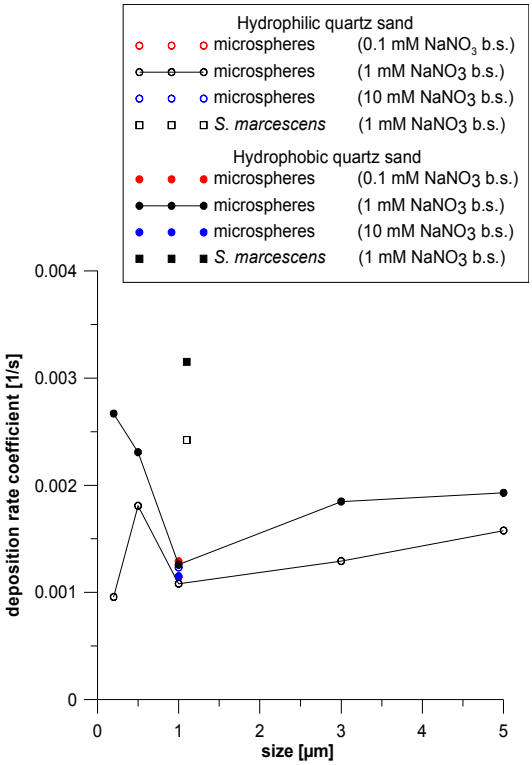

Fig. 3.38: Deposition rate coefficients for both sand types.

3.4.6 Discussion: Hydrophilic and hydrophobic quartz beads and quartz sand

3.4.6.1 Final comparison of TBCs for microorganisms and tracers

Fig. 3.39 shows a comparison of the 1 µm spheres and the bacteria *Serratia marcescens* in different matrices.

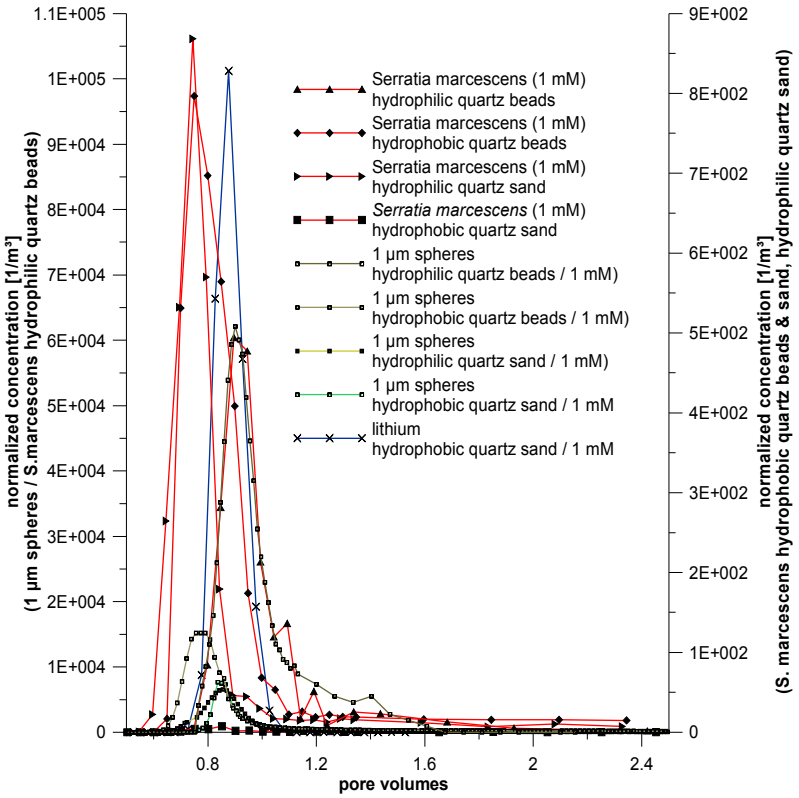

Fig. 3.39: Comparison of microorganisms and 1 µm spheres for all matrix types.

The artificial hydrophilic quartz beads are characterized by the most homogeneous matrix type and show the highest conformity between bacteria and microspheres. The additional treatment with silane means an increase in complexity that yields more differences between the microorganisms and microspheres. Natural quartz sand means an additional increase in heterogeneity (i.e. more complex pore space geometry, higher roughness and less uniformly round shape of sand particles) and therefore more difference in behavior.

A natural matrix type in a field test site means an additional increase of complexity and therefore differences between microspheres and microorganisms are expected to increase accordingly.

However, the differences described between the microspheres and microorganisms tend to cover the overall correlation of the colloidal tracers and biocolloids - the similar shape of the TBC and equal general transport behavior.

Additionally, there are differences between the microbial tracer types as well. The applied bacteria behave differently from the bacteriophages. So results from bacteriophages can not easily be used to predict the behavior of bacteria and vice versa.

3.4.6.2 Influence of detection limit on FDT

The FDT has been used in several studies to characterize the transport behavior of colloids compared to solutes [Mahler et al. 1998, Auckenthaler et al. 2002, Pronk et al. 2006]. However, the FDT is strongly influenced by the detection limit which is lower for colloids than for solutes; thus, preceding colloids are no surprise. This can be clearly seen from a logarithmic diagram of some of the TBCs of this study (Fig. 3.18, Fig. 3.20, Fig. 3.22, Fig. 3.29, Fig. 3.32).

However, an extension of TBCs to earlier times (which is possible by linear extension to earlier times in logarithmic diagrams) does not necessarily mean that the solutes then arrive at the same time as the colloids or precede them. This methodology is uncertain when data show variations (which is often the case for colloids), or the degree of extension is too large (which is the case for

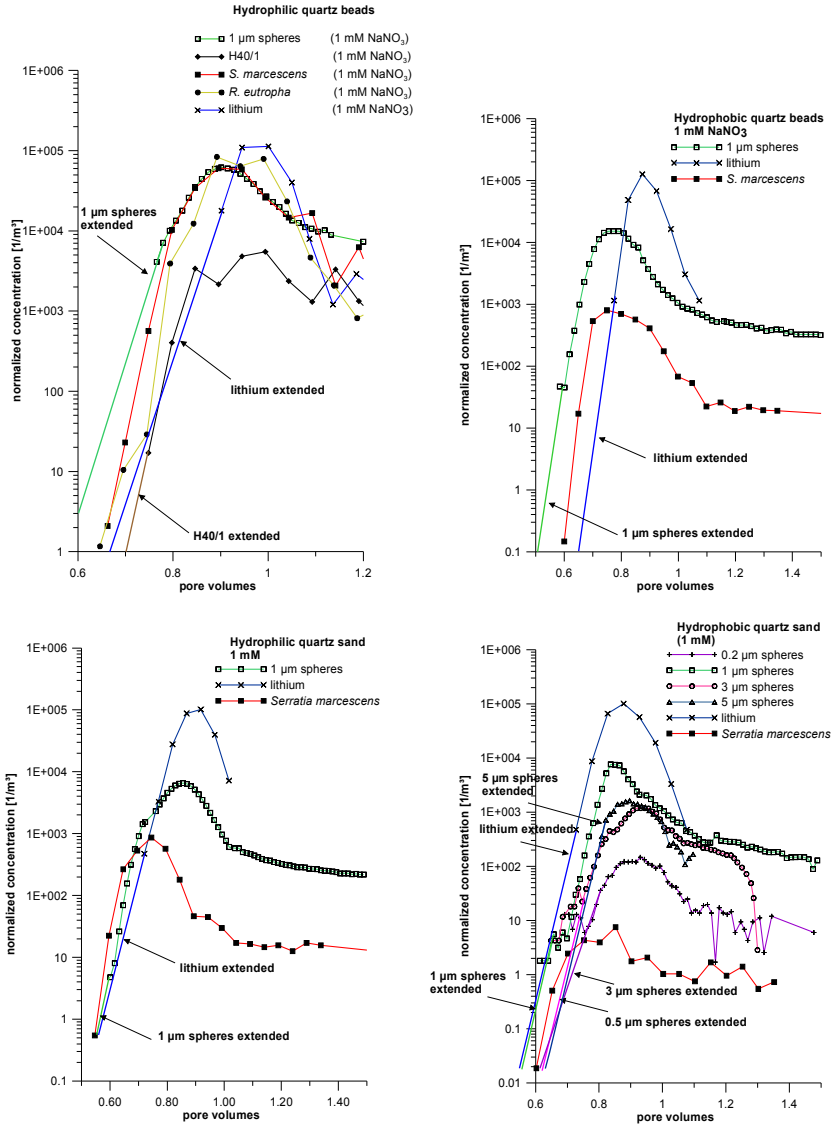

Fig. 3.40: Extended TBCs.

solutes). In all cases, peak times provide a better means to evaluate the colloid/solute relationship.

For the study presented here, an extension to earlier times does generally not result in other relationships of colloids compared to solutes (Fig. 3.40). However, the extension of lithium resulted in one case in preceding lithium compared to H40/1. Typically, the colloids that preceded before remain preceding and those which previously were retarded (according to the FDT) remain retarded.

In conclusion, the influence of the detection limit on the FDT is correct but the impact of this behavior on general transport characteristics is overestimated. Peak shift analysis should be used to evaluate the transport behavior of colloids with respect to solutes.

3.4.6.3 Peak shift analysis

In laboratory tests, the solute conservative tracers show a sharper TBC and a higher peak concentration than any particle tracers. The travel times for the solutes are around one pore volume whereas the travel times for the particle tracers differ significantly – some precede, some show retardation.

Earlier arrival of particles is usually explained by size or pore exclusion processes, whereas retardation can be explained by sedimentation or attachment. According to equation 36, filtration not only a loss of particles but also a shift of the peak to earlier times, which conflicts somehow with the exclusion concept. Peak shift analysis after Zhang et al. 2001 is one way to distinguish between preceding particles due to exclusion (i.e. different advection) or deposition. For further description of the procedure see Zhang et al. 2001.

The procedure includes the calculation of the peak shift by using the equation of Grolimund et al. 1998 that incorporates the deposition rate coefficient of the particle tracers. This value is compared to the actually observed peak shift between the colloidal tracer and the conservative tracer. When the observed peak shift is significantly higher than the calculated peak shift, differential advection can be assumed.

Tab. 3.19, Tab. 3.20, Tab. 3.21 and Tab. 3.22 illustrate the results of the peak shift analysis for hydrophilic and hydrophobic quartz beads and sand.

From peak shift analysis it can be generally assumed that not all microspheres or microorganisms experience differential advection, which means that pore or size exclusion processes are operating.

Tab. 3.19: Results of the peak shift analysis for the tracer tests in hydrophilic quartz beads.

	relative recovery RR	Δt_{peak} observed	Δt_{peak} calculated	differential advection?	retardation?
	[ ]	[ ]	[ ]		
matrix: hydrophilic quartz beads					
background solution: 1 mM $NaNO_3$					
microspheres					
[µm]					
0.2	0.413	5.051	0.246	yes	no
0.5	0.262	-0.164	0.328	no	no
1	0.875	9.897	0.041	yes	no
3	0.178	-5.667	0.411	no	yes
5	0.158	-2.587	0.452	no	yes
microorganisms					
H40/1	0.089	0.370	0.616	no	no
S. marcescens	0.879	10.226	0.041	yes	no
R. eutropha	0.941	10.595	0.041	yes	no
background solution: 10 mM $NaNO_3$					
microspheres					
[µm]					
0.2	0.205	4.116	0.753	yes	no
0.5	0.252	-0.748	0.586	no	yes
1	0.376	9.730	0.544	yes	no
3	0.165	3.368	0.795	yes	no
5	0.179	6.985	0.753	yes	no

Tab. 3.20: Results of the peak shift analysis for the tracer tests in hydrophobic quartz beads.

	relative recovery RR	Δt_{peak} observed	Δt_{peak} calculated	differential advection?	retardation?
	[ ]	[ ]	[ ]		
matrix: hydrophobic quartz beads					
background solution: 1 mM $NaNO_3$					
microspheres					
[µm]					
0.2	0.170	1.378	0.620	yes	no
0.5	0.129	5.036	0.715	yes	no
1	0.248	11.734	0.572	yes	no
3	0.117	-16.532	0.620	no	yes
5	0.069	-6.461	0.858	no	yes
microorganisms					
S. marcescens	0.016	14.252	1.431	yes	no
background solution: 10 mM $NaNO_3$					
microspheres					
[µm]					
0.2	0.096	5.497	1.024	yes	no
0.5	0.073	4.896	1.070	yes	no
1	0.169	5.035	0.838	yes	no
3	0.066	-14.688	0.931	no	yes
5	0.039	0.647	1.256	no	no

Tab. 3.21: Results of the peak shift analysis for the tracer tests in hydrophilic quartz sand.

	relative recovery RR	Δt_{peak} observed	Δt_{peak} calculated	differential advection?	retardation?
	[ ]	[ ]	[ ]		
matrix: hydrophilic quartz sand					
background solution: 0.1 mM $NaNO_3$					
microspheres					
[µm]					
1	0.111	18.427	1.549	yes	no
background solution: 1 mM $NaNO_3$					
microspheres					
[µm]					
0.2	0.175	10.292	1.321	yes	no
0.5	0.028	5.978	2.415	yes	no
1	0.121	6.966	1.458	yes	no
3	0.060	-1.753	1.731	no	yes
5	0.040	2.517	2.141	yes	no
microorganisms					
S. marcescens	0.011	18.876	3.189	yes	no
background solution: 10 mM $NaNO_3$					
microspheres					
[µm]					
1	0.074	-2.022	1.686	no	yes

Tab. 3.22: Results of the peak shift analysis for the tracer tests in hydrophobic quartz sand.

	relative recovery RR	Δt_{peak} observed	Δt_{peak} calculated	differential advection?	retardation?
	[ ]	[ ]	[ ]		
matrix: hydrophobic quartz sand					
background solution: 0.1 mM $NaNO_3$					
microspheres					
[µm]					
1	0.101	10.214	0.858	yes	no
background solution: 1 mM $NaNO_3$					
microspheres					
[µm]					
0.2	0.003	-5.606	1.764	no	yes
0.5	0.008	-2.755	1.526	no	yes
1	0.086	4.846	0.858	yes	no
3	0.018	-7.553	1.240	no	yes
5	0.019	-1.710	1.288	no	yes
microorganisms					
S. marcescens	0.000	2.850	2.098	no	no
background solution: 10 mM $NaNO_3$					
microspheres					
[µm]					
1	0.084	-0.475	0.763	no	yes

The two bacteria *Serratia marcescens* and *Ralstonia eutropha* show differential advection whereas the bacteriophage H40/1 shows a peak shift that is smaller than the calculated peak shift. For the hydrophobic quartz sand *Serratia marcescens* shows no differential advection or retardation, which might be an effect of the low recovery rate.

The 1 µm spheres show differential advection in most experiments. In quartz sand at high ionic strength, the 1 µm spheres experience significant retardation. The microorganisms were not tested under these circumstances.

Larger microspheres (3 µm and 5 µm spheres) show a larger tendency for retardation and usually are not transported faster than the conservative solute. Size exclusion concepts assume that larger particles cannot enter smaller pores and are therefore traveling faster in the center of larger pores than the solutes, which can enter all types of pores. The presented results show that in most experiments the retardation processes override this effect.

Smaller microspheres (0.2 µm, 0.5 µm and 1 µm spheres) generally show differential advection and are less retarded.

4 Field tests

4.1 Overview

In all aquifer types (karst, fractured, porous), field tests were carried out. Two test sites are located in Baden-Württemberg (Germany), two sites are transboundary aquifers between Bavaria (Germany) and Vorarlberg (Austria) and one test site is situated in Switzerland (Fig. 4.1).

The test site in fractured Granite – Lindau – is located in the southern Black Forest (Fig. 4.2), Baden-Württemberg (Germany). The karst aquifers Hölloch and Hochgrat-Gunzesried are located in the Alps resp. alpine foreland, Bavaria (Germany); the test site Yverdon-les-Bains is located in the Swiss alpine foreland, in the canton Vaud. In the Upper Rhine Valley, a porous aquifer near the small community Merdingen (Baden-Württemberg, Germany) was tested.

The Lindau gallery is located in the Albtal granite and intersects an ore dyke that shows enhanced hydraulic conductivity. Previous tests focused on the general hydrogeology of the gallery and its connection to the adjacent rock as well as modeling aspects [Himmelsbach 1993, Witthüser 2002, Bäumle 2003]. The recent tracer tests (Tab. 4.1) highlighted the differences between colloidal and solute tracers as well as new modeling approaches.

The geological and hydrogeological characterization of the karst test site Hochgrat-Gunzesried breaks fresh ground. The test site is located near the small community Gunzesried, in the Allgäu part of the Subalpine Molasse zone (Fig. 4.2). In a preliminary study, the geology and general hydrogeology, as well as hydrochemistry and spring water microbiology were studied. Further studies focused on two tracer experiments with fluorescent and colloidal tracers (Tab. 4.1).

The second karst test site – the Hölloch cave system – is located in the Kleinwalsertal Valley, and belongs to the Gottesacker-Hochifen karst system already thoroughly investigated in previous studies [Goldscheider 1998, Goldscheider 2002, Goldscheider 2005, Goldscheider et al. 2001, Goldscheider et al. 2002]. Two combined and comparative tracer tests in the Hölloch cave system with solutes and colloidal tracers were carried out under different flow conditions – low flow and high flow. Additional data from a sampling station at a karst spring nearby were evaluated with statistical approaches to further validate the tracer tests.

The third karst test site, Yverdon-les-Bains, was used in cooperation with the Center of Hydrogeology (CHYN). Tracer tests with colloidal and solute

tracers were used to understand a deep geothermal karst system between a swallow hole and the two main karst springs.

In the Upper Rhine Valley, a test site was chosen that has been used for hydrogeological investigations for over two decades [Käss 2004]. For the first time microbial, solute and colloidal tracers were applied in a comparative and combined tracer test and wells sampled for a period of more than nine months (Tab. 4.1).

Fig. 4.1 shows the location of the test sites projected onto a relief map. Fig. 4.2 projects the field test sites onto a geological map and Tab. 4.1 gives an overview over the applied tracers in each test site.

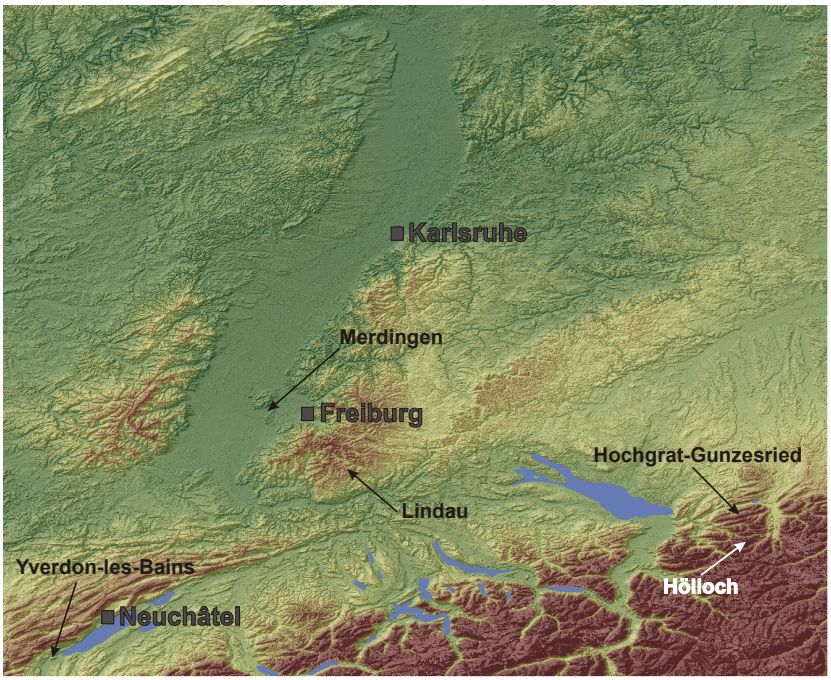

Fig. 4.1: Location of the test sites Lindau, Hochgrat-Gunzesried, Hölloch, Yverdon-les-Bains and Merdingen (elevation data: SRTM3: http://seamless.usgs.gov/index.asp).

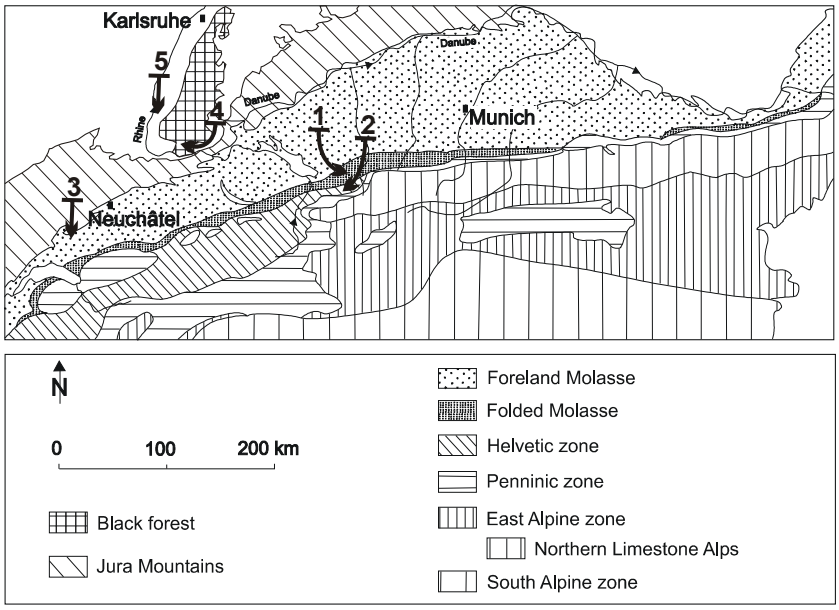

Fig. 4.2: Geology and location of the test sites: 1 Hochgrat-Gunzesried, 2 Hölloch, 3 Yverdon-les-Bains, 4 Lindau and 5 Merdingen (modified after Schwerd 1996).

Tab. 4.1: Applied tracers for each field test site.

		aquifer				
		fractured	**karst**			**porous**
		Lindau	Hochgrat -Gunzesried	Hölloch	Yverdon -les-Bains	Merdingen
particle tracer	microspheres					
	1 µm	X	X	X	X	X
	2 µm				X	X
	3 µm	X				
	5 µm			X	X	X
	6 µm	X				
	S.marcescens					X
fluorescence tracer	uranine	X	X	X	X	X
	amidorhodamine G	X		X		
	eosin		X			
	sodium-naphthionate		X			
	pyranine		X			
	sulforhodamine B			X		X
salt tracer	LiCl	X				
	SrCl	X				
	NaCl	X				

4.2 Fractured Granite

4.2.1 Geology

The Black Forest basement is part of the Variscian orogeny and has been uplifted and eroded since the Eocene in the course of the Upper Rhine Graben development. In the western part of the Black Forest, it is bordered towards the Upper Rhine Valley by an escarpment of up to 1000 meters. In the northern, eastern and southern parts, the Black Forest is covered by permo-triassic cap rock. The crystalline basement is composed of Paleozoic metamorphic and magmatic rock. In the Black Forest the basement mainly belongs to the Moldanubian Zone, the Saxothuringian Zone is exposed only in the northernmost Black Forest.

In the southern Black Forest, several intrusive rocks are exposed which can be distinguished into a pre and a post tectonic series [Schaltegger 2000]. The pre tectonic series is of Viséan age and consists of the Badenweiler Lenzkirch Zone (BLZ) (Fig. 4.3) that contains the Klemmbach-Schlächtenhaus, Blauen and Malsberg granite (Fig. 4.3). The pre- or syn-tectonic series are 340 to 330 Myr old and are deformed as a consequence of a thrust fault of the Central Gneiss Complex (CGC) over the Badenweiler-Lenzkirch Zone (Fig. 4.3). The post-tectonic granites are the St. Blasien, Albtal, Schluchsee and Bärhalde Granites, which have an intrusion age of 336 – 330 Myr. These do not show any signs of deformation. Both series took place during a shorter time window than previously assumed [Schaltegger 2000].

The test site is located in the Albtal granite. The intrusion age for the Albtal Granite is about 334 Myr [Schaltegger 2000]. It is a massive rock that contains potash feldspars that form up to 10 cm long porphyroblasts within a coarse-grained matrix of quartz, feldspar and biotite. On its southern border, the Albtal Granite is cut off by a dextral strike-slip fault with an offset of approximately 4 km – the Vorwald fault (Fig. 4.3). Along the Vorwald fault, the Albtal Granite is tectonically in contact with paragneiss. In the East and West, the Albtal Granite is bordered by gneiss as well, in the north St Blasien Granite is exposed. Late variscian dykes – composed of Granite Porphyry and Rhyolite – intersect the granites. For the granite porphyry near the community Präg, an age of 332 Myr was determined [Schaltegger 2000]. The granite porphyry of the test site has a thickness of between 50 meters and several tens of meters, has a strike of 120°-140° and a dip of 60°-85° towards the Northeast. The Albtal Granite is overlain at the test site by the so-called Berglesand, which is a weathering product that is about 25 meters thick.

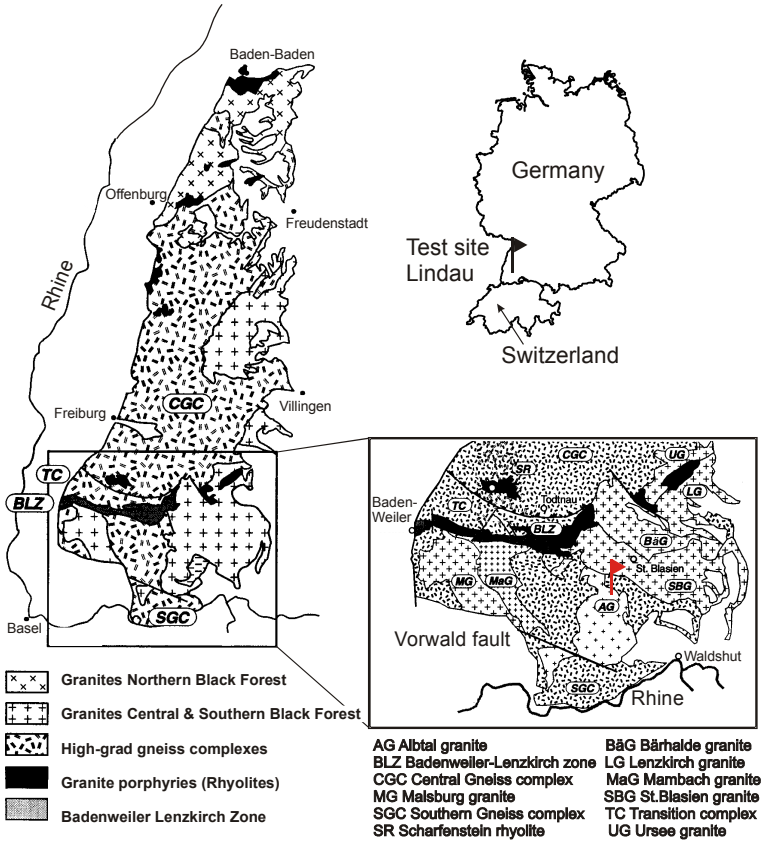

Fig. 4.3: Location and geology of the test site Lindau in the Southern Black Forest; modified after Schaltegger 2000.

4.2.2 Lindau Gallery

The Lindau gallery (Fig. 4.4) has been used for science and research since 1980 by the Department of Applied Geology, University of Karlsruhe. It has been characterized geologically and hydraulically in order to simulate the fate and transport of solutes in fractured aquifers [Himmelsbach 1993, Witthüser 2002, Bäumle 2003].

The gallery is located 6.5 km southeast of the community of Todtmoos and 14.5 km northwest of the city of Waldshut on the western side of the Schwarzbachtal Valley (Fig. 4.4). The tunnel entrance is situated at an altitude of approximately 850 m, and after 400 meters in length the gallery splits into two partition tunnels that penetrate the ore dyke after 40 and 100 meters, respectively and end afterwards in an dyke-parallel pit (Fig. 4.4). From the parallel pit 22 boreholes were drilled into the adjacent rock area (towards the ore dyke and the adjacent area). The instrumentation allows a use for hydraulic tests. The overlaying burden is less than 90 meters thick (Fig. 4.5).

The gallery was originally built by Schluchseewerke GmbH and investigated from 1955 to 1980. Primarily, it was used for pre-investigations that anticipated a pump storage hydro power plant. At the narrowest part of the Schwarzbachtal Valley, a dam with a height of 70 m was planned, the storage capacity was calculated to be about 70 Mm³ and the covered area about 320 hectares. The investigations concerning the planning and building laws gave a high hydraulic conductivity of the ore dyke Hermann (Fig. 4.5), which has a strike of 5° and a dip of 70°-80°. Water losses below the dam and resulting stability or economical problems were very probable. The high hydraulic conductivity was supposed to be controlled by concrete injections.

The ore dyke is 1 m thick, but its thickness varies between several decimeters and three meters [Himmelsbach 1993]. The high hydraulic conductivity of the ore dyke Hermann is caused by centimeter-large opened fractures and cavernous openings that are caused by fluorite pseudomorphosis after quartz [Himmelsbach 1993]. Tectonic stress yields to closely-spaced dyke-parallel fractures. On both sides of the dyke exists a fracture zone with a width of approximately 10 meters in the hydrothermally altered adjacent rock with enhanced conductivity. Additional dykes (granite porphyry, rhyolite) of lower hydraulic conductivity intersect the ore dyke with a strike in NW-SE direction. In the adjacent rock, fractures developed as a result of the temperature differences during intrusion and cooling-down, which yield to a certain conductivity. The widely-spaced Albtal Granite has a low hydraulic conductivity.

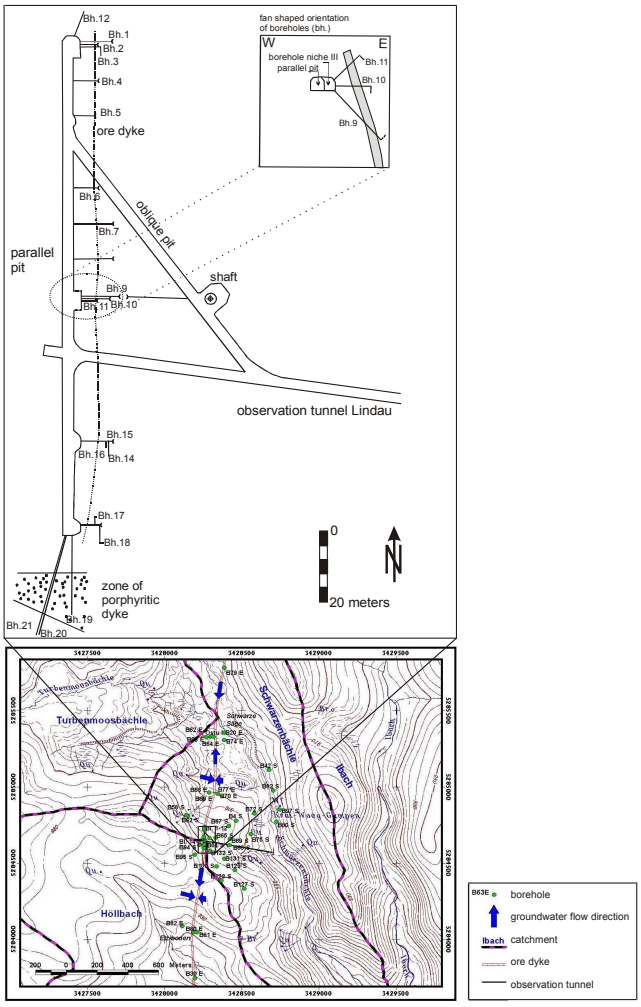

Fig. 4.4: Lindau gallery: tunnel scheme and location of observation wells; modified after Bäumle 2003.

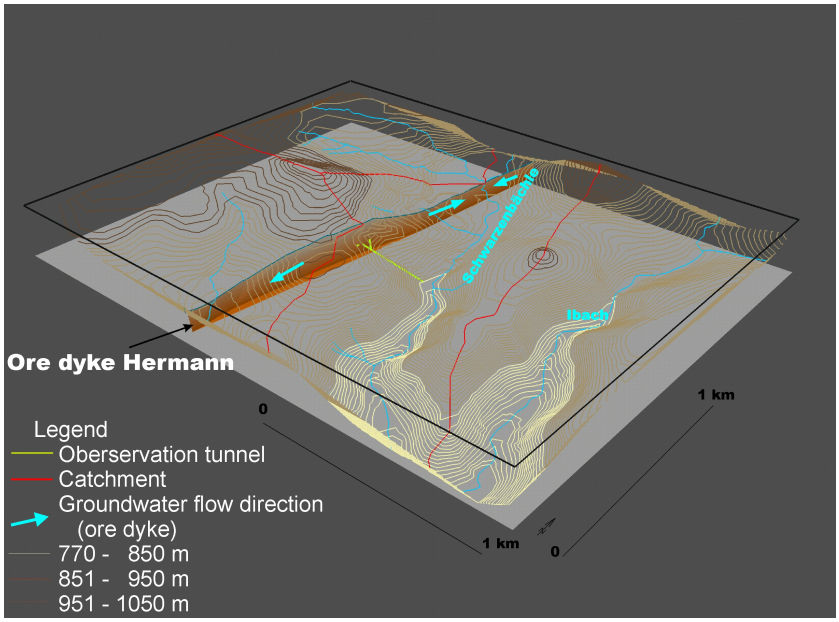

Fig. 4.5: Lindau gallery and the ore dyke in a 3-dimensional view.

With the previously mentioned concrete fan, the ore dyke was supposed to be sealed and water loss below the dam fully avoided. The concrete fan is almost 20 meters thick and intersects the ore dyke in two hydraulically independent parts. The southern part includes borehole Nº14 - Nº21, the northern part borehole Nº1 - Nº12 (central part: Nº6 - Nº11). The southern part drains towards the Höllbach creek, the northern part towards the Schwarzenbach creek (Fig. 4.4, Fig. 4.5).

Himmelsbach 1993 showed for the central part (Nº6 - Nº11) that water flow stagnates and therefore an artificially induced flow field is not superposed by a natural flow field. A vertical limit at a depth of 40 meters is caused by the lateral reduction and offset of the ore dyke, as well as the consecutive closing of fractures with increasing depth [Witthüser 2002]. On both sides of the ore dyke the hydrothermally altered adjoining rock of lower conductivity acts as limit. Thus, the test site can be classified as a two-dimensional vertical-planar flow system of parallel fractures with free water surface area.

4.2.3 Previous tracer tests

The previous tracer tests are mainly described in the dissertations Himmelsbach 1993, Himmelsbach et al. 1994, Witthüser 2002 and Bäumle 2003. This chapter is focused on the injection strategy and the results of the tracer tests carried out by Himmelsbach, Witthüser and Bäumle.

Within the scope of these tracer tests there were two types of boreholes used as injection points, either boreholes drilled from the ground surface or drilled from the gallery into the adjacent rock. In the first case, sampling points were boreholes nearby and natural outlets [Himmelsbach 1993]. Later tests included the gallery as well as sampling area [Bäumle 2003]. Additional tests were completely carried out inside the gallery flow system. Boreholes inside the gallery were used as injection points and other boreholes as sampling points [Himmelsbach 1993, Witthüser 2002, Bäumle 2003]. An overview over all previous tracer tests in the Lindau gallery or the adjacent area is given by Bäumle 2003.

Injections are done either by injection lances [Himmelsbach 1993] or by double packers [Witthüser 2002, Bäumle 2003]. Injection lances consist of a PVC-pipe with an inner diameter of 12 mm that is connected at its end to a injector with radial openings. Tracers are dissolved prior to injection in a volume of 1 L and injected through a bypass afterwards. A dead volume of 20-30 L can be assumed for this injection type [Himmelsbach 1993]. During monopole-tests [Himmelsbach 1993] the injection borehole was closed after injection (Tab. 4.3) – no further water volume is added; in dipole-tests tracer-free water was injected continuously during the entire test.

Witthüser and Bäumle carried out several monopole-tests and firstly choose the injection lances introduced by Himmelsbach. Then, the tracer was dissolved in 1 L and injected with 10 L tracer-free casing fluid under a pressure of 6 bar (Tab. 4.3). In order to estimate the influence of the injection type on the hydraulic parameters, an alternative injection procedure was tested – the double-packer system. The double-packer was installed in such a way that the 1-meter-long packer interval lays in the fracture zone with the highest hydraulic conductivity. Different borehole combinations were tested as injection and sampling assembly. From this point on, results are only discussed for the combination borehole 8 and 10 (borehole 8 as injection point and borehole 10 as sampling point).

For the monopole-test with double-packer system, the tracer uranine was dissolved in 1 L water and introduced with 5 L of tracer-free fluid (Tab. 4.3). The tracer was measured online with a GGUN-FL (University of Neuchâtel), few manual samples were taken for comparison [Witthüser 2002]. The tailing of the curve showed significant fluctuating concentration values for the applied

solute tracer uranine which influences the quality of the modeling results negatively. The erroneous fluctuations were found to be caused by the instrument due to an interference by nearby electrical wires.

Within the scope of two additional tracer tests at this borehole combination, the double packer was used and the injection volume was 1 L and 2 L, respectively, the flushing volume was 20 L (21 L in total) and 5 L (7 L in total), respectively [Bäumle et al. 2001]. Tab. 4.2 and Tab. 4.4 give an overview over the applied tracers and the hydraulic parameters for these tests. Bäumle used electrostatically neutral microspheres for this test. The fluorescent tracers were analyzed by laboratory fluorometers, thus erroneous fluctuations were eliminated. The total sampling time was about 100 hours; during the first 10 hours the sampling interval was shorter, the interval increased with increasing time after injection.

As injection volumes for further tracer tests at additional borehole combinations 20-60 L were used and a significant disturbance of the flow field by the injections was assumed [Bäumle 2003].

Tab. 4.2: Results from a tracer test with an injection lance for the test distance borehole Nº8 - Nº10 [Bäumle et al. 2001].

injection device tracer		**injection lance** uranine	T4
V_{tracer}	[L]	1.00	1.00
$V_{case\ fluid}$	[L]	20.00	20.00
Q	[L/s]	0.222	0.222
M	[g] [n]	0.50	0.25
t_1	[h]	0.75	0.75
V_{max}	[m/h]	15.50	15.50
t_o	[h]	3.25	3.50
V_o	[m/h]	3.56	3.31
R	[%]	74.00	76.00

Tab. 4.3: Modeling results of an SFDM.

injection device tracer		**injection lance** uranine	**double packer** uranine	**injection lance** pyranine	pryranine	deuterium
v_{tracer}	[L]	1	1	1	1	1
$v_{case\ fluid}$	[L]	10	5	21	21	21
Q	[L/s]	0.142	0.133	0.097	0.096	0.096
M	[g] [n]	1	0.5	2	2	300
t_1	[h]			1.11	1.15	1.25
v_{max}	[m/h]	15.29				
t_{peak}	[h]			2.58	2.58	2.73
R	[%]	43	33	71	72	35
a	[$s^{-0,5}$]	0.001	0.002	0.012	0.010	0.014
t_o	[h]	15.27	6.67	1.58	1.61	1.53
Pe	[]	2	15	33	50	50
b	[µm]	133	206	184	184	
v	[m/h]	0.73	1.71	3.6	3.6	3.6
D_{hl}	[m²/h]	4.10	1.32			
α_l	[m]	5.60	0.77	0.34	0.22	0.22
ε_f	[%]	1.3	0.8			
D_e	[m²/h]	1.26E-09	2.00E-12			
Reference		Witthüser 2002		Himmelsbach 1993 Himmelsbach et al. 1992		

Witthüser and Bäumle showed that the injection device and procedure significantly influence the hydraulic properties of all tracers. An injection lance means generally a higher total injection volume, which yields in general to a higher recovery rate and to slightly different transport parameters. Matrix diffusion (applying the $t^{-1.5}$-criterion) is very likely to occur in tests with injection lances. A double packer system means a lower total injection volume and results in a lower recovery of all tracers. In such a case where the injection volume is kept high (which is technically possible with a double packer as well) the recovery rate increases (Tab. 4.2, Tab. 4.3, Tab. 4.4). But tracer tests are difficult to interpret as long as the hydraulic boundary conditions are not equal – which is unfortunately the case for all the previously mentioned tests. The two tests described in Bäumle et al. 2001 were carried out with different injection volumes, and they also used different flow rates at the production borehole (0.8 m³/h respectively 0.6 m³/h). Although the maximum flow velocity

decreases after injection volume reduction in this test, the median flow velocity increases for uranine (Tab. 4.2, Tab. 4.4). This can be explained by the apparent matrix diffusion effect in the first test, which yields to a higher dominating transit time than for the experiment where uranine showed no influence of matrix diffusion.

For the 1 µm spheres a TBC with a strong tailing could be observed, which could not be fully attributed to matrix diffusion, whereas for the fluorescent tracers and salts matrix diffusion could not be observed. Thus, more detailed experiments with substances of different diffusion properties and improved injection conditions are recommended [Bäumle et al. 2001].

Tab. 4.4: Results from a tracer test with a double packer injection system for the distance between borehole 8 and 10 [Bäumle et al. 2001], so.-na.=sodium-naphthionate.

injection device:				**double packer**					
tracer	V_{tracer} [L]	$V_{case\ fluid}$ [L]	Q [L/s]	M [g]; [n]	t_1 [h]	v_{max} [m/h]	t_o [h]	v_o [m/h]	R [%]
uranine	2	5	0.167	1.00	1.42	7.9	2.08	5.38	5.2
SRB	2	5	0.167	5.00	1.33	8.4	2.25	4.98	5.5
pyranine	2	5	0.167	5.00	1.25	9.0	2.17	5.17	1.0
so.-na.	2	5	0.167	20.00	1.25	9.0	2.25	4.98	4.0
Br^-	2	5	0.167	362.00	1.17	9.6	2.25	4.98	5.3
C^-	2	5	0.167	436.50	1.50	7.5	2.17	5.17	4.2
Li^+	2	5	0.167	85.50	1.33	8.4	2.25	4.98	3.0
Sr^{2+}	2	5	0.167	198.50	1.50	7.5	2.17	5.17	1.2
YG 1µm	2	5	0.167	2.30E+10	1.17	9.6	1.92	5.84	1.2
Red 1µm	2	5	0.167	2.30E+10	1.25	9.0	1.92	5.84	0.9

4.2.4 Tracer tests 2005

4.2.4.1 Goals

According to the results of the previous tests, new tracer tests were carried out that were designed to consider the following aspects:

- Injection volume: The injection volume was shown to strongly

influence the transport behavior. A smaller volume seemed to yield to more accurate results. Therefore the volume was subsequently reduced down to a limit (that was to be defined).

- Dead volume: The dead volume was shown to influence the transport behavior as well, and a loss of tracer can be explained by the dead end volume inside the injection device or in dead end fractures. Additional injections show the actual influence and importance of this volume.
- Diffusion processes: To evaluate the importance of matrix diffusion processes, substances with different diffusion coefficients should be applied: fluorescent solutes, salts and differently sized microspheres.
- Sampling strategy: Manual sampling requires more personal effort, but delivers more accurate results (when sampling intervals are small). Online measurements bear a higher risk of data loss (in cases where the power supply is deficient or interrupted) but deliver data of a higher resolution (when manual sampling intervals are large). Both methods need to be combined and adjusted to the existing conditions.

These tests had to be performed without the application of microbiological tracers. The previous laboratory tests found that microspheres are an appropriate means to simulate the overall transport behavior of the microorganisms and therefore the differently sized microspheres are used to evaluate the microbial risk for fractured aquifers.

4.2.4.2 Tracer test performance

The tracer tests in March 2005 inside the Lindau gallery were carried out in consideration of the strategy described below.

The combined and comparative tracer test with multiple injections was carried out in March 2005 between the boreholes Nº 8 as injection point and Nº 10 as production borehole. The double packer was introduced into the borehole so that the injection interval lay in a zone of enhanced hydraulic conductivity in the contact zone of the ore dyke and the granite, whereas the dyke-wards packer was taken to the impermeable granite. Thus, a back-drop of tracer was largely impeded (Fig. 4.6).

For the injection procedure an injection cartridge that is directly linked to the injection pipe inside the packer was used that contains a volume of 10 mL (Fig. 4.9). The cartridge provides a device to keep the injection volume low, in order to avoid the previously mentioned problems with larger injection volumes.

A description of the experimental setup is given in Fig. 4.7. A total of 537 samples was manually taken for the analysis of all tracers (colloids, fluorescence tracers, salt tracers), during shorter time intervals by the sampling personnel, and later by automatic samplers. The fluorescent tracers were analyzed with the laboratory fluorometer (LS55, PerkinElmer), the particle tracers were evaluated with fluorescence microscopy (Standard FL, Zeiss) and the salt tracers lithium and strontium were analyzed with atomic absorption spectroscopy (AAS, PerkinElmer), chloride was analyzed photometrically (MPM3000, WTW).

Additional online measurements of pH, electrical conductivity and temperature, as well as fluorescence (Fig. 4.7, Fig. 4.8) provided additional information – especially when the sampling interval increased. For the online measurement of electrical conductivity, pH-value and temperature, WTW field equipment was used (SenTix81) and monitored by the software MultiLabpilot (WTW). The fluorescence tracers were monitored online with an GGUN-FLOW flow through fluorometer (University of Neuchâtel).

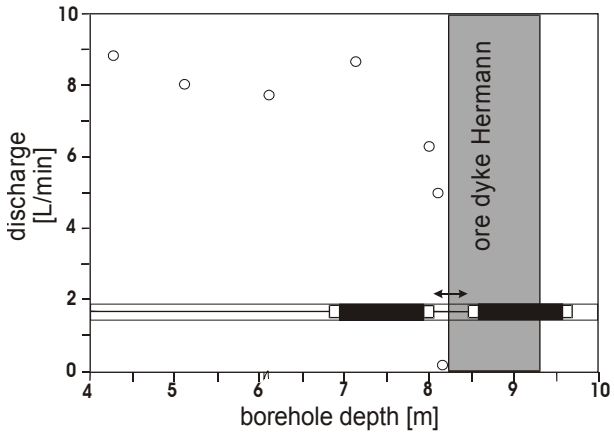

Fig. 4.6: Final packer location projected in borehole 8 in relation to the ore dyke and the discharge through borehole 8 with regard to the packer interval; modified after Witthüser 2002.

An overview over the consecutive injections and the applied tracers is given in Tab. 4.5. After the injection of 0.7 L, no signal of the conservative tracer was observed, therefore it was assumed that the injection volume was too low for

the tracer to leave the injection borehole and tracer was still present in the borehole's dead volume. Therefore, an additional injection was conducted with a larger total injection volume of 3 L, and a conservative tracer was applied to check the hypothesis. This injection is referred to as the 1st injection in the following. During a second injection, a total of 2.1 L of colloid-free tracer and flushing fluid was introduced and in a final third injection 1.5 L completely tracer-free fluid was injected.

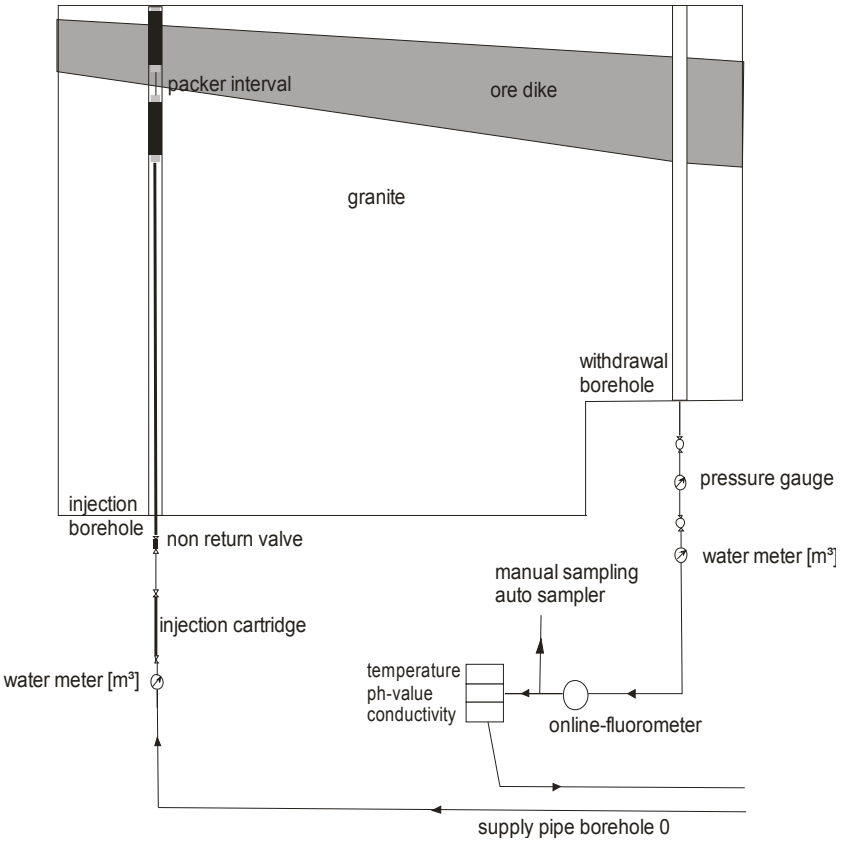

Fig. 4.7: Experimental setup with injection borehole 8 (left) and production borehole 10 (on the right).

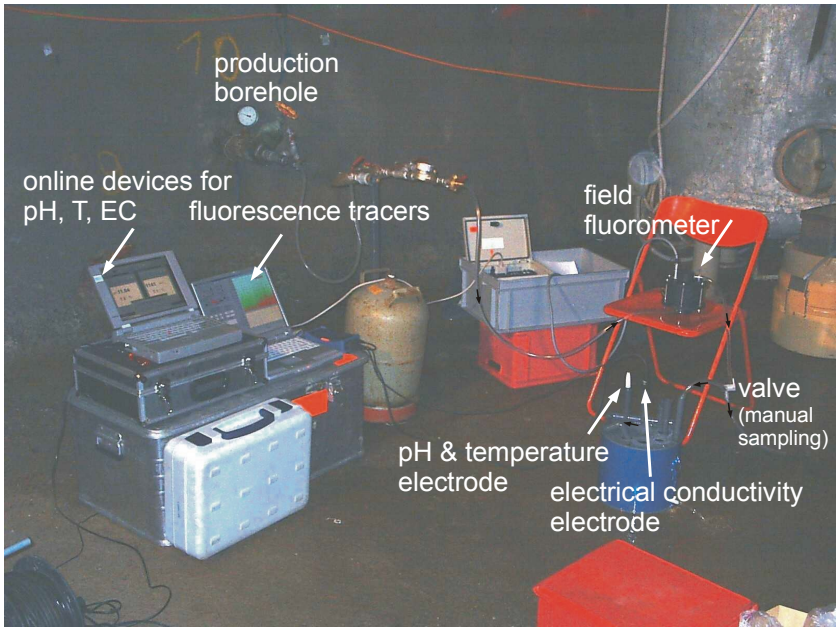

Fig. 4.8: Production borehole with online instruments (Photograph: Michel D. Lambert).

Tab. 4.5: Overview over the injected tracers and injection order.

	solute tracer	**particle tracer**
1st injection	0.505 g uranine	4.55E+10 1 µm spheres 5.04E+09 3 µm spheres 3.15E+08 6 µm spheres
	1.532 g uranine 500 g lithiumchloride	
2nd injection	2 g amidorhodamine G 500 g strontiumhexahydrate	
3rd injection	1.5 L tracer-free water from borehole 0	

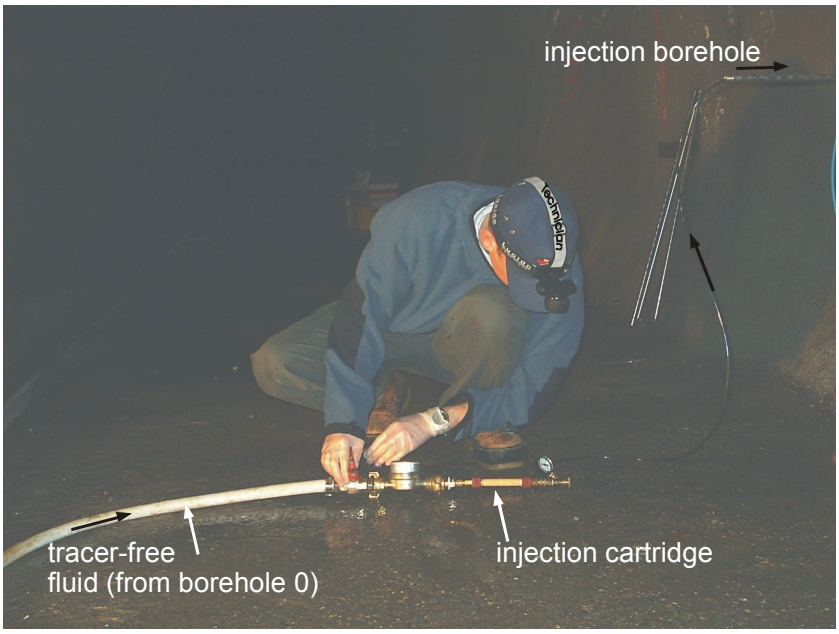

Fig. 4.9: Injection through the cartridge.

4.2.5 Results and discussion

4.2.5.1 General aspects

The flow conditions during the tracer tests were kept constant. The online measurement of the electrical conductivity gives a first pulse of relatively high electrical conductivity fluid (Fig. 4.10), which is the result of previously injected tracers that remained in the borehole and were remobilized after opening the production borehole. After the conductivity reached a constant low level, tracer tests started.

The online measurement of the temperature gave no significant fluctuation

in the first interval (Fig. 4.10) or during the tests. The pH probe shows fluctuations during the entire interval, which is very probably an effect of the instrument's specifications, which hinder online measurements in a flow tube system. Manual measurements gave a constant pH-value of 8.3.

The hydraulic head was monitored by the use of manometers at each borehole over the entire test interval and was found to be constant – however, possible variations in decimeter or centimeter scale cannot be evaluated due to the quality of the manometers.

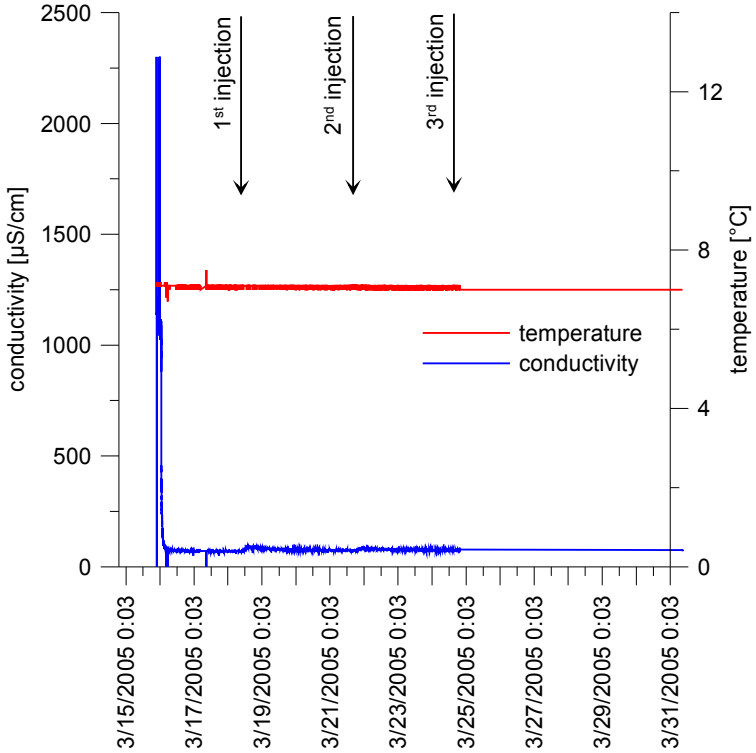

Fig. 4.10: Online measurement of temperature and conductivity during the entire test interval.

4.2.5.2 Tracer breakthrough curves

Tab. 4.6 and Tab. 4.7 give an overview of the main transport parameters of the applied tracers after the first and second injection (recovery calculated for the entire TBC, or when multiple peaks occur, only first peak calculated).

Tab. 4.6: Basic results of the first injection.

		1 µm spheres	3 µm spheres	6 µm spheres	uranine	Li^+	Cl^-
Q	[L/s]	0.125	0.125	0.125	0.125	0.125	0.125
R	[%]	1.17	0.06	0.06	34.98	30.07	23.43
t_1	[h]	0.75	2.17	2.42	0.92	0.92	2.17
v_{max}	[m/h]	14.93	5.16	4.63	12.17	12.17	5.16
t_{peak}	[h]	3.08	2.33	2.50	4.08	4.08	3.58
v_{peak}	[m/h]	3.64	4.81	4.48	2.75	2.75	3.13
c_{peak}	[n/100mL] [µg/L]	2.62E+04	1.00E+03	18.00	38.72	845.20	6.50E+03

Tab. 4.7: Basic results of the second injection.

tracer		amidorhodamine g	Sr^{2+}
Q	[L/s]	0.125	0.125
R	[%]	30.10	12.81
t_1	[h]	8.37	3.28
v_{max}	[m/h]	1.34	3.41
t_{peak}	[h]	24.73	6.73
v_{peak}	[m/h]	0.45	1.66
c_{peak}	[n/100mL] [µg/L]	4.10	108.00

Fig. 4.11, Fig. 4.14 and Fig. 4.15 give the results of the TBC for all applied tracers (please note the different axis for the solute tracers) and Fig. 4.12 and Fig. 4.13 for the particle tracers and uranine.

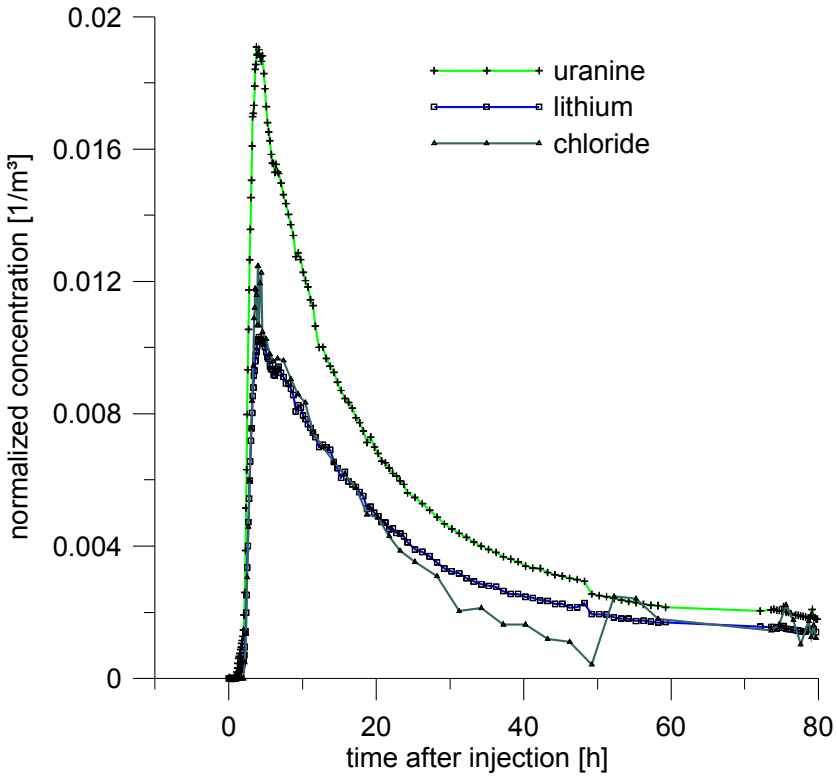

Fig. 4.11: Normalized TBC of uranine, lithium and chloride for the 1st injection.

The solute TBC for the first injection shows that all three tracers, uranine, lithium and chloride, behave relatively similarly. However, the normalized concentration of the fluorescent tracer is slightly higher than for lithium and chloride, which indicates a higher recovery rate for uranine and less sorption than for lithium and chloride. Both lithium and chloride show very similar TBCs, especially in the peak area; the tailing of the chloride is more irregular. Therefore it can be assumed that cation exchange processes are not significant for the lithium breakthrough.

The microspheres give very low recovery rates (1.17% for the 1 µm spheres, 0.06% for the 3 µm and 6 µm spheres) and narrow TBCs with a sharp peak, whereas the uranine TBC shows a more pronounced tailing of the curve

(Fig. 4.12). The FDT for the 1µm spheres (0.75 h) precedes the solutes uranine (0.92 h), lithium (0.92 h) and chloride (2.17 h), whereas the FDT for the larger microspheres follows the solutes (Tab. 4.6). The peak times for the microspheres (1 µm spheres: 3.08 h; 3 µm spheres: 2.33 h and 6 µm spheres: 2.5 h) are significantly smaller than for the solutes. Uranine and lithium peak at 4.08 h and chloride at 3.58 h after the injection. For peak shift analysis after Zhang et al. 2001 please see chapter 3.4.6.3 Peak shift analysis.

Larger microspheres (3 µm and 6 µm) cannot be remobilized by the following injections. The effect of the two following injections on the 1 µm spheres is negligible – the tailing with the second 1 µm spheres peak contributes to 0.12% of the recovery; the second peak without tailing contributes to 0.02%.

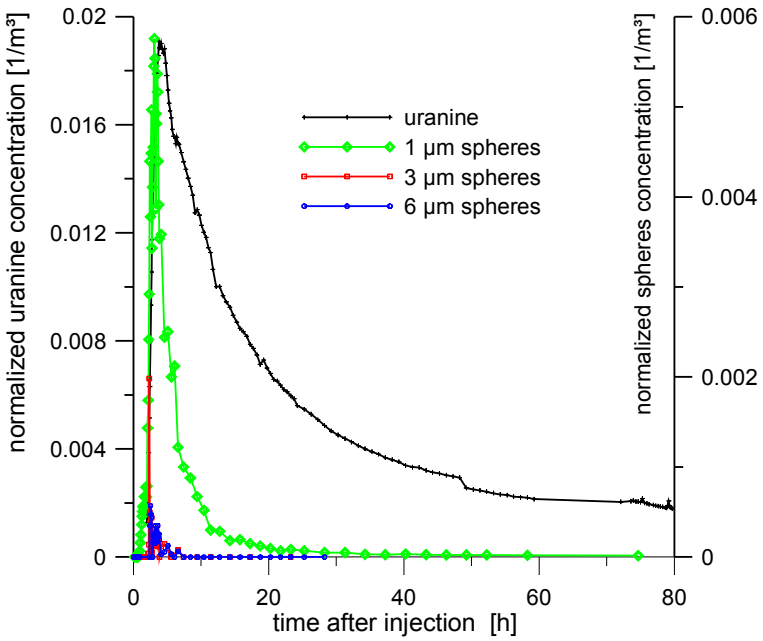

Fig. 4.12: Entire normalized TBC of the microspheres and uranine for the 1st injection (please note the different axis scale).

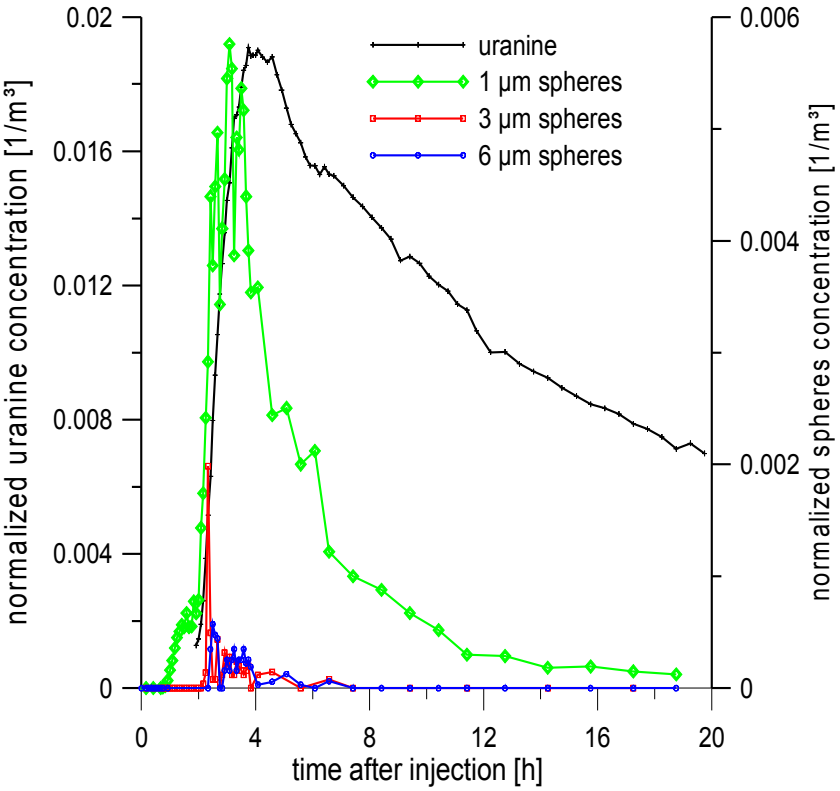

Fig. 4.13: Detailed normalized TBC of all microspheres and uranine, please note the different axis scale for solutes and particles.

The fluorescence tracer uranine shows additional peaks after the 2nd and 3rd injection, although no additional uranine was introduced into the system. Lithium shows comparable results – two additional injections, one with other solutes and one without tracers yield two additional peaks.

In both cases the additional peaks show lower concentrations than the previous ones. For uranine the 1st/2nd peak concentration relation is 3.1, for the 2nd /3rd peak concentration it is 2.8. The lithium peak relation of the first peaks is 1.9 and for the later peaks it is 2.3. Thus, both tracers show a remobilization after each injection which is in the same range for each tracer and lower for

uranine compared to lithium. Hence, uranine shows a more conservative behavior than lithium.

It can be assumed that the remobilized tracers come from either the injection borehole or the tracer volume already introduced into the system – however, it cannot be clearly distinguished between these two sources. The longer travel times for the later peaks (3.75 h, 5.5 h and 4.25 h for uranine peaks; 4.08 h, 7.58 h and 8.25 h for lithium peaks) can potentially be attributed to slightly different injection conditions, i.e. the injection volume decreased (1st injection: 3 L, 2nd injection: 2.1 L and 3rd injection: 1.5 L), which should result generally in increasing travel times compared to the first injection.

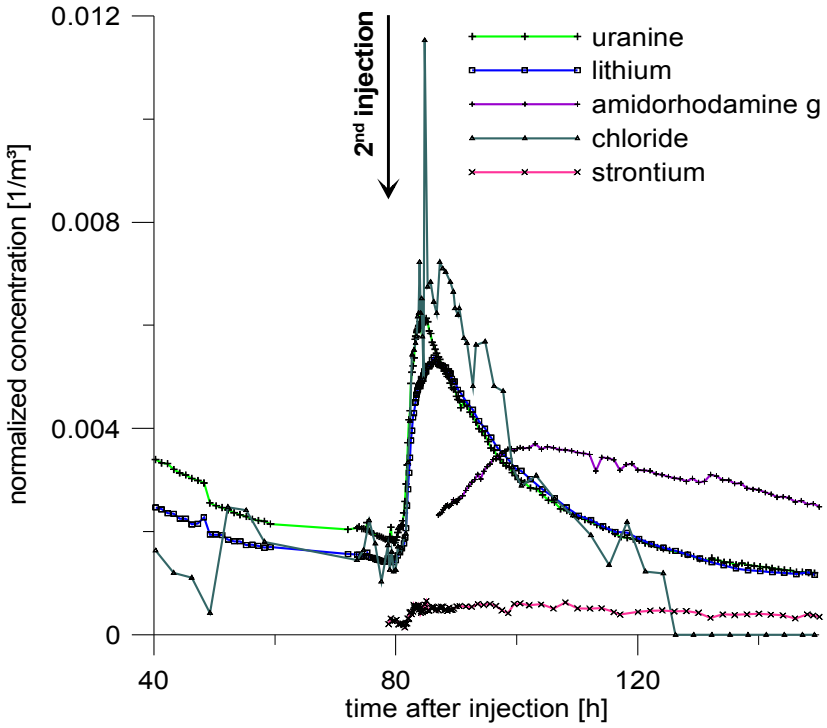

Fig. 4.14: Normalized TBC for the solute tracers for the second injection.

The amidorhodamine g and strontium introduced (2nd injection) result in TBCs that are significantly retarded compared to all other solute tracers. Strontium reached a plateau value, amidorhodamine showed a pronounced tailing. Amidorhodamine g was not remobilized after the 3rd injection and strontium only to a low extent (relation of second to first strontium peak: 2.6). The overall concentrations are small.

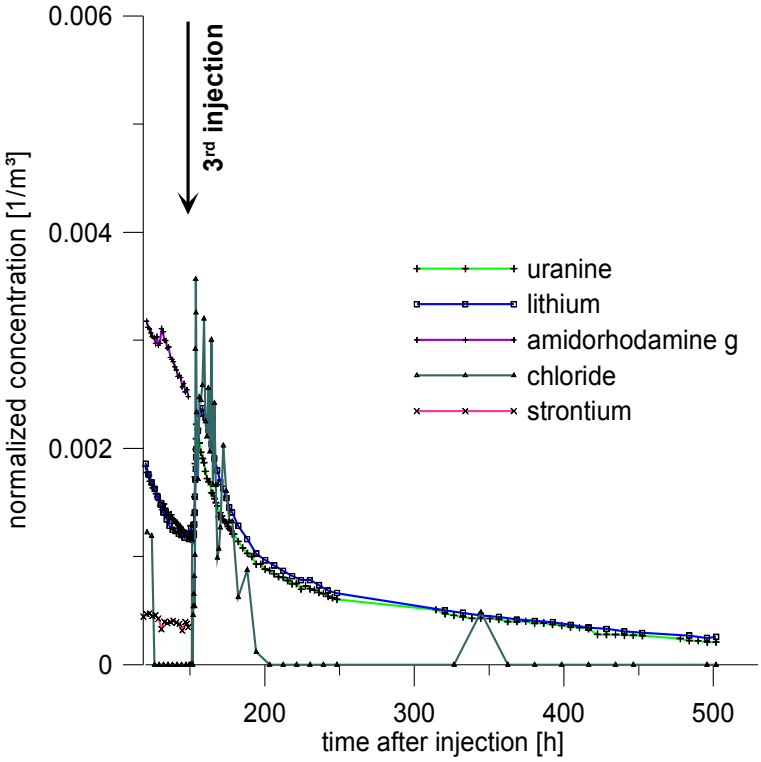

Fig. 4.15: Normalized TBC of all solute tracers for the 3rd injection.

The injection volumes of strontium and amidorhodamine are adequate, the other tracers were mobilized and thus injection volume was shown to be sufficient. Significant retardation or exchange processes seem to occur for

strontium and amidorhodamine g. Strontium is known to be highly effective in cation exchange. Thus, it can be assumed that the introduction of strontium into the system has influenced the behavior of the later lithium peaks (lithium is less effective in cation exchange).

4.2.5.3 Modeling results

Based on the parameters shown in Tab. 4.8 three modeling approaches were tested for the solute and particle tracers: a conventional ADM (advection dispersion model / CXTFIT), an SFDM (single fissure dispersion model / Traci95) and a 2RNE (two region non-equilibrium model / CXTFIT).

Tab. 4.8: Flow distance and basic parameters.

		Bh 8 – Bh 10
X	[m]	11.4
ΔH	[m]	2
Q	[m³/s]	1.25E-04

The basic equations and parameters for the ADE, the SFDM and the 2RNE were described in chapter 2.5 Solute and colloid transport.

The conventional ADM is not able to fit the TBC of the particle or solute tracers when the coefficient of determination (R^2) is used for evaluation of the fit quality. On the other hand, a visual inspection of TBCs and fitted values generally provides a good means to distinguish between parts of the TBC where the fit might be relatively good and parts where fitted values show weaknesses that might come from strongly varying data points (as reported in Witthüser 2002). Then the R^2 calculated for the entire TBC might stand for low fit quality, although the visual inspection demonstrates a good quality as seen for the uranine TBC (Fig. 4.17).

Thus, the best fit results for the ADM of selected tracers are shown in Tab. 4.9. The results show that processes might occur that are generally not covered by a conventional ADM, and thus other modeling approaches have to be used to quantify the hydraulic parameters.

Tab. 4.9: ADM modeling results.

	ADM			
	v_0 [m/h]	D_L [m²/h]	α [m]	R^2
1 µm spheres	2.856	2.061	0.72	0.942
3 µm spheres	4.858	0.009	0.00	0.833
uranine (1st peak)	0.002	4.078	1941.9	0.938
amidorhodamine g	0.0001	0.908	9078.0	0.914
lithium (1st peak)	0.0004	3.582	10179.0	0.949
chloride (1st peak)	0.699	3.384	4.84	0.887
chloride (2nd peak)	0.379	2.738	7.22	0.835

As described in Witthüser 2002, the SFDM shows weaknesses in modeling the tailing of the TBC, whereas the peak is well fitted by the SFDM (Fig. 4.17). The results are listed in Tab. 4.10. Further DLVO modeling partly uses the results of the SFDM modeling or the parameters depending on SFDM modeling (e.g. parameter b) (Tab. 4.11, Tab. 4.12). These parameters are of minor importance for the DLVO calculation and results are interpreted only quantitatively (see peak shift) where the SFDM-derived parameters are considered to be of sufficient quality.

The evaluated SFDM parameters for uranine differ from the values obtained from Witthüser 2002 (W 2002). The effective fracture width is reduced by the factor two in the test in 2005 (W 2002: 206 µm; G 2005: 107 µm). The dispersion coefficient increased slightly (W 2002: 3.67E-04 m²/s; G 2005: 9.56E-04 m²/s), the fracture porosity decreased (W 2002: 0.8%; G 2005: 0.5%) and the effective diffusion coefficient increased (W 2003: 2.0E-12 m²/s; G 2005: 2.90E-10 m²/s).

This means that the results from 2005 give a wider TBC than the results from 2002. Thus the advection part of the TBC is smaller and diffusion effects

have increased, which results in a decrease of the Peclet number (W 2002: 15; G 2005: 4). However, the $t^{-1.5}$-criterion for matrix diffusion [Tsang 1995] is not fulfilled (Fig. 4.16), therefore the tailing cannot be interpreted as an effect of matrix diffusion. An explanation might be technical difficulties during injection and the dead volume inside the borehole. Triple packers provide a means to further increase the accuracy of injection of tracer towards the production borehole (double packer injection results in a radial injection in all directions, towards the production borehole and backwards). However, this system was not available for the tests.

The modeling of lithium and chloride gave similar results compared to the uranine, which indicates that the results are not tracer specific.

For the calculation of the effective diffusion coefficient, a matrix porosity of 5% was assumed referring to Witthüser 2002. For the solute tracers, the effective diffusion coefficient is two orders of magnitude higher than the results from Witthüser. However, the tailing cannot be interpreted as matrix diffusion – as previously shown (Fig. 4.16). An alternative explanation might be the dead volume in the borehole or the tracer volume remaining in the fractures near the borehole.

Due to the weaknesses of the SFDM in fitting the tailing of the TBC, it was abstained from fitting of the additional peaks by the SFDM.

The microsphere results show that a smaller fracture porosity is available for particles (1 µm: 0.2%; 3 µm: 0.1% and 6 µm 0.2%) than for solutes. This is consistent with the theory of size or pore exclusion processes operating for particles (whereas solutes are not affected by this and can use a larger pore space). The TBC is narrow and thus the advective part is more dominating (i.e. the Peclet number is higher) and the dispersion coefficient is smaller for the microspheres. The dispersion length α_L is significantly smaller for the microspheres, and the effective diffusion coefficient (again under the consumption of a matrix porosity of 5%) is higher for the 1 µm and 6 µm spheres – however, again as is the case for the solutes, they do not fulfill the Tsang-criterion of matrix diffusion.

Matrix diffusion is considered to be a reversible process: when concentration in the flow channel decreases, substance from the matrix can flow back into the main pathways and cause a tailing of the TBC. This process can be assumed for the solutes, but not for microspheres. The tailing of the microspheres is too low, so that a significant remobilization could not be observed.

Tab. 4.10: SFDM modeling results.

	SFDM						
	t_o [h]	v_o [m/h]	D_L [m²/h]	α [m]	P_e [-]	a [$s^{-0.5}$]	R [%]
1 µm spheres	3.22	3.546	1.107	0.312	36.52	0.0491	0.98
3 µm spheres	2.32	4.919	0.007	0.001	8101.1	0.0117	0.03
6 µm spheres	3.02	3.772	1.701	0.451	25.3	0.0504	0.03
uranine (1st peak)	9.02	1.264	3.440	2.722	4.19	0.0354	18.23
lithium (1st peak)	10.8	1.056	3.343	3.166	3.6	0.0310	12.16
chloride (1st peak)	8.75	1.302	2.996	2.300	4.96	0.0376	11.36

Tab. 4.11: Fit parameters of the SFDM and derived hydraulic parameters for the microspheres.

		1 µm spheres	3 µm spheres	6 µm spheres
a	[$s^{-0.5}$]	0.05	0.01	0.05
t_o	[s]	11574	8345	10879
P_e	[-]	37	8101	25
b	[µm]	302	419	321
v	[m/s]	9.85E-04	1.37E-03	1.05E-03
D_L	[m²/s]	3.08E-04	1.94E-06	4.73E-04
α_L	[m]	0.312	0.001	0.451
ε_f	[%]	0.2	0.1	0.2
D_e	[m²/s]	4.38E-09	4.83E-10	5.23E-09

Tab. 4.12: Fit parameters of the SFDM and derived hydraulic parameters for the solutes.

		uranine	**lithium**	**chloride**
a	[$s^{-0.5}$]	0.04	0.03	0.04
t_o	[s]	32472	38873	31507
P_e	[-]	4	4	5
b	[µm]	107	81	111
v	[m/s]	3.51E-04	2.93E-04	3.62E-04
D_L	[m²/s]	9.56E-04	9.29E-04	8.32E-04
α_L	[m]	2.72	3.17	2.30
εf	[%]	0.5	0.6	0.5
D_e	[m²/s]	2.90E-10	1.26E-10	3.46E-10

In order to obtain the DLVO parameters of the microspheres and to conduct peak shift analysis, the SFDM results were used and implemented in the equations that had previously been used for porous media. For porosity values, the fracture porosity (ε_f) was used and for grain size the main fracture half-width (b) applied which seems to provide an accurate simplification. This simplification means a loss in accuracy of the data values which hampers a direct comparison of data from porous media (the matrix for which the applied equations were developed) and fractured media, but has the advantage that most parameters are already obtained by an SFDM. In addition, for peak shift analysis only a qualitative analysis is necessary.

The peak shift analysis showed a clear trend (Tab. 4.13). Microspheres are definitely transported faster than the solutes because of their differential advection due to size or pore exclusion processes. Additionally, the FDT for 3 µm and 6 µm spheres is not lower than for the solutes, therefore the lower detection limit assumed for microspheres does not camouflage exclusion processes.

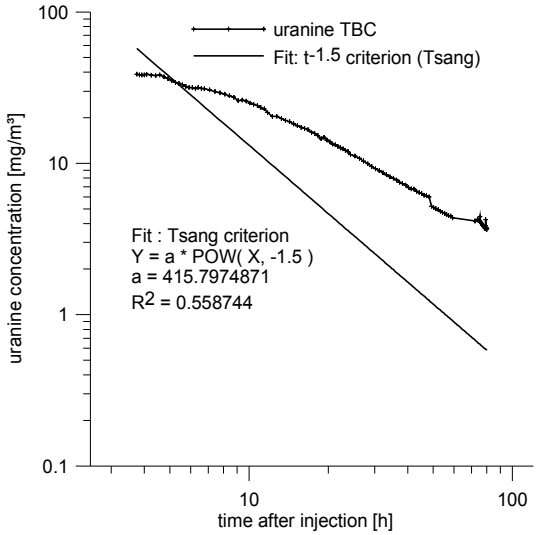

Fig. 4.16: Evaluation of the Tsang-criterion for the uranine TBC.

Tab. 4.13: Results of peak shift analysis.

	relative recovery RR [ ]	**Δ_{tpeak} observed** [ ]	**Δ_{tpeak} calculated** [ ]	**differential advection?**	**retardation?**
microspheres [µm]					
1	0.033	17.9	12.3	yes	no
3	0.002	37.9	13.6	yes	no
6	0.002	33.3	17.2	yes	no

Tab. 4.14 gives the results of the simplified DLVO calculations. It shows that filter coefficients are lower for smaller microspheres and the attachment efficiency is highest for the 1 µm spheres, the smallest microsphere size class. This means that a collision of 1 µm spheres with collector walls results more often in an attachment than for larger microsphere size classes.

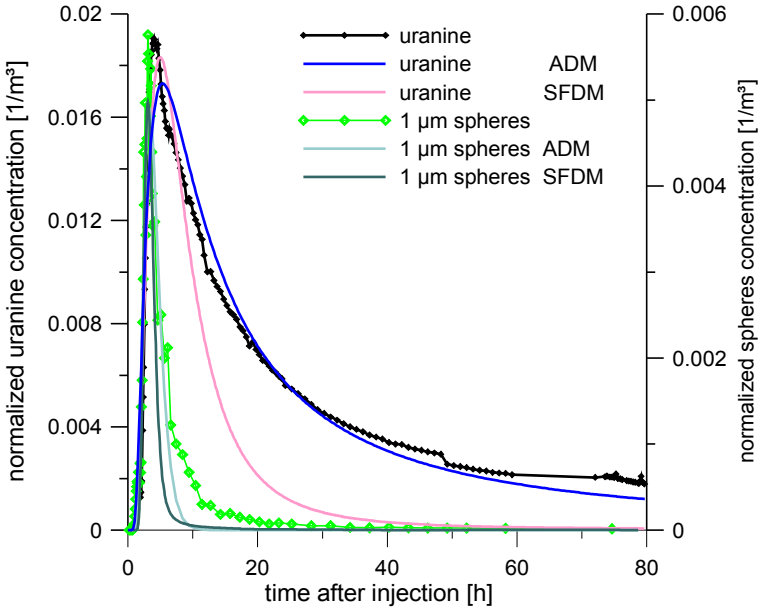

Fig. 4.17: TBCs of uranine and 1 µm spheres and the ADM and SFDM modeling results.

Due to the failure of accurate tailing modeling (SFDM), a two-region non-equilibrium model (2RNE) was applied for microspheres and all solute tracers. The results are shown in Tab. 4.15.

Therefore, the 2RNE was applied, which was originally developed to describe the tailing effects in porous media due to an exchange between mobile water in larger pores and immobile water in finer pores or absorbed water. Field & Pinsky 2000 applied this approach for karst aquifers where karst conduits contain mobile water and the adjacent rock or still water zones (e.g. in siphons) represent the immobile fluid. Birk et al. 2005, Geyer et al. 2007 and

Göppert & Goldscheider (accepted) showed that a 2RNE is in general the better choice for a reproduction of the tailing of TBCs compared to conventional ADM approaches for karst systems.

Tab. 4.14: DLVO results for the microspheres.

			microspheres		
			1 µm	3 µm	6 µm
recovery		[%]	1.17	0.06	0.06
effective porosity	ε_f	[%]	0.2	0.1	0.2
deposition rate coefficient	κ	[1/s]	6.93E-04	7.79E-04	1.08E-03
filter coefficient	λ	[1/m]	1.11	1.37	1.39
single-collector removal efficiency	η	[ ]	2.80E-04	4.26E-04	3.72E-04
single-collector contact efficiency	η_o	[ ]	1.06E-02	5.28E-02	2.08E-01
attachment efficiency	α	[ ]	2.64E-02	8.08E-03	1.79E-03

Fractured aquifers are in several aspects supposed to behave comparably to karst aquifers. Fractures can be considered as mobile fluid areas and the adjacent rock matrix stands for the immobile fluid part. Thus, the 2RNE was applied for all tracers, and results with a good visual correlation or a good R^2 are listed in the following. The resulting TBCs for uranine and the 1 µm and 3 µm spheres are given in Fig. 4.19.

For uranine and lithium the first peaks were first inversely modeled by the 2RNE, afterwards forward modeled and original data reduced by fitted data so that the following peaks were reduced by the tailing effect. Fig. 4.18 illustrates this method for the uranine TBC. This method was applied for uranine, lithium and chloride peaks as long as the coefficient of determination proved a good fit quality. For the 2RNE microsphere modeling original data were used, and a smoothing of the data points did not have to be conducted.

The mean flow velocity of the microspheres is significantly higher than for the solutes. The later peaks of uranine, lithium and chloride give main flow velocities that are about one order of magnitude lower. The narrow peak of the 3 µm spheres results in a low dispersion coefficient, the dispersion coefficient is higher for the 1 µm spheres and the solutes that produce comparable dispersion coefficients. The dispersion lengths of the later solute peaks are extremely long, some even longer than the distance between the two boreholes.

Tab. 4.15: 2RNE modeling results.

	2RNE					
	v_0 [m/h]	D_L [m²/h]	α [m]	β	ω	R^2
1 µm spheres	2.061	0.737	0.36	0.609	1.009	0.96
3 µm spheres	3.834	0.006	0.002	0.786	1.002	0.94
uranine (1st peak)	0.462	0.632	1.37	0.294	1.988	0.98
uranine (2nd peak)	0.043	1.753	40.91	0.571	9.695	0.93
uranine (3rd peak)	0.035	0.508	14.59	0.204	9.696	0.91
lithium (1st peak)	0.391	0.780	1.99	0.333	2.202	0.97
lithium (2nd peak)	0.021	1.866	88.48	0.701	15.440	0.97
lithium (3rd peak)	0.012	0.723	60.62	0.329	23.320	0.96
chloride (1st peak)	0.724	0.282	0.39	0.289	2.425	0.96
chloride (2nd peak)	0.436	2.542	5.84	0.001	100	0.85
amidorhodamine g	0.188	0.133	0.71	0.294	3.220	0.94

The higher values of the partition coefficient β of the microspheres indicate a larger volume of mobile water compared to the solutes. The mass transfer coefficient ω that describes the rate of exchange between mobile and immobile parts shows that the exchange tendency is lower for the microspheres. This is in line with the finding that the microspheres cannot be remobilized to a large extent by additional injections of microsphere-free water.

Compared to karst systems [Göppert & Goldscheider (accepted)], the partition coefficient is lower for both solutes and particles, thus there is a smaller proportion of mobile water that can be explained by the fracture geometry that produces more options for immobile water compared to a conduit-characterized karst system.

Although the 2RNE was not originally developed for fractured media, the model gave reasonable results and provided a good fit quality for most tracers in these experiments. With the 2RNE it was possible to forward model the TBCs of several tracers and consider the different peaks separately.

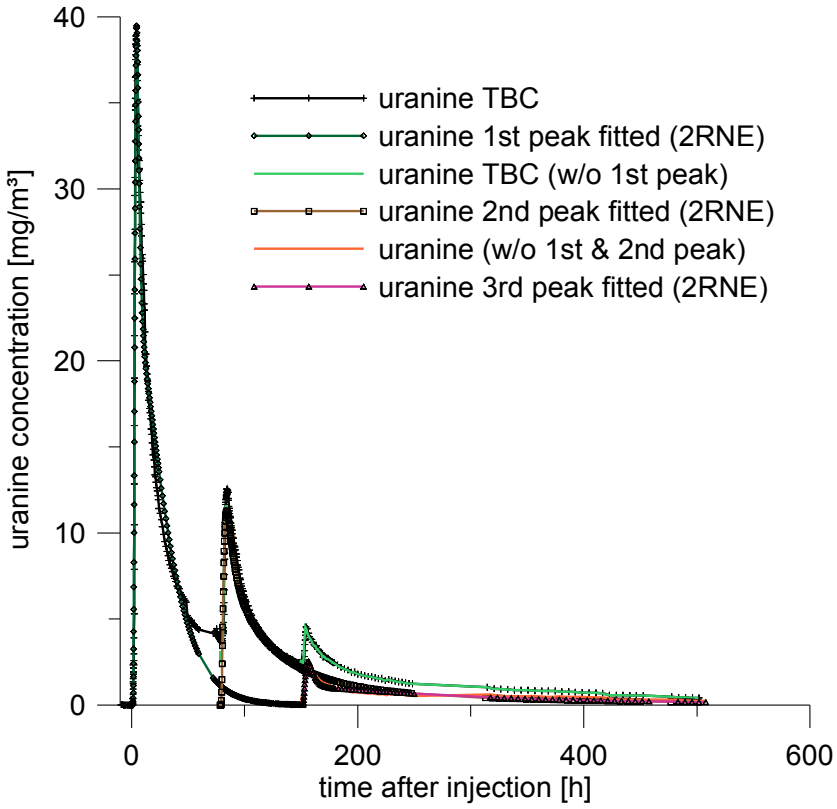

Fig. 4.18: Peak separation of the uranine TBC by using 2RNE data.

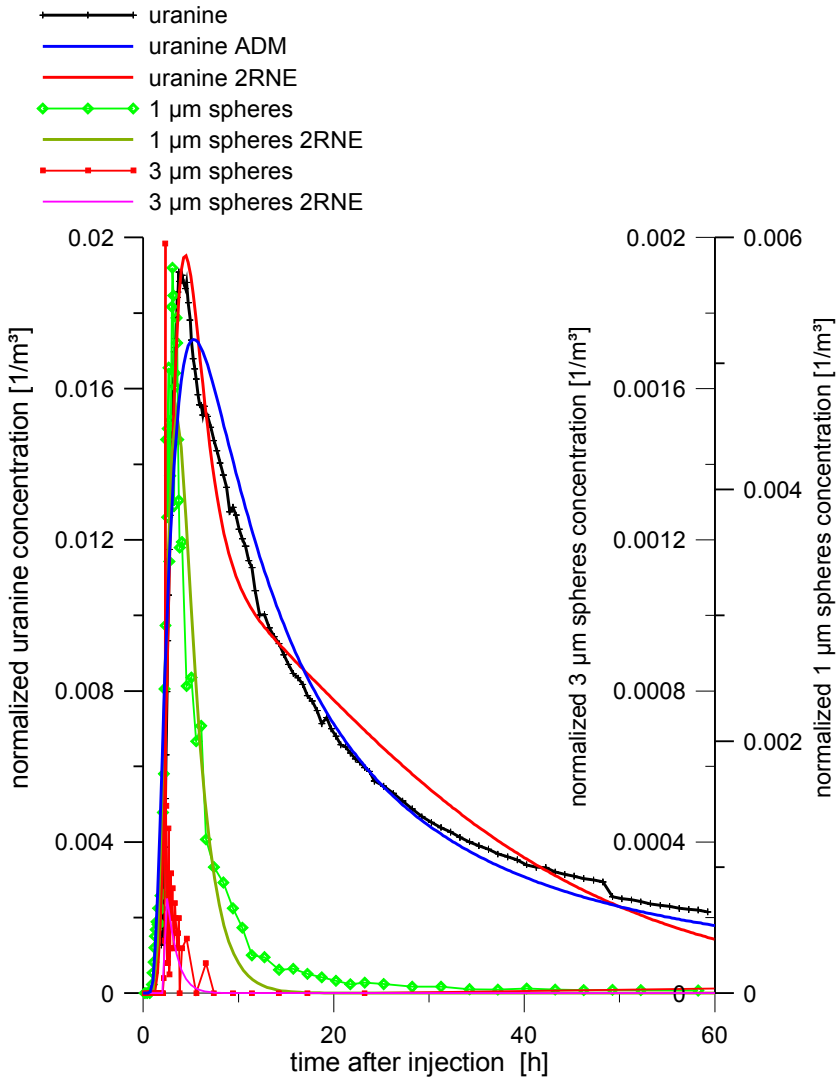

Fig. 4.19: 2RNE results for uranine, 1 µm and 3 µm spheres.

4.2.6 Conclusion

These tests prove that particle tracers experience different advection than solutes and that particle tracer produce a preceding maximum of concentrations – for all microsphere sizes, even the largest applied microsphere size class of 6 µm. The maximum concentration of colloids thus appears earlier than expected compared to solute behavior and is shown not to be an effect of detection limits or peak shift due to filtration. Contamination with colloidal contaminants reaches a maximum more quickly, but decreases rapidly and does not show a distinct tailing. This means that a potential contamination with microorganisms might occur in higher concentrations that do not last as long as solutes. Therefore protection schemes need to be adjusted accordingly. Sampling intervals can vary strongly, a shorter contamination peak can be overlooked more easily and the contamination might enter the drinking water cycle – this should be considered as well.

Although the recovery rate is small for microspheres, the recovery for the larger microspheres is larger than expected, compared to the smaller microspheres. For drinking water purposes this implies that even larger microorganisms (e.g. Cryptosporidium oocysts) can enter the fracture fluid and might cause illnesses. The main fracture width is about 100 µm, and thus easily accessible even for larger microspheres (or microorganisms) with a size of about 6 µm. Filtration or exclusion are supposed to operate only in smaller fractures – which results in a decrease in recovery. This fits well with the finding of these tests.

A direct combination of microspheres, solutes and microorganisms in field tracer tests would lead to more easily transferable findings and is thus generally preferable. However, the clear trend of the microsphere results implies that microorganism behavior can be assumed to be similar.

The tests confirmed also the dependency of the hydraulic parameters on the injection procedure [Witthüser 2002]. A higher injection volume gives generally higher recovery rates (Fig. 4.20), higher flow velocities and produces an apparent matrix diffusion which can not be approved when double-packer systems are applied. The $t^{-1.5}$-criterion of Tsang could not be observed for any of the applied tracers, neither the microspheres nor the solutes. Further increasing of injection accuracy by triple-packers might yield to more appropriate modeling results.

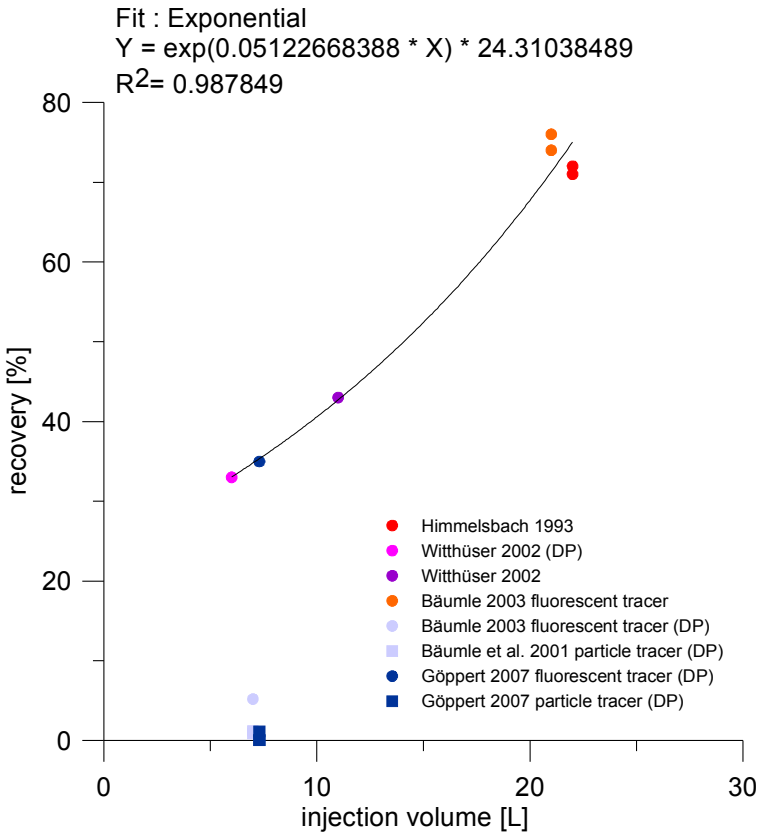

Fig. 4.20: Influence of injection volume on the recovery rate.

4.3 Karst

4.3.1 Hochgrat – Gunzesried: karstified conglomerates

4.3.1.1 Overview

The test site Hochgrat-Gunzesried is a transboundary aquifer between the federal states of Vorarlberg (Austria) and Bavaria (Germany) (Fig. 4.21). Hittisau is an Austrian community near the western margin of the test site and Gunzesried is the German community near the eastern margin. The highest peak is the Hochgrat ("*high rim*") with an altitude of 1833 m (Fig. 4.41). The morphology of the test site is dominated by a SW-NE-orientated mountain chain – the so-called Hochgrat-chain which belongs to the similarly orientated Nagelfluh-chains. The Hochgrat-chain with the Hoher Häderich (Fig. 4.41) in the west and the Mittelberg mountain in the east delimitates the test site in the Northwest; the mountain chain from Koppachstein in the west and Tennenmooskopf in the east constitutes the Southeast border. The Hochgrat chain is separated from the southern chain by two morphological (and tectonic)

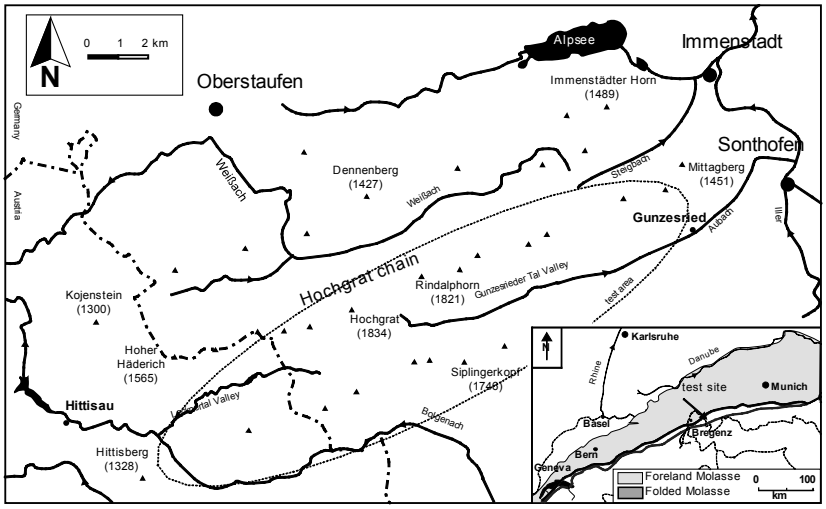

Fig. 4.21: Test site Hochgrat-Gunzesried, modified after Göppert et al. 2003.

depressions with an anticline in between – the so-called Leiterberg mountain. Lecknertal Valley and Autal Valley are glacially altered, whereas the nearby mountains were acting as Nunatakers.

4.3.1.2 Climate

Close to the Hochgrat-Gunzesried test site, the weather station in Hittisau (Vorarlberg) is located at an altitude of 790 m. The mean total annual precipitation is about 1999 mm (1938-2006), with a maximum during summer (Fig. 4.22). The precipitation at the weather station is seen to be rather a lower limit since the test site reaches up to 1833 m elevation where a higher precipitation value can be expected. The mean annual air temperature is 7.8°C with an maximum in summer (Fig. 4.22). A mean annual air temperature of 0°C can be expected for an elevation of 2100 m. The snow coverage in Hittisau lasts for almost three months (Fig. 4.23) – at higher elevation snow can last until summer in shadowy mountainous areas facing away from the sun and can fall in summer as well.

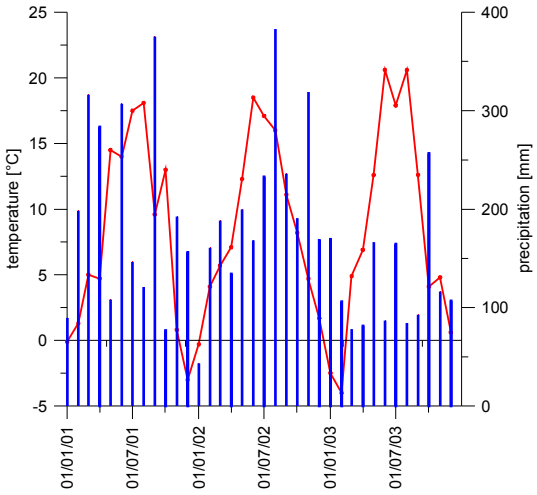

Fig. 4.22: Precipitation and temperature of the weather station Hittisau for the years 2001 to 2003 (data: Vorarlberger Landesregierung, Bregenz).

Precipitation and temperature based on climate data provided by the local authority (Amt der Voarlberger Landesregierung, Bregenz) for the investigation

interval are shown in Fig. 4.22.

A long time (since 1938) of daily variations gave a temperature increase of 1.1°C over 50 years (Fig. 4.24) and an increase of precipitation, which indicates the influence of climate change on the northern Alps. The strong increase of temperature goes along with recent climate prognoses for the northern Alps, which is three times greater than the average global warming [Agrawala 2007]. There is an increase of the average annual precipitation for this test site, which generally meets recent prognoses that predict a decline of averaged regional precipitation in summer and an increase in winter precipitation [Agrawala 2007].

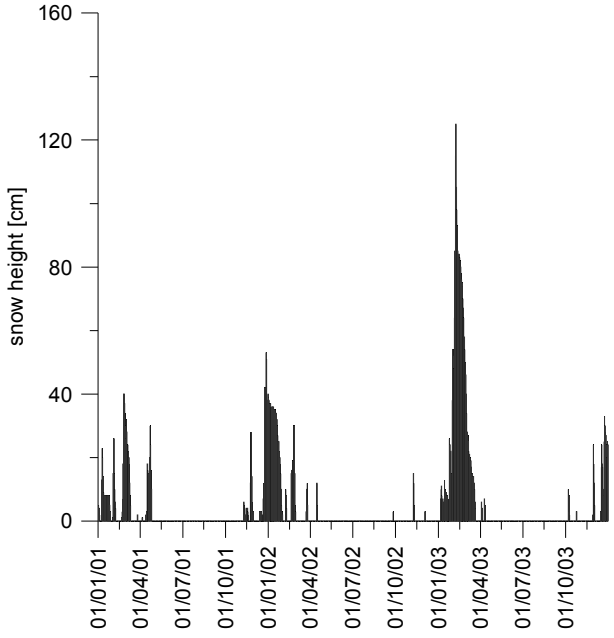

Fig. 4.23: Snow height in Hittisau during the investigation interval (data: Amt der Vorarlberger Landesregierung, Bregenz).

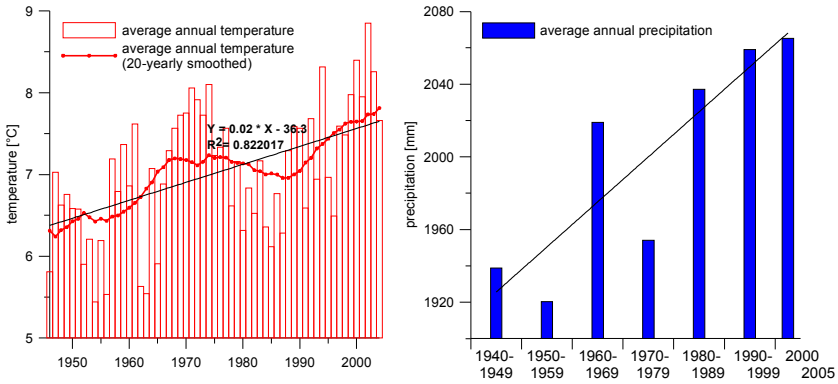

Fig. 4.24: Increase of temperature and precipitation for the Hittisau weather station (data: Amt der Vorarlberger Landesregierung).

4.3.1.3 Goals

- Geology: The geology of the test site was mapped in the framework of projects at a relatively small scale [Muheim 1934, Vollmayr 1958] by applying differing geological classification approaches, including biostratigraphy and lithostratigraphy [Scholz 1999], which lead to obscurities in naming or classifying the rock. No detailed geological map with a survey of water bearing strata (conglomerates) has previously been available. One primary goal was therefore to provide a detailed geological map showing the dimension of the water bearing strata based on easily comprehensible lithological criteria.

- Karst forms: Before these investigations started, this area was never investigated hydrogeologically, and karst features in the subalpine molasse zone were almost unknown in literature. The second intention was therefore to provide an overview over the karst features, especially the hydraulically important ones like swallow holes, dolines and ponors that allow a direct connection between potentially contaminated surface and ground water.

- Microbiology: The area is used for agricultural purposes (cattle pasture and hunting) and tourism. Little was known about the microbial water quality. Since the microbial quality offers insights into the hydraulic behavior of an aquifer, the microbial (and chemical) water quality had to be investigated after spring mapping and characterization.

- Hydrogeology: The hydrogeology of the test site was unknown prior to this investigation. Therefore, based on the abovementioned findings, tracer tests had to be done in order to classify the aquifer as fractured or karst aquifer. The role of the conglomerates for groundwater hydraulics and the influence of tectonics on the flow behavior is of importance.
- Groundwater Protection: By applying different tracer types (solutes and colloids), the potential influence on ground water that is used for drinking water purposes had to be evaluated.

4.3.1.4 Geology

Geographically, the test site is situated at the northern margin of the Alps. Geologically it belongs to the folded subalpine molasse zone which is part of the Alps since it was affected by the Alpine orogeny. The basic alpine geology is shown in Fig. 4.2. The test site belongs to the folded or subalpine molasse zone which edges the northern Alps and ranges from Geneva in the west to Vienna in the east (Fig. 4.2) and represents the sediments of the alpine foreland basin.

The area was flooded twice by the sea and became lacustrine and fluviatile afterwards. Thus the strata can be distinguished into the following formations: Lower and Upper Marine- and Freshwater Molasse.

In the Oligocene and Miocene, the area was used as a sedimentation area of larger northward orientated rivers that transported debris from the Alps into the foreland. The Lower Freshwater Molasse in Vorarlberg and Oberallgäu can be divided into three large gravel fans (from west to east): Pfänder-, Hochgrat and Nesselburg-Fan. The test site is located in the central Hochgrat-Fan (Fig. 4.25) and named after the highest summit, Hochgrat (Fig. 4.26).

The Lower Freshwater Molasse (LFM) is usually divided into the Weissach, Steigbach and Kojen members. Due to previous disagreements in member classification [Scholz 1999], a lithological interpretation approach was preferred. Thus the LFM was subdivided into conglomerates and marls or sandstones. This makes it possible to divide the formation into karstifiable rocks (carbonate conglomerates) and non-karstifiable ones (marls & non-carbonatic sandstones).

The sequence of strata in the test site consists of an intercalation of carbonatic conglomerates that have a thickness of up to 60 meter (Fig. 4.26) and marl layers that have a thickness of up to 15 meter (Fig. 4.25). More than 75% of the conglomerates consists of carbonate [Schütz 1991] and is thus predisposed to karstification processes. Matrix and cement are both carbonatic, however radiolarian (silica) and other non-soluble rock pebbles

occur as well. The pebbles can reach a size of more than 50 centimeters in diameter, yet a diameter of 5 to 10 cm is most common. Marls are of low resistance and thus subject to erosion. Hence, in steep rock formations, marls are often present in morphological depressions. Surface drainage often occurs on marls, which causes additional erosion.

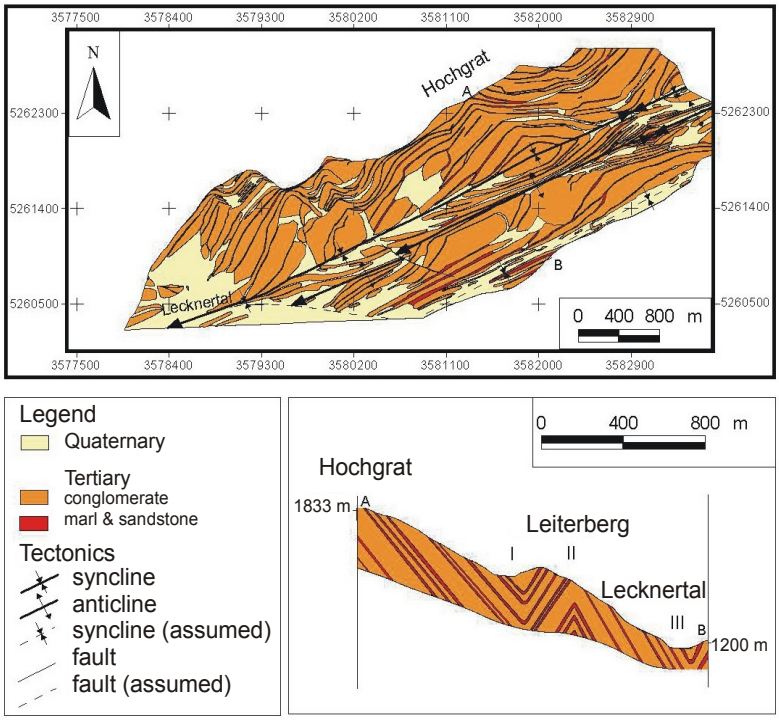

Fig. 4.25: Geology of the Hochgrat area [Göppert et al. 2003].

The test site is characterized by two synclines (I and III in Fig. 4.25) and one anticline (II in Fig. 4.25) in between these. Along the strike of the fold axis the

syncline culminates three times, from west to east near the following locations: Leiterberg (Fig. 4.26), east of Untergelchenwang-Alp and near the Rote Wand north of the Au-Alp. Further west and east the axis is covered by Quaternary deposits.

Fig. 4.26: Thick conglomerates with larger pebbles of up to 50 cm near Scheidwang-Alp (left) and view of Hochgrat and Leiterberg with the syncline inbetween (right).

4.3.1.5 Geomorphology: Karst features

4.3.1.5.1 General

The conglomerates consist of about up to 75% carbonate minerals in both matrix and cement [Schütz 1991] and are thus predisposed to karstification processes. Although there is a large variety and number of karst landforms, they were almost unknown to literature prior to these investigations and are therefore described below. A report of karst features from a nearby area in the same formation describes doline-like structures [Scholz & Strohmenger 1999]. In the following, all occurring karst feature types are described, especially those that are of importance for groundwater flow characteristics.

4.3.1.5.2 Karren

Corrosive features like rinnen- or kluftkarren occur on bedding planes, especially in the more highly elevated parts of the test site, where Quaternary deposits do not cover the conglomerate layers (Fig. 4.27). Matrix and grains are both affected by chemical dissolution. Near valley floors where Quaternary

deposits are more common, conglomerate bedding planes might be covered by impermeable deposits, thus karren can more often be observed at higher elevations. However, rinnenkarren occur even on rocks in rock fall masses at low elevation, for example at the entrance of the Lecknertal Valley, where a rockfall mass with a volume of 10 x 10^7 m³ [Seijmonsbergen et al. 2005] and rocks of several meters in diameter (1.5 m³ to 4000 m³) lay. Then rillenkarren follow the dip of the rock surface and the roots of trees or other vegetation that usually cover the rock surface.

Fig. 4.27: Karrenfield on a northwards orientated conglomerate bedding plane near Untergelchenwang-Alpe (left) and rillenkarren in conglomerate nearby on Rindalphorn mountain (right).

4.3.1.5.3 Dolines

The test site is characterized by a large number of small-scale dolines, usually with active ponors. In the test site, three detailed mappings gave more than 150 dolines, 80% of which drain the adjacent area through active swallow holes (ponors). For the Leiterberg site, on an area of 20 ha 32 dolines were mapped, nearby Lache-Alp 102 dolines (Fig. 4.28, Fig. 4.31, Fig. 4.42) on 40 ha and nearby Rindalphorn mountain 32 dolines on 12.5 ha (Fig. 4.34).

The dolines typically have a small diameter (a few meters up to 20 meters) and are lined up along the strike of the conglomerate layers directly in conglomerates or associated with them (Fig. 4.28, Fig. 4.29, Fig. 4.30). They are identifiable on aerial pictures and from laser scan data as well (Fig. 4.30, Fig. 4.34). Where conglomerates are not covered by other sediments, dolines are formed in the conglomerates or at least show a ponor that developed in the conglomerates. When conglomerates are covered with other sediments, then

in most cases at least the ponor is linked to the conglomerates (Fig. 4.29). The doline depth is about a few meters to 10 meters, and some doline floors provide an entrance shaft that might be linked to a deeper cave system.

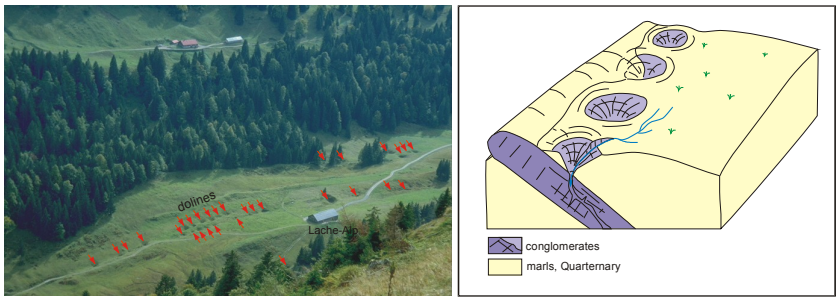

Fig. 4.28: Aligned dolines near Lache-Alp (left) and sketch of dolines aligned with conglomerate layers (right) (modified after Göppert et al. 2002).

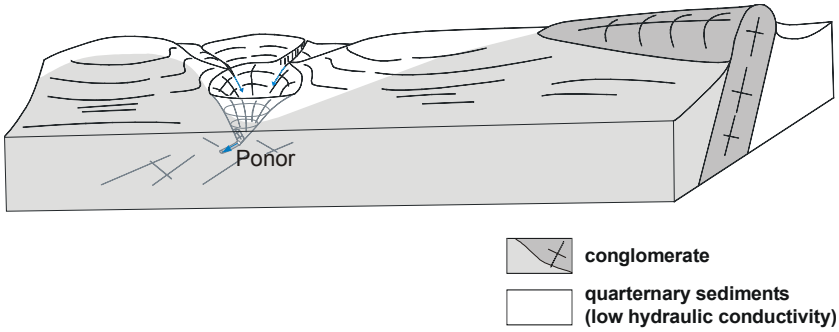

Fig. 4.29: Schematic sketch of the doline type at the valley floor shown in Fig. 4.30.

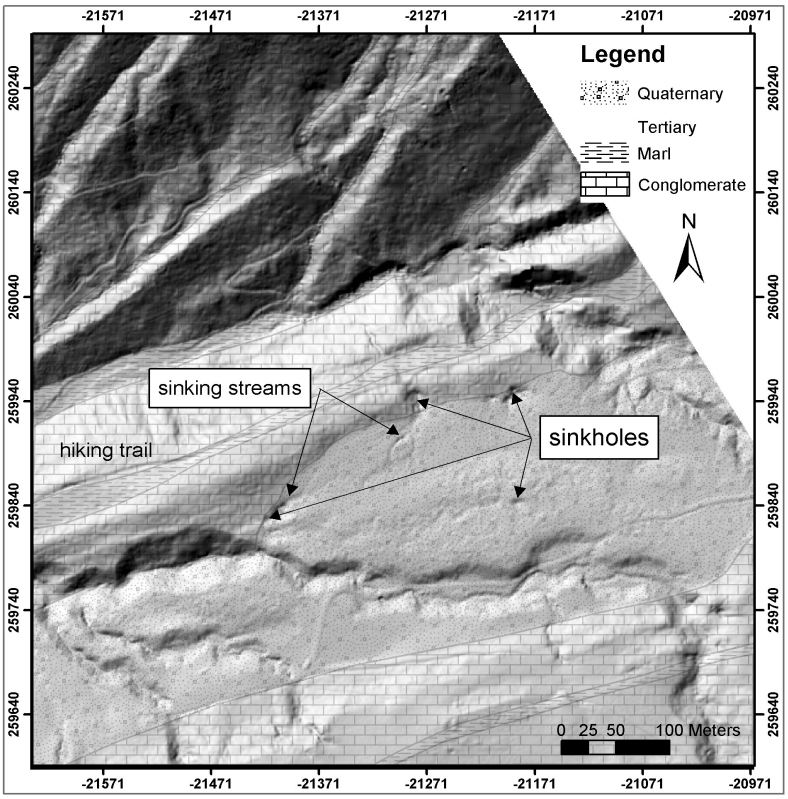

Fig. 4.30: Laser scan model of the sinkhole area near Höfle-Alp (Laser scan data: Landesvermessungsamt Feldkirch / LVA).

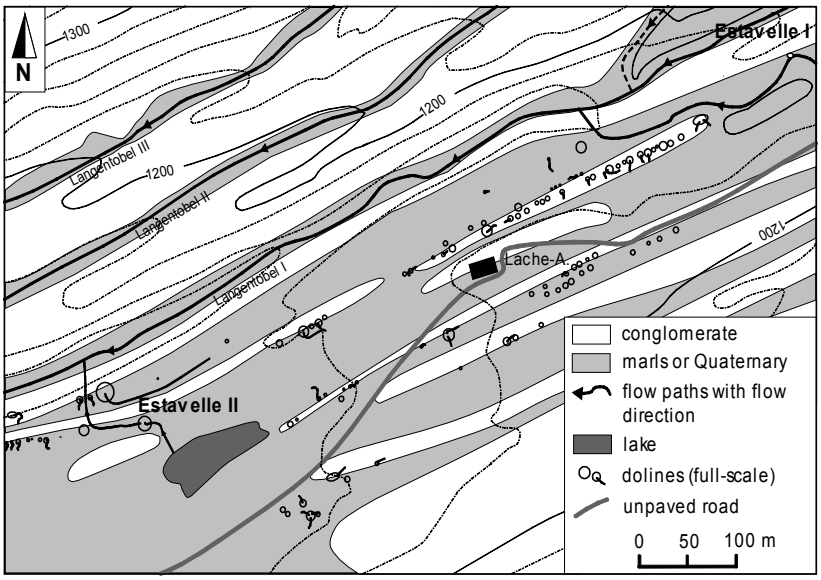

Fig. 4.31: Detailed map of dolines, ponors and estavelles nearby Lache-Alp (modified from Göppert et al. 2002).

4.3.1.5.4 Poljes

Poljes are by definition large, flat-floored, enclosed depressions in karst terrains [Ford & Williams 2007]. Ford and Williams (2007) define three elements after Gams 1978 that must be met for a depression to be classified as a polje:

1. flat floor in rock or in alluvium
2. closed basin with a steeply rising marginal slope at least on one side
3. karstic drainage

They vary strongly in size and thus this is not supposed to be a relevant parameter [Ford & Williams 2007]. Poljes can be subdivided into border poljes that develop where soluble and impermeable bedrock meet and structural poljes where tectonics forms depressions of soluble rocks that are filled with

less permeable rocks [Ford & Williams 2007].

In the study area, there are several small-scale depressions with a flat floor and underground drainage (Fig. 4.34). The area of the floor typically does not exceed 1 km² – to avoid the polje definition problems, henceforth they are called small-scale poljes or simplified to polje. There are two types of poljes here: one in glacial cirques and the other in synclines (Fig. 4.33). The poljes in glacial cirques occur at relatively high elevations and are usually close to being perfectly circular. For the polje near the Hohenfluhalpkopf mountain, an older terrace a few meters above the recent valley floor with paleoponors at the downhill side could be observed (Fig. 4.32). Those poljes can be classified as border poljes. The second polje type is located in syncline depressions; these have an elliptical shape. Ponors occur on both sides of the polje (uphill and downhill) (Fig. 4.32).

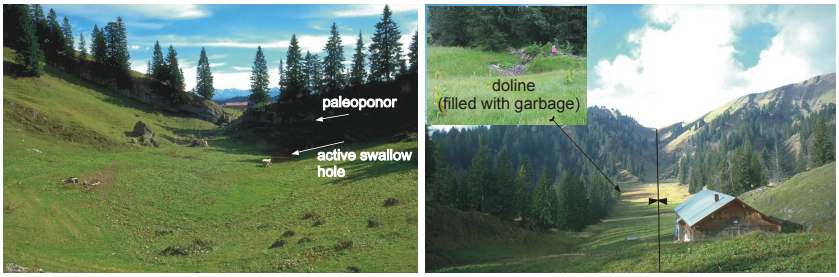

Fig. 4.32: Small-scale poljes in a glacial cirque (left) and in a syncline depression (right).

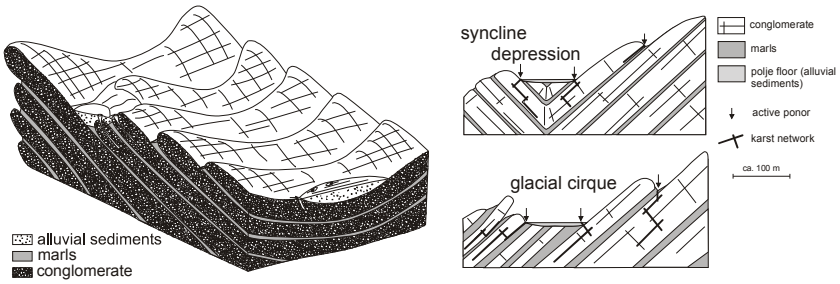

Fig. 4.33: Location (left) and structural control of poljes in a glacial cirque and in a syncline depression (right), modified after Göppert et al. 2003.

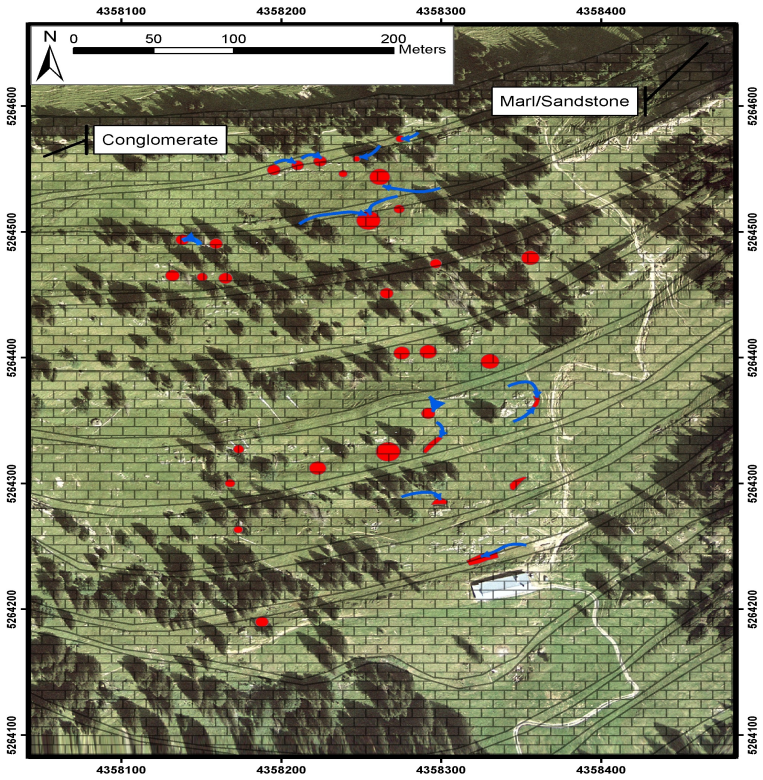

Fig. 4.34: Dolines (red) (with ponors), sinking streams (shown in blue) and geology at a relatively high elevation near the Rindalphorn mountain (aerial picture provided by: Land Surveying Office of Bavaria in Munich).

4.3.1.5.5 Karst springs, estavelles and surface waters

The Hochgrat-Gunzesried test site is located at the continental water divide between the Danube and Rhine. West of Scheidwang-Alpe are the Lecknertal Valley and Obergelchenwangtobel Valley, which drain towards Hittisau and the

Rhine, east of it is the Autal Valley, which drains towards Gunzesried and the Danube.

During the summer months, the Aubach Creek usually loses water towards the alluvial valley floor and dries up. After rainfall events, the Aubach Creek level rapidly rises and decreases again. Several glacial terrace levels have to be crossed by the Aubach Creek before it reaches the community of Gunzesried. At each step, conglomerates are exposed and water discharges either diffusively or at a small number of karst springs. When water reaches the alluvial sediments, it usually seeps into in the underground through diffuse inputs.

In the west, the Lecknerbach Creek tributes to a small semi-artificial lake (Lecknersee Lake) and the valley floor is covered by moraine material that prevents sinking. The relatively steep Obergelchenwangtobel Creek sinks and resurges several times at a small scale (in the range of tens of meters) due to the step-like pattern of the conglomerate layers (Fig. 4.35). Whenever it crosses a step in topography, it is very likely that a karst spring forms a tributary to the creek (Fig. 4.35) that loses water further downstream when the conglomerate bedding plane is intersected by fractures that are only lightly covered by alluvium or Quaternary deposits.

The inclined alternation of thick conglomerates and thin marls favors the formation of small creeks in the depressions where marls are exposed.

Several karst springs and two estavelles (Fig. 4.31, Fig. 4.36) show high water level fluctuations that are directly linked with hydrological conditions or stream water level. Two karst springs are used for the water supply of the community of Hittisau, and other karst springs are used for local water supply. None of the springs of the test site has been named before, so it was decided to name them in geographical terms.

The estavelles near the Lache mountain hut (Fig. 4.36) act as springs during high water levels and swallow holes during low water levels. When a stream sinks before it reaches the estavelle, a shaft with a diameter of approximately 30 cm blocked by rocks can often be directly observed. Several springs show cave-like entrances (Fig. 4.37), and one karst spring actually discharges through a small cave-like entrance area (Fig. 4.35). Further inspection by speleologists can be recommended!

The discharge is usually rather moderate (about 10 L/s during low flow conditions) and varies strongly. During periods without rainfall they can dry up, and after storm rainfall discharge increases rapidly. The discharge of the karst spring near the Lache mountain hut (Fig. 4.37) was measured after storm rainfall and found to be 415 L/s.

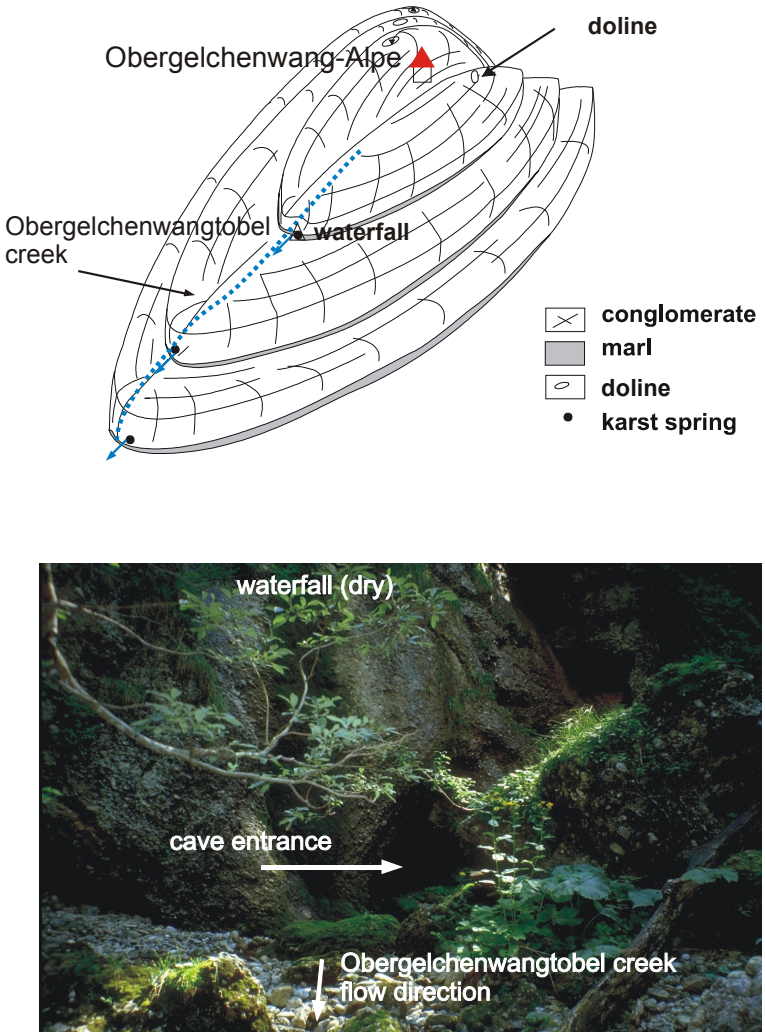

Fig. 4.35: Sketch of the Obergelchenwangtobel Creek with karst springs and dolines (above) and photograph of the karst spring that is located below a waterfall (below).

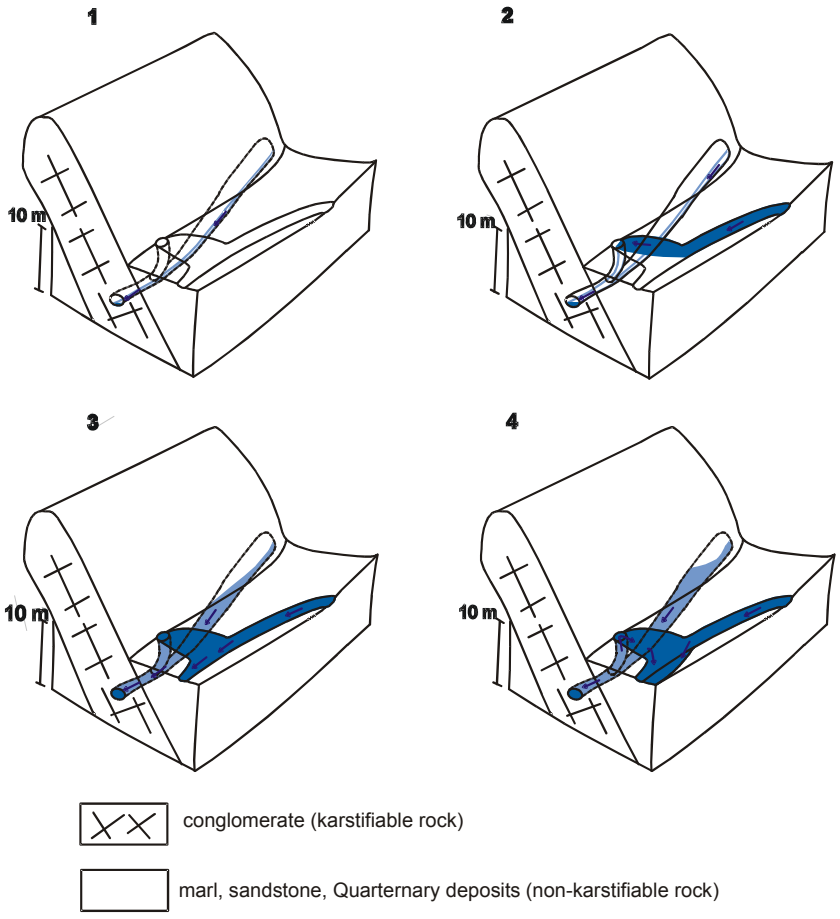

Fig. 4.36: Functionality of the estavelle (No. I) nearby the Lache-Alp. 1: no discharge of the adjacent creek, 2: creek sinks completely into the estavelle which acts as swallow hole, 3: karst water level rises and creek overflows the estavelle, 4: karst water level rises even more so that estavelle acts as spring.

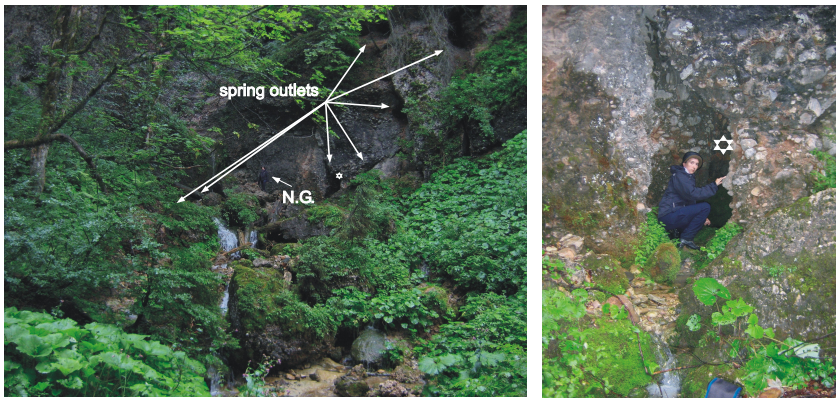

Fig. 4.37: Karst springs with several outlets near the Lache mountain hut at low flow conditions (total discharge: 16 L/s). Higher elevated spring outlets are only active when the water level rises (left), cave-like karst spring (right – detail of left photo, please note the star for orientation). Photograph: Ingo Göppert.

4.3.1.6 Hydrochemistry

All springs located in the test site were characterized hydrogeologically and sampled for hydrochemistry analysis at least once. The hydrochemical water quality meets the demands of the drinking water ordinance, whereas the microbial water quality is not satisfying.

Bicarbonate is the dominant anion for all spring waters (164 - 253 mg/L) and calcium (43 - 76 mg/L) the dominate cation (Fig. 4.38). Magnesium occurs as well, which reflects the limestone-dolomite-composition of the conglomerates. The contents of chloride, sulfate, phosphate, nitrate, silicon, potassium and sodium are all below 8 mg/L.

The bicarbonate water showed no significant variation in its composition in the test site. The different samplings do not show a time-dependent variation of the hydrochemical composition. This might be an effect of the small number of sampling campaigns.

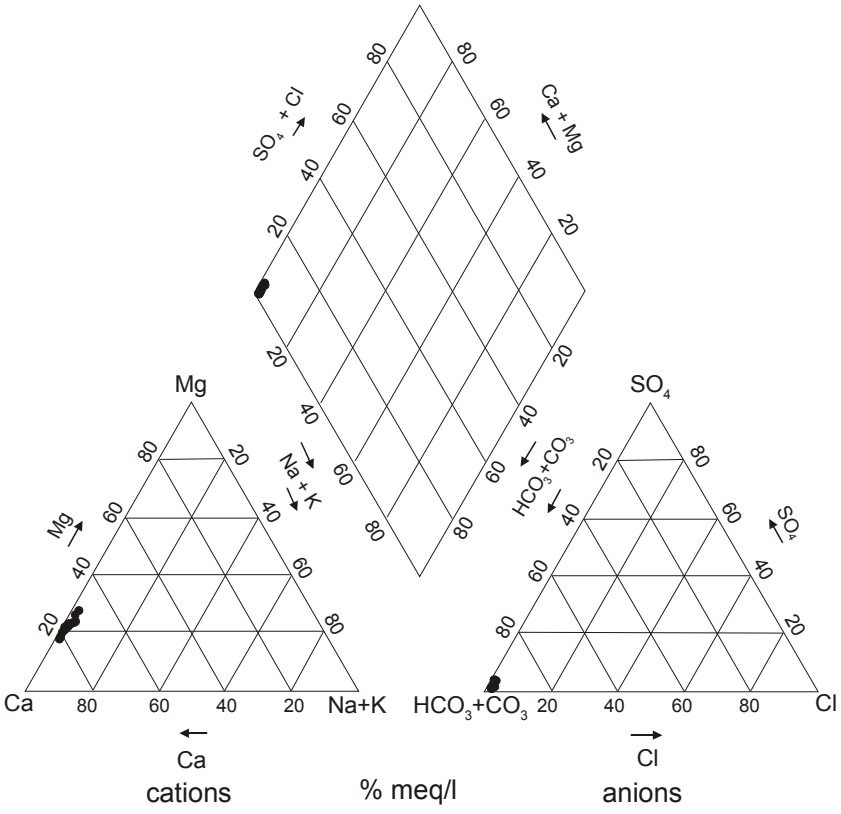

Fig. 4.38: Piper diagram of all spring waters.

4.3.1.7 Microbial drinking water quality

In total, 28 springs were tested in summer 2003 within a hydrogeological sampling reference day. 16 springs were additionally tested in fall and 13 springs in winter (depending on the accessibility of springs). Spring water was tested for faecal indicator bacteria, including coliform bacteria, *Escherichia coli*, colony counts (22°C and 37°C) and enterococci. The limits of the drinking water ordinance are given in Tab. 4.16. The analysis followed certified

standards (Tab. 4.16) and was done by the Environmental Institute of the State of Vorarlberg and the Chemical Laboratory Dr. K. Fässler.

Tab. 4.16: German limits for the microbial parameters tested in this study according to DVGW 2001 and applied analytical methods.

	limit	analytical method
coliform bacteria	not detectable in 100 mL	EN ISO 9308-1
Escherichia coli	not detectable in 100 mL	membrane filtration, Fluorocult ECD Agar
colony counts at 22°C	100 / mL	EN ISO 6222
colony counts at 37°C	100 / mL	EN ISO 6222
enterococci	not detectable in 100 mL	EN ISO 7899-2

None of the sampled spring waters meets the demands of the drinking water ordinance in terms of microbial quality (Fig. 4.39). All springs, especially the karst springs, were found to be highly contaminated, even with enterococci. It is noteworthy that *E. coli* and enterococci are of high sanitary significance, whereas the others (coliforms and colony forming units) are of medium to low sanitary significance, although these can be indicative of other pathogens that were not directly measured.

The number of bacteria differs depending on land-use activities in the recharge area. At higher elevations, cattle are brought down earlier in the year and thus microbial contamination is lower in winter than in fall. Karst springs at lower elevations show comparable results. The karst springs whose recharge area was occupied by cattle for a shorter time interval show a significantly lower microbial contamination in winter. Karst springs near a pasture that is used longer show a higher concentration in winter. Although land use activities end at the end of summer when cattle are brought down from the mountain pastures into the valley, microbial contamination can still persist.

The karst spring near Au-Alp forms a swampy outlet area where a conglomerate layer plunges into impermeable Quaternary sediments. This spring shows higher microbial contamination in winter. The area was used much longer due to the low elevation.

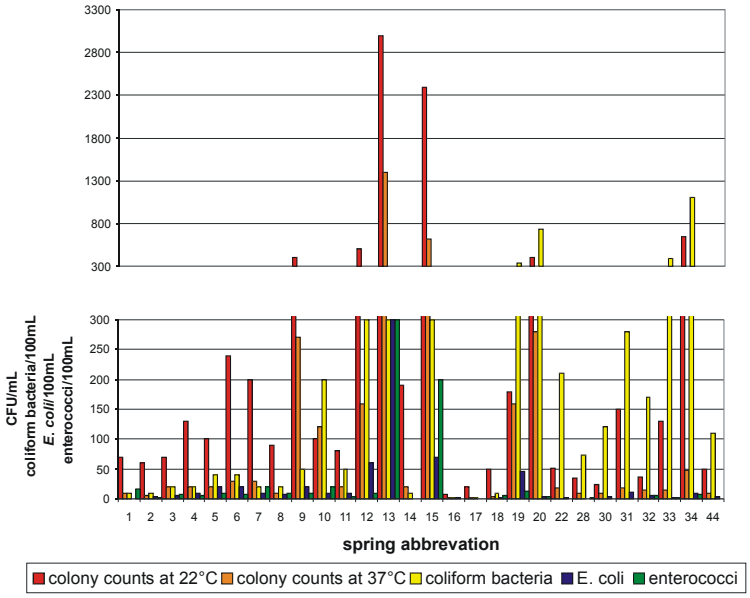

Fig. 4.39: Comparison of the summer microbial spring water quality, modified from Göppert & Hötzl 2006.

4.3.1.8 Tracer tests

4.3.1.8.1 General overview

Two multi-tracer tests were carried out during high flow conditions (Fig. 4.40). The goal of the first tracer test was to understand the general hydrogeology of this system and to characterize the solute flow behavior based on new, detailed lithological mapping of the western part of the test site that is orientated towards the Rhine. The second tracer test was built upon the first tracer test findings and carried out in the eastern part of the area that flows towards the Danube. Within the second tracer test, solutes and particles were injected together.

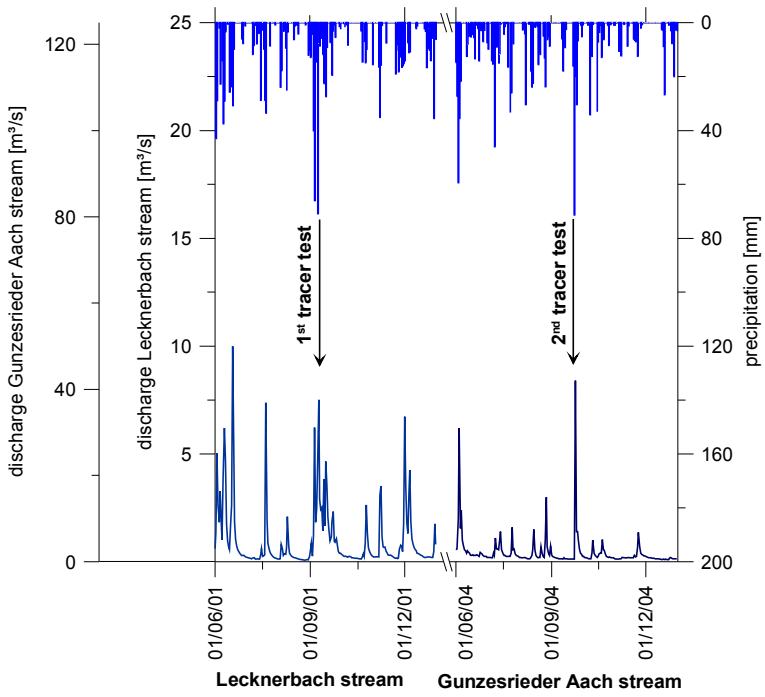

Fig. 4.40: Flow conditions of the two tracer tests in the Lecknertal Valley and precipitation recorded in Hittisau (data: Amt der Vorarlberger Landesregierung).

A geographical overview of all the injection and sampling points (water samples and charcoal dye receptors) is given in Fig. 4.41.

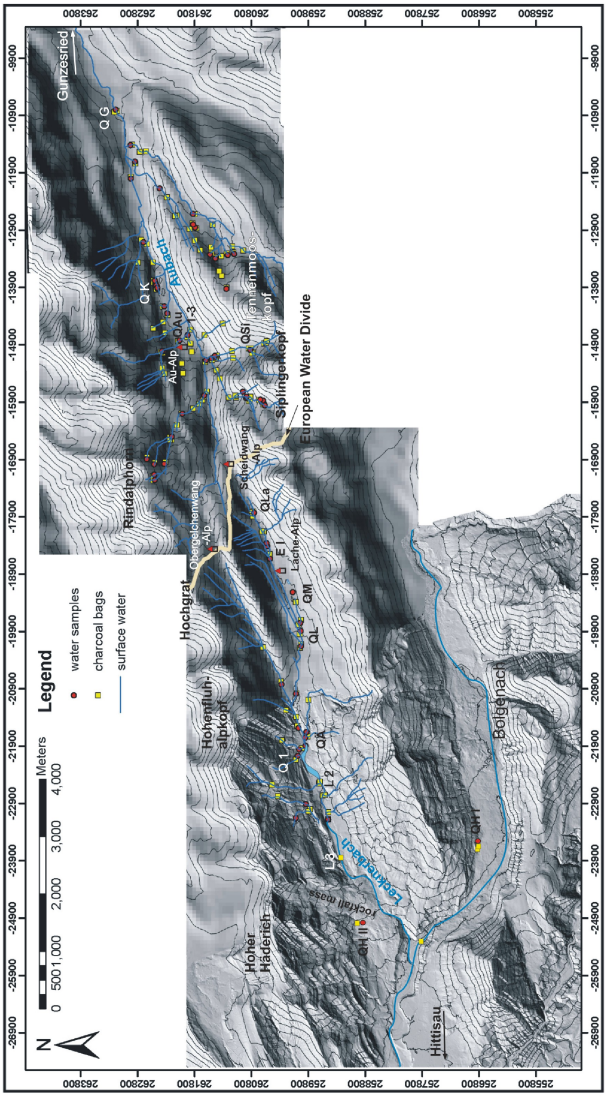

Fig. 4.41: Location of the sampling points for the two tracer tests.

4.3.1.8.2 Tracer test in the western part

The tracer test in the western part of the area (Rhine catchment area) was carried out under high flow conditions (Fig. 4.40). An overview over the tested area is given in Fig. 4.42 and results are shown in a terrain model (Fig. 4.44).

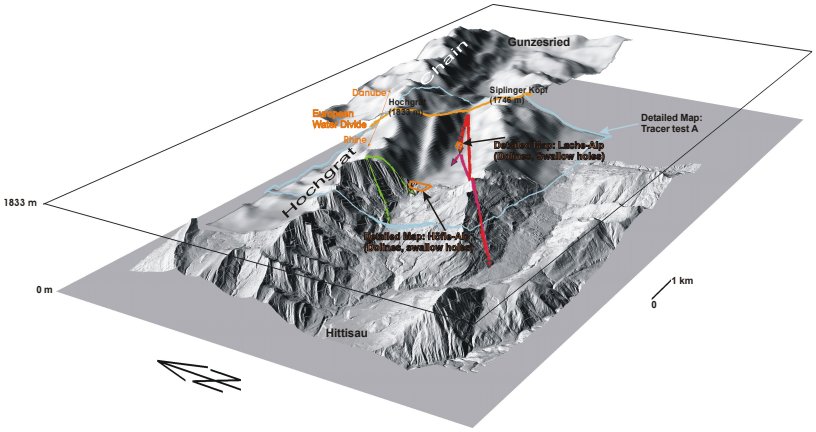

Fig. 4.42: Terrain model of the study area of the first tracer tests in the Rhine catchment area of the Hochgrat-Gunzesried test site (data: Land Surveying Offices Feldkirch, Austria & Munich, Germany).

The first tracer test was focused on the main transport characteristic. No data from comparable test sites in carbonate conglomerates was available, so flow parameters that were used for planning the tracer test and sampling intervals were based on general assumptions.

There are three injection points in dolines, and all tracers were injected into active swallow holes.

The first injection point (I 1) was an active swallow hole in a doline that lays

in still water sediments that are near a plunging conglomerate layer (Fig. 4.43) 250 meters west of the European Water Divide at an altitude of 1330 meters near Scheidwang-Alp. The flow rate of the sinking stream at the time of injection was about 5 L/s. 2 kg eosin were injected to tag the water flow along the strike of the strata. The longest possible connection between this injection point and the sampling point (in this case the QHI Spring used for the water supply of Hittisau) was 7.7 km.

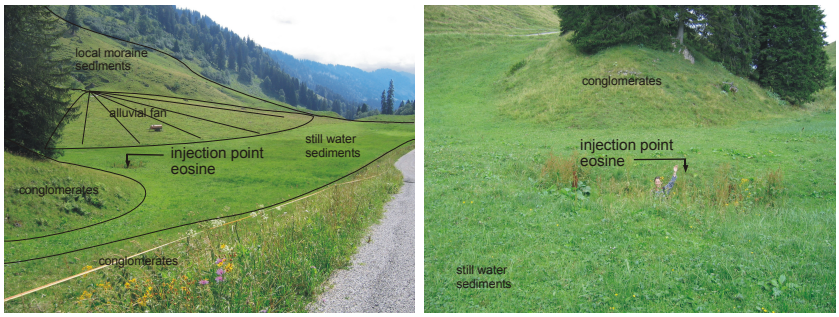

Fig. 4.43: Injection point of eosin in the first tracer test near Schweidwang-Alp in an active swallow hole (overview left, details right).

In the second injection (I 2), 0.5 kg sulforhodamine b was injected into a doline further downhill, near Lache-Alp to label a shorter distance along the valley. The third injection point (I 3) was directly beneath the Hochgrat-chain rim, near the Hohenfluhalpkopf mountain. 1 kg uranine was injected into a doline with a ponor that drains into a vertical shaft of at least 14 meters in depth. The flow rate of the sinking stream was about 5 L/s for both cases.

The uranine was intended to mark flow across the strike of the conglomerate intercalation, possibly along fractures or faults.

16 sampling points were observed by water samples and additionally 10 of them were monitored using charcoal bags. 30 additional observation points were equipped with charcoal bags. The entire sampling period lasted about 50 days. 324 water samples and 104 charcoal bags were analyzed by spectrofluorometry (Perkin Elmer, LS 50 B).

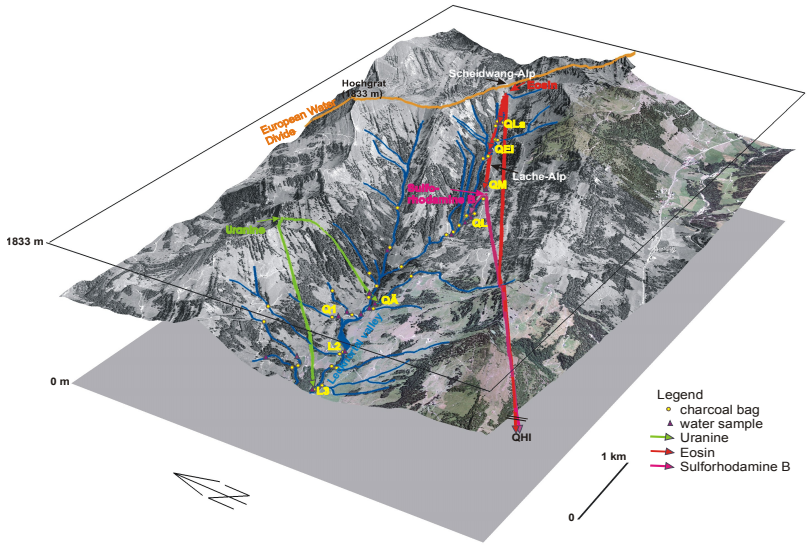

Fig. 4.44: Sampling and injection points and results of the first tracer test in a terrain model (data: Land Surveying Offices Feldkirch, Austria & Munich, Germany).

All three tracers were detected at various sampling points in either water samples or charcoal bags. A selection of the sampling points with the highest measured concentrations is given in Tab. 4.17.

The tracers eosin and sulforhodamine b (SRB) actually proved water flow along the strike of the strata up to a length of 7.7 km (for eosin), even a mountain was crossed subterraneously (Fig. 4.44). The most distant sampling point was the drinking water spring of the community Hittisau, a karst spring on the opposite side of the next mountain chain. Thus, the catchment area of this spring was proven to extend up to the injection point near the European Water Divide (EWD) that should be included in a groundwater protection area. The second tracer SRB reached this spring in concentrations below the detection limit in water, but was detected in charcoal due to the cumulative effect of dye adsorbing onto charcoal.

SRB was detected after 4.8 h for the first time in the Langentobel Stream

where it infiltrated diffusely through several karst fissures at the bottom of the stream; a single fissure or drowned spring could not be detected – however, a 20-meter-wide exfiltration area was detected using charcoal bags.

The tracer eosin was later detected additionally at the estavelle E I (Fig. 4.45) - FDT: 48.2 h - and at a spring further down the valley (Q M) – FDT: 21.9 h. The recovery rate for those (Q EI and Q M) was below 1%, which indicates that the uppermost outlet (Q La) with almost 95% recovery is the main spring outlet where the tracer occurs first and in higher concentrations. Spring discharges for these springs could only be estimated and not directly measured due to heavy weather conditions, so the values have to be considered with care.

Tab. 4.17: Selected results from the first tracer test.

injection point **sampling point**	**I 1 (eosin)** **QLa**	**I 2 (SRB)** **QL**	**I 3 (uranine)** **QÄ**
t_1 [h]	3.0	4.8	121
t_{peak} [h]	5.0	4.8	361.6
c_{peak} [µg/L]	3961.80	42.55	0.17
v_{max} [m/h]	286	62.5	38.8

Uranine was detected in four sampling points at the southern foot of the mountain chain. The overall concentration as well as flow velocities are significantly lower across the strata. At the sampling point Q HS, the tracer occurs after 49 h for the first time, at the sampling locations Q 1 and L 2 after 120 h (5 days) and at Q Ä (Fig. 4.46) the tracer occurred after 361 h (15 days) for the first time. Peaks are always very narrow (Fig. 4.46), but show significant tracer responses in the charcoal bags.

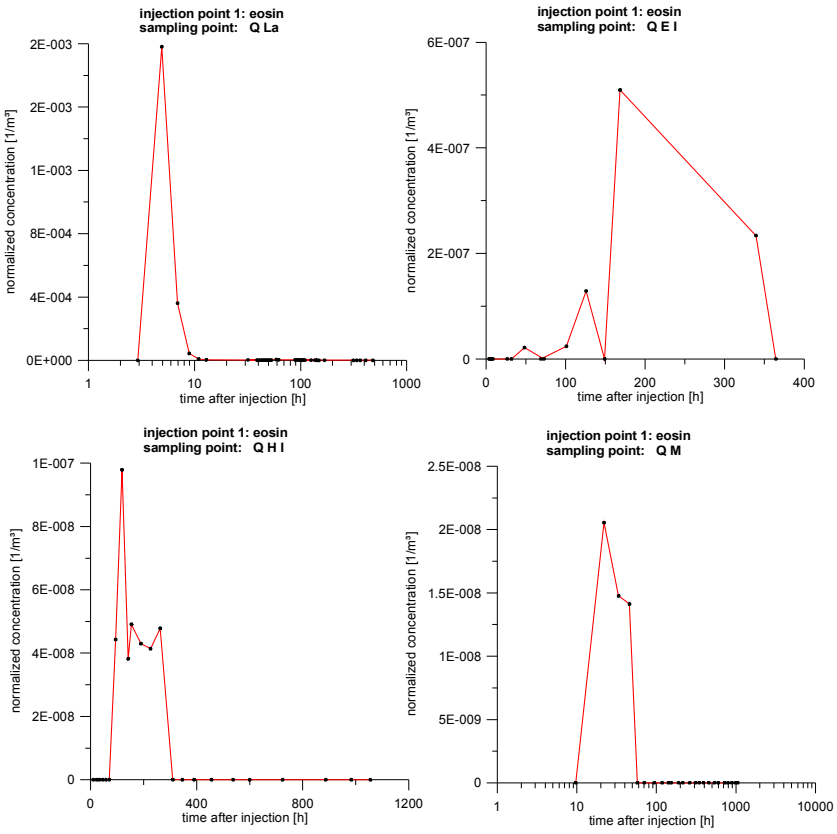

Fig. 4.45: TBCs of eosin for selected sampling points (please note the different time and concentration axes).

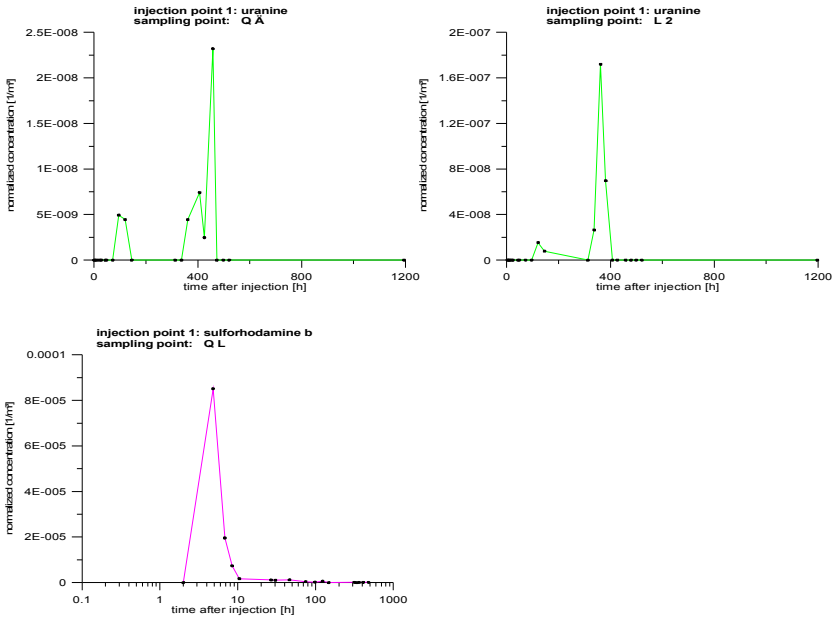

Fig. 4.46: TBCs of uranine and sulforhodamine b (please note different axis scales).

The TBCs (Fig. 4.45, Fig. 4.46) usually show a very narrow peak with a steeply rising and falling limb. This is a result of the very high flow velocities (Tab. 4.17). Although the sampling interval was adjusted during the tracer test (i.e. shortened), a detailed TBC could not be obtained because of the high flow velocities. Due to the spikiness of the TBC, modeling approaches tend to fail, and even the ADM in most cases leads to erroneous results, which can be reported from other karst test sites with comparable flow velocities and shape of TBCs as well [Goldscheider 2002]. Therefore only one TBC, from the Q La Spring, provides adequate modeling results with an ADM and 2RNE (Tab. 4.18).

Tab. 4.18: ADM and 2RNE results for the Q La sampling point and the tracer eosin.

		ADM					
		v [m/h]	**D_L** [m²/h]	**α** [m]			**R²**
eosin	Q La	140.3	54.1	0.386			0.9660
		2RNE					
		v [m/h]	**D_L** [m²/h]	**α** [m]	**β**	**ω**	**R²**
eosin	Q La	136.2	0.6	0.004	0.821	2.475	0.9998

The modeling results for the karst spring group near Lache-Alp (Fig. 4.37) show a high proportion of mobile water (Tab. 4.18), high flow velocities and a relatively low dispersion due to the narrow TBC. The results can be compared to those of classical karst areas [Goldscheider 2002, Ford & Williams 2007].

4.3.1.8.3 Tracer test in the eastern part

Based on the results of the first tracer test, a second multi-tracer test in the Danube catchment area east of Scheidwang-Alp was carried out with solutes and particles as well. Due to rapid flow velocities of the first test and the direct connections between injection and sampling points, the amount of tracer was reduced for the second test. An overview of the tested area is shown in Fig. 4.47.

The second tracer test included 4 injections. Two injections involved solutes and particle tracers, two injection points only solute tracers. The second tracer test had the following main goals:

- The results of the first test were to be verified for a larger area and a different catchment area in comparable tectonical and geological composition.
- Additional tectonical settings were to be tested to find out their role for underground drainage.

- The behavior of solutes and particles was to be compared and consequences for groundwater protection pointed out.

Thus, like in the first experiment, an injection point in a glacial cirque (at relatively high altitude) was used to test the underground drainage along the strike of the strata and across it (I 4) (Fig. 4.48, Fig. 4.49, Fig. 4.51). In the glacial cirque north of the Siplinger Kopf mountain 223 g of eosin and 4.32×10^{11} 1 µm spheres were injected into a sinking stream with a flow rate of 5 L/s. It drains the adjacent cirque and directly sinks into open karst fissures that are several decimeters wide.

At a comparable elevation (but not in a glacial cirque) 300 g of pyranine (I 5) were injected (Fig. 4.49) to label the water flow along the strike of the strata along the same mountain chain (Fig. 4.50) which lies south of the Hochgrat-chain. The tracer was injected into a sinking stream (flow rate: 10 L/s) that drains into a doline with a diameter of more than 20 meters and a depth of more than 20 meters.

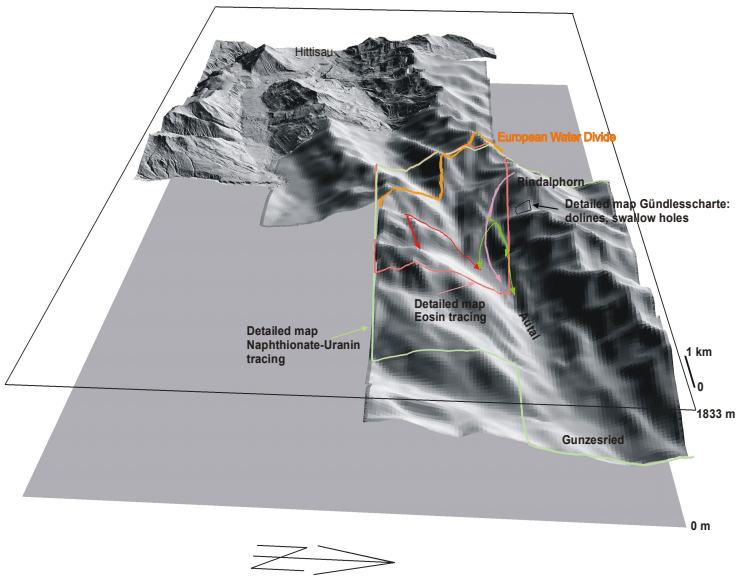

Fig. 4.47: Overview of the topography of the second multi-tracer test (data: Land Surveying Offices Feldkirch, Austria & Munich, Germany).

In a doline south of the Rindalphorn mountain (I 6) (Fig. 4.50) (east of Hochgrat) 3 kg of sodium-naphthionate were injected into a stream that had a sinking rate of 4 L/s. This injection point is in a comparable position with the injection point of uranine in the first test.

To trace the drainage of a syncline (Fig. 4.48, Fig. 4.50) 150 g of uranine and 4.55×10^{11} 1µm spheres were injected into a sinking stream (sinking rate: 6 L/s) that drains the area north of Rote Wand.

Fig. 4.48 gives an overview over the hydrogeological setting of the injection points I 4 in a glacial cirque and I 7 in a syncline of the second tracer test.

At 43 locations water samples were taken and charcoal bags installed. An additional 50 locations were equipped with charcoal bags, mainly in streams or creeks, in order to set limits for possible diffusive outlets. In total 459 water samples were analyzed for fluorescent dyes and 130 water samples for microspheres. 83 charcoal bags were analyzed for fluorescent dyes (some got lost because of the heavy weather conditions and flooding).

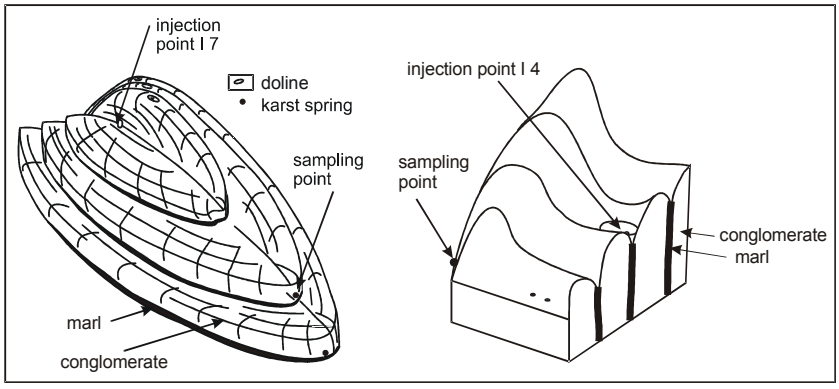

Fig. 4.48: Block diagram of the hydrogeological setting of the two injection points in a syncline (left) and glacial cirque (right).

With this tracer test two main flow directions were detected. The underground connection between injection point I 4 (Siplinger Kopf) and the karst spring group Q Si (Fig. 4.54, Fig. 4.56) was traced with eosin and 1 µm spheres (red) (Fig. 4.51) and followed the strike of the strata and crossed underground the northern foothills of the Siplinger Kopf mountain. At low concentrations eosin traveled across the strata and reached a karst spring at

valley floor elevation (Q A1) (Fig. 4.56).

The second main flow path between injection point I 7 and the karst springs near Au-Alp (Q Au) was marked with uranine and 1 µm spheres (yellow-green) (Fig. 4.50, Fig. 4.52, Fig. 4.54, Fig. 4.55). It follows the syncline axis. It is noteworthy that the tracers were injected into a swallow hole that lies west of the fold axis culmination (Fig. 4.49). The proven main connection between I 7 and Q Au indicates that water flow had to cross underground the culmination to reach the Q Au Springs. Little flow divergence occurs in a way that with a delay of 2.1 hours uranine was also detected in a smaller karst spring west of the culmination (Q RW) and with a delay of 59.1 hours (Fig. 4.53) in a karst spring that is located south of the syncline where also eosin could be detected in low concentrations (Q A1). 1 µm spheres were detected 8.1 hours later at the karst spring group Q K.

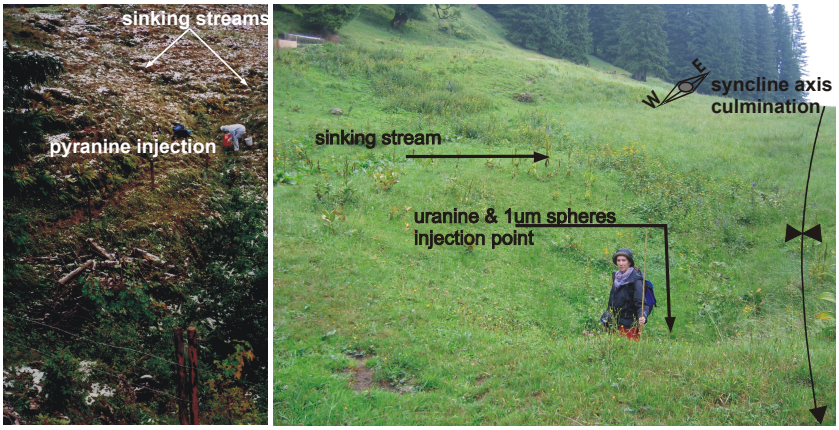

Fig. 4.49: Injection of pyranine into a sinking stream (left) north of Tennenmooskopf mountain and injection point of uranine and 1 µm spheres in a plunging syncline (right, photo not taken during test).

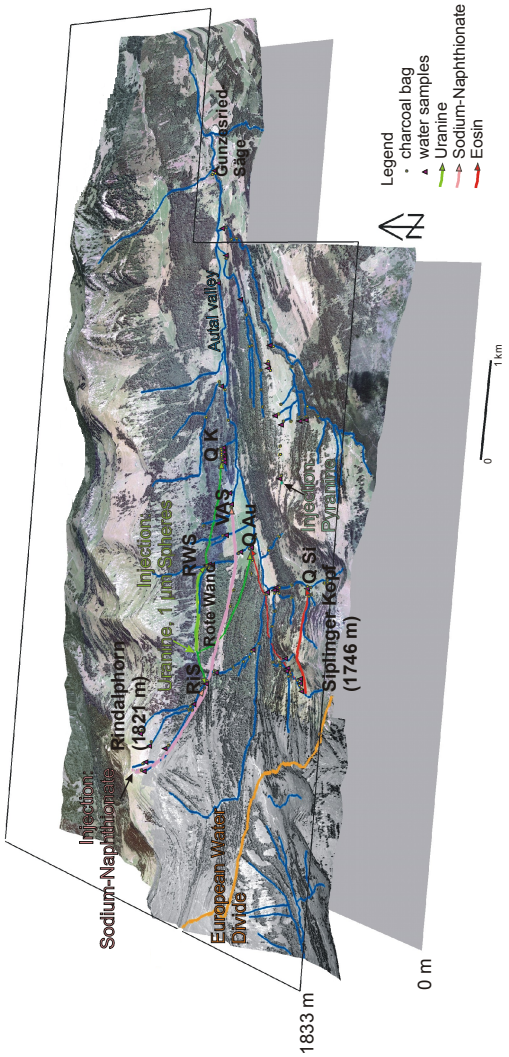

Fig. 4.50: Location of the second tracer test (sampling points, injection points, proven connections) (aerial pictures and elevation data: Land Surveying Offices Feldkirch, Austria & Munich, Germany).

Additional minor flow paths were detected with sodium-naphthionate. Indeed, none of the water samples contained sodium-naphthionate, but it was analyzed in charcoal of in total six independent sampling points (BRW, QVA 1-2, QK 1-3) (Fig. 4.54). With charcoal bags, only the time interval in which tracer occurred can be defined. All naphthionate detections for all six sampling points are found in charcoal bags that cover the time interval from 7 days up to 14 days after injection.

Pyranine could not be detected at any of the sampling points (Fig. 4.54), in water samples or in charcoal bags although all adjacent rivers or stream were sampled or equipped with charcoal – charcoal bags were subsequently renewed for a period over more than two months. So it can be assumed that pyranine might have been degraded as an effect of microbial activity. A similar behavior for pyranine was reported from karst tracer tests in the thermal water system of Stuttgart, where 140 kg of pyranine disappeared [Goldscheider et al. 2001].

The maximum flow velocities of 185 m/h (eosin) and 190 m/h (uranine), respectively, are relatively high (Tab. 4.19) and are a sign of a well developed karst system. The maximum flow velocities of the simultaneously injected microspheres are lower (146 m/h and 114 m/h) (Tab. 4.19). The differences of particles and solutes in the FDT might be overestimated due to the (possibly too large) sampling interval.

The maximum concentrations occur at a similar time (Tab. 4.19), so no preceding peak of microspheres was observed for both particle tracings.

It is noteworthy that the uranine flow divergence can not be observed for the simultaneously injected microspheres that travel only the fastest flow path to the karst springs Q K1-3 where in turn uranine could not be observed. Similar behavior can be observed for the eosin and the simultaneously injected microspheres. The microspheres travel along with the eosin the fastest flow path and cannot be observed across the strike of the strata (Q M).

Due to the spikiness of the TBC, only uranine microsphere results of Q Au and eosin and microspheres of Q Si were modeled with more advanced analytical approaches (CXTFIT – ADM & 2RNE), which provided generally a relatively good fit quality (Tab. 4.20, Tab. 4.21, Fig. 4.57, Fig. 4.58, Fig. 4.59, Fig. 4.60).

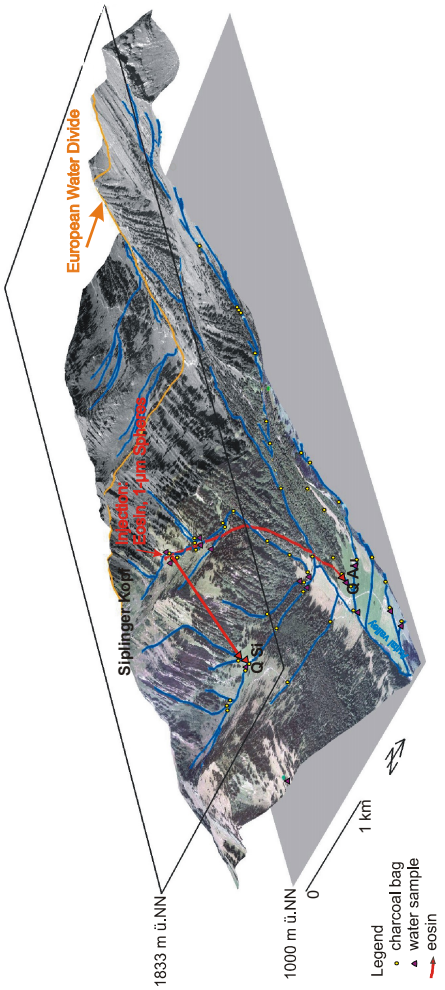

Fig. 4.51: Results of the eosin tracing (sampling points, injection points, proven connections) (aerial pictures and elevation data: Land Surveying Offices Feldkirch, Austria & Munich, Germany).

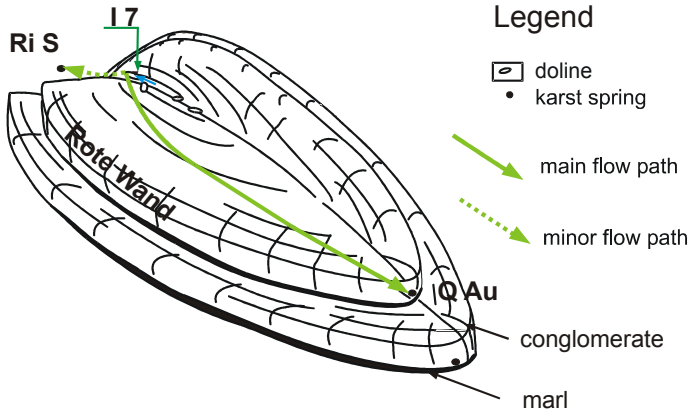

Fig. 4.52: Block diagram that explains the drainage of the syncline proven by uranine and 1 µm spheres.

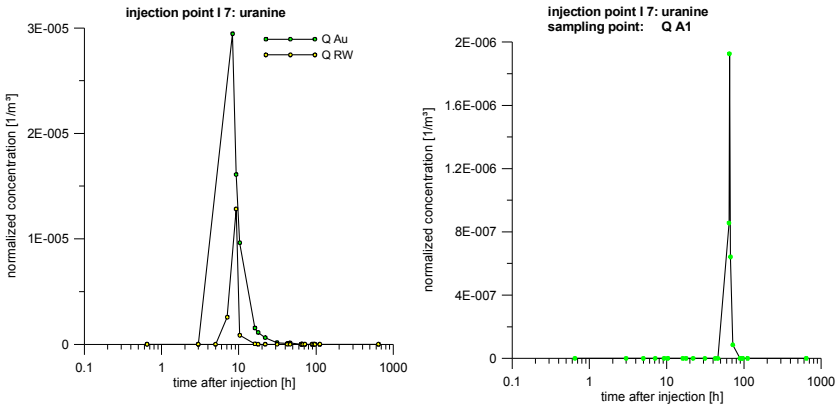

Fig. 4.53: TBCs of uranine for the sampling points Q Au, Q RW and Q A1.

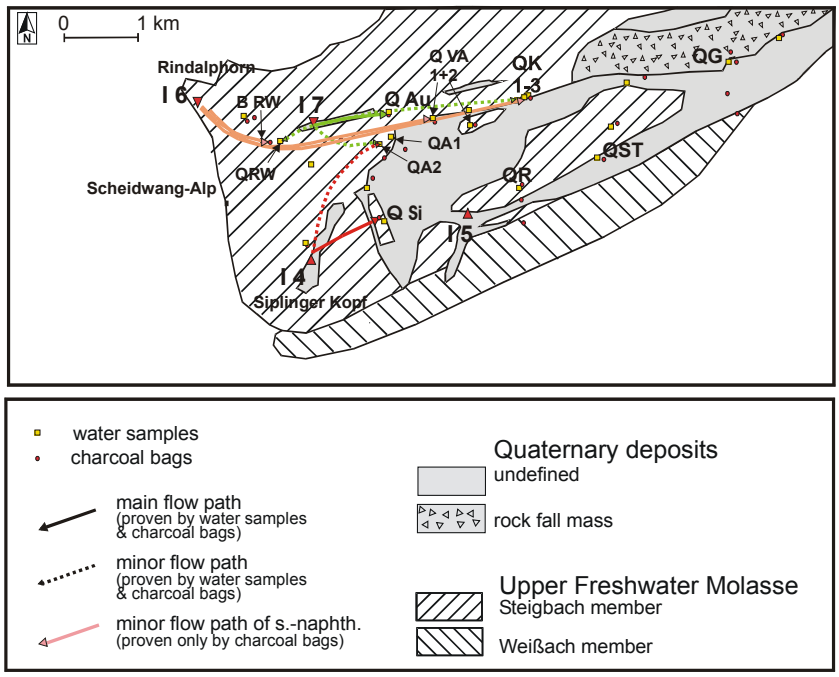

Fig. 4.54: Geology and tracer test results for all injections of the second tracer test in the Danube catchment area of the Hochgrat-Gunzesried test site.

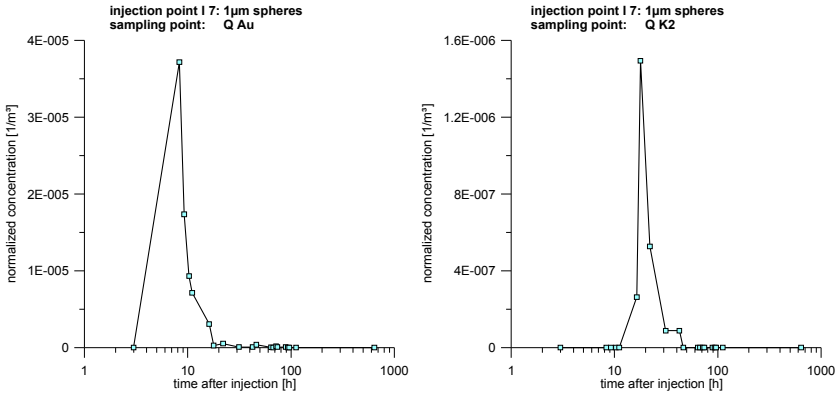

Fig. 4.55: TBCs of 1 µm spheres at the sampling locations Q Au and Q K2.

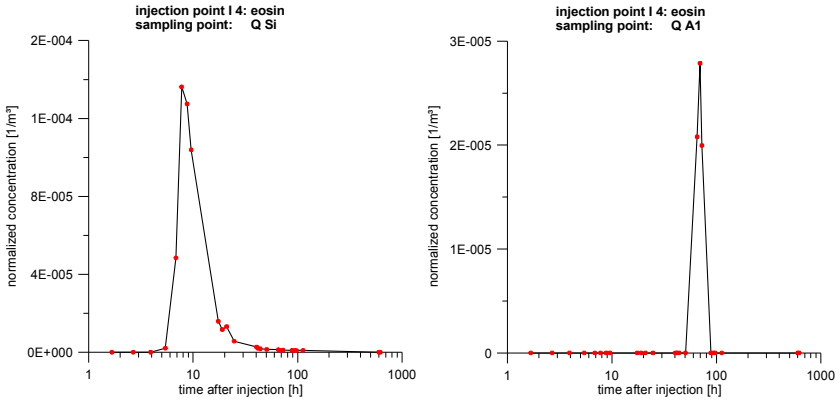

Fig. 4.56: TBCs of eosin for the sampling locations Q Si and Q A1.

Tab. 4.19: Results for spheres and solutes of injections 4 and 7.

injection point **sampling point** **tracer**	**I 4** **Q Si** **eosin**	**I 4** **Q Si** **1 µm spheres**	**I 7** **Q Au** **uranine**	**I 7** **Q Au** **1 µm spheres**
t_1 [h]	5.4	6.8	5.0	8.3
t_{peak} [h]	7.8	7.8	8.3	8.3
c_{peak} [n/100mL] [µg/L]	500	30.4	1690	4.4
v_{max} [m/h]	184.5	146.4	190.0	114.0

Tab. 4.20: ADM modeling results for eosin, uranine and spheres for the sampling points Q Si and Q Au and recovery calculated with fitted data.

	tracer	sampling point	**ADM**			
			v [m/h]	**DL** [m²/h]	**α** [m]	**R²**
I 4	eosin	Q Si	115.30	1282	11.119	0.9756
	1 µm spheres	Q Si	111.50	1987	17.821	0.9881
I 7	uranine	Q Au	123.80	1805	14.580	0.9852
	1 µm spheres	Q Au	148.00	4620	31.216	0.9832

Tab. 4.21: 2RNE modeling results of eosin, uranine and spheres of sampling points Q Si and Q Au.

tracer	sampling point	2RNE v [m/h]	D_L [m²/h]	α [m]	β	ω	R^2
I 4 eosin	Q Si	87.57	407.4	4.652	0.692	1.691	0.9979
1 µm spheres	Q Si	111.40	2009	18.034	0.999	0.950	0.9881
I 7 uranine	Q Au	106.90	669	6.258	0.814	0.722	0.9998
1 µm spheres	Q Au	143.40	2308	16.095	0.898	0.187	0.9984

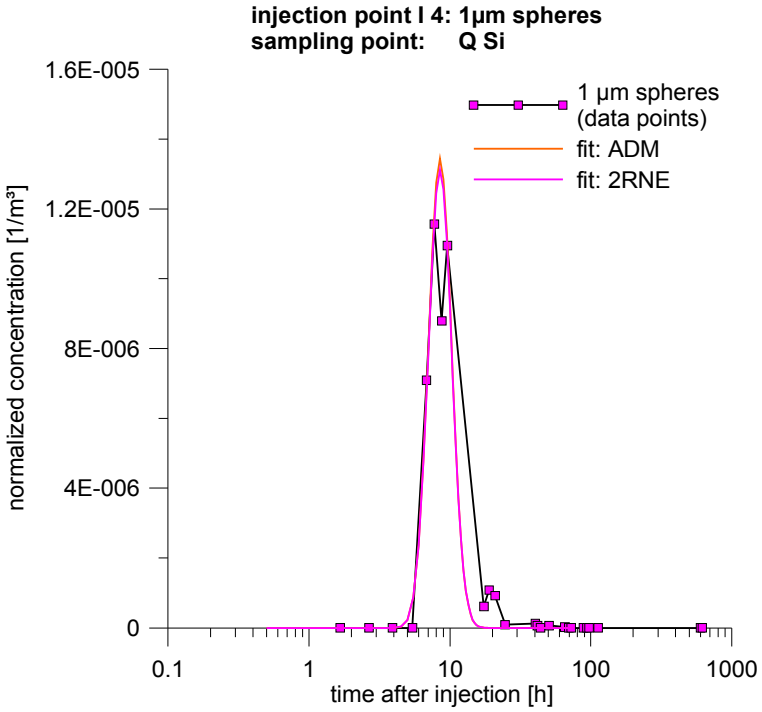

Fig. 4.57: Modeling results (ADM and 2RNE) for 1 µm spheres injected in I 4.

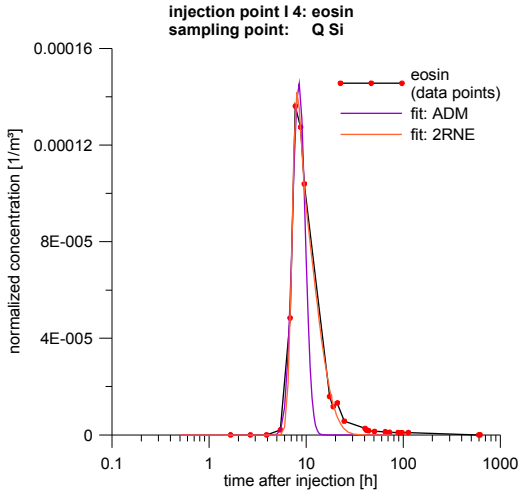

Fig. 4.58: Modeling results of eosin (I 4)

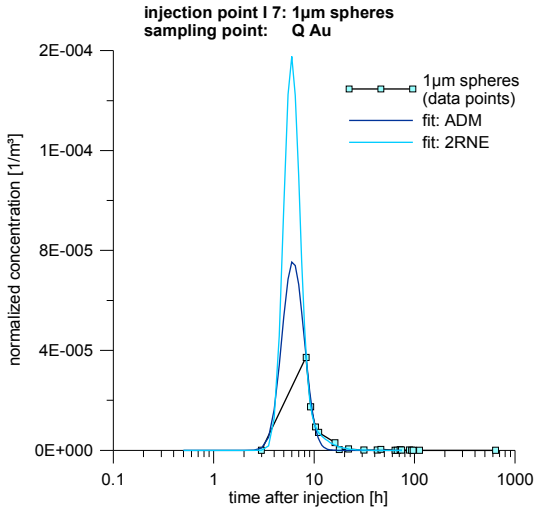

Fig. 4.59: Modeling results for 1 µm spheres injected in I 7.

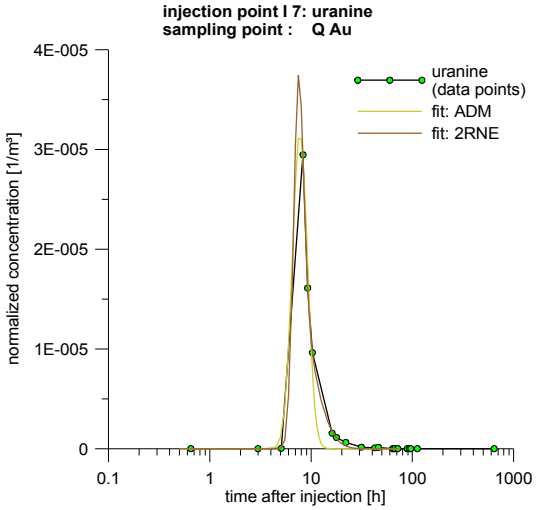

Fig. 4.60: Modeling results for uranine (I 7).

The modeling results of both applied methods (ADM and 2RNE) indicate a high mean flow velocity (Tab. 4.20, Tab. 4.21) for both solutes and particles. The calculated recovery shows for eosin and uranine that the sampling points Q Si respectively Q Au are not the only relevant outlet points of this system. The recovery for the 1 µm spheres injected in I 7 is higher than for the solute tracer, which argues for additional uranine outlet points (that indeed exist with Q RW and Q A1 where no microspheres have been observed).

The high partition coefficient β shows that there is a high proportion of mobile fluid, whereas the immobile fluid parts are negligible (Tab. 4.21). The proportion of mobile fluid for microspheres is larger than for the solutes and the tendency for exchange between the two fluid parts is larger for the solutes than for the particles.

A visual inspection of the TBCs and the modeled data show that both approaches (ADM and 2RNE) are not able to reproduce the curves appropriately, which is caused in large part by the spikiness of the TBCs (for both solutes and microspheres).

In the case of injection 4, both fits of both tracers underestimate the recovery significantly (Tab. 4.22) and reproduce the first detections and peak

times adequately, but the ADM does not match the falling limb of the curves (which causes the reduced recovery) and the 2RNE only for eosin. In all cases, they gave similar peak times for solutes and particles (Tab. 4.23).

Tab. 4.22: Comparison of calculated recovery rates based on observed and fitted data.

	tracer	sampling point	**R** basic data [%]	**R** ADM [%]	**R** 2RNE [%]
I 4	eosin	Q Si	77.9	27.91	49.39
	1 µm spheres	Q Si	5.16	3.31	3.26
I 7	uranine	Q Au	48.50	32.40	39.68
	1 µm spheres	Q Au	56.93	91.54	>100

For the injection 7, microspheres show a more spiky TBC such that the first detection is at the same time the maximum concentration, which may cause additional uncertainty. By applying the two fit approaches, the TBCs for the microspheres can be extended to times where no data exist – however this may yield more speculative results than for the previously mentioned microsphere modeling (I4). Both fits of the falling microsphere limb are quite good (Fig. 4.59) whereas the TBC extended to earlier times shows a higher peak concentration and therefore recovery increases for the microspheres (Tab. 4.23). The 2RNE yields an overestimation of the peak, which results in a recovery rate that exceeds 100%. Through extending the microspheres TBC to earlier times, the microsphere FDT and peak times are smaller for both approaches (ADM and 2RNE) than for uranine.

The fits for uranine (Fig. 4.60) show that the ADM is not able to fit the tailing of the curve whereas the 2RNE yields to more appropriate results and a good tailing fit. Thus, the recovery rate of the 2RNE model is higher (Tab. 4.22).

Both modeling approaches have to be considered with care, and for interpretation spreadsheet evaluation is given preference. According to this, microspheres are not preceding and thus no peak shift analysis (or filtration parameters) need to be calculated.

Tab. 4.23: Comparison of basic data and modeling results for t_1, t_{peak} and recovery for the sampling points Q Si and Q Au.

			I 4		I 7	
			eosine Q Si	1 µm spheres Q Si	uranine Q Au	1 µm spheres Q Au
	FDT	[h]	5.4	6.8	5.0	8.3
	t_{peak}	[h]	7.8	7.8	8.3	8.3
	R	[%]	77.72	5.16	48.50	56.93
ADM	**FDT**	[h]	2	1.5	1.5	1
	t_{peak}	[h]	8.5	8.5	7.5	6.5
	R	[%]	27.88	3.22	32.37	84.76
2RNE	**FDT**	[h]	1.5	4.5	6.0	2
	t_{peak}	[h]	8.5	8.5	11.5	6.5
	R	[%]	33.39	3.22	49.33	81.60

4.3.1.9 Discussion

The Hochgrat-Gunzesried test site offers a large number of surface karst landforms. It can clearly be classified as an area with landforms that are underlain by an aquifer with the hydrogeological characteristics of a classical karst area, which is proven by the hydrogeological investigations.

The results of the tracer tests show that the underground connections follow two main orientations: along the strike of the strata or fold axes and lateral thereto. The connection along the strike of the strata or fold axis is more direct; both flow velocities and concentrations are higher. Thus a potential contamination can easily enter the underground via swallow holes or sinking streams and is transported rapidly through the karst system. Lateral to the conglomerate-marl intercalation, the water flow is generally slower and concentrations are lower but transit times were also shorter than 50 days for this case.

As a result of the large number of potential infiltration possibilities (through active ponors etc.) and the small-scale heterogeneity, detailed mapping is

required in order to find appropriate groundwater protection areas.

Both tracer tests were carried out under high-flow conditions, so the determined flow velocities represent maximum values. For middle or low water conditions, smaller flow velocities can be expected, which does not necessarily mean lower concentrations of contaminants (low water conditions may mean a lower dilution and thus a higher concentration). Under such flow conditions, particles are shown not to precede the solutes. A behavior which can also be reported for high flow conditions for another karst test site (see 4.3.2 Hölloch: cave system). Flow velocities are so fast that both substances travel nearly equally fast, even peak times of the particles and solutes are similar. There is a high proportion of mobile water, which results in a generally higher recovery of particles. For low water conditions a more distinct difference between particles and solutes can be expected.

By applying different tracers, diverse flow paths can be traced. Solute tracers show a greater tendency for flow divergence than particle tracers do. In turn, particle tracers tagged a longer flow distance. This is not necessarily an effect of the lower detection limit of particles. It can be also explained by the stronger tendency of particles in traveling along the fastest flow path whereas the solute tracers show higher dispersion.

All sampled springs are highly microbiologically contaminated and do not meet the demands of the drinking water ordinance. Appropriate protection areas are highly desirable.

4.3.2 Hölloch: cave system

4.3.2.1 Introduction

The Hölloch cave system in the German-Austrian Alps (Fig. 4.61, Fig. 4.62) belongs to one of the most sensational karst landscapes in the Alps. The Hölloch cave has a surveyed length of 9343 meters and is part of the Hochifen-Gottesacker karst system which developed in folded Cretaceous sedimentary rocks. It is to date Germany's longest cave. The natural cave entrance is a vertical shaft of 80 meters in height. A secondary cave entrance has been built by speleologists in order to be able to access the cave independently from weather conditions and to avoid several siphons [Stautz & Wolf 2006]. Most cave parts belong to Germany, whereas the only relevant outlet, the Sägebach Spring, is part of the Austrian Kleinwalsertal Valley. At this date, the cave is not open to the public.

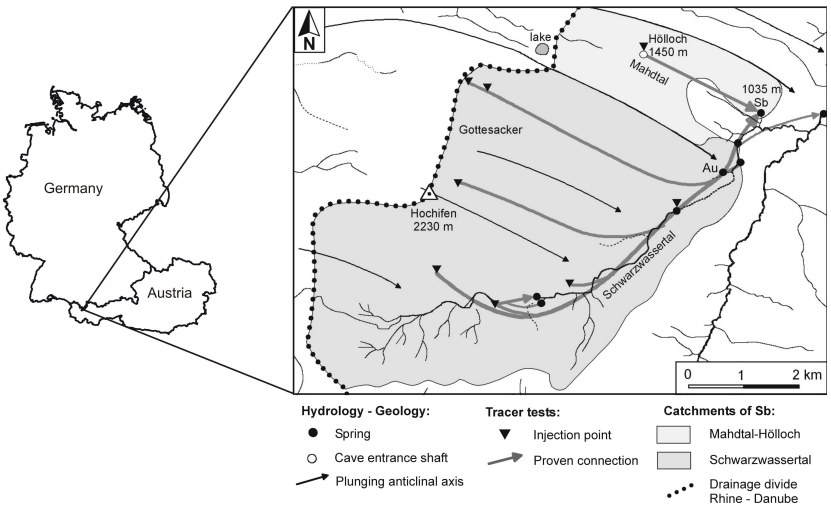

Fig. 4.61: Location and hydrogeological map of the Hölloch test site [Göppert & Goldscheider (accepted)].

4.3.2.2 Goals

The Hochifen-Gottesacker area has been subject to hydrogeological investigation since 1996 [Goldscheider 1998, Goldscheider 2002, Goldscheider 2005, Goldscheider & Göppert 2006]. Thus detailed geological maps and hydrogeological concepts already exist for large parts of the Hochifen-Gottesacker area. However, the Hölloch cave system has not been investigated using modern hydrogeological tools. The main goals for the Hölloch cave system investigation are the following:

- Verification of the general flow system and transport parameters.
- Spring hydrograph analysis with respect to particle transport.
- Comparison of particle and solute tracers at different flow conditions.
- Testing of different analytical modeling tools for both tracer types.

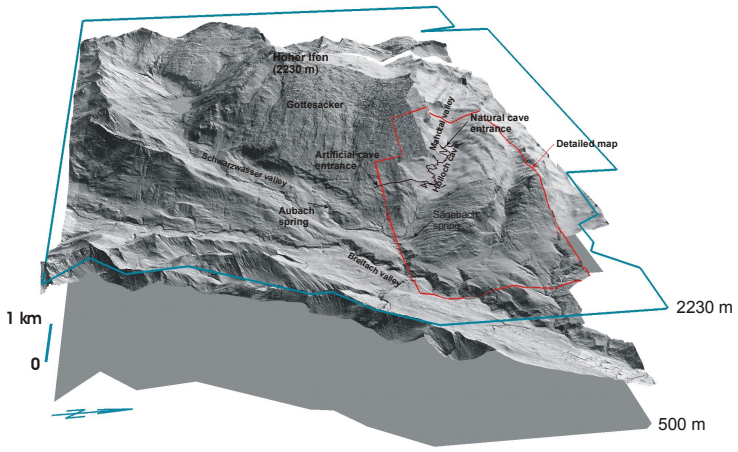

Fig. 4.62: Block diagram of the test site with the Hochifen-Gottesacker karst system and the Hölloch cave (projected onto land surface) (data: Land Surveying Offices Feldkirch, Austria & Munich, Germany).

4.3.2.3 Hydrology

The nearby weather station in the community of Baad (Kleinwalsertal, Austria) is located at an altitude of 1305 meters. The mean annual precipitation is 2158 mm with a major maximum in summer (Fig. 4.63). The mean annual air temperature for Baad is 5.6°C.

Fig. 4.62 gives an overview over the area and shows the location of the Hölloch cave and a nearby karst spring (Aubach Spring), which is equipped with data loggers for water level, electrical conductivity, temperature and turbidity.

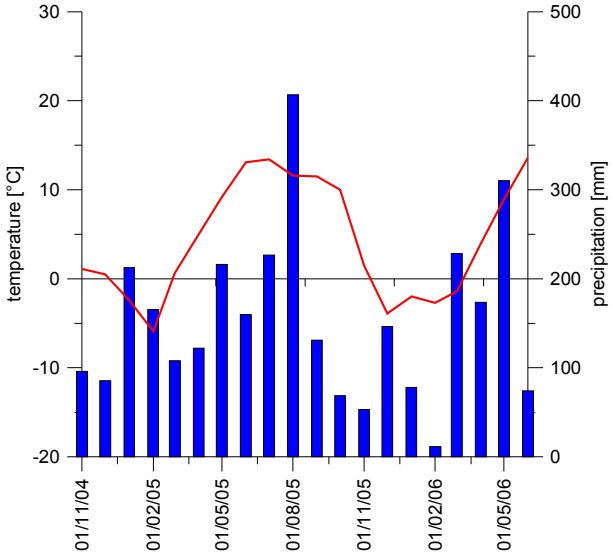

Fig. 4.63: Temperature and precipitation for the weather station Baad during the investigation interval (data: Vorarlberger Landesregierung).

The simple relationship between sediment load (in this case turbidity T) and discharge (Q) for a hydrological event provides a methodology for characterizing the karst system. Five examples for different T-Q relationships were defined by Williams 1989 for rivers. For a detailed description of the different T-Q relationship classes see Williams 1989. The Aubach system belongs to the Class V for a medium rainfall event: *Figure eight* type (Fig. 4.64). The turbidity peaks first after the rainfall event, whereas the water level peaks second. The falling limb of the turbidity shows that it does not decrease to its level before the rainfall event started. This shows that at least for this event, sediment is still transported whereas no additional water outflow of this system can be observed. During storm rainfall events, when precipitation exceeds a certain level (in this case 59.2 mm rainfall), the T-Q is expected to flip to a Class I: *Single valued line* type (Fig. 4.65). This indicates that the two curves peak at the same time, but show a different spread: the turbidity curve is narrower than the discharge curve.

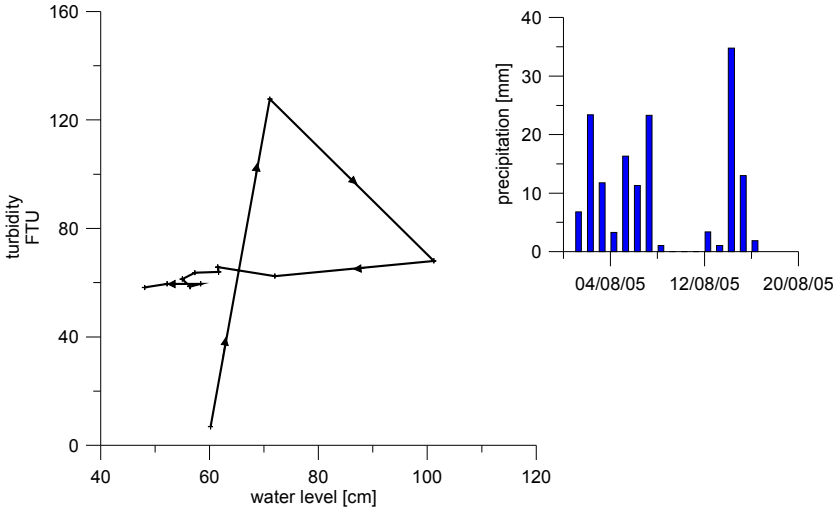

Fig. 4.64: Diagram of the turbidity with water level for a rain event which classifies the Aubach Spring as a Class V type (Figure eight type) (left); precipitation recorded at the nearby weather station Baad (right) (data: Vorarlberger Landesregierung, Bregenz) [Williams 1989].

Statistical analysis by auto-correlation and Fourier transformation for karst springs is described in more detail in Massei et al. 2006 and applied for the Aubach Spring in order to quantify the influence of rainfall on turbidity (as a parameter for the particle load) and electrical conductivity or temperature in a more statistical manner.

The calculation of the autocorrelation function (Fig. 4.66) of each signal (precipitation, conductivity, turbidity and water level) and the amplitude spectrum obtained by Fast Fourier Transformation (FFT) allows a quantification of the temporal effect of an event on subsequent measurements (memory effect) and the frequency of those.

Cross-analysis between the signals conductivity, turbidity and water level (output signals) with rainfall (input signal) give a means of quantifying the response of the system (output signals) to rainfall.

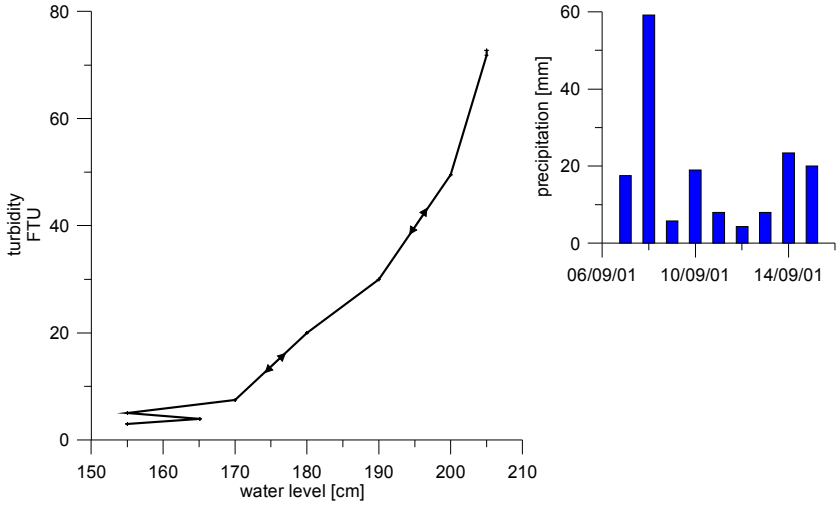

Fig. 4.65: T-Q-diagram which classifies the Aubach Spring as a Class I type (left); precipitation recorded at the nearby weather station Baad (right) (data: Vorarlberger Landesregierung, Bregenz) [Williams 1989].

In this study, continuous wavelet analysis allows to pinpoint the time at which different peaks of a signal actually occur. For further description of the applied analysis procedure see Massei et al. 2006. Detailed explanations of the applied statistical methods are provided in Box et al. 1994, Larocque at al. 1998, Padilla & Pulido-Bosch 1995 and Torrence & Compo 1998.

The autocorrelation functions of water level, turbidity and conductivity gave a short memory effect (Fig. 4.66). The fit function: $y = a_1 * \ln(L) + a_o$ (L = time lag; a_o correlation amplitude for L = 1 day [ ]; a_1 rate of decrease [1/d]) is calculated for all time series (Fig. 4.66). The differences in both values of a_o and a_1 for conductivity, water level and turbidity are rather small. The speed of information loss, the value a_o, is highest for turbidity and slightly smaller for water level and conductivity. The decrease rate a_1 is thus also very similar for all three parameters, but turbidity is decreasing slightly more slowly (Fig. 4.66). The autocorrelation function of rainfall at this scale shows no periodicities and appears fairly random, shortly after zero lag-time it drops down to zero and remains there.

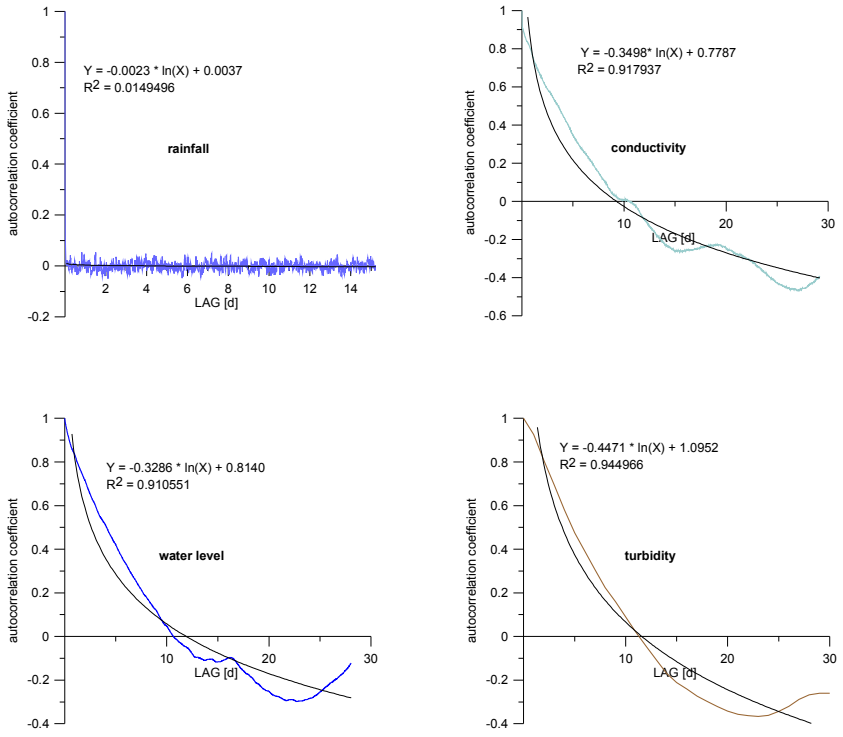

Fig. 4.66: Autocorrelation functions of rainfall, conductivity, water level and turbidity.

The energy spectrum of the autocorrelation function shows that no peaks can be distinguished for rainfall which remains close to the background noise (Fig. 4.67). For the other signals several peaks can be distinguished. Conductivity shows a single peak at 0.03/d, discharge at 0.03/d, 1/d and 2/d and turbidity at 1.9/d, 7.3/d. Thus, turbidity and conductivity show a smaller tendency for periodicities than the water level. For water level and turbidity, a weak tidal influence can be found (at ~2/d), however, variations are very small. The clear 1/d peak of water level might be related to daily snow melting. A further interpretation and temporal localization of peaks is given by wavelet analysis.

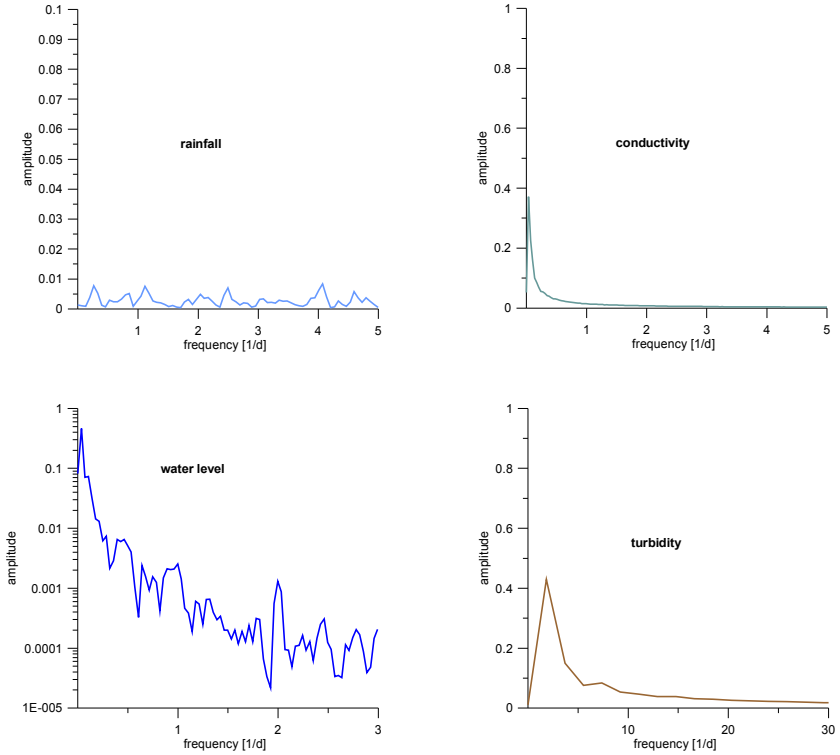

Fig. 4.67: Energy spectra of rainfall, conductivity, water level and turbidity (obtained by FFT of the corresponding autocorrelation functions).

Cross-correlation (Fig. 4.68) shows a strong influence of rainfall on discharge, conductivity and turbidity. The quality of rainfall data (only daily data) hampers a more detailed interpretation of the cross-correlation spectra. However, it is clearly visible that turbidity increases (time lag 0-1 day after signal), discharge increases (after 1 day) and water temperature first decreases (after 2 days) and conductivity decreases as well (after 2 days). Rainfall represents an input of less mineralized water, thus a negative peak of conductivity can be observed. The decrease in water temperature might be caused by cold water inflow from higher altitudes. All cross-correlation responses are very narrow (Fig. 4.68), which indicates a fast drainage system.

The weak tidal component of the water level is visible from wavelet analysis

that was conducted following the procedure described in Massei et al. 2006. The strong daily variations of water level (1/d) (Fig. 4.70) that are caused by snow melt are also described in Goldscheider 2002 by visual comparison of spring hydrograph data. The daily variations in water temperature are also visible from wavelet analysis (Fig. 4.69). They precede the daily water level peaks slightly (Fig. 4.69, Fig. 4.70).

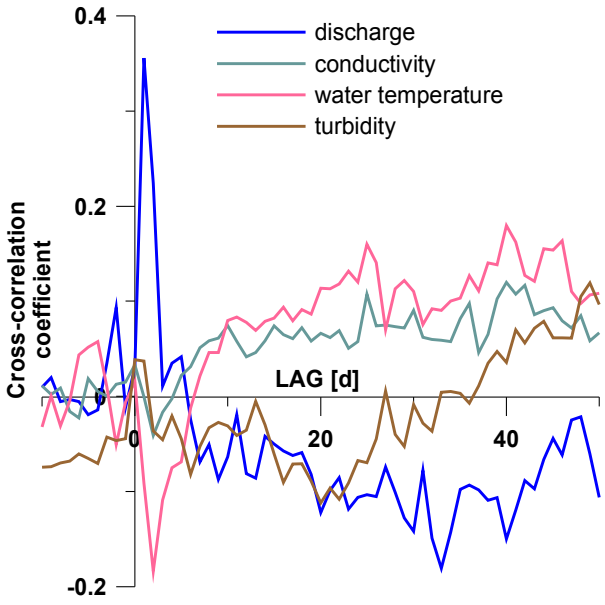

Fig. 4.68: Cross-correlation functions for discharge/rainfall, conductivity/rainfall, water temperature/rainfall and turbidity/rainfall of the Aubach Spring.

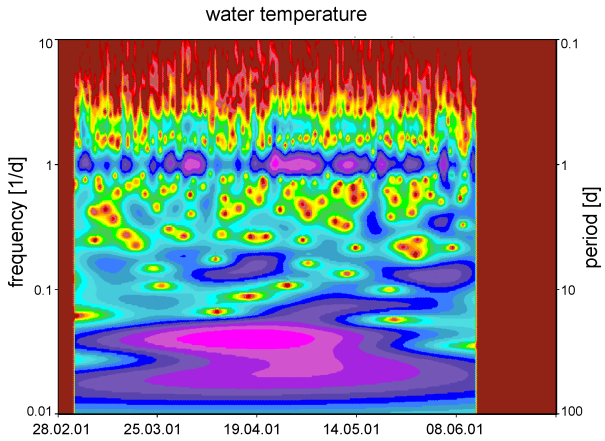

Fig. 4.69: Wavelet spectrum of water temperature data from the Aubach Spring.

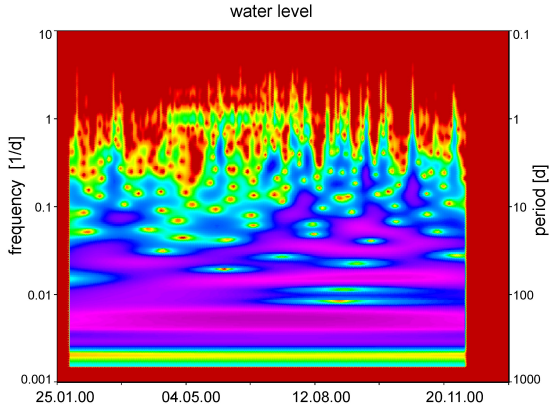

Fig. 4.70: Wavelet spectrum of water level data from the Aubach Spring.

4.3.2.4 Geology

In the surrounding area the four main alpine tectonic units are exposed relatively close by (Fig. 4.71): Subalpine Molasse, Helvetic nappes, Penninic nappes and Austro-Alpine nappes. During the Alpine orogeny the three latter ones were thrust from south to north on top of each other and partly thrust onto the Molasse sedimentary basin. The tectonically shortened Folded Molasse zone consists of an intercalation of conglomerates, sandstones, marls and clays and belongs tectonically to the Alpine fold belt.

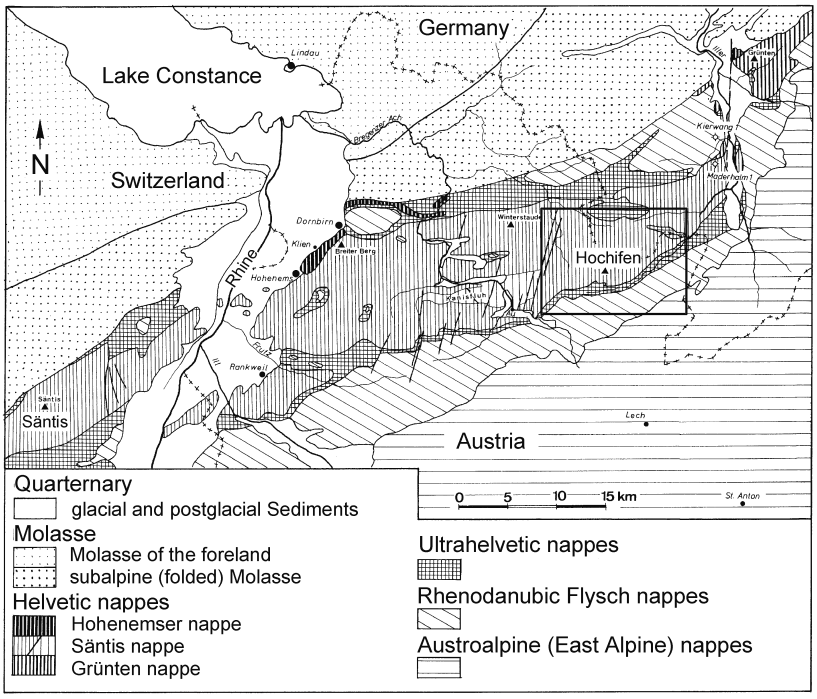

Fig. 4.71: Geological overview of Vorarlberg, the Hochifen-Gottesacker test site with the Hölloch cave; modified after Wyssling 1986.

The tectonically higher Helvetic nappes (Fig. 4.72), which plunge towards the east, consist mainly of Jurassic and Cretaceous sedimentary rocks. The test site forms part of the Helvetic Säntis nappe, the largest thrust sheet (Fig. 4.71), which forms a tectonic half-window. The Rhenodanubic Flysch belongs to the Penninic nappes; it consists of clayey sandstone and is separated from the Helvetic nappes through the Ultrahelvetic nappes that form a complex Mélange zone.

The Austro-Alpine nappes are tectonically on top of the thrust pile and form large parts of the Northern Limestone Alps. They outcrop further southeast.

The karst aquifer is formed by the Cretaceous, 100-meter-thick Schrattenkalk (Fig. 4.72). This is a pure limestone that consists of up to 97% calcite. It is intensively fractured and intersected by faults, intensively karstified and shows a large number and variety of karst features on its surface [Goldscheider 2002]. The underground karst system is well developed, with high flow velocities, short transit times and rapid reaction on hydrological events characterize the Gottesacker-Hochifen karst system that is developed in the Schrattenkalk.

The Schrattenkalk is underlain by the Drusberg formation (Apt-Alb). The Drusberg marls form as lower aquiclude the basis of the karst aquifer.

There is no surface drainage in the Hochifen-Gottesacker area. Rainfall sinks immediately underground via karst shafts or swallow holes. However, near the Hölloch entrance shaft in the Mahdtal Valley (Fig. 4.72) water can accumulate after heavy rainfall events on impermeable moraine material or overlaying impermeable rocks and fall into the Hölloch shaft to flow afterwards inside the cave together with the Hölloch Creek (Fig. 4.73, Fig. 4.74).

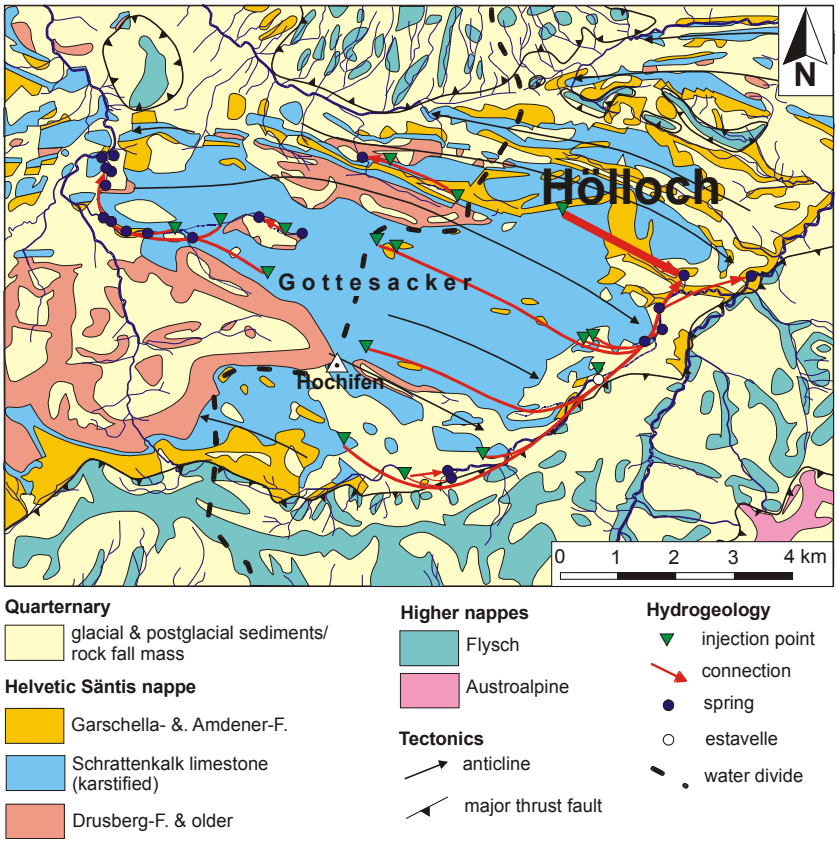

Fig. 4.72: Geological map of the Gottesacker-Hochifen and Hölloch area [Goldscheider 2002].

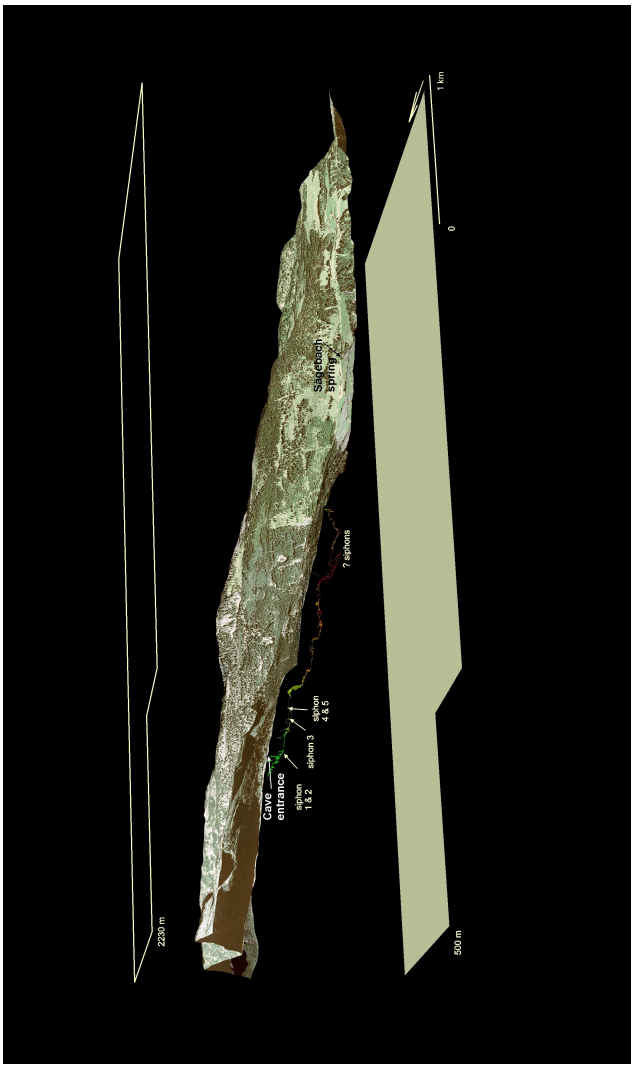

Fig. 4.73: Hölloch cave system with landscape (data: Land Surveying Office Feldkirch, Austria and Caving Club Sonthofen).

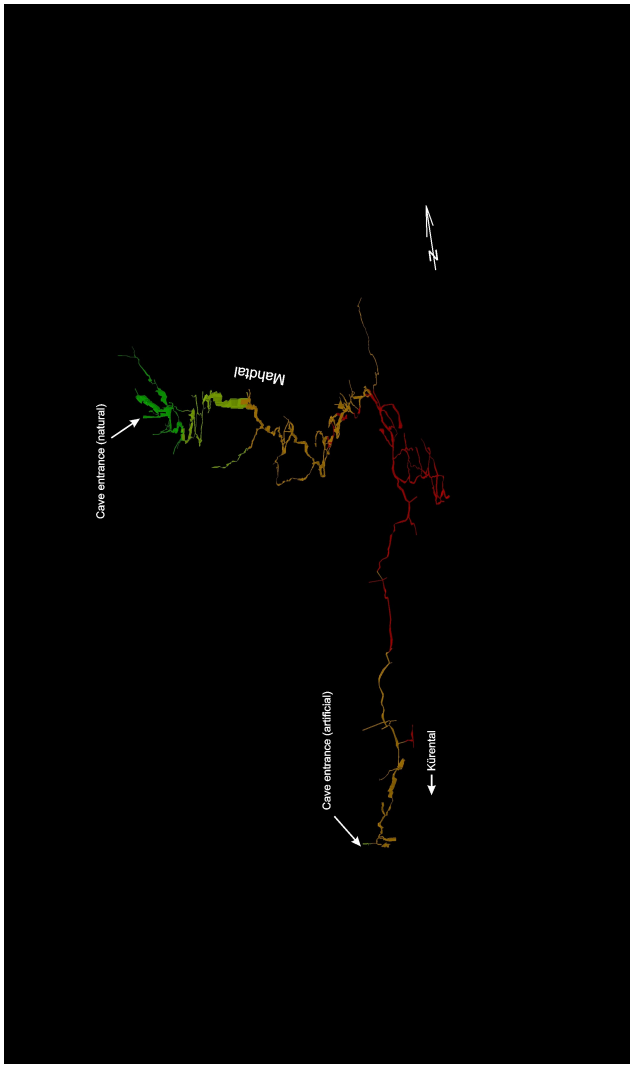

Fig. 4.74: Hölloch cave (view towards northwest).

4.3.2.5 Tracer tests

Previous tracer tests in the Hochifen-Gottesacker area determined that plunging synclines form the main underground flow paths, whereas anticlines are local water divides [Goldscheider 2002, Goldscheider 2005]. The investigated Hölloch cave system is located in the Mahdtal Valley (Fig. 4.73) syncline which plunges towards the Schwarzwassertal Valley, i.e. in a southeast direction. At its lower end, the cave continues towards the southwest, which is very likely a former hydrological base level [Stautz & Wolf 2006]. In the 1950s, a quantitatively not interpretable tracer test was performed with uranine, which revealed the Sägebach Spring as the only relevant outlet of this system.

Two tracer tests were carried out between the Hölloch entrance shaft and the Sägebach Spring (Fig. 4.73, Fig. 4.74). The first tracer test was carried out under stable low flow conditions and the second test during snow melt and storm rainfall and thus under varying high flow conditions. The tracers were injected into the Hölloch Cave Creek near the entrance shaft at an elevation of 1450 m; Sägebach Spring (2.5 km downstream, elevation: 1035 m), Mahdtal Valley Creek and Schwarzwasserbach Creek were sampled. A list of the injected tracers for both tests is given in Tab. 4.24.

Tab. 4.24: Injected tracers of both tracer tests.

tracers	1st tracer test low flow conditions	2nd tracer test high flow conditions
colloids	9.1×10^{10} 1 µm spheres 3.2×10^{9} 5 µm spheres	9.1×10^{10} 1 µm spheres
solutes	200 g uranine 200 amidorhodamine g	200 g uranine

During both tests an automatic ISCO sampler was installed at the Sägebach Spring, and additional water samples were taken manually at the Sägebach Spring and at the previously mentioned sampling locations. Due to temperatures of -20°C, during the first test the automatic ISCO sampler was placed into a purpose-built insulated box equipped with a heat lamp (Fig. 4.75). The analysis of the 5 µm spheres was done by Klotz GmbH, the analysis of particles and solutes by AGK and CHYN laboratories.

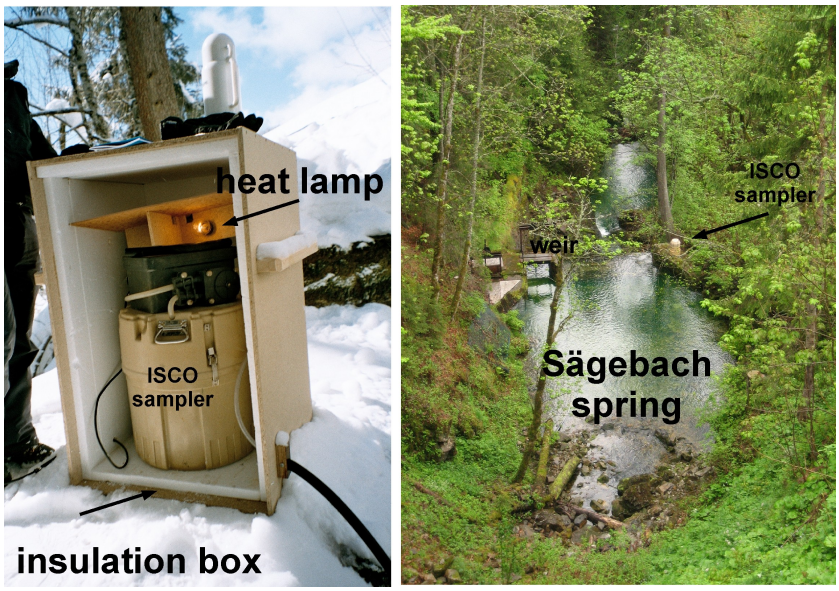

Fig. 4.75: Heated insulation box at the Sägebach Spring (left) and Sägebach Spring with ISCO sampler (right). Photographs: Nico Goldscheider, Andreas Wolf.

Discharge was measured several times during the tests manually by the salt dilution method. In 2005 the Sägebach Spring discharge was nearly constant 172 L/s, the discharge of the cave stream was estimated at 20 L/s. In 2006, the spring discharge was measured three times (582, 2691 and 1035 L/s). The continuously measuring pressure probe (water level measurement interval: 15 min) of a karst spring nearby, the Aubach Spring, was used to interpolate between the manual measurements (data: Landeswasserbauamt Bregenz).

The catchment of both springs overlap, so this seems to be an adequate method. With the two tests, it was possible to control qualitative test results from the 1950s, and to examine the hydraulic properties of colloidal and solute tracers during different flow conditions.

4.3.2.6 Results and discussion

4.3.2.6.1 Tracer test during constant low flow

During low flow conditions the uranine FDT is about 66.4 h after injection and peaks at a concentration of 9.25 µg/L after 98.3 h (Tab. 4.25, Fig. 4.76). The recovery for uranine is about 98.5%, which indicates that the Sägebach Spring is the only relevant outlet of the Hölloch system. The TBC shows a single peak and a small tailing (Fig. 4.76).

Tab. 4.25: Summary of tracer test results (1st test: low water conditions); modified after Göppert & Goldscheider (accepted).

		symbol	unit	low water	
				uranine	1-µm spheres[2]
Basic data	injection quantity	M	g ; n[1]	200	9.10E+10
	spring discharge rates	Q	L/s	constant: 172	
	time of first detection (FDT)	t_1	h	66.4	65.4
	peak time	t_p	h	98.3	83.4
	peak concentration	C_p	µg/L ; n/L[1]	9.25	4400
	normalized peak concentration	C_p/M	m^{-3}	4.62E-5	4.84E-5
	maximum velocity	v_{max}	m/h	37.7	38.3
	peak velocity	v_p	m/h	25.4	30.0
	recovery	R	%	98.5	75.1
ADM	mean flow velocity	v	m/h	24.8	28.1
	mean transit time	t_0	h	100.9	89.0
	longitudinal dispersion	D_L	m^2/h	514	619
	longitudinal dispersivity	α	m	20.8	22.0
	coeff. of determination	R^2	-	0.988	0.814
2RNE	average mobile fluid velocity	v_m	m/h	25.5	n.d.
	corresponding transit time	t_m	h	98.0	n.d.
	longitudinal dispersion, mobile-fluid phase	D_m	m^2/h	395.1	n.d.
	longitudinal dispersivity	α	m	15.5	n.d.
	partition coefficient	β	-	0.92	n.d.
	mass transfer coefficient	ω	-	0.39	n.d.
	coefficient of determination	R^2	-	0.999	n.d.

[1] units for microspheres, uranine
[2] on the basis of corrected data series

The 1 µm spheres show a more irregular TBC (Fig. 4.77). Several samples from 27 to 57 h after injection contain small numbers of 1 µm spheres (up to 106/100mL). After several samples (i.e. after 8 h) without any microspheres, breakthrough of 1 µm spheres restarts 65 h after injection. This second part of the microsphere TBC fits with the uranine TBC (Fig. 4.79), which means that the 1 µm spheres are slightly preceding. Thus it seems sound to use this second part of the 1 µm spheres TBC for further modeling and interpretation. However, the first detections indicate that a smaller amount of microspheres travels faster than solutes and might use preferential flow paths, for instance smaller conduits or with higher flow velocities, but lower flow rates.

The first 5 µm spheres were detected after 73 h. The concentration peaks after 105 h (Fig. 4.77) with a number of 38/100 mL; recovery is about 48%. Due to the irregularities, the 5 µm sphere TBC was not chosen for further modeling. But, interestingly, the results show that particles of this size (i.e. the size of *Cryptosporidium* cysts) can travel this far (2.5 km).

Microspheres and uranine are modeled with an ADM and a 2RNE. The modeling results for the test during low flow are listed in Tab. 4.25. The 2RNE fit for the 1 µm spheres yields an unacceptable coefficient of determination, thus those modeling results are not listed and not considered for interpretation. For uranine the residual concentration, which shows where and how strongly fit results differ from data, is included into Fig. 4.76.

Both model approaches can fit the rising limb and peak of the TBCs. The ADM of uranine fails to fit the tailing of the curve, whereas the 2RNE is able to fit the entire TBC fairly well, which is obvious from a consideration of residual concentrations (Fig. 4.76).

The irregularities of the microsphere TBCs hamper a more advanced modeling approach. The most irregular data points were removed from the TBC so that a coefficient of determination of 0.8 was obtained. The ADM approach is more robust considering irregular TBCs; the ADM fit parameters do not vary much when data points are removed, whereas the 2RNE acts very sensitively on any smoothing procedure.

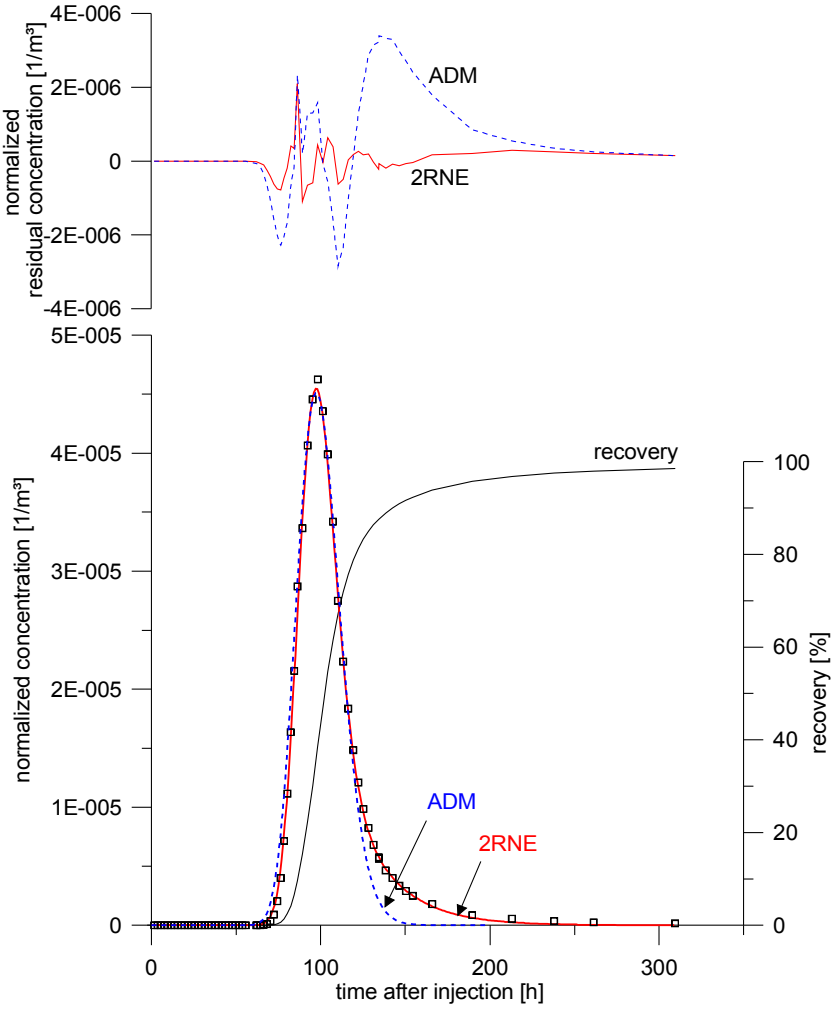

Fig. 4.76: Uranine results during low flow conditions, observed values (squares) and fitted data with residual concentrations (modified after Göppert & Goldscheider (accepted)).

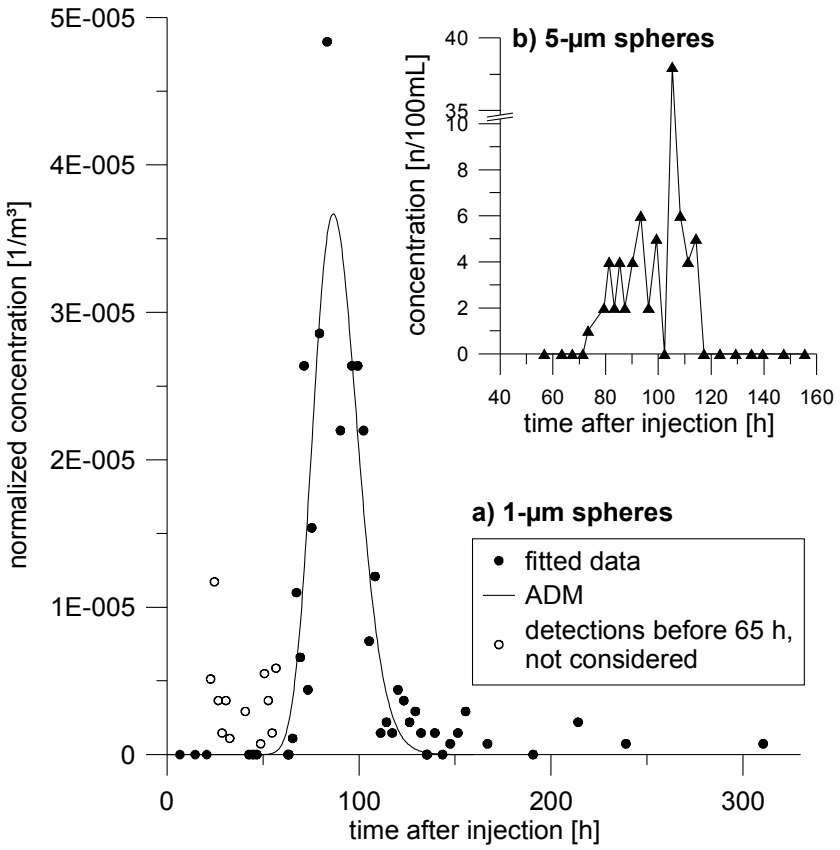

Fig. 4.77: Results for both microsphere sizes during low flow conditions [Göppert & Goldscheider (accepted)].

4.3.2.6.2 Tracer test during high flow

During summer high flow conditions, uranine has an FDT of 12.8 h, significantly before the FDT of the previously described low flow test (Tab. 4.26, Fig. 4.78, Fig. 4.79). Uranine peaks with a concentration of 15.6 µg/L after 17.3 h. The 1 µm spheres FDT precedes the solute tracer slightly, the

FDT is 11.5 h and the maximum concentration of 6120/L is reached after 17.5 h. Recovery for uranine is 99.8%, for the 1 µm spheres recovery is 42.1%. This shows that a certain amount of microsphere attenuation occurs even at high flow conditions and accordingly high flow velocities. Both tracers show similar flow velocities, although the microsphere TBC is narrower than the uranine TBC (Fig. 4.78).

Tab. 4.26: Summary of tracer tests results (2nd tracer test during high flow conditions); modified after Göppert & Goldscheider (accepted).

		symbol	unit	high water	
				uranine	1-µm spheres
Basic data	injection quantity	M	g ; n[1]	200	9.10E+10
	spring discharge rates	Q	L/s	variable: 580-2691	
	time of first detection (FDT)	t_1	h	12.8	11.5
	peak time	t_p	h	17.3	17.5
	peak concentration	C_p	µg/L ; n/L[1]	15.63	6120
	normalized peak concentration	C_p/M	m^{-3}	7.82E-5	6.73E-5
	maximum velocity	v_{max}	m/h	196.1	217.4
	peak velocity	v_p	m/h	144.9	142.9
	recovery	R	%	99.8	42.1
ADM	mean flow velocity	v	m/h	136.9	139.8
	mean transit time	t_0	h	18.3	17.9
	longitudinal dispersion	D_L	m^2/h	2584	224
	longitudinal dispersivity	α	m	18.9	1.60
	coeff. of determination	R^2	-	0.987	0.862
2RNE	average mobile fluid velocity	v_m	m/h	138.3	146.3
	corresponding transit time	t_m	h	18.1	17.1
	longitudinal dispersion, mobile-fluid phase	D_m	m^2/h	2239.0	137.5
	longitudinal dispersivity	α	m	16.2	0.94
	partition coefficient	β	-	0.93	0.92
	mass transfer coefficient	ω	-	0.19	1.13
	coefficient of determination	R^2	-	0.997	0.985

[1] units for microspheres, uranine

Uranine shows two additional peaks (after 30 h and 44 h) that are clearly a result of discharge peaks which are caused by storm rainfall events (Fig. 4.78). Typically, multiple peaks in TBCs in karst systems are explained by multiple flow paths. Due to the obvious relationship between the discharge and the TBC peaks, the variable flow rates are a more likely explanation. There are two scenarios for a second peak conceivable: a) the preceding minimum is an effect of dilution and b) the peak is an effect of remobilization at higher flow rates. The uranine minimum coincides with the discharge maximum and thus

a) seems to be more probable. Both curves are fitted with an ADM and a 2RNE. The 2RNE reveals a better fit of the entire curve including the tailing that the ADM is not able to fit (Fig. 4.78).

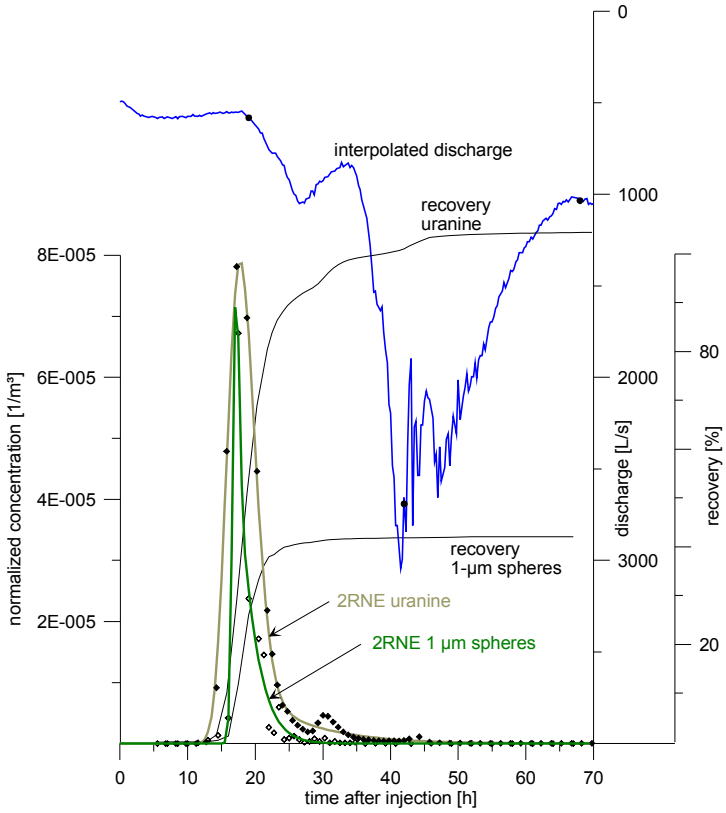

Fig. 4.78: Results of both tracers during high flow conditions and interpolated discharge (Aubach discharge data: Landeswasserbauamt Bregenz) Göppert & Goldscheider (accepted)].

4.3.2.6.3 Discussion

During low flow conditions the 1 µm microspheres travel faster than the solutes, the peak concentration occurs 15 h earlier (Fig. 4.79) and the mean

transit time, calculated by ADM, is 12 h shorter (12%). This is clearly an effect of peak shift due to different advection of colloids. Such a pronounced peak shift and a coincidentally high recovery cannot be explained by peak shift due to filtration processes. At high flow conditions, such an effect cannot be observed. In that case the mean transit time for microspheres is only 0.4 h (2%) shorter than for uranine. Generally, transit times are shorter during high flow conditions and flow velocities much higher. The entire high flow TBC including tailing is over before low flow TBC has even begun (Fig. 4.79).

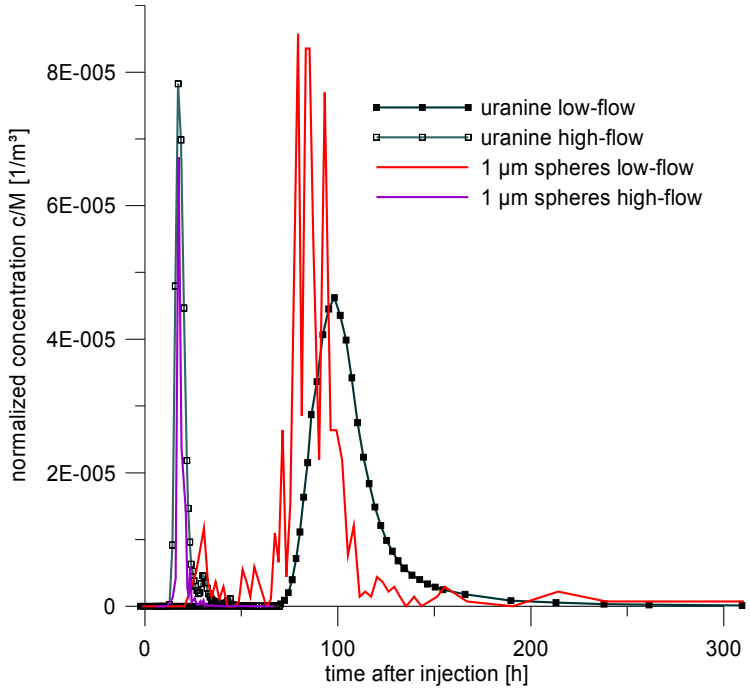

Fig. 4.79: Comparison of TBCs from both tracers for both tests (results for high flow precede TBCs for low flow).

Recovery of uranine (nearly 100%) confirms that indeed the Sägebach Spring is the only relevant outlet of the Hölloch system. The particles appear to have a recovery of about 75% during low flow and 48% during high flow which indicates that even in karst conduits significant attenuation of particles is operating. For the larger 5 µm spheres a certain influence of gravitational

forces can be assumed whereas the 1 µm spheres can be attenuated by attachment onto rock surfaces, clay particles or filtration in cave sediments.

During low flow the microspheres show a slightly higher dispersivity than uranine (22 m compared to 21 m), during high flow dispersivity is smaller (1.6 m compared to 19 m), which causes a narrower TBC. Thus it can be assumed that particles travel along the fastest flow path and – due to the lower recovery – tend to attach onto rock surfaces or other particles as a result of the more likely occurring collisions during high flow and are thus removed from water flow.

The 2RNE gives similarly high partition coefficients (0.92 to 0.93). This illustrates that for this karst system generally a high volume fraction of the fluid region is mobile. And the mass transfer coefficients show (for uranine) that at higher flow rates the mass transfer is smaller. However, due to the non-unique combinations of dispersivity and mass transfer coefficients, the results of the 2RNE have to be considered with care.

The influence of flow rate and flow velocities on maximum concentrations is obvious. Generally, there are two opposing influences. Higher flow rates cause higher dilution and, on the other hand, higher flow velocities and narrower TBCs. A transformation of the ADM yields that the peak concentration is proportional to the relation of velocity/discharge when all other parameters are constant. Then the relationship can be described as follows [Göppert & Goldscheider (accepted)]:

$$\begin{aligned} \frac{c_p,h}{c_p,l} &= \frac{(\frac{v}{Q})_h}{(\frac{v}{Q})_l} \\ h &= high\ flow \\ l &= low\ flow \end{aligned} \tag{38}$$

In the present case (low flow: Q = 172 L/s; v = 145m/h; high flow at peak concentration: Q = 582 L/s; v = 25.4 m/h) the abovementioned relationship v/Q is 0.249 during high flow and 0.148 during low flow. From equation 38 maximum concentrations should be 1.7 times higher during high flow. By dividing the actually measured concentrations (high flow maximum concentration: 15.63 µg/L, low flow maximum concentration: 9.25 µg/L) a value of 1.7 is obtained which proves the accuracy of this simple equation.

It has to be considered that the discharge of the Sägebach Spring increases only by a factor of 3.4 during high flow, whereas the flow velocity increases by

a factor of 5.7. This is a deviation from what can be expected in a karst system. In karst, higher flow rates usually cause higher flow velocities and larger flow-through cross-sectional areas. Discharge should thus increase more than flow velocity (referring to the condition of flow continuity: $Q = v \cdot A$).

However, the deviation can be explained by the hydrogeological situation of the Sägebach Spring. The Sägebach Spring receives a base flow component from the Schwarzwassertal catchment, whereas flow velocity is strongly dependent from water flow velocity in the Hölloch cave system which varies more than the discharge [Göppert & Goldscheider (accepted)].

The two modeling approaches reproduce the TBCs of uranine and 1 µm spheres well. However, irregularities of the TBC prevent a 2RNE modeling of the 1 µm spheres results from low-flow conditions.

Both models allow a fit of the rising limb and the peak concentrations, but only the 2RNE is able to fit the tailing of the TBCs adequately. Thus the coefficient of determination is higher for the 2RNE than for the ADM (Tab. 4.25, Tab. 4.26). This finding confirms the results of Field & Pinsky 2000 and Birk et al. 2005 for solutes in karst systems.

The tracer tests show that colloids in the size of pathogens can be transported in this karst system over a distance of about 2.5 km. The C*ryptosporidium*-sized microspheres (5 µm) were injected only during low flow, but they reach the Sägebach Spring in detectable concentrations. Equivalent numbers of infectious *Cryptosporidium* cysts might cause illnesses. The 1 µm spheres experience attenuation processes, however, large amounts of microspheres are recovered in the Sägebach Spring and normalized maximum concentrations are comparable to those of solutes. Bacteria in comparable diameters might thus be transported rapidly and in high numbers which might cause infections.

These findings should be considered and implemented into protection strategies. Karst systems often show significant microbial contamination at karst springs, especially (but not only) after storm rainfall events. Autochthonous remobilized colloids (and bacteria) peak first [Pronk et al. 2006] and allochthonous colloids or microorganisms form a second peak for a test site in Switzerland (see 4.3.3 Yverdon-les-Bains: deep karst system). The present study demonstrates that even at low flow conditions a certain amount of particles can be transported that is able to cause illnesses and influence the water quality in a negative way.

Furthermore, these tests illustrate that different analysis methods of colloids reveal reliable results in field tracer tests over distances of 2.5 km. The automatic sampling device was able to take water samples under extremely low temperatures and uranine results partly confirmed the quantitative tracer

tests from the 1950s.

The statistical analysis yields results that confirm the particle and solute tracing results: different flow conditions might change the transport conditions of colloids with respect to solutes. Both methods should be applied together (if possible).

Contamination during low water conditions is transported to the spring more rapidly than expected from solute transport behavior. Therefore a microbial contamination might occur earlier than indicated from solutes and thus result in a hygienically problematic water quality. Flow velocities increase strongly during high water conditions. Protection strategies based on moderate water conditions underestimate the contamination peaks and flow velocities. They need to be adjusted accordingly. For this test site, FDTs of several hours up to a few days are obtained and a flow distance of 2.5 km. For the delineation of protection zone II, the 50 day limit is used. In this case this limit goes along with a flow distance of 30 km during low flow and more than 165 km during high flow. For the Sägebach Spring, protection zone II would cover the entire catchment area as shown in Fig. 4.61. In the course of a reasonable protection zone definition, areas that do not contribute actively to contamination should be excluded. This implies that areas have to be evaluated with regard to their importance and influence on water quality. Unlike an evaluation of solute contaminants, for the evaluation of microbial contaminations woodland with game animals should be included as hazards.

4.3.3 Yverdon-les-Bains: deep karst system

4.3.3.1 Introduction

The test site Yverdon-les-Bains was investigated hydrogeologically by the karst research group at the CHYN (University of Neuchâtel): Dr. N. Goldscheider, M. Pronk and Dr. J. Zopfi, who provided the opportunity to participate for a common tracer test during low flow conditions. The intention of the working group is to characterize the transport in the deep karst system nearby the village of Yverdon-les-Bains (Fig. 4.80). The interaction of DOC, natural particles and bacteria between a swallow hole that drains an intensively agriculturally used area and two karst springs that are used for the water supply of Yverdon-les-Bains is of prime importance.

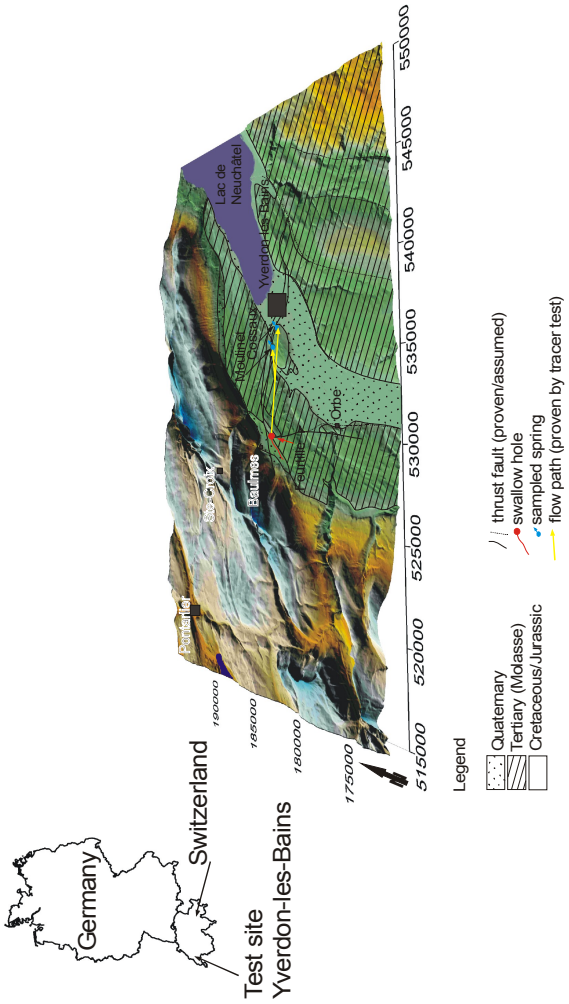

Fig. 4.80: Location and elevation model with geology of the Yverdon-les-Bains test site (elevation data provided by Swisstopo).

The location and geology of the Yverdon-les-Bains test site in the Swiss plateau are illustrated in Fig. 4.80 and Fig. 4.81. For details of previous investigations see: Pronk et al. 2006, Pronk et al. 2007 and Goldscheider et al. 2006.

4.3.3.2 Location and Geology

The Yverdon-les-Bains test site is situated in the Swiss plateau (Swiss Molasse basin) near the Jura mountain foothills in the Canton Vaud on the southwestern end of the Lake Neuchâtel (Fig. 4.80, Fig. 4.81). The area is intensively used for agriculture. The swallow hole Feurtille (F) drains the adjacent field. The karst springs Cossaux (C) and Moulinet (M) are used for the water supply of Yverdon-les-Bains and are frequently contaminated, thus a connection between swallow holes and springs was expected. Both springs are the outlet of a deep geothermal system that is entered via boreholes which supply the thermal bath of Yverdon-les-Bains. To date, the spring catchment area beyond the Feurtille swallow hole is not known.

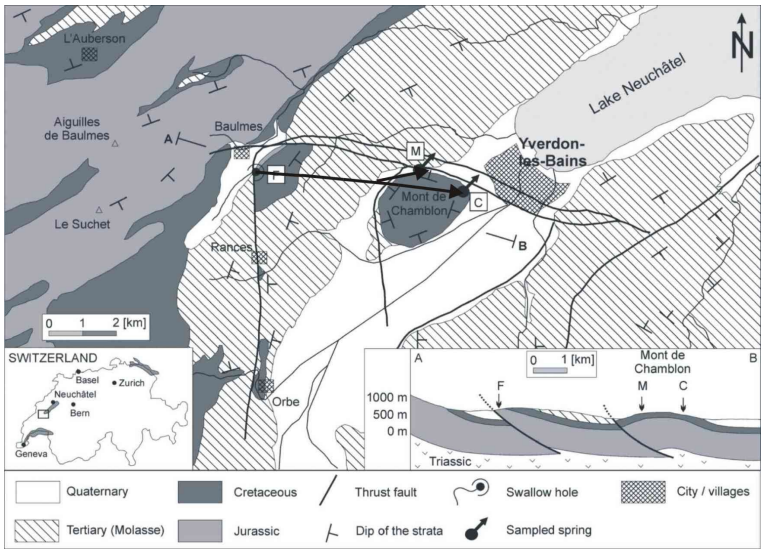

Fig. 4.81: Geological map and cross-section of the Yverdon-les-Bains test site with connection between the injection point Feurtille (F) and the sampling points Moulinet (M) and Cossaux (C); Pronk et al. 2006.

The main karst aquifer is formed by Upper Jurassic limestone which is 400 meters thick. Valanginian limestone (30 - 50 meters thick) and Hauterivian limestone (30 - 60 meters thick) are karstified as well. They are divided by thin marl layers, however, and are hydraulically connected with each other [Goldscheider et al. 2006]. Via complex fold-and-thrust tectonics, the karst aquifer is exposed in the Mont de Chamblon mountain (Fig. 4.80), which forms a hydrogeological window.

The Feurtille swallow hole (Fig. 4.82) is situated in Jurassic limestone at the western window near the community of Baulmes at an elevation of 600 m, whereas the two karst springs Moulinet and Cossaux are located at the Mont de Chamblon foothills in Cretaceous limestone at an altitude of 450 m (Fig. 4.81).

The two springs contain four water components: one from deep geothermal circulation from several hundreds of meters of depth, cold and mildly contaminated water from the Malm aquifer, cold and frequently contaminated water from the Feurtille swallow hole and local water from the Mont de Chamblon area [Pronk et al. 2006].

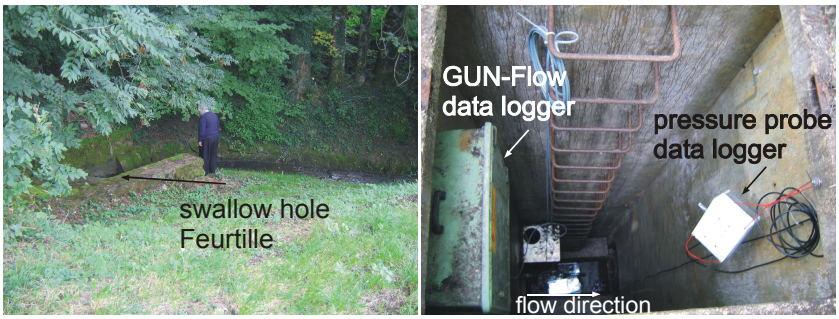

Fig. 4.82: Feurtille swallow hole (left) and shaft with data loggers (right).

4.3.3.3 Tracer tests

4.3.3.3.1 General overview

Via tracer tests at low, middle and high flow conditions, the general hydraulic behavior of this deep karst system was examined by the co-operation partner. The microbiological contamination and the DOC distribution are monitored continuously (Fig. 4.82) [Pronk et al. 2006]. The test site is temporarily equipped with an online particle counter; additionally, water samples are analyzed for microorganisms at regular intervals by the co-operation partner at the Laboratory of Microbiology (LAMUN, University of Neuchâtel).

Through a tracer test with fluorescent tracers during low water it was determined that recovery is lower for the spring that is located further away (Feurtille-Cossaux distance: 6.3 km), but with a notably earlier FDT for this spring (Tab. 4.27, Fig. 4.84). During mean and high flow conditions, the recovery is always smaller for the more distant Cossaux Spring than for the Moulinet Spring (Feurtille-Moulinet distance: 4.8 km) (Fig. 4.83). While the recovery of the Cossaux Spring decreases at increasing water levels (12.3% to 1.6%), the recovery of the Moulinet Spring increases (16.8% to 27%). The total recovery for both springs remains nearly constant (low to high flow: 29.1%, 28.5% and 28.6%).

The FDT flip at high flow conditions. During low flow and medium flow, the tracer arrives first at Cossaux (260 h and 81.9 h for Cossaux, compared to 292 h and 86.9 h for Moulinet). At high flow the tracer is measured at Moulinet before it reaches Cossaux (40.3 h for Moulinet and 43.5 h for Cossaux). The reason for this behavior can be explained by an extension of the conceptual model of this karst system presented in Pronk et al. 2006. Cossaux receives an additional inflow from the deep geothermal system, thus the recovery is always smaller than for Moulinet Spring. When the water level increases the recovery decreases for Cossaux because of this deep component (which mainly derives from the Jura mountains, thus the water level experiences a certain topographically induced pressure that seems to exceed the other components). Moulinet does not receive such a deep inflow; the discharge which is marked by the tracer increases and thus the recovery increases.

For the FDT a similar picture can be drawn. During low and medium flow traced water reaches first the Cossaux Spring and then the Moulinet Spring. When the importance of the non-traced base flow component increases, the Moulinet Spring first receives the traced water from the swallow hole which seems then to be a more direct connection.

Fig. 4.83: Moulinet Spring (left), sampler at Moulinet Spring (middle; photograph: N. Goldscheider) and injection of the fluorescent tracer into the concrete-encased swallow hole (right; photograph: M. Pronk).

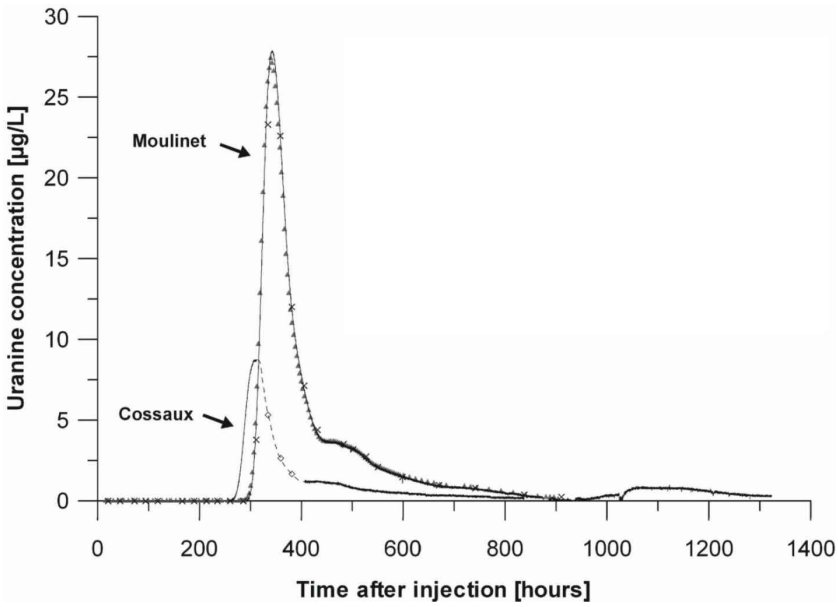

Fig. 4.84: Uranine TBC for the Cossaux and Moulinet karst springs from a previous tracer test [Pronk et al. 2006].

Tab. 4.27: Uranine results from previous tracer tests [Pronk et al. 2006].

Hydrologic conditions	Cossaux springs			Moulinet springs		
	t_1 [h]	Q [L/s]	R [%]	t_1 [h]	Q [L/s]	R [%]
low-flow	260.0	43	12.3	292.0	19	16.8
median-flow	81.9	52	3.2	86.9	120	25.3
high-flow	43.5	61	1.6	40.3	320	27.0

4.3.3.3.2 Goals of microsphere tracer test at average flow conditions

In performing the comparative tracer test the following questions should be addressed:

- Are colloidal tracers applicable in a deep karst system?
- Does the solute and colloidal transport behavior differ in a deep geothermal karst system?
- Is it possible to find an appropriate fit of the solute and colloidal data by conventional ADM (or SFDM) and more advanced modeling approaches (2RNE)?
- Can the colloidal tracer test be used to identify the source of particle peaks?
- What influence on water quality goes along with the swallow hole?

4.3.3.3.3 Tracer test 2005

In order to answer the abovementioned questions a combined tracer test was carried out. On June 02, 2005 a fluorescent tracer and two sizes of microspheres were injected into the Feurtille swallow hole at average flow conditions (Tab. 4.28). Both springs (Moulinet and Cossaux) were sampled manually for particle tracers and online for the fluorescent tracer uranine. For the microsphere analysis brown glass bottles with a volume of 200 mL were used and the analysis was done at the AGK laboratory using a fluorescence microscope. For uranine an online-flow-through fluorometer was used (Fig. 4.82) (GGUN-Flow, Schnegg, University of Neuchâtel). Water samples for detection of fluorescent tracers were taken sporadically for comparison reasons. The discharge was recorded continuously.

Tab. 4.28: Tracers injected into the Feurtille swallow hole during average flow conditions.

tracers	tracer test June 2005 average flow conditions
colloids	2.28×10^{11} 1 µm spheres 2.84×10^{10} 2 µm spheres
solutes	1 kg uranine

4.3.3.4 Results and discussion

4.3.3.4.1 Description of the TBCs

All tracers were found at both springs. The Moulinet Spring shows an FDT for uranine of 86.4 h and reaches a concentration maximum of 25.16 µg/L after 103.8 h. The TBC has a regular shape with a steeply rising limb and a long tail. The microspheres both show a more irregular TBC (Fig. 4.85, Fig. 4.86). The FDT of the 1 µm spheres is at 85.4 h, i.e. they arrive 1 h before the uranine FDT (Tab. 4.29). The concentrations vary between 0.5 and 40/100 mL. The concentration maximum of 1200/100 mL is reached after 96.8 h and precedes that of uranine by 7 h. After 105 h the main TBC of 1 µm spheres ends, approximately when uranine reaches the maximum concentration. The 2 µm spheres have an FDT of 94.4 h and reach the maximum concentration of 3.8/100mL after 100.8 h. The 2 µm spheres recovery is 0.15%, the recovery of the 1 µm spheres is 4.02%.

The more distant Cossaux Spring gives lower concentrations for all tracers, which goes along with a lower recovery rate (Tab. 4.29). The reduction factor is highest for 1 µm spheres (134), one order of magnitude lower for uranine (15.8) and smallest for the 1 µm spheres (7.5).

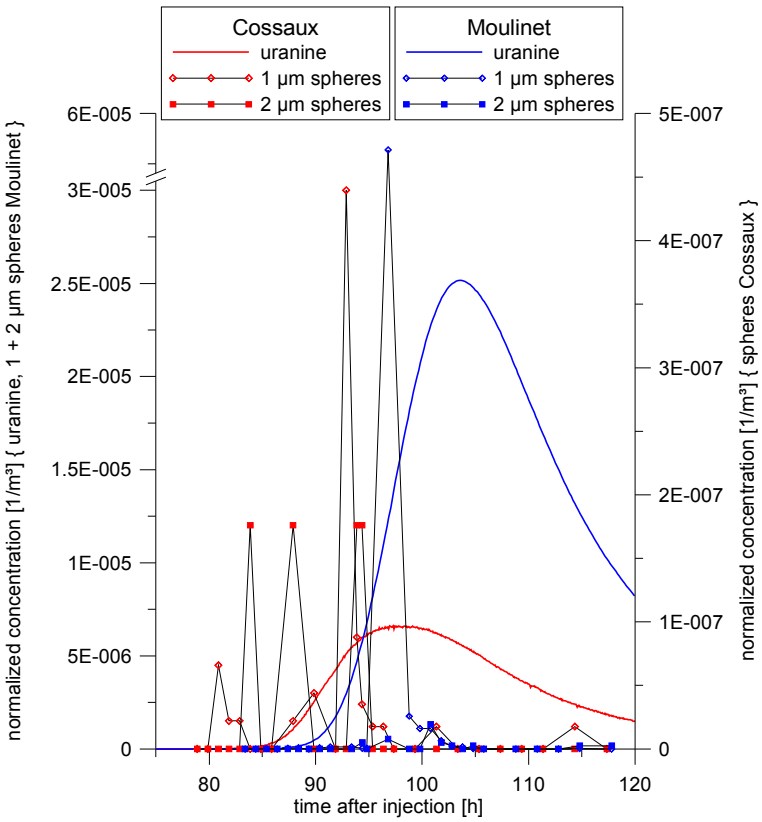

Fig. 4.85: Normalized concentrations of all tracers for both springs (note the break in the left y-axis).

All tracers reach the Cossaux Spring before they can be detected at the Moulinet Spring. First to arrive are the 1 µm spheres (80.9 h), afterwards uranine (81.8 h) and 2 µm spheres. The maximum concentration of 1 µm spheres is reached after 92.9 h with a concentration of 10/100 mL whereas uranine peaks after 97.5 h and 6.61 µg/L. The 2 µm spheres do not show a peak, the values vary between 0 and 0.5/100mL.

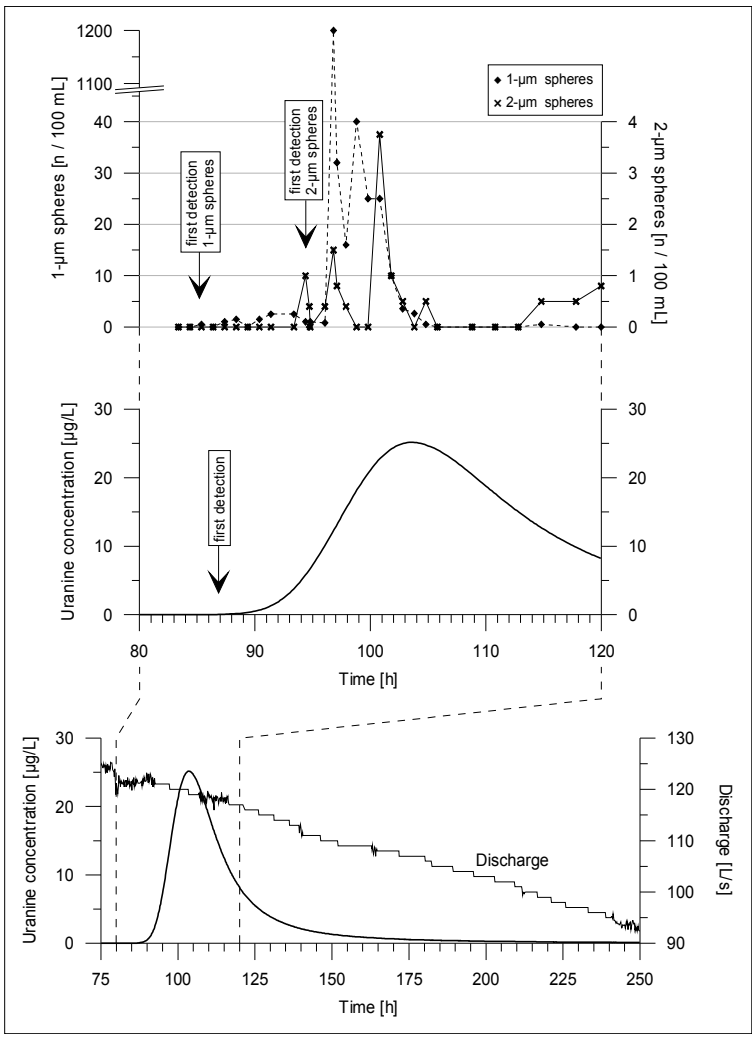

Fig. 4.86: Absolute concentrations of all applied tracers and discharge of the Moulinet Spring [Goldscheider et al. 2006].

Tab. 4.29: Results of microspheres and uranine for the tracer test during medium flow conditions.

	Cossaux			Moulinet		
	1µm spheres	2µm spheres	uranine	1µm spheres	2µm spheres	uranine
t_1 [h]	80.87	83.87	81.81	85.4	94.4	86.4
t_{peak} [h]	92.87	83.7 – 94.35	97.51	96.8	100.8	103.8
c_{peak} [n/100mL] [µg/L]	10	0.5	6.6	1200	3.8	25.2
R [%]	0.03	0.02	1.6	4.02	0.2	25.3

4.3.3.4.2 Modeling results and discussion

The uranine and 1 µm sphere results for the Moulinet Spring were used to apply an ADM and a 2RNE model, for the Cossaux Spring only uranine was used to apply an ADM and 2RNE which were not able to fit the microsphere TBC due to the irregularities of the microspheres' TBCs (Tab. 4.30, Tab. 4.31). For comparison, the observed microspheres data are also displayed (Fig. 4.88).

Tab. 4.30: ADM results for uranine and 1 µm spheres for the Moulinet Spring and uranine for the Cossaux Spring.

tracer	sampling point	ADM			
		v [m/h]	**DL** [m²/h]	**α** [m]	**R²**
uranine	Moulinet	45.08	636.9	14.128	0.9595
1 µm spheres	Moulinet	49.43	5.145	0.104	0.9990
uranine	Cossaux	62.24	1366	21.947	0.9612

For CXTFIT ADM and 2RNE evaluation, the online TBCs of uranine had to be filtered to achieve a lower number of input values (2034 values were filtered

down to 50 values). Near the concentration peak the time interval was upscaled to 1 h, towards first detection the time interval was two to three hours and along the tailing of the curve an increasing time interval of up to 14 hours had to be chosen.

Tab. 4.31: 2RNE results of uranine and 1 µm spheres for the Moulinet Spring and uranine for the Cossaux Spring.

tracer	sampling point	2RNE					
		v [m/h]	D_L [m²/h]	α [m]	β	ω	R^2
uranine	Moulinet	43.16	254.10	5.887	0.919	1.124	0.9989
1 µm spheres	Moulinet	49.54	5.496	0.111	0.9996	0.026	0.9991
uranine	Cossaux	60.44	258.30	4.274	0.890	2.557	0.9972

The modeling results show that although the ADM is the more robust modeling approach, the 2RNE is able to fit the rising limbs, peak concentrations and the tailings of the TBCs better (Fig. 4.87, Fig. 4.88). The fit quality generally is better for the 2RNE approach. The tailing of the Moulinet results for uranine can be fitted by the 2RNE, whereas the visual inspection of the fit quality of the uranine tailing of the Cossaux Spring reveals weaknesses in both approaches.

The ADM and 2RNE approaches make little differences for the 1 µm spheres due to the spikiness of this TBC. The 2RNE illustrates that the 1 µm spheres do not show much tendency for mass exchange (ω = 0.026) and the partition coefficient of 0.9996 indicates that there is a large proportion of mobile fluid phase.

Partition coefficients for the solutes are in the same range, however the mass transfer coefficient indicates that there is a larger tendency of the solutes for exchange processes. The flow velocities for solutes are lower than those of the microspheres (Tab. 4.30, Tab. 4.31) and the peak travel times are significantly shorter for the 1 µm spheres (Tab. 4.29). Although the recovery is rather low for the microspheres, Fig. 4.87 illustrates that the normalized peak

concentration is larger for the 1 µm spheres (at the Moulinet Spring) than for the solutes. The earlier peak times cannot be explained by peak shift due to filtration, it is very probably an effect of different advection. This observation is consistent with findings of Pronk et al. 2006, who reported earlier arrival of particles (turbidity, bacteria) compared to solutes (TOC, nitrate) following storm rainfall.

The longitudinal dispersion coefficient is much larger for the solutes than for the microspheres.

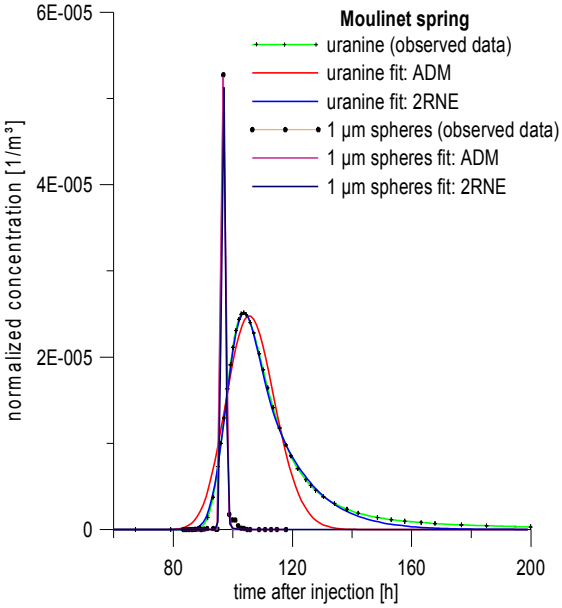

Fig. 4.87: Comparison of observed and fitted data of the Moulinet Spring (uranine data provided by M. Pronk, CHYN).

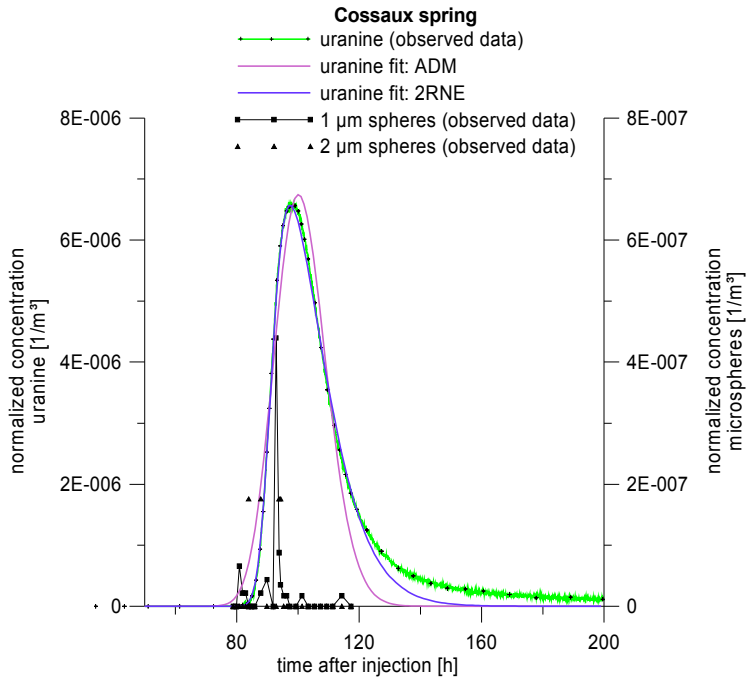

Fig. 4.88: ADM and 2RNE fitted uranine data and observed microsphere data from the Cossaux Spring (uranine data provided by M. Pronk).

In conclusion, microsphere tracers were successfully applied in this deep geothermal karst system over distances of up to 6.3 km. The TBC were partly eligible to be fitted with conventional ADM and a more sophisticated 2RNE. Uranine TBCs can be fitted by both approaches.

The microspheres illustrate the rapid flow path between the swallow hole and the two karst springs. This is of great impact for the hygienic groundwater quality of the two springs. Bacteria-sized microspheres travel faster than the solutes, and thus expose the karst springs to a potential hygienic risk that cannot be expected from solute transport. For the groundwater protection schemes in the Yverdon area this behavior has to be considered particularly with regard to the intensive land use in the surrounding area, which is a frequent source of microbial contamination.

4.4 Porous Aquifer

4.4.1 Merdingen: Upper Rhine Valley

4.4.1.1 Introduction and Location

The Merdingen test site (Fig. 4.89) is located in alluvial deposits of the Upper Rhine Valley. Approximately 300 km long and up to 35 km wide, the Upper Rhine Valley stretches out from the Jura mountains near Basel to the Rhenish Slate Mountains northwest of Frankfurt. The Southern Upper Rhine Valley is bordered by the Vosges mountains in the west and the Black Forest in the east (Fig. 4.90). The Rhine Valley is the central part of a Graben system that traverses from the Oslo-Graben in the North to the Rhône-Graben in the South throughout Europe [Illies 1977, Pflug 1982, Hüttner 1991]. The Upper Rhine Valley is characterized by different development phases in the southern, central and northern sections, which goes along with a dislocation of the subsidence area to north [Geyer & Gwinner 1991]. Vertically it can be subdivided into an Variscian basement with Pre-Cambrian to Carboniferous rocks. These are overlain by Permo-Jurassic rocks that are intersected by numerous faults. They are covered by Eocene to Quaternary sediments that are up to 3500 meters thick.

The graben formation started as the result of an Eocene crustal extension. During the Miocene the stress field changed its orientation. Sinistral strike-slip faults in the longitudinal direction of the graben with oblique principal stress (NW-SE) resulted in a subsidence of the southern and northern graben areas, while in the Rastatt-Bruchsal area a sill was formed, the so-called Karlsruher Schwelle. During the Miocene the magmatic rocks of the Kaiserstuhl arose through variscian structures, the continuation of the Bonndorfer Zone.

Quaternary sands and gravel form the most important alluvial aquifer in the Upper Rhine Valley. Underlaying Tertiary and Mesozoic rock as well as the vulcanites of the Kaiserstuhl are aquitards or aquicludes. The Quaternary sand and gravels can be composed heterogeneously both laterally and vertically and thus hydraulic properties can vary strongly. Water table contours show that near Freiburg the underground drains in northwestern direction. In the east the influence of the Black Forest becomes noticeable, whereas in the west the Rhine influences the groundwater outflow. Here it is north orientated.

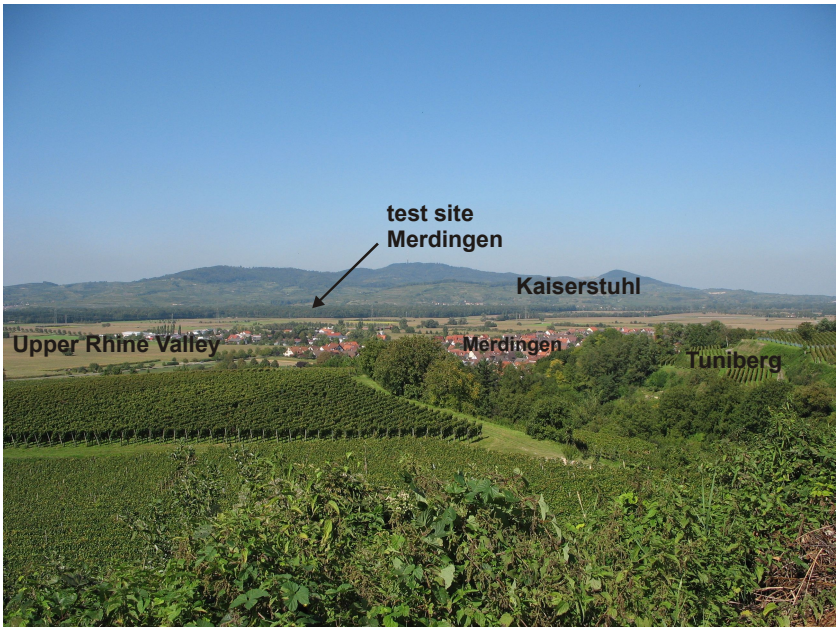

Fig. 4.89: View from Tuniberg towards the Merdingen test site (northwest of the community Merdingen) in the Upper Rhine Valley and Kaiserstuhl in the background.

The test site is located between the Kaiserstuhl and the Tuniberg, and is situated in the so-called East-Rhine-Channel that belongs lithostratigraphically to the Upper Rhine Valley. The sediments (mainly gravel) are of alpine origin, well sorted and are of higher permeability [GwD Südlicher Oberrhein 2004]. Groundwater flow is northeast orientated.

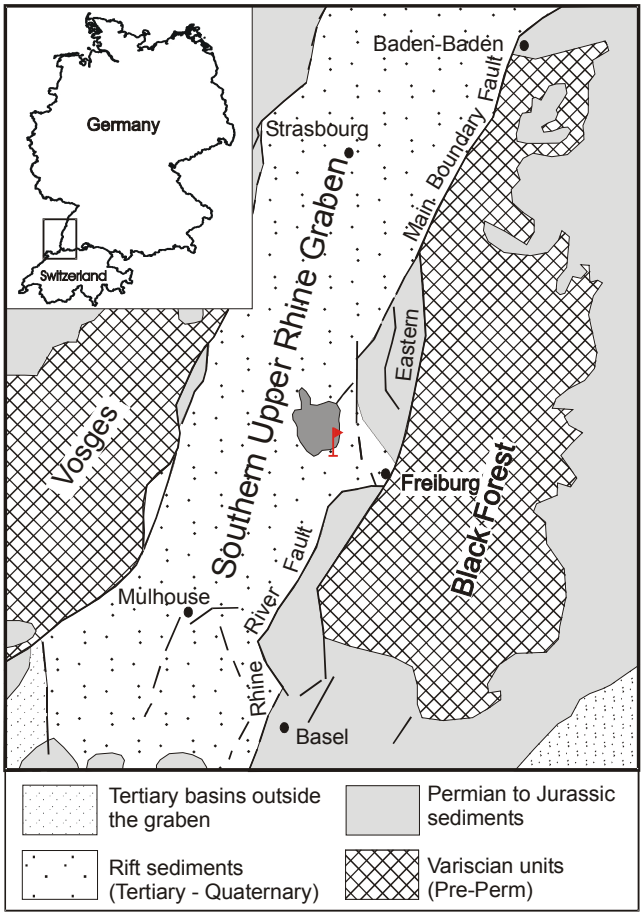

Fig. 4.90: Geology of Southwest Germany with the location of the Merdingen test site (flag) in the Upper Rhine Valley; modified after Bauer et al. 2005.

4.4.1.2 Test site

The test site has been used for groundwater tracing tests since 1979. The alluvial aquifer consists of permeable sands and gravels that are 20 meters thick and covered by a clay and humus layer of approximately one meter. The depth to the water table varies between 1.4 and 1.7 m. The water table gradient is 0.34‰ in northeastern direction. The grain size fraction includes medium and coarse gravel, the effective porosity is about 0.20 [Käss 2004]. The 3 meter deep wells are screened in the upper groundwater horizon in a depth of 1.5 to 2.5 meters (Fig. 4.91). In total, 13 wells are present; 12 wells with a maximum horizontal distance of 200 meters are used for groundwater tracing (Fig. 4.91). The distances to the injection well (N°0) are 3.1, 6.25, 12.5, 50, 100 and 200 meters. At a distance of 25 meters, a fan of 5 wells is located.

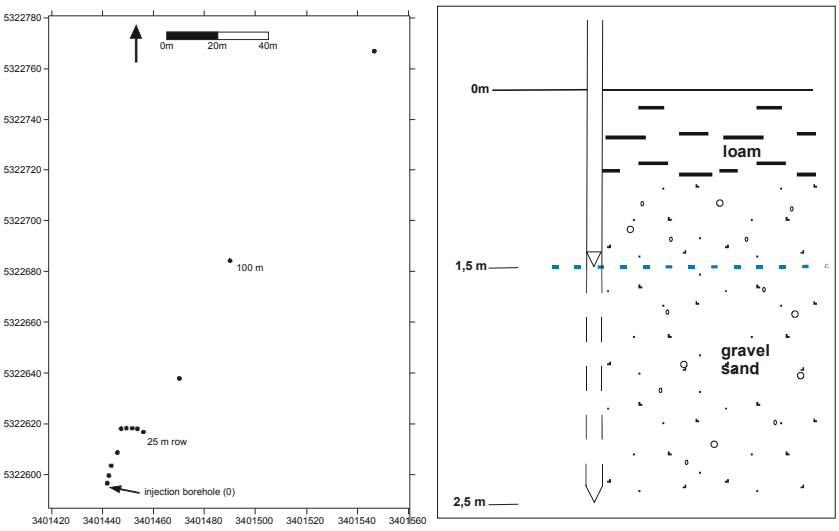

Fig. 4.91: Location of the wells at the Merdingen test site (left) and underground cross-section (right, modified after Käss 2004).

The primary test site contained two fans with a total of more than 130 boreholes. The test site – previously covered by trees – was hit very hard by the two storms Lothar (1999) and Wiebke (1990). Only the previously mentioned 13 wells were maintained afterwards. The area was not reforested after the clearing work, today it is covered by bushes and the remaining few

trees. Since this is a shallow alluvial aquifer it is expected to be strongly influenced by this change in surface coverage. Thus, the hydraulic parameters gained in previous tests have to be considered with care. The general flow field is not expected to show any change.

Previous electrical underground surveillance was described in De Carvalho Dill et al. 1992. From a cross section some 50 meters east of the test field it emerged that the uppermost layer with a thickness of up to 5 meters has varying but high resistivity (between 300 and 900 Ωm). Further down, the resistivity decreases (100 - 300 Ωm; layer with a thickness of 20 meters) until it reaches the bottom clay layer with a resistivity of below 100 Ωm.

The VLF-R method for the upper horizon for 129 points with a distance of 5 meters that covered the entire primary test site resulted in a heterogeneous picture of the resistivity distribution. Elliptical, channel-like fillings with a transversal width of some 5 meters showed enhanced resistivity (more than 300 Ωm), whereas resistivity inbetween decreases to less than 200 Ωm. The underground flow paths from the injection borehole to the sampling points are proven to pass several channel sections with different resistivities.

In 2007, three line profiles were surveyed by electrical tomography in order to understand the detailed geological underground structure near the sampling locations and to check the underground properties with more sophisticated methods than in earlier investigations.

The instrument used for electrical imaging (instrument: Campus Tigre; acquisition software Imager Pro 2000, Version 1.0.5) (Fig. 4.92) uses 32 electrodes. 4 electrodes are subsequently automatically switched on following a computer-controlled measuring schedule. This procedure combines sounding and profiling and, after inversion, a two-dimensional image of the electrical resistivity is obtained which can be related to the hydraulic conductivity [Bechtel et al. 2007]. Dry material has a higher resistivity than similar wet material; under similar moisture conditions gravel has a higher resistivity than silt or clay [Fetter 2001].

Profiles are inverted by the Res2Dinv software (Version 3.56.26). By increasing the electrode spacing profiles reach greater depth which was applied for profile N°3. Two profiles (N°1 and 2) (Fig. 4.92) of a length of 31 meters and an electrode spacing of 1 m were measured, one additional profile (N°3) was 155 meters long and used 5 m electrode spacing.

Fig. 4.92: Equipment provided by CHYN (left; photograph: N. Goldscheider) and measured profile N°2 with electrodes (detail) (right).

All of the profiles illustrate that the underground is heterogeneous. The uppermost layer of profile 1 indicates that the surface is relatively dry (and thus has a relatively high electrical resistivity) (Fig. 4.94). This might be an effect of the hot summer temperatures and the lack of sun protection by trees along the profile. The bottom loam layer with low resistivity (blue colors) that represents the aquifer base can be clearly determined through electrical imaging. Inbetween the resistivity varies.

Profile 2 perpendicular to flow direction (Fig. 4.93, Fig. 4.94) shows that two channels with enhanced resistivity (thus enhanced hydraulic conductivity, purple colors) lay on both sides of the profile. In the center is an area with resistivity values of about 100 Ωm, this can be seen as a zone of lower permeability where no significant transport can be expected. Both findings cannot be seen from the rough surveillance of the 1990s.

Profile 3 goes along the flow path (Fig. 4.93, Fig. 4.94). It shows that the injection borehole (the vertical line at a length of 7 meters) reaches a permeable area. Along the profile a zone with lower resistivity is passed that is followed by an elliptic zone with higher resistivity values. This observation is contradictory to the findings from electromagnetic measurements reported in De Carvalho Dill et al. 1992.

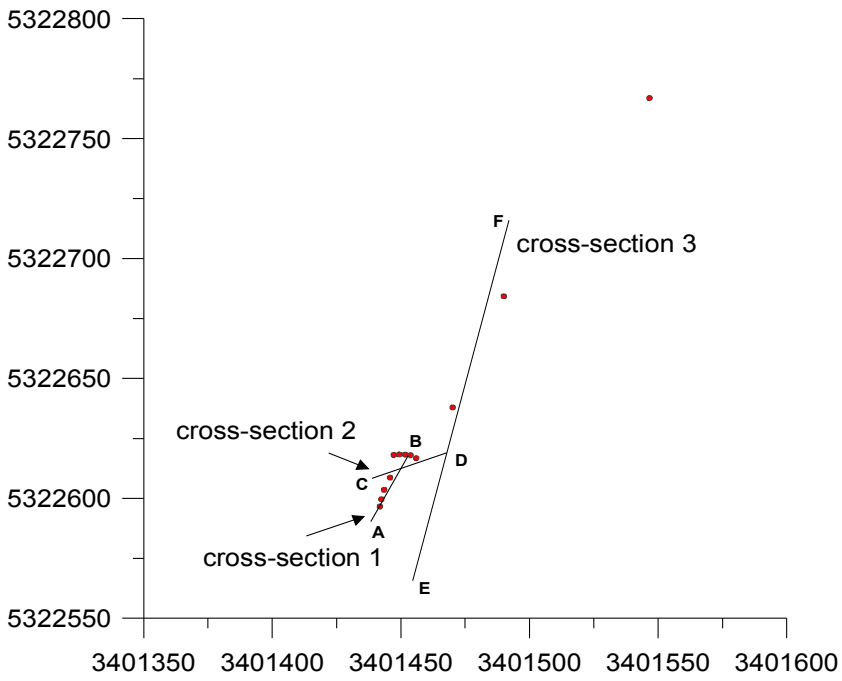

Fig. 4.93: Location of the electrical tomography profiles.

Both profiles show that the uppermost parts are covered with a loamy layer that is also described from the borehole profile (Fig. 4.91). Vertical resolution is better for the profiles with more closely spaced electrodes. So the relatively thin loamy cover layer can be better seen in profiles 2 and 3 than in profile 1.

The results of the electrical tomography give a very heterogeneous picture of the underground with flow channels and zones that vary at a small-scale (resistivity varies more than 400 Ωm in 10 meters). That finding has been previously found as well. But in detail the structure is much more complex than indicated from older measurements that only partly seem to reflect the underground properties due to the averaging over the depth. The EI profiles reflect the underground properties much better than the electromagnetic map. More electrical tomography profiles are needed to resolve the underground with its heterogeneity more adequately.

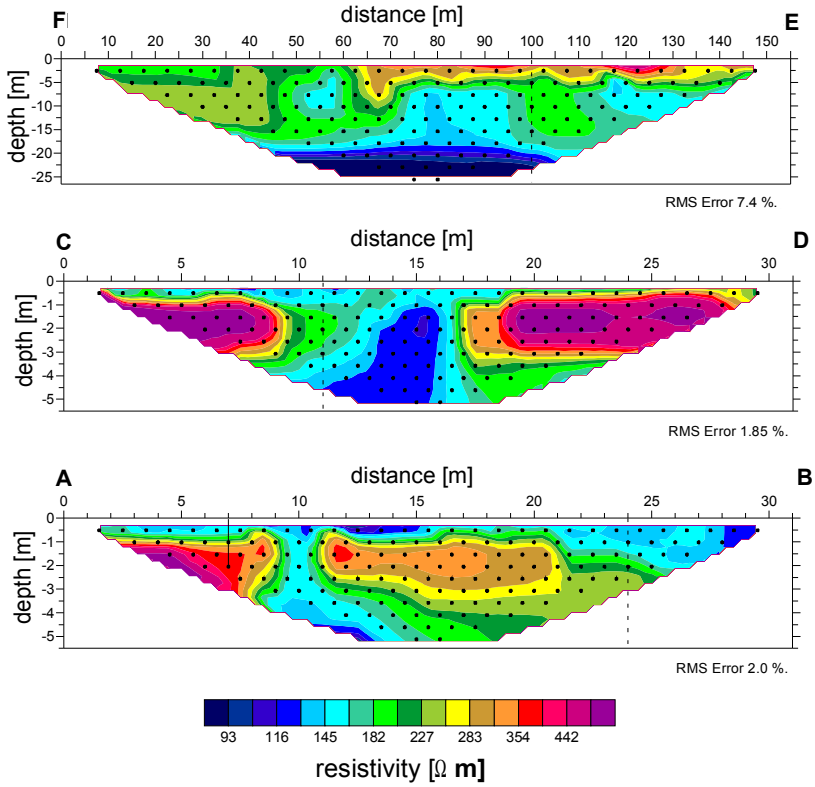

Fig. 4.94: Electrical tomography profiles (dotted vertical lines are intersection lines with other profiles, the solid line represents a projection of the injection borehole).

4.4.1.3 Previous tracer tests

A first tracer test with uranine was carried out in 1979 in Merdingen [Käss 2004]. Uranine is the most injected tracer there (14 times of in total 25 tests in a time interval from 1979 to 1998) (Tab. 4.32). Uranine is used as a conservative tracer. Compared to other tracers in alluvial aquifers, uranine shows more conservative properties; only bromide was shown to give a lower

dispersivity and higher flow velocities. Other tracers were injected to calculate retardation factors with regard to uranine: eosin 1.3; sulforhodamine b 1.4; tinopal 38; lithium 1.7; sodium 1.2; potassium 5.1; rubidium 36; cesium 42; strontium 10; cadmium 108; atrazine 2.4 and terbutylazin 1.9.

Tab. 4.32: List of previous tracer tests carried out in this part of the test site (compiled after Käss 2004).

N°	date	injection point	solute tracer			particle tracer
1	01.09.1979	0	uranine			
2	01.07.1980	0	eosin			
3	21.07.1981	0	sulforot			
4	21.02.1982	6	pyranine			
5	26.03.1982	0				*E.coli*
6	06.04.1982	6	rhodamine b			
7	16.07.1982	2	pyranine			
8	15.08.1982	0	uranine			
9	16.08.1982	0				*E.coli*
10	07.09.1982	6	urea			
11	09.04.1983	4 – 6	urea			
12	23.06.1983	0	uranine			
13	24.06.1983	0				*Serratia marcescens*
17	14.10.1984	0	frigantin			
19	14.04.1986	0	uranine	HOECHST 1687		
20	20.08.1986	0	uranine	naphthionate	lithium	
22	05.04.1988	0	uranine	tinopal csb x	cadmium	microspheres
23	31.03.1989	0	uranine	sulforot	CsCl	T4 phages
25	17.05.1990	0	uranine	naphthionate	$SrBr_2$	
27	30.04.1991	0	uranine	leukophor	$SrBr_2 \times 6H_2O$	
29	10.06.1992	0	uranine			
31	25.05.1994	0	uranine			
32	18.04.1996	0	uranine	NaF		
33	30.03.1998	0	uranine	1,5- naphthalene-disulfonate	2- naphthalene-sulfonate	
34	15.06.1996	0	uranine	Basyntan		

Exemplarily the results of the years 1984 (Tab. 4.33) and 1991 (Tab. 4.34) are described. The flow velocities for wells near the injection borehole (6.25 and 12.5 meters) are very high values of up to 22.5 m/d, it was assumed that this is a result of a oversized injection volume and that these flow velocities are not representative for the entire test site [De Carvalho Dill et al. 1992]. The

uranine results vary depending on the investigation time. In 1984 a mean flow velocity of 1.92 m/d was determined for uranine at borehole 25, in 1991 a value of 3.4 m/d. These values are generally in the same range (Tab. 4.33, Tab. 4.34), but prove that the time interval of the tracer test has to be included into the interpretation. Thus a direct comparison of different tracer substances is only valid when they are injected at the same time.

Tab. 4.33: Tracer test results of uranine for the year 1994 [Käss 2004].

distance	[m]	**25** uranine
t_1	[h]	37
t_0	[h]	92
t_m	[h]	312
v_m	[m/d]	1.92
v_m	[m/h]	0.08
D_L	[m²/h]	2.02

Tab. 4.34: Results from 1991 of uranine and bromide injections [De Carvalho Dill et al. 1992].

distance	[m]	**6.25**	**12.50**		**25**		**50**
tracer		uranine	uranine	bromide	uranine	bromide	uranine
α_L	[m]	0.46	3.6	1.6	4.6	1.8	6.6
v	[m/d]	22.5	3.9	6.0	3.4	4.8	2.9

4.4.1.4 Goals

For the tracer tests in Merdingen the following issues were of prime importance:

- What are the differences between the colloidal, solute and bacterial tracers in an alluvial aquifer? Do they show the same characteristics as indicated by laboratory tests?
- Do colloidal tracers or microorganisms travel faster than solutes at a field scale? How long can they be observed?
- How does the transport length of up to 200 meters influence the transport properties of the different tracers? Is it possible to track colloidal tracers over this distance?
- Can analytical models be used to fit the TBCs adequately?
- Does the coverage change due to storm damage appear to have an effect on the hydraulic flow parameters?

4.4.1.5 Tracer test 2005

On June 8, 2005 microspheres, solutes and bacteria were injected into borehole N^{o}0, the quantities are given in Tab. 4.35.

Tab. 4.35: Tracers applied at the Merdingen test site.

tracer	quantity
1 µm spheres	2.28E+11
2 µm spheres	2.84E+10
5 µm spheres	3.20E+09
Serratia marcescens	3.0E+09
uranine	10.03 g
sulforhodamine b	48.7 g

Tracers were dissolved and filled into two 2 L wide-necked glass flasks with a ground neck: one flask for bacteria, the second flask for microspheres and solutes. In order to avoid infiltration into the unsaturated zone by a water table increase, the tracer was introduced by a pumping technique: water is pumped from the injection borehole to the flask with microspheres and fluorescent tracers through a cap system with Drechsel-head, afterwards to the flask with bacteria and after this back into the injection borehole (Fig. 4.95).

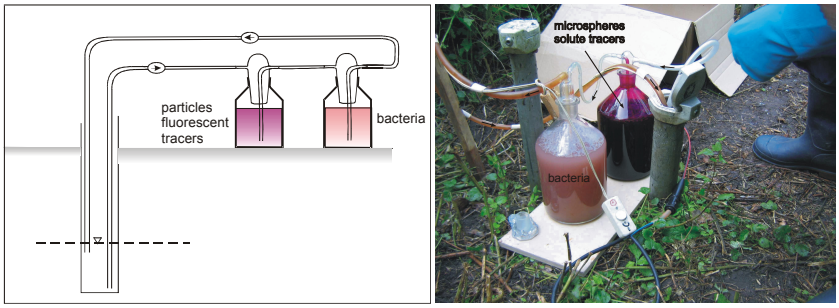

Fig. 4.95: Injection by circulation pumping (left: sketch, right: photo of the initial stadium of pumping).

Over a time span of 171 days, 21 sampling campaigns were conducted. Immersion pumps were used for sampling, three sets of brown glass bottles with a volume of 250 mL were used and split for analysis at the AGK, Käss and Klotz GmbH laboratories.

The analysis of the 1 µm and 2 µm spheres was done by counting under a fluorescence microscope, fluorescent tracers were analyzed using the spectrofluorometer (LS 55, AGK laboratory). The 5 µm spheres were analyzed with the particle counter with fluorescence detection (Syringe, Klotz GmbH) and bacteria were counted by Prof. Dr. W. Käss (Umkirch).

All samples were analyzed for fluorescent tracers and the 1 µm and 2 µm spheres. 5 µm spheres were counted up to day 58. All water samples of sampling locations 3.1, 6.25, 12.5 and 25 were analyzed on *Serratia marcescens*, sampling points 50 and 100 were analyzed up to day 71 and sampling point 200 up to day 58.

4.4.1.6 Results and discussion

Tracer test results are summarized in Tab. 4.36 and Tab. 4.37. Concentrations (normalized) for the 1 µm and 5 µm spheres, *Serratia marcescens* and uranine are given in Fig. 4.98, Fig. 4.99, Fig. 4.100 and Fig. 4.101. The TBCs of the sampling locations in 6.25 m, 12.5 m, 25 m, 50 m, 100 m and 200 m distance are given in Fig. 4.102. Sulforhodamine b behaves similarly to uranine, although recovery is expected to be lower. In the following, only the results for uranine are discussed.

Tracer breakthrough starts at the sampling point next to the injection point (3.1 m distance) after 2 hours, which means that the first sample already contains all tracers. Thus the FDT for this sampling point is equal for particle tracers and solutes. With increasing distance from the injection point, FDTs are (equal or) later and the peak times as well.

In order to compare the behavior of particles and solutes, the FDT and peak times are combined in Fig. 4.96 and Fig. 4.97. The comparison of the FDT (Fig. 4.96) illustrates that this value varies strongly depending on tracer type and quality of the TBC (more spiky TBCs give more varying parameters and are associated with a relatively high degree of uncertainty). The FDTs of *Serratia marcescens*, the 1 µm spheres and uranine show similar behavior up to sampling point 25 m. Sampling point 50 m gives slightly different results. At a larger distance, *Serratia marcescens* was not observed – but it is very likely that *Serratia marcescens* occurred at these points after sampling ended.

The comparison of the peak times (Fig. 4.97) shows that *Serratia marcescens* is typically in the range of the times of the 1 µm spheres, i.e. below the uranine peak times. The 1 µm spheres show a greater tendency to reflect this behavior, although it does not provide a perfect fit of this behavior. The bacteria peak times end – again – at sampling point 50 m. Interestingly, for the more distant sampling points (here: after 50 meters distance) the behavior of solutes and microspheres flips. At smaller distances microspheres have usually faster peak times than solutes, after 50 meters flow distance they show slower peak times. This indicates that longer flow distances result in an increase of retardation, which in turn results in greater peak times.

The maximum flow distance of bacteria is 50 meters and hence shorter than for the other tracers. The samples from 100 m were analyzed for bacteria until the peak for microspheres and uranine had passed; the analysis of *S. marcescens* was brought to completion earlier – however, it is very likely that the bacteria occurred shortly after completion.

Microspheres and fluorescent tracers were detected at the most distant sampling point of 200 meters.

Some TBCs include only few detections of tracers (Fig. 4.102), thus the results (Tab. 4.36) have to be considered with care.

After completion of the sampling campaign not all sampling points were tracer free. After the end of the test still significant concentrations of microspheres (1 µm and 2 µm spheres) and uranine were present, a behavior that can be clearly seen from the three dimensional TBCs (Fig. 4.98, Fig. 4.101). This tailing has a strong effect on the dispersion coefficients and dispersion lengths (Tab. 4.37). For the calculation of the dispersion parameters the basic equation of Käss 2004 was used. The spikiness of all tracer TBCs (Fig. 4.102) hampers a more sophisticated modeling approach like a 2RNE. When only few tracer detections could be observed, the calculation of dispersivity parameters was abandoned.

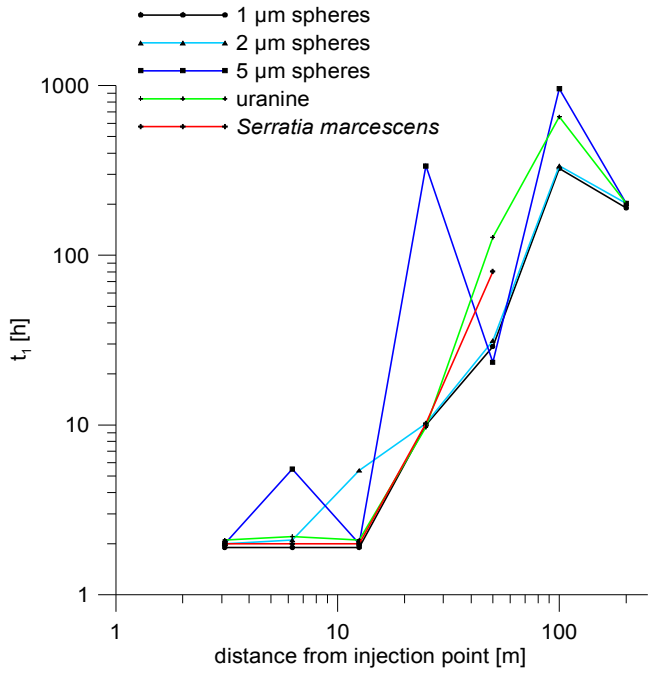

Fig. 4.96: FDT related to distance from injection point for all tracers.

Tab. 4.36: Basic results from the tracer test in Merdingen.

		1 µm spheres	2 µm spheres	5 µm spheres	*Serratia marcescens*	uranine	SRB
sampling point **3.1 m**							
t_1	[h]	2	2	2	2	2	2
v_{max}	[m/h]	1.6	1.6	1.6	1.6	1.6	1.6
t_p	[h]	2	2	2	2	5.2	5.2
v_{peak}	[m/h]	1.6	1.6	1.6	1.6	0.6	0.6
c_{peak}	[n/100mL]	5.10E+06	9.80E+05	3.20E+04	>1.0E+08		
	[µg/L]					1.60E+04	8.20E+04
sampling point **6.25 m**							
t_1	[h]	2.0	2.1	5.5	2.0	2.1	2.1
v_{max}	[m/h]	3.13	2.98	1.14	3.13	2.98	2.98
t_p	[h]	10.3	5.5	5.5	23.1	10.3	10.3
v_{peak}	[m/h]	0.61	1.14	1.14	0.27	0.61	0.61
c_{peak}	[n/100mL] [µg/L]	3.30E+06	5.20E+05	8.17E+02	>1.0E+08	1.10E+04	5.90E+04
sampling point **12.5 m**							
t_1	[h]	2.0	5.4	2.0	2.0	2.0	2.0
v_{max}	[m/h]	6.25	2.31	6.25	6.25	6.25	6.25
t_p	[h]	10.2	10.2	10.2	5.4	23.3	23.3
v_{peak}	[m/h]	1.23	1.23	1.23	2.31	0.54	0.54
c_{peak}	[n/100mL]	2.80E+05	4.10E+04	1.27E+02	>1.0E+08		
	[µg/L]					4.90E+03	2.20E+04
sampling point **25 m**							
t_1	[h]	10.2	10.2	336.0	10.2	9.8	56.5
v_{max}	[m/h]	2.46	2.46	0.07	2.46	2.55	0.44
t_p	[h]	336.0	336.0	336.0	80.5	335.6	202.0
v_{peak}	[m/h]	0.07	0.07	0.07	0.31	0.07	0.12
c_{peak}	[n/100mL]	300	100	2	1.40E+05		
	[µg/L]					1.20E+03	1.74E+02
sampling point **50 m**							
t_1	[h]	31.4	31.4	23.4	80.3	127.6	127.7
v_{max}	[m/h]	1.59	1.59	2.14	0.62	0.39	0.39
t_p	[h]	336.0	336.0	23.4	80.3	335.6	654.7
v_{peak}	[m/h]	0.15	0.15	2.14	0.62	0.15	0.08
c_{peak}	[n/100mL]	8.80E+04	9.30E+03	15	500		
	[µg/L]					1.52	2.83
sampling point **100 m**							
t_1	[h]	336.0	336.0	959.0	-	655.0	1705.0
v_{max}	[m/h]	0.30	0.30	0.10		0.15	0.06
t_p	[h]	1392.0	959.0	959.0	-	655.0	1705.0
v_{peak}	[m/h]	0.07	0.10	0.10		0.15	0.06
c_{peak}	[n/100mL]	2.50E+04	1.60E+03	3	-		
	[µg/L]					0.06	0.02
sampling point **200 m**							
t_1	[h]	202.0	202.0	202.0	-	202.0	959.0
v_{max}	[m/h]	0.99	0.99	0.99		0.99	0.21
t_p	[h]	1705.0	1705.0	202.0	-	1705.0	1705.0
v_{peak}	[m/h]	0.12	0.12	0.99		0.12	0.12
c_{peak}	[n/100mL]	2.58E+07	5.12E+06	2	-		
	[µg/L]					0.09	0.58

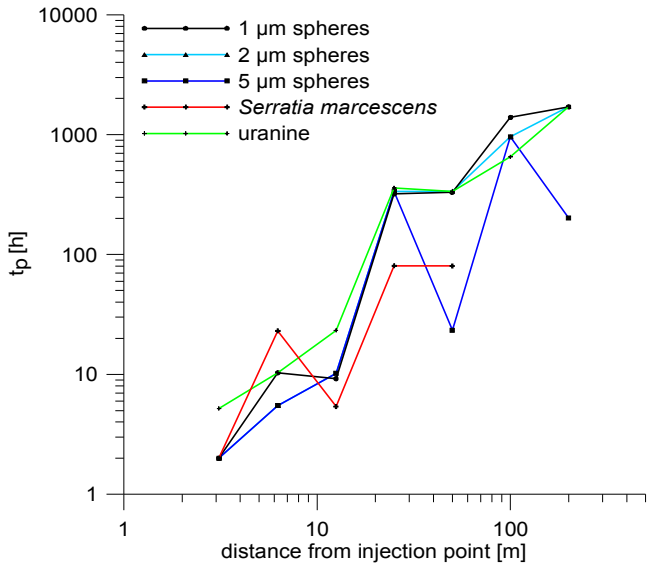

Fig. 4.97: Peak times with distance from injection point for all tracers.

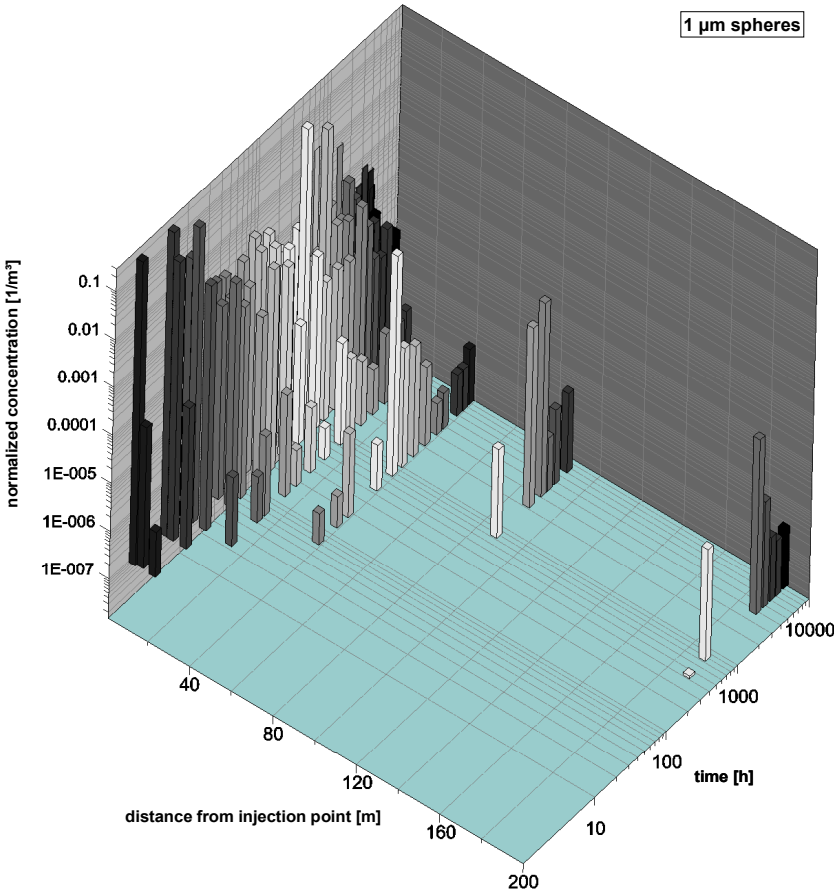

Fig. 4.98: 1 µm sphere normalized concentration for all sampling points over the entire time interval.

It can be expected that dispersion coefficients increase with increasing transport length. The calculated dispersion coefficients (Tab. 4.37) show that this occurred for 1 µm spheres, and less clear for the 2 µm spheres. Both the values for uranine and those for *Serratia marcescens* differ. However, the spikiness of the TBC results in weaker dispersion parameters and thus have to be considered with care.

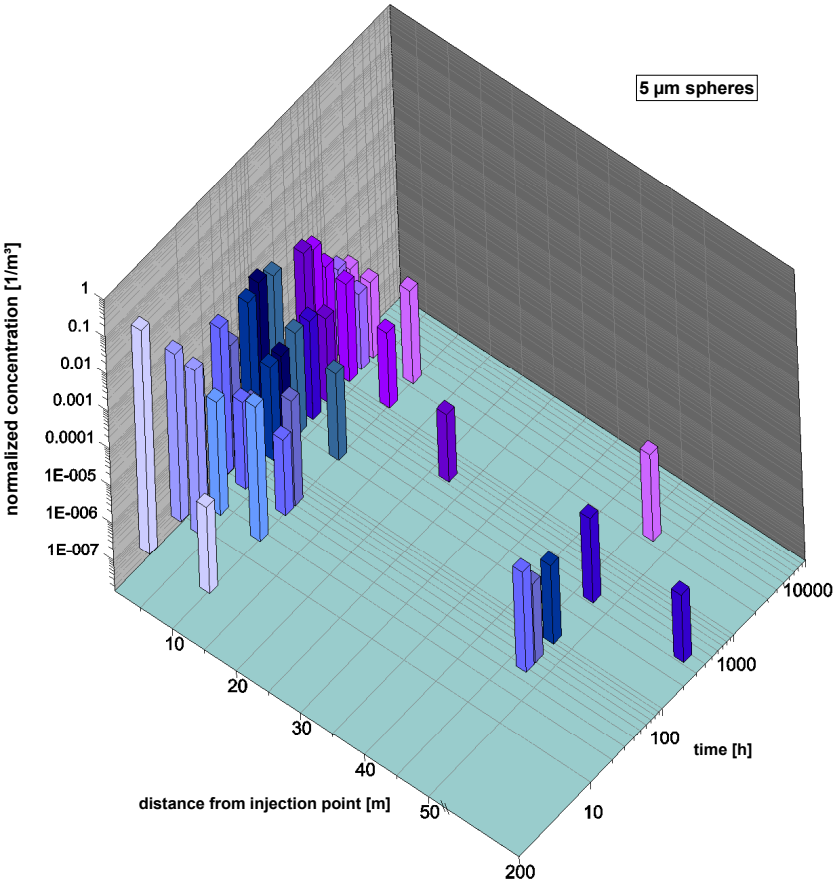

Fig. 4.99: Summarized results of the 5 µm spheres (analysis ended after 58 days).

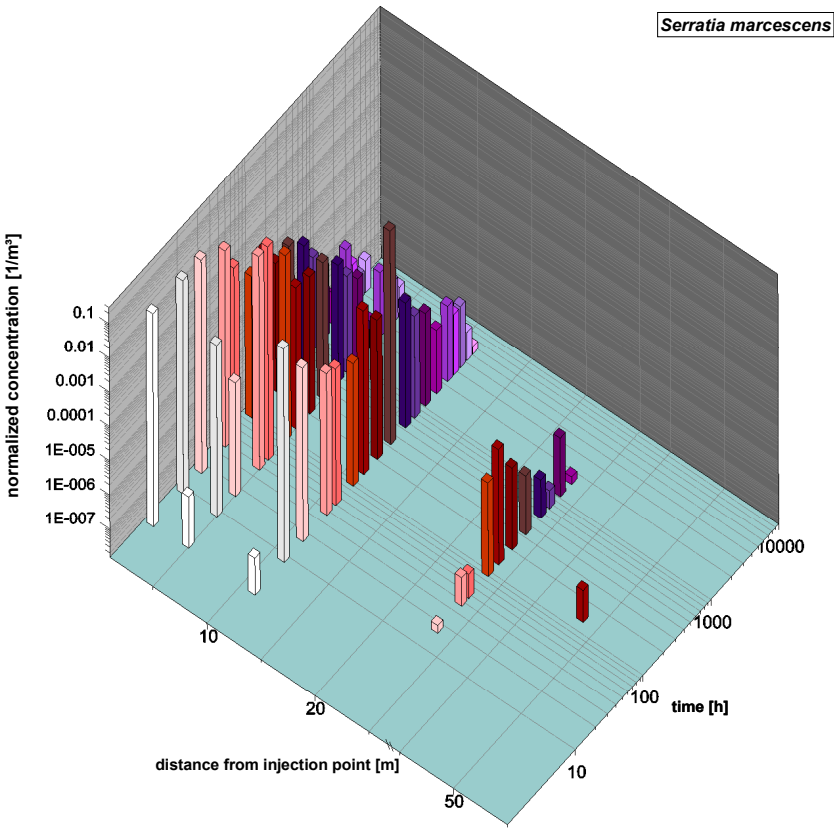

Fig. 4.100: Normalized Serratia marcescens concentrations for all samples.

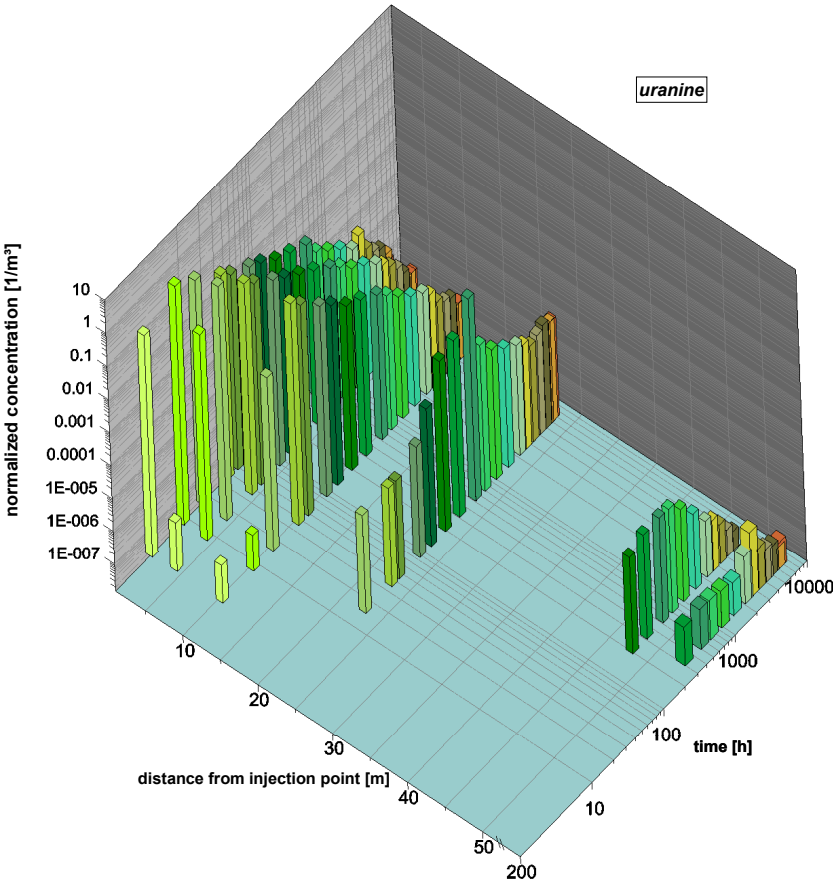

Fig. 4.101: Normalized uranine concentrations for all water samples.

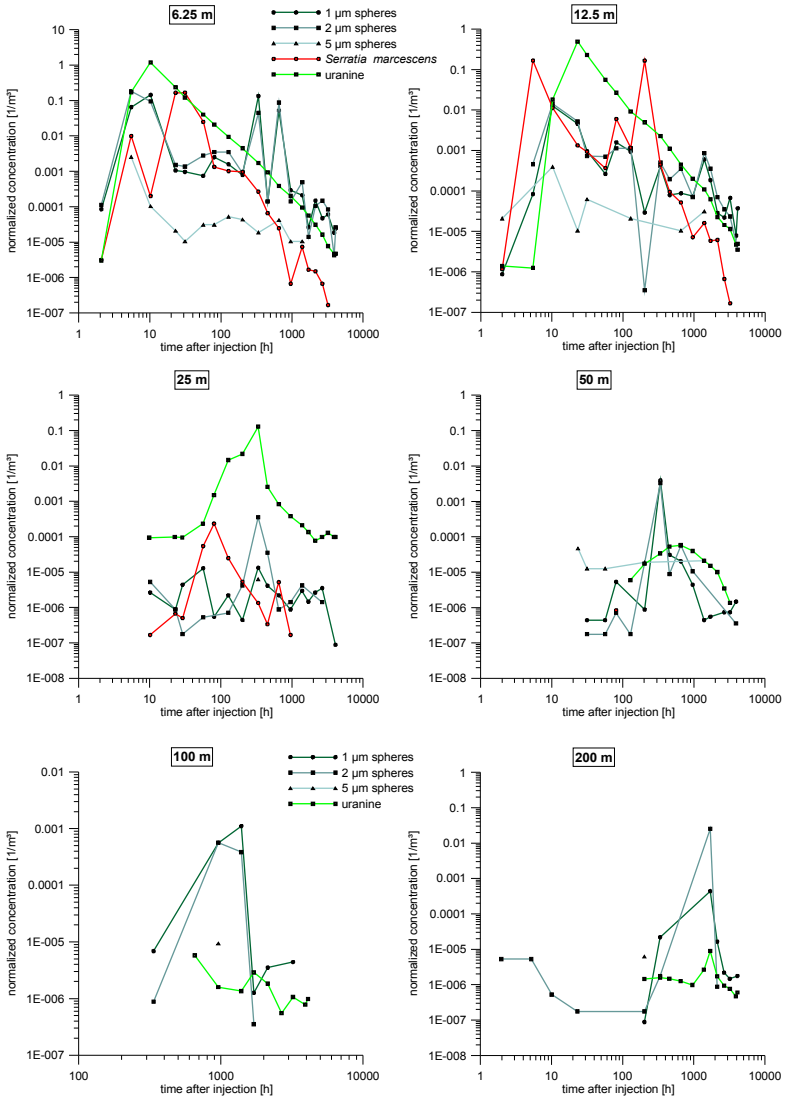

Fig. 4.102: TBC of all tracers at sampling points in 6, 12, 25, 50, 100 and 200 meters distance.

Tab. 4.37: Calculated dispersivities and dispersion lengths (as described in Käss 2004).

sampling point	tracer	D_L [m²/h]	α [m]
6.25	1 µm spheres	0.01	0.39
	2 µm spheres	0.01	0.71
	5 µm spheres	0.54	17.41
	Serratia marcescens	0.18	0.90
	uranine	0.85	3.15
12.5	1 µm spheres	0.06	4.81
	2 µm spheres	0.06	4.76
	5 µm spheres	0.06	3.28
	Serratia marcescens	0.04	0.69
	uranine	3.20	7.97
25	1 µm spheres	0.16	8.78
	2 µm spheres	0.03	0.39
	Serratia marcescens	53.75	172.96
	uranine	0.03	0.39
50	1 µm spheres	0.52	3.52
	2 µm spheres	0.11	0.77
	uranine	1.92	17.40

The analysis technique using the fluorescence microscope gave reliable results for the small microspheres (1 µm and 2 µm). Although time consuming, counting by microscope is to date the only technique that can be used to count the microspheres in this type of tracer test.

For the first time the particle counter with fluorescence detection was applied for a tracer test in an alluvial aquifer. The results prove that this device delivers reliable results: the analyzed 5 µm spheres can be detected up to the most distant sampling location. Concentrations of 5 µm are expectedly low, but result in reliable TBCs. 5 µm is about the size of human pathogens like Cryptosporidium cysts. It is shown that particles of this size can travel over a distance of 200 m in an alluvial aquifer. The last detection of 5 µm spheres comes from a sample taken after 58 days. With that sample the sampling interval for 5 µm spheres ended, but it can be assumed that microspheres could have been detected after 58 days as well.

The bacteria counting (done by Prof. Dr. W. Käss) showed that, besides the tracer bacteria, more background bacteria are present in the aquifer than known from previous tracer tests. This can be interpreted as a result of the change in vegetation from tree-covered to rather bush-covered, which might - due to more intensive root penetration of the uppermost soil layer - provide a more direct opportunity for microorganisms to reach groundwater.

The last detection of bacteria was found after 134 days, this implies that bacteria can survive underground and travel for more than 50 days in an alluvial aquifer. The combination of differently sized microspheres, a bacterial tracer and solutes covers a large range of possible contamination scenarios. The test has shown that particle tracers precede the solute tracers like uranine or SRB. The bacterium *Serratia marcescens* was detected after 50 days, the limit that is used to delineate protection zone II. Thus, it can be assumed that an introduction of particles or microorganisms into groundwater affects the groundwater quality over a longer time period than assumed. For the delineation of groundwater protection zones in alluvial aquifers, tracer tests with colloids or (harmless) microorganisms are highly recommended.

5 Conclusions and outlook

5.1 Background

Pathogenic contamination of groundwater resources is still a major problem in many areas of the world. To date, hydrogeological experiments in either laboratory scale (to study the general transport behavior of pathogens, particles or solutes) or field tests (to upscale those findings) do not provide sufficient knowledge to understand all transport mechanisms. Field investigations are always site specific, and transferability to other geological environments, hydrologic conditions or larger scale is generally problematic. Political interests and conflicts in land use management make water treatment an essential means; when it fails (or when treatment technology is not available as is the case in many developing countries) pathogen outbreaks occur and may lead to preventable illness and deaths. There is still a long way to go towards lasting protection against pathogenic contaminations in our groundwater resources.

This thesis contributes to the understanding of bacterial and viral transport in laboratory scale in comparison to colloids or solute tracer, provides a methodology to conduct laboratory studies and offers an understanding of combined colloidal and solute transport under different hydrological conditions in different aquifer types through the variety of field investigations . However, a doctoral thesis represents only a small piece of the puzzle in solving the entire set of problems.

Generally, field tests provide the opportunity to directly study the transport behavior of microorganisms, particles or solutes. Results from laboratory studies might meet with problems during upscaling. Therefore, field tests should be given preference in the interpretation of colloidal and solute transport. However, the direct application of microorganisms during field tests is strongly restricted in Germany. This is why the application and validation of surrogates like microspheres or other colloids was tested. To validate the microspheres in field tests, a combination of both microspheres and microorganisms is needed.

The microspheres were tested in five different aquifers, one fractured aquifer, three karst test sites and one alluvial aquifer. For one karst aquifer different hydrological conditions were tested (low and high flow). In the alluvial aquifer particles, solutes and microorganisms were tested; the other tests used only particles and solutes.

The main conclusions refer to the analysis technique and more generally to the laboratory tests and field investigations. For a detailed description of laboratory or site specific results and findings please see the conclusions at the end of each chapter.

5.2 Improved methods for the analysis of microspheres

The lack of appropriate measurement techniques for the analysis of fluorescent microspheres hampers the application of microspheres in laboratory tests. The technique of counting under a fluorescent microscope delivers results for field tests but has not been recently validated by other analytical methods.

This thesis fills this gap. The microsphere counting under a fluorescent microscope was validated by applying other instruments (spectrofluorometer and particle counter) and shown to deliver reliable results. An online measurement method for laboratory scale investigations was implemented in order to obtain direct results during laboratory column test operations so that sampling intervals could be optimized. A very small injection volume could be used during pulse tests and the sampling volume was kept at 100 µL, which delivers a very high resolution of data.

A particle counter with fluorescent detection was used as well. A special syringe and vessel allow analysis of smaller volumes than for field investigations. This particle counter was used to validate the spectrofluorometer data and particle counting results gained by using the fluorescent microscope.

The advantage of the counting technique by using the fluorescence microscope is the low detection limit. The main disadvantage is the time consuming procedure. By applying different analysis methods – fluorometry and particle counters – for a set of samples, the microscope method was shown to deliver reliable results.

5.3 A new software tool to evaluate spectrofluorometric data

The spectrofluorometric data was evaluated by a newly created software tool that allows to transfer the large data quantities to a file type that can be read by other evaluation programs. The spectrum files can be reduced by background files; calibration parameters allow to directly obtain the

concentration. The software follows the procedure described in Fig. 5.1 and provides the means for a rapid data evaluation by spectrofluorometry which has a detection limit that is several orders of magnitude lower than conservative measurement methods like photometry.

5.4 New insights into colloid transport on a laboratory scale

The FDT is generally used to characterize the particle and solute transport. Particle FDTs are known to precede the solutes in most cases. However, this was later on considered to be an effect of different detection limits and not one of different advection. Particles have a much lower detection limit than the solutes and thus can be detected first. By using a logarithmic scale for representation of TBCs, this can be checked via extension of the rising limb of solutes downwards to the detection limit of solutes. This procedure did not necessarily give other results for the laboratory tests presented here than indicated by simple FDT analysis. The effect of the detection limit on the particles was clearly overestimated.

Due to the abovementioned ambiguities a stronger parameter was tested: the peak travel time. This parameter was shown by Zhang et al. 2001 to be influenced by filtration. Filtration causes a peak shift towards earlier times. Zhang et al. applied peak shift analysis in order to distinguish between preceding particles due to filtration or due to different advection. By following this procedure, it was shown that for the 1 µm spheres and for most other size classes as well generally different advection (size or pore exclusion) is operating, whereas peak shift due to filtration occurs when recovery is very low.

5.5 Hydrophobic sand as improved filter

The laboratory results showed that microspheres, bacteria and phages are much more filtered in hydrophobic quartz sand compared to a hydrophilic matrix. In conclusion, the hydrophobic sand type should be of high relevance for water treatment.

5.6 Solute and colloid transport in a fractured aquifer

The fractured aquifer illustrated that the microspheres clearly precede the solutes although the degree of filtration is high and thus recovery is low. This

means for this aquifer type that contamination travels faster than expected from solute transport and – when a constant source of contamination exists – filtration operates but not all particles are filtered out. On the other hand it was shown that the microspheres do not show a large tendency for remobilization. Thus a contamination might be fixed as soon as particles are filtered out.

5.7 Solute and colloid transport in karst aquifers during different hydrological conditions

Karst aquifers are characterized by high flow velocities and a low storage capacity. Hydrological conditions have a strong influence on the transport behavior.

The Hochgrat-Gunzesried test site was characterized hydrogeologically for the first time. Surface investigations revealed a large number of karst features. Hydraulic parameters showed clearly that the underground behaves like a karst aquifer. The tracer test during high flow gave similar flow behavior for particles and solutes, TBCs were fitted by ADM and 2RNE approaches. For the Hölloch test site this behavior was very obvious and more pronounced than expected. For high flow TBC has already ended at times when TBC has not even started during low flow. Microspheres were shown to travel faster than solutes during low flow, but at equal velocities during high flow. The different flow behavior during low and high flow is due to the wide range of flow velocities, a finding that is very difficult to implement into protection schemes.

The results from the Yverdon-les-Bains test site showed that microspheres and solutes are applicable in a geothermal karst system over flow distances of more than 6.3 km. TBCs can be evaluated by the model approaches. Microspheres precede the solutes clearly.

5.8 Solute and colloid transport in an alluvial aquifer

For the first time bacteria, microspheres and solutes have been simultaneously introduced in an alluvial aquifer and spreading monitored up to a distance of 200 meters for a time span of more than 171 days. The results show that bacteria can travel longer distances than expected and survive for a longer time than predicted and assumed in delineation procedures. Although the TBCs for particles and microorganism are irregular, they show a common behavior in peak times and FDTs. The TBC of solutes is more regular; normalized concentrations for solutes are usually higher than for particles.

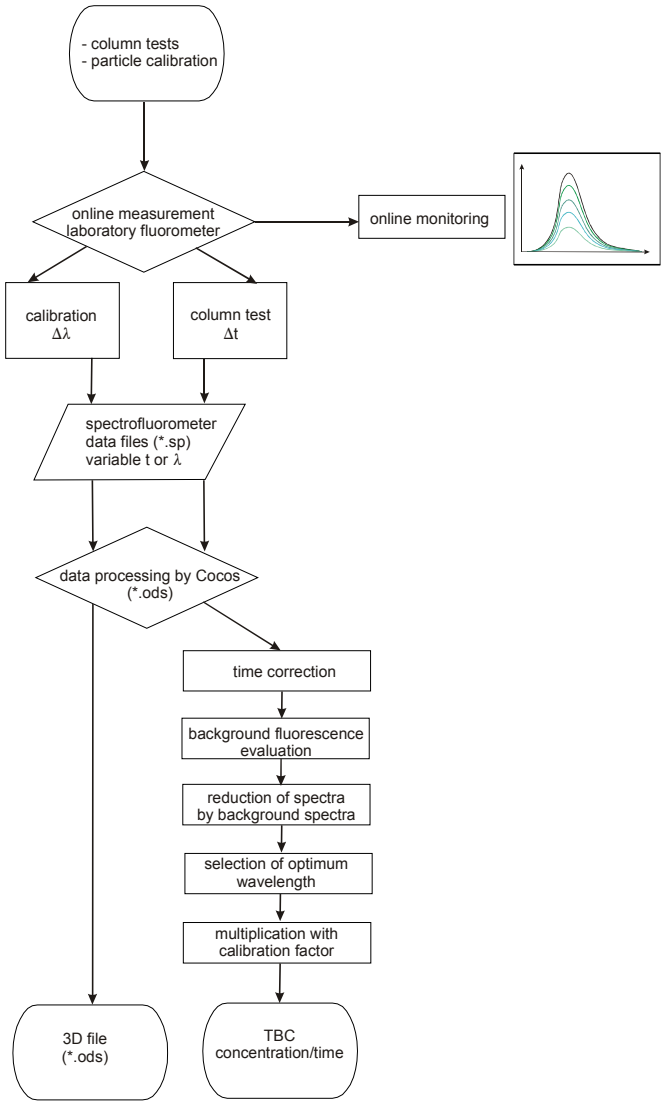

Fig. 5.1: Flowchart on the software functionality.

Different analytical tools were tested on their applicability for TBCs of field tests. The 2RNE delivered generally a better fit of the tailing of TBCs, whereas the ADM delivered more robust parameters. Only when TBCs are too spiky do both modeling approaches fail.

5.9 Recommendations and outlook

Generally, the field tests proved that the particle counter with fluorescent detection is applicable under field conditions and delivers reliable results, but still fluorescence counting by using a fluorescent microscope is the only method for particle counting of smaller size classes in field tests. Microorganisms, like the injected *Serratia marcescens*, and the 1 µm microspheres show a number of similarities in their transport characteristics. Thus it can be concluded that the 1 µm spheres provide an acceptable means to simulate the transport of *Serratia marcescens* and similar bacteria. However, due to the large variety of microorganisms, this finding has to be considered with care and future tests are to be carried out to validate this findings for other microorganisms. As a contribution in solving groundwater quality problems this thesis provides a certain variety of approaches for future research.

The laboratory software tool might be extended to other data file types, so that it can be used for other spectrofluorometry types as well. A future application might be the online measurement of unsaturated columns with automated reduction of interference signals caused by air cells.

The particle counter with fluorescence detection was shown to deliver reliable results for a specific particle size and fluorescence wavelength. Instrument development with the objective of extending the instruments' capabilities to other size classes or different wavelengths is of interest.

Hydrophobic quartz sand was shown to lead to the highest filtration capacity for microorganisms. Thus this sand treatment technique should be included into future research concerning sand filters for groundwater treatment purposes.

The influence of hydrologic conditions in field tests strongly affects the transport behavior of solutes and colloids and the relationship between them. This type of test points out the actual range of contamination that might occur, especially for karst aquifers. In order to sustainably protect groundwater resources investigations should be done during different hydrologic conditions.

The quality of field data often hampers the interpretation through more sophisticated modeling approaches. In this case, shorter time intervals might yield better interpretable results.

Finally, the application of microorganism tracers combined with fluorescent particles or solute tracers is shown to deliver interesting and valuable results for the understanding of the underground flow behavior. When hygienic problems are of concern, this experimental approach should be used to yield transferable parameters.

6 References

Agrawala, S. (2007): Climate change in the European Alps.- 128 p; Organisation for Economic Co-operation and Development OECD.

Auckenthaler, A. & Huggenberger, P. (2003): Pathogene Mikroorganismen im Grund- und Trinkwasser.- 184 p; Basel (Birkhäuser).

Auckenthaler, A., Raso, G. & Huggenberger, P. (2002): Particle transport in a karst aquifer: Natural and artificial tracer experiments with bacteria, bacteriophages and microspheres.- Water Sci Technol: 46 (3), 131-138.

Bauer, M., Eichinger, L., Elsass, P., Kloppmann, W. & Wirsing, G. (2005): Isotopic and hydrochemical studies of groundwater flow and salinity in the Southern Upper Rhine Graben.- Int J Earth Sci: 94, 565-579.

Bäumle, R. (2003): Geohydraulic characterisation of fractured rock flow regimes. Regional studies in Granite (Lindau, Black forest, Germany) and Dolomite (Tsumeb Aquifers, Northern Namibia).- Diss Univ Karlsruhe, 138 p.

Bäumle, R., Behrens, H., Einsiedl, F., Goldscheider, N., Grust, K., Hötzl, H., Käss, W., Kennedy, K., Kinzelbach, W., Kozel, R., Müller, I., Müller, J., Niehren, S., Rossi, P., Schnegg, P.-A., Seiler, K.-P., Witthüser, K., Wohnlich, S. & Zojer, H. (2001): Comparative tracer studies in groundwater.- Beitr z Hydrogeol: 52, 103-230.

Bechtel, T.D., Bosch, F.P. & Gurk, M. (2007): Geophysical methods.- In: Methods in karst hydrogeology. International Contributions to Hydrogeology. Goldscheider, N. & Drew, D. (eds.): 171-199; London/Leiden/New York/ Philadelphia / Singapore (Taylor & Francis).

Benischke, R., Goldscheider, N. & Smart, C. (2007): Tracer techniques.- In: Methods in karst hydrogeology. International Contributions to Hydrogeology. Goldscheider, N. & Drew, D. (eds.): 147-170; London/Leiden/New York/ Philadelphia / Singapore (Taylor & Francis).

Birk, S., Geyer, T., Liedl, R. & Sauter, M. (2005): Process-based interpretation of tracer tests in carbonate aquifers.- Ground Water: 43 (3), 381-388.

Box, G., Jenkins, G. & Reinsel, G.C. (1994): Time Series Analysis: Forecasting

and Control.- 598 p; Upper Saddle River, New Jersey (Prentice Hall).

Büringer, H. (2006): Trinkwasserversorgung in Baden-Württemberg.- Statistisches Monatsheft Baden-Württemberg: 5, 28-31.

De Carvalho Dill, A., Gerlinger, K., Hahn, T., Hötzl, H., Käss, W., Leibundgut, Ch., Maloszewski, P., Müller, I., Oetzel, S., Rank, D., Teutsch, G. & Werner, A. (1992): Porous Aquifer - Test Site Merdingen (Germany).- Steir Beitr z Hydrogeol: 43, 251-280.

DVGW (1995): Richtlininen für Trinkwasserschutzgebiete, 1. Teil: Schutzgebiete für Trinkwasser.- Technische Regel: Arbeitsblatt W 101, 23 p.

DVGW (2001): Verordnung zur Novellierung der Trinkwasserverordnung vom 21.Mai 2001.- 46 p.

European Union (1998): Council Directive 98/83/EC of 3 November 1998 on the quality of water intended for human consumption.- Official Council of the European Communities L 330/32: 23 p.

European Union (2000): Directive 2000/60/EC of the European Parliament and of the Council of 23 October 2000 establishing a framework for Community action in the field of water policy.- Official Council of the European Communities L 327/1: 74 p.

Everett, D.H. (1972): Definitions, Terminology and Symbols in Colloid and Surface Chemistry - Part I, Appendix to Manual of Symbol and Terminology for Physicochemical Quantities and Units.- Pure Appl Chem: 31 (4), 579-638.

Fetter, C.W. (2001): Applied Hydrogeology.- 598 p; Upper Saddle River, New Jersey (Prentice Hall).

Field, M.S. & Pinsky, P.F. (2000): A two-region nonequilibrium model for solute transport in solution conduits in karst aquifers.- J Contam Hydrol: 44, 329-351.

Ford, D. & Williams, P. (2007): Karst Hydrogeology.- 562 p; Chichester (Wiley).

Gams, I. (1978): The polje: the problem of its definition.- Zeitschr f Geomorphol: 22, 170-181.

GwD Südlicher Oberrhein (2004): Freiburger Bucht.- Materialien, Gewässer: 6, 47 p.

Geyer, O.F. & Gwinner, M.P. (1991): Geologie von Baden-Württemberg.- 482 p; Stuttgart (E.Schweizerbart'sche Verlagsbuchhandlung).

Geyer, T., Birk, S., Licha, T., Liedl, R. & Sauter, M. (2007): Multitracer test approach to characterize reactive transport in karst aquifers.- Ground Water: 45(1), 36-45.

Goldscheider, N. (1998): Hydrogeologische Untersuchungen im alpinen Karstgebiet Gottesacker und Schwarzwassertal (Allgäu / Vorarlberg).- Vorarlberger Naturschau: 4, 247-294.

Goldscheider, N. (2002): Hydrogeology and vulnerability of karst systems - Examples from the northern alps and the Swabian Alb.- Schr Angew Geol Karlsruhe: 68, 1-236.

Goldscheider, N. (2005): Fold structure and underground drainage pattern in the alpine karst system Hochifen-Gottesacker.- Eclogae geol Helv: 98 (1), 1-17.

Goldscheider, N. & Göppert, N. (2006): Das Wasser im Hölloch - Hydrogeologie .- in: Stautz, G. & Wolf, A. (eds): Das Hölloch im Mahdtal - 100 Jahre Höhlenforschung im Kleinwalsertal.- 245-253; Meckenheim (Lambach).

Goldscheider, N. & Drew, D. (2007): Methods in karst hydrogeology.- International contributions to hydrogeology: 26, 264 p.

Goldscheider, N., Hötzl, H. & Käss, W. (2001): Comparative tracer test in the alpine karst system Hochifen-Gottesacker, German-Austrian Alps.- Beitr z Hydrogeol: 52, 145-158.

Goldscheider, N., Göppert, N. & Pronk, M. (2006): Comparison of solute and particle transport in shallow and deep karst aquifer systems.- 8th Conf. Limestone Hydrogeology, September 21-23, 2006, Neuchâtel, Switzerland.

Goldscheider, N., Göppert, N., Pochon, A. & Scholz, H. (2002): Karst development in conglomerates in the northern Alps and consequences for groundwater protection.- In: Carrasco, F., Duran, J.J. & Andreo, B. (eds.): Karst and environment .- 61-67; Nerja, Malaga.

Goldscheider, N., Göppert, N., Rodenbücher, A. & Staib, R. (2004): Partikelzähler und Fluoreszenzdetektion.- Wasser: 1, 28.

Göppert, N. & Goldscheider, N. (accepted): Solute and colloidal transport in an alpine karst conduit system during high and low-flow conditions.- Ground Water.

Göppert, N. & Hötzl, H. (2006): Microbial monitoring and particle tracing as tools for assessing the hygienic risk of alpine karst springs.- AQUAinMED Internat Congr, April 24-28, 2006, Malaga, Spain.

Göppert, N., Goldscheider, N. & Scholz, H. (2002): Karsterscheinungen und Hydrogeologie karbonatischer Konglomerate der Faltenmolasse im Gebiet Hochgrat und Lecknertal (Bayern/Vorarlberg).- Beitr z Hydrogeol: 53, 21-44.

Göppert, N., Goldscheider, N. & Hötzl, H. (2003): Overview of karst development in carbonate conglomerates in Europe: A contribution to the IGCP 448 "World Correlation on Karst Ecosystems".- Internat Conf Karst Hydrogeology & Ecosystems, June 3-6, 2006, Bowling Green, USA.

Grolimund, D., Elimelech, M., Borkovec, M., Barmettler, K., Kretzschmar, R. & Sticher, H. (1998): Transport of in situ mobilized colloidal particles in packed soil columns.- Environ Sci Technol: 32, 3562-3569.

Han, J., Jin, Y. & Wilson, C.S. (2006): Virus retention and transport in chemically heterogeneous porous media under saturated and unsaturated flow conditions.- Environ Sci Technol: 40, 1547-1555.

Happel, J. (1958): Viscous flow in multiparticle systems: Slow motion of fluids relative to beds of spherical particles.- A I Ch E J: 4, 197-201.

Himmelsbach, T. (1993): Untersuchungen zum Wasser- und Stofftransportverhalten von Störungszonen im Grundgebirge (Albtalgranit, Südschwarzwald).- Schr Angew Geol Karlsruhe: 23, 238 p.

Himmelsbach, T., Hötzl, H. & Maloszewski, P. (1994): Forced gradient tracer tests in a highly permeable fault zone.- Applied Hydrogeol: 3, 40-47.

Hofmann, T. (2004): Kolloide - Die Welt der vernachlässigten Dimensionen.- Chem unserer Zeit: 38, 24-35.

Hofmann, T., Baumann, T., Bundschuh, T., v.d. Kammer, F., Leis, A., Schmitt,

D. Schäfer, T., Thieme, J., Totsche, K.-U. & Zänker, H. (2003): Aquatische Kolloide I: Eine Übersichtsarbeit zur Definition, zu Systemen und zur Relevanz.- Grundwasser: 4, 203-212.

Hunkeler, D., Goldscheider, N., Rossi, P. & Burn, Ch. (2006): Biozönosen im Grundwasser.- Umwelt-Wissen Nr. 0603, Bundesamt für Umwelt, Bern, 113 p.

Hüttner, R. (1991): Bau und Entwicklung des Oberrheingrabens, Ein Überblick mit historischer Rückschau.- Geol Jb E: 48, 17-42.

Illies, H.J. (1977): Ancient and recent rifting in the Rhinegraben.- Geol En Mijnbouw: 56 (4), 329-350.

Johnson, W.P., Li, X. & Assemi, S. (2007): Deposition and re-entrainment dynamics of microbes and non-biological colloids during non-perturbed transport in porous media in the presence of an energy barrier to deposition.- Adv Water Resour: 30, 1432-1454.

Kaddu-Mulindwa, D., Filip, Z. & Milde, G. (1983): Survival of some pathogenic and potential pathogenic bacteria in groundwater.- IAHS Publ.: 142, 1137-1145.

Käss, W. (2004): Geohydrologische Markierungstechnik - Lehrbuch der Hydrogeologie.- 2. Auflage (9), 557p; Berlin, Stuttgart (Gebrüder Borntraeger).

Kozel, R. & Schürch, M. (2005): Hydrogeologie - Grundwasser unter der Lupe.- Bundesamt für Wasser und Geologie BWG - Aquaterra: 2, 16 p.

Kreft, A. & Zuber, A. (1978): Physical meaning of dispersion equation and its solution for different initial and boundary conditions.- Chem Eng Sci: 33(11), 1471-1480.

Kretzschmar, R., Barmettler, K., Grolimund, D., Yan, Y.-d., Borkovec, M. & (1997): Experimental determination of colloid deposition rates and collision efficiencies in natural porous media.- Water Resour Res: 33 (5), 1129-1137.

Larocque, M., Mangin, A., Razack, M. & Banton, O. (1998): Contribution of correlation and spectral analyses to the regional study of a large karst aquifer (Charente, France).- J Hydrol: 205 (3-4), 217-231.

Lawrence, A.R., Macdonald, D.M.J., Howard, A.G., Barrett, M.H., Pedley, S., Ahmed, K.M. & Nalubega, M. (2001): Guidelines for assessing the risk to

groundwater from on-site sanitation.- 97 p; British Geological Survey, Commissioned Report DR/01/142.

Liesch, T. (2006): Ermittlung der Grundwassergefährdung mit Hilfe künstlicher neuronaler Netze.- Schr Angew Geol Karlsruhe: 73, 169 p.

Lytle, D.A., Johnson, C.H. & Rice, E.W. (2002): A systematic comparison of the electrokinetic properties of environmentally important microorganisms in water.- Colloids & Surfaces B: Biointerfaces: 24(2), 91-101.

Mahler, B.J., Bennett, P.C. & Zimmerman, M. (1998): Lanthanide-labeled clay: A new method for tracing sediment transport in karst.- Ground Water: 36 (5), 835-843.

Maloszewski, P. & Zuber, A. (1985): On the theory of tracer experiments in fissured rocks with a porous matrix.- J Hydrol: 79, 333-358.

Massei, N., Dupont, J.P., Mahler, B.J., Laignel, B., Fournier, M., Valdes, D. & Ogier, S. (2006): Investigation transport properties and turbidity dynamics of a karst aquifer using correlation, spectral, and wavelet analyses.- J Hydrol: 329, 244-257.

McCarthy, J.F. & Zachara, J.M. (1989): Subsurface transport of contaminants.- Environ Sci Technol: 23 (5), 496-502.

McCarthy, J.F., McKay, L.D. & Bruner, D.D. (2002): Influence of ionic strength and cation charge on transport of colloidal particles in fractured shale saprolite.- Enivron Sci Technol: 36, 3735-3743.

Montgomery, M.A. & Elimelech, M. (2007): Water and sanitation in developing countries: including health in the equation.- Environ Sci Technol: 41 (1), 17-24.

Muheim, P.F. (1934): Die subalpine Molassezone im östlichen Vorarlberg.- Eclogae geol Helv: 27, 181-297.

Padilla, A. & Pulido-Bosch, A. (1995): Study of hydrographs of karstic aquifers by means of correlation and cross-spectral analysis.- J Hydrol: 168 (1-4), 73-89.

Pflug, R. (1982): Bau und Entwicklung des Oberrheingrabens.- Erträge d Forsch: 184, 1-145.

Pochon, A. & Zwahlen, F. (2003): Ausscheidung von Grundwasserschutzzonen bei Kluft-Grundwasserleitern.- Praxishilfe. Vollzug Umwelt. Bundesamt für Umwelt, Wald und Landschaft, Bundesamt für Wasser und Geologie, Bern, 83 p.

Pronk, M., Goldscheider, N. & Zopfi, J. (2007): Particle-size distribution as indicator for fecal bacteria contamination of drinking water from karst springs.- Environ Sci Technol: 41, 8400-8405.

Pronk, M., Goldscheider, N. & Zopfi, J. (2006): Dynamics and interaction of organic carbon, turbidity and bacteria in a karst aquifer system.- Hydrogeol J: 14 (4), 473-484.

Rajagopalan, R. & Tien, C. (1976): Trajectory analysis of deep-bed filtration with the sphere-in-cell porous media model.- Am Inst Chem Eng: 22, 523-533.

Rehfeldt, K., Tompson, A., Hassan, A., Reimus, P. & Halford, K. (2004): The role of dispersion in radionuclide transport - data and modeling requirements.- U.S. Department of Energy, 1/1-6/7.

Rossi, P. (1994): Advances in biological tracer techniques for hydrology and hydrogeology using bacteriophages.- Dissertation Neuchâtel University, 133 p.

Ryan, J.N. & Elimelech, M. (1996): Review: Colloid mobilization and transport in groundwater.- Colloids Surfaces A: Physicochem Eng Aspects: 107, 1-56.

Schaltegger, U. (2000): U-Pb geochronology of the Southern Black Forest Batholith (Central Variscan Belt): timing of exhumation and granite emplacement.- Int J Earth Sci: 88, 814-828.

Schindler, P. (2003): Fäkale Verunreinigungen im Trinkwasser.- FLUGS-Seminar Wasser - Reservoir des Lebens. Aktuelle Fragen zur Wasserversorgung und -hygiene, 6. Oktober 2003, Nürnberg, 9 p.

Schoenen, D., Botzenhart, K., Exner, M., Feuerpfeil, I., Hoyer, O., Sacré, C. & Szewzyk, R. (2001): Beobachtungen über parasitenbedingte Ausbrüche durch Trinkwasser und Maßnahmen zu deren Vermeidung - Teil III: Seuchenhygienische Anforderungen.- Bundesgesundheitsbl - Gesundheitsforsch - Gesundheitsschutz: 44, 377-381.

Scholz, H. (1999): Die "klassische" Molasse-Gliederung vom Südrand des Molassebeckens in Südwestbayern - bewährt oder problematisch?- N Jb Geol

Paläont Abh: 214 (3), 391-413.

Scholz, H. & Strohmenger, M. (1999): Dolinenartige Sackungsstrukturen in den Molassebergen des südwestbayerischen Alpenvorlandes.- Jber Mitt oberrhein geol Ver: 81, 275-283.

Schütz, J. (1991): Mineralspektren von Molasse und Flysch im Gunzesrieder Achtal.- Materialien z Geographie: 18, 109 p.

Schwerd, K. (1996): Erläuterungen zur Geologischen Karte von Bayern 1:500.000.- Bayerisches Geologisches Landesamt: 329 p.

Seijmonsbergen, A.C., Woning, M.P., Verhoef, P.N.W. & de Graaff, L.W.S. (2005): The failure mechanism of a Llate Glacial Sturzstrom in the Subalpine Molasse (Leckner Valley, Vorarlberg, Austria).- Geomorphology: 66, 277-286.

Stautz, G. & Wolf, A. (2006): Das Hölloch im Mahdtal - 100 Jahre Höhlenforschung im Kleinwalsertal.- 378 p; Meckenheim (Lambach).

Toride, N., Leij, F.J. & van Genuchten, M.T. (1999): The CXTFIT code for estimating transport parameters from laboratory or field tracer experiments.- Research Report No.137. Riverside, California: US Salinity Laboratory, USDA, ARS.

Torrence, C. & Compo, G.P. (1998): A practical guide to wavelet analysis.- Bull Am Meteorol: 79, 61-78.

Tsang, Y.W. (1995): Study of alternative tracer tests in characterising transport in fractured rock.- Geophys Res Lett: 22(11), 1421-1424.

Tufenkji, N. (2007): Modeling microbial transport in porous media:Traditional approaches and recent developments.- Adv Water Resour: 30, 1455-1469.

Tufenkji, N. & Elimelech, M. (2004): Correlation equation for predicting single-collector efficiency in physicochemical filtration in saturated porous media.- Environ Sci Technol: 38, 529-536.

Umweltbundesamt (1997): Human- und ökotoxikologische Bewertung von Markierungsmitteln in Gewässern - Empfehlungen eines Arbeitskreises beim Umweltbundesamt.- Grundwasser: 2, 61-64.

Vollmayr, T. (1958): Erläuterungen zu Blatt 8426 Oberstaufen.- Geol. Kt.

Bayern 1:25000, 55 p.

Werner, A. (1998): Hydraulische Charakterisierung von Karstsystemen mit künstlichen Tracern.- Schr Angew Geol Karlsruhe, 169 p.

West, J.M., Pedley, S., Baker, S.J., Barrot, L., Morris, B., Storey, A., Ward, R.S. & Barret, M. (1998): A review of the impact of microbial contaminants in groundwater.- Environmental Agency of England and Wales, R&D Technical Report, 139 p.

WHO (1999): Emerging and Reemerging Infectious Diseases and Antimicrobial Resistance.- 15 p.

WHO (2006): Dufour, A., Snozzi, M. & Koster, W. : Assessing Microbial Safety of Drinking Water.- 296 p.

Williams, G.P. (1989): Sediment concentration versus water discharge during single hydrologic events in rivers.- J Hydrol: 111, 89-106.

Witthüser, K. (2002): Untersuchungen zum Stofftransport in geklüfteten Festgesteinen unter besonderer Berücksichtigung der Matrixdiffusion.- Schr Angew Geol Karlsruhe, 64, 145 p.

Worthington, S.R.H., Smart, C.C. & Ruland, W.W. (2003): Assessment of groundwater velocities to the municipal wells at Walkerton.- Proceedings of the 2002 joint annual conference of the Canadian Geotechnical Society and the Canadian chapter of the IAH, Niagara Falls, Ontario, 1081-1086.

Wyssling, G. (1986): Der frühkretazische Schelf in Vorarlberg und im Allgäu - Stratigraphie, Sedimentologie und Paläogeographie.- Jb Geol B-Anst: 129 (1), 161-265.

Zhang, P., Johnson, W.P., Piana, M.J., Fuller, C.C. & Naftz, D.L. (2001): Potential artifacts in interpretation of differential breakthrough of colloids and dissolved tracers in the context of transport in a zero-valent iron permeable reactive barrier.- Ground Water: 39 (6), 831-840.

Zuber, A. (1974): Theoretical possibilities of the two well pulse method.- Isotope techniques in groundwater hydrology, 277-294.

Zwahlen, F. (2004): COST Action 620 Vulnerability and risk mapping for the protection of carbonate (karst) aquifers.- 297 p.